“Always question, always wonder.”

Members of the jury

Chairman

Prof. Dr J. Colpaert, Hasselt University, Diepenbeek, Belgium.

Promoter

Prof. Dr T. Junkers, Hasselt University, Diepenbeek, Belgium.

Co-promoters

Prof. Dr A. Ethirajan, Hasselt University, Diepenbeek, Belgium.

Prof. Dr N. Hellings, Hasselt University, Diepenbeek, Belgium.

Other members

Prof. Dr D. Vanderzande, Hasselt University, Diepenbeek, Belgium.

Prof. Dr J. Hendriks, Hasselt University, Diepenbeek, Belgium.

Prof. Dr S. Van Vlierberghe, Ghent University, Ghent, Belgium.

Prof. Dr E. de Vries, VU Amsterdam, Amsterdam, The Netherlands.

Preface

Sometimes, all it takes is a closer look to discover the true beauty of something. It is out of this mindset that a new technique was born, called fluorescence microscopy. In the blink of an eye, it developed into an indispensable and fundamental method to visualize biological entities in life sciences. A literal manifestation of the saying that a light shines the brightest in the dark, it has granted researchers the opportunity to study all aspects of life with unprecedented detail. It has truly expanded our perspective on the world we live in and how we interact with it on a daily basis.

With many key factors in play, fluorescence microscopy is only as powerful as it weakest link in the chain. One of those important links is the fluorphore used to label the structure that requires investigation. A multitude of new bioimaging probes have come into existence over the past decades, each with their own benefits and drawbacks. Despite the already impressive array of materials at hand, science never stands still. Out of this urge of continuous innovation, a new potential candidate has arose, namely nanoparticles constructed out of conjugated polymers. It is their unique combination of excellent optical properties and biocompatibility that makes them outstanding fluorophores. Unfortunately, an essential feature required for usage in biomedical applications is still lacking for many conjugated polymer nanoparticles, namely the ability to functionalize their surface due to the absence of anchoring points. Hence this dissertation focuses to overcome this obstacle through the design of NP constructs out of recently developed functional poly(*p*-phenylene vinylene) (PPV).

The dissertation is a composition of four manuscripts, preceded by a general introduction and followed by a discussion. The introduction provides a review of the emergence as well as the current status of the field of PPV-based bioimaging probes. The summary encompasses all findings and puts them into perspective to address the different research aims. To conclude, a section is devoted to the future perspective with regard to the use of functional PPVs for bioimaging purposes.

Table of contents

List of figures

Chapter 1

Chapter 2

Chapter 3

Chapter 4

Chapter 5

List of tables

Chapter 2

Chapter 3

Chapter 4

Chapter 5

List of abbreviations

Ab	Antibodies
APS	Ammonium persulfate
ATR-IR	Attenuated total reflection infrared
BBB	Blood-brain-barrier
B_{NP}	Fluorescence brightness
BRET	Bioluminescence resonance energy transfer
BSA	Bovine serum albumine
C_2H_3N	Acetonitrile
C_2H_4INO	Iodoactemide
$CDCl_3$	Deuterated chloroform
CH_2O_2	Formic acid
$CHCl_3$	Chloroform
CN-PPV	Poly(2,5-di(hexyloxy)cyanoterephthalyidene)
CNS	Central nervous system
CPM-*co*-MDMO-PPV	2-(5'-methoxy-carbonylpentyloxy)-5-methoxy-1,4-phenylenevinylene
CRET	Chemiluminescence resonant energy transfer
CSF	Cerebrospinal fluid
CX_3CL1	Fractalkine
Đ	Dispersity
DAPI	Diamidino-2-phenylindole
DCC/DMAP	Dicyclohexylcarbodiimide/4-dimethylaminopyridine
DCM	Dichloromethane
DLS	Dynamic light scattering
DMEM	Dulbecco's modified eagle medium
DMSO	Dimethyl sulfoxide
DTT	Dithiothreitol
EBM-2	Endothelial cell basal medium
EDC	1-ethyl-3-(3-dimethylaminopropyl)carbodiimide
EDX	Energy-dispersive x-ray
EGF	Recombinant human epidermal growth factor

EGM-2-MV	Microvascular endothelial cell growth medium
FACS	Fluorescence-activated cell sorting
FCS	Fetal calf serum
FITC	Fluorescein isothiocyanate
FLIM	Fluorescence lifetime imaging microscopy
FRET	Fluorescence resonance energy transfer
H_2O_2	Hydrogen peroxide
HC	Hydrocortisone
HMEC-1	Human microvascular endothelial cells
hydrochloric acid	HCl
IMDM	Iscove's modified dulbecco's medium
MDMO-PPV	Poly((2-methoxy-5-(3',7',-dimethyloctyloxy))-1,4-phenylenevinylene)
MEH-PPV	Poly(2-methoxy-5-(2-ethylhexyloxy)-1,4-phenylenevinylene)
MPS-PPV	Poly(5-methoxy-2-(3-sulfo-propoxy)-1,4-phenylene-vinylene)
MS	Multiple Sclerosis
MTT	Methylthiazolyldiphenyl-tetrazolium bromide
MW	Molecular weight
NaOH	Sodium hydroxide
NH_4CO_3	Ammonium bicarbonate
NIR	Near-infrared
NMR	Nuclear magnetic resonance
NP	Nanoparticle
OH-PEG-NH_2	Hydroxyl-polyethylene glycol-amine
P/S	Penicillin/streptomycin
PALM	Photoactivated localization microscopy
PBMC	Peripheral blood mononuclear cell
PBS	Phosphate buffered saline
PDI	Polydispersity index
PEG	Polyethylene glycol
PFA	Paraformaldehyde
PFBT	Poly((9,9-dioctylfluorenyl-2,7-diyl)-co-(1,4-benzo-(2,1',3)-thiadiazole))

PMT	Photomultiplier tube
PPV	Poly(*p*-phenylene vinylene)
QD	Quantum dot
QY	Quantum yield
RESOLFT	Reversible saturable optically linear fluorescence transitions
rM-CSF	Macrophage colony stimulating factor
SDS	Sodium dodecyl sulfate
SOFI	Super-resolution optical fluctuation imaging
SSIM	Saturated structured-illumination microscopy
STED	Stimulated emission depletion
STORM	Stochastic optical reconstruction microscopy
sulfo-NHS	Sulfo-N-hydroxysulfosuccinimide
TEM	Transmission electron microscopy
TEMED	Tetramethylethylenediamine
THF	Tetrahydrofuran
UBiLim	University Biobank Limburg

Chapter 1

Introduction and aims

1.1 The evolution of learning to see more profoundly

Science is an endless journey to charter the unknown possibilities of existence. Yet answers are not only found by discovering new places but also by looking at old ones with a new set of eyes. Therefore, innovation in visualization techniques lies at the heart of almost every domain in science. A particular invention in the 17th century that has been the source of significant advances in the field of biology is the microscope. With the aid of this ingenious device, many secrets have been unveiled with regard to the building blocks of living organism and their working mechanisms.

1.1.1 The first microscope

The oldest, simplest and most widely used form of microscopy is the light microscope. An expertly crafted device, in which the specimen under investigation is illuminated with light, focused using glass lenses. It showed pioneering researchers, like Hooke and van Leeuwenhoek, that our body is actually a metropolis containing 37.2 trillion citizens [1]. Significant insights into how these cellular entities operate, both individually and as a collaborating unit, as well as what they are made from are still gained to this date with the aid of this remarkable device. However, despite the many novel technical developments and improvements in manufacturing methods over the past centuries, a limited optical detection proved to be a roadblock for solving more advanced research questions.

1.1.2 The birth of fluorescence microscopy

In 1852, Sir George Gabriel Stokes introduced the world to a new phenomenon. In his famous paper "*On the refrangibility of light*", he showcased that some substances could absorb light with a specific wavelength and within nanoseconds re-emit it, but with a longer wavelength [2]. In his article, Stokes classified this event 'dispersive reflexion', although he disclosed in a footnote that he did not particularly liked the appellation and if he needed to coin a word for the observed phenomenon he would rather call it fluorescence, from fluorspar (Figure 1-1), as the analogous term opalescence was derived from the name of a mineral. Consequently, the term fluorescence was born. The fundamental characteristic of the shift in wavelength would further on become known as Stokes' shift.

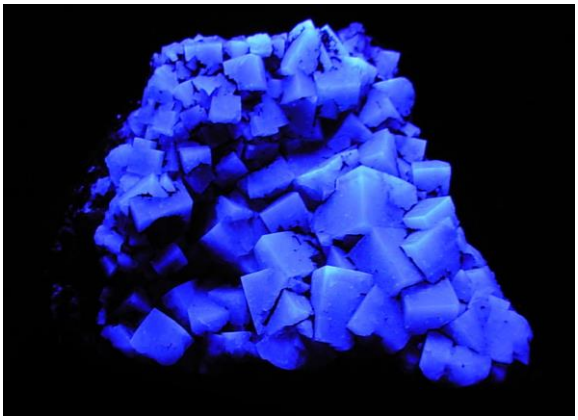

Figure 1—1: Fluorspar emitting fluorescence.

It was the discovery of this new type of luminescence that laid the foundations for a novel powerful imaging technique, fluorescence microscopy [3]. By taking advantage of the Stokes shift it facilitates the complete filtration of excitation light without obstructing any of the emitted wavelengths. This unique approach to contrast is superior to absorption-based techniques in which specimens are stained with agents that absorb light. The concluding amount of signal provides only a small difference compared to the background when the object is small, which is problematic and in sharp contrast to fluorescence microscopy where light emitting substances are more distinguishable from the background if no autofluorescence is present. As a result, fluorescence microscopy has developed into a fundamental microscopy technique for studying all types of biological specimens, fixed or alive, and enables specific as well as selective detection of molecules at low concentrations with an excellent signal-to-noise ratio.

1.1.3 Imaging in a focal plane and super-resolution

Despite these impressive features, indiscriminate excitation of the entire specimen remained an inescapable disadvantage in wide-field fluorescence microscopy, as it results in most of the fluorescent photons emerging from out-of-focus fluorophores. A solution to this complication was presented in the form of confocal laser scanning microscopy [4]. The main difference can be traced back to the form of the detector, which is a large area detector for the conventional system and a small point detector for confocal laser scanning microscopy. In this way,

photodetection is confined to light emanating from a focal volume, resulting in improved lateral resolution, unique depth discrimination and reduction in scattered light. This allows for high-resolution imaging in three dimensions.

Compared to other imaging techniques like electron microscopy, however, a lower spatial resolution caused by the diffraction of light still limits fluorescence microscopy. For the lateral direction this is 200-300 nm and for the axial direction this is 500-700 nm, which is approximately the same size or larger than many subcellular structures. During the last decades, a solution for this diffraction barrier problem has been found in the form of "super-resolution" microscopy [5, 6]. A primary example that exceeds the limit of diffraction is stimulated emission depletion (STED) microscopy, which uses 'patterned excitation'. Other super resolution methods include reversible saturable optically linear fluorescence transitions (RESOLFT), saturated structured-illumination microscopy (SSIM), stochastic optical reconstruction microscopy (STORM), photoactivated localization microscopy (PALM), super-resolution optical fluctuation imaging (SOFI), etc. These techniques have yielded the visualization of cellular structures in all dimensions, which were normally not resolvable, with unprecedented detail and have elucidated biological processes at the cellular as well as molecular scale.

Given these historical advancements, it is not inconceivable that in the short- to medium-term future, new technical developments will further revolutionize the field of fluorescence microscopy. Along with continued enhancements in the design of the devices one might also contemplate about novel imaginative fluorophore designs that could push the applicability of the bioimaging technique to novel grounds. Especially as they significantly influence the detection limit and reproducibility of fluorescence microscopy as well as the efficiency of labeling specific structural targets.

1.2 The use of fluorophores for biomedical imaging

Over the past decades, many thousands of fluorescent probes have been formulated to provide scientists with the means of labeling virtually any imaginable aspect of a biological system. They constitute the cornerstone of fluorescence microscopy and can be defined as a construct that possesses inherent fluorescent traits.

1.2.1 The modus operandi of a fluorophore

The working mechanism of fluorophores can be best demonstrated through the Jablonski diagram (Figure 1-2) [3, 7].

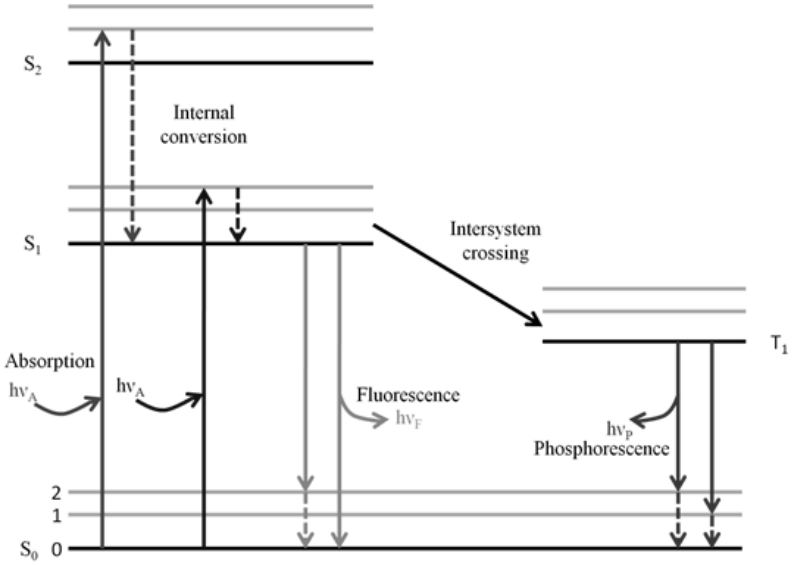

Figure 1—2: Jablonski diagram.

When (fluorescent) compounds are in their low-energy 'ground state' (S_0) and encounter a photon, of which the energy is inversely related to its wavelength ($E = h \times c/\lambda$; E = photon energy, h = Planck constant, c = speed of light in vacuum, λ = photon wavelength), an electron can be excited in a matter of femtoseconds culminating in it residing in a high-energy 'excited' state (S_1). If the quantity of energy exceeds the amount needed for the exact transition from the ground state to the lowest energy level of S_1, a change in vibration, rotation and or a move to an even higher electronic orbital (S_2) can ensue. The electron will nonetheless

shed its absorbed energy through internal conversion (S_2 to S_1) and vibrational relaxation until it reaches the lowest energy level of S_1. Then it relocates back to its 'ground state', which results in the expulsion of a photon whose energy covers the gap between S_1 and S_0. If the emission occurs between states of the same spin (S_1 to S_0), the process is called fluorescence. If there is a difference in spin state between the initial and final state (T_1 to S_0) due to intersystem crossing, the emission of light is called phosphorescence.

1.2.2 Organic dyes

One of the most extensively used types of fluorophores is the organic dye. Often these compounds possess a certain degree of conjugation, resulting in an energy difference between ground and excited state that is small enough to allow for excitation through low-energy photons of the visible part of the electromagnetic spectrum. These exemplar fluorophores can be separated into dyes of which the emission derives from optical transitions delocalized over the whole chromophore (resonant dyes), such as rhodamines and cyanines, or from intramolecular charge transfer transitions (CT dyes), like coumarins [8]. The majority of organic dyes can be categorized under the former and possesses narrow absorption and emission bands with a small Stokes shift, moderate-to-high quantum yields (QY) and high molar absorption coefficients. The latter have well-separated, broader absorption and emission bands as well as lower QYs and molar absorption coefficients. Despite the seemingly limitless toolbox of organic dyes at hand, not every purpose can be served, as they still suffer from one or a combination of shortcomings such as a low intensity (especially problematic for near-infrared), tendency to photobleach, poor Stokes shift that leads to cross talk and fast cellular clearance [8-10].

1.2.3 Fluorescent proteins

Aside from organic dyes, fluorescent proteins are a popular pick when it comes to bioimaging. Their key advantage lies in their ability to be genetically encoded and therefore be produced by living cells and organisms. Consequently, there is no need for chemical procedures or additional labeling. The most famous fluorescent protein is the green fluorescent protein (GFP). It has the additional benefit that

its production does not require any additional enzymes or cofactors in comparison to other fluorescent proteins [11, 12]. Since its discovery, various other mutants have been manufactured over the years, such as blue, cyan and yellow fluorescent protein derivatives [13]. Unfortunately, these derivatives often require secondary mutations to increase their brightness, given their inherent fluorescent capabilities are rather weak. In addition to this, most fluorescent proteins have a disappointing sensitivity and are susceptible to pH variations [12]. As a result there is still considerable interest in finding brighter and more stable fluorophores, especially for advanced bioimaging applications.

1.2.4 Nanoparticle-based fluorophores

Nowadays, by virtue of its enormous prodigious potential, nanotechnology has become inseparably intertwined with many different fields, including that of bioimaging. Through the use of nanoparticles (NPs), novel fluorophores are under active development for multidisciplinary research. NPs are generally defined as particles of which the size range is located within the nanometer range [14]. They exhibit unique properties, such as an increased surface area to volume ratio [15], which makes them interesting candidates for designing novel bioimaging probes with.

To avert some of the earlier described problems of organic dyes, like a low brightness and photobleaching, they can be encapsulated in a suitable inorganic/polymeric nanocarrier. In this configuration, the surrounding matrix serves both as a protective shell and dye isolator [16]. This counters photodegradation and confines the effects caused by the surrounding environment to which the dye would normally be exposed, such as poor solubility and the presence of oxygen. An additional benefit is the presence of multiple fluorophores per synthesized NPs, resulting in an enhancement of the fluorescence brightness. However, despite these improvements, problems can still emerge that are associated with the physical traits of the dye and the employed materials. Examples are the exclusion of dye, leading to erroneous interpretations and toxicity related issues, and self-quenching [17-19].

Another prominent example that showcases the innovative capabilities of NPs designed for bioimaging is the colloidal inorganic semiconductor NP, also known as quantum dot (QD). QDs are single semiconductor crystals with a diameter of only a few nanometers that are used in a core-shell buildup [20]. For most biomedical imaging applications, the core-material consists out of cadmium selenide or cadmium telluride and the shell out of zinc sulfide. QDs are acclaimed for their size-tunable narrow emission (quantum confinement), extremely broad absorption spectrum, high QYs (even in the near-infrared region) and resistance to photobleaching. Despite these superior optical properties, other obstacles face them. Their viability as a biological label is still under debate as a consequence of various encountered issues like *in vivo* degradation and short as well as long-term cytotoxicity issues [21, 22].

Although these two classes of nanoparticle-based fluorophores are able to overcome various shortcomings of other fluorophores, like organic dyes and GFP, the remaining number of limitation ensures that research aimed at designing novel fluorophores remains ongoing. In this regard, a very promising class of fluorophore has surfaced in the past decade.

1.3 Conjugated polymer nanoparticles

This novel class is nanoparticle-based fluorophores made up of conjugated polymers. Even though this bioimaging probe has only been introduced very recently, already major headway has been made. An argument for the remarkable research output in this area is the fact that conjugated polymer NPs are blessed with an impressive collection of advantageous properties as fluorescent tags. They possess an excellent fluorescent brightness, high emission rates and two-photon excitation cross-sections, outstanding photostability, non-blinking characteristics and demonstrate non-toxic behavior [10, 23-26]. It is this extraordinary array of properties that has generated the high demand for use in advanced biomedical imaging applications. As a result, NPs have been developed out of many conjugated polymer variants and material combinations, spanning the full range of the visible spectrum and beyond. Some noteworthy examples of employed conjugated polymers for bioimaging are polyfluorenes, poly(phenylene ethylene)s, fluorine based copolymers and poly(phenylene vinylene)s (PPV).

Nevertheless this dissertation will focus on the latter class of conjugated polymers, namely PPV and its derivatives.

1.3.1 The ways of the conjugated polymer

The first encounter with conjugated polymers can be traced back to a remarkable uncovering made by Heeger, Mac Diarmid and Shirakawa in 1977 [27]. Their research findings demonstrated that through doping with oxidizing reagents, the conductivity of the polymer polyacetylene could be increased. Since then, a wide assortment of conjugated polymers has been developed as they merge the mechanical and processing assets of polymers with the impressive electrical and optical properties affiliated with a semiconductor.

Conjugated polymers are composed of alternating single (σ-bonds) and double bonds (π-bonds), resulting in the atoms along the unsaturated polymer backbone being sp or sp^2 hybridized. As a consequence, the electrons of the π-bonds are delocalized and polarizable which creates a semiconductor-band structure. This structure consists of a conduction (devoid of electrons) and valence band (rich in electrons), with a bandgap fluctuating between 0.5 and 4.0 eV. As a result, conjugated polymers are amazing light-harvesting molecules that can interact with electromagnetic radiation and emit fluorescence [28]. When exposed to photons that contain sufficient energy, an electron can transfer from the valence into the conduction band and create an electron-hole pair (exciton). Subsequently, this electron will fall back to the valence band as a product of electrostatic interactions, which will lead to the emission of fluorescence of which the wavelength depends on the magnitude of the band gap.

1.3.2 Conjugated polymer nanoparticles synthesis routes

Conjugated polymers can be formulated into NPs by two prime methods: the direct and post-polymerization method [10, 23, 24]. Direct polymerization employs heterophase systems, enabling the *in situ* generation of conjugated polymer NPs from low molecular weight monomers through polymerization in a dispersing medium that is a bad solvent for the formed polymer. The method opens doors to a broad scope of NPs with regard to particle structure and size control and provides access to polymers that would normally be insoluble in any solvent. There are four

main categories of direct polymerization: dispersion, emulsion, miniemulsion and microemulsion polymerization.

In case of dispersion polymerization the reaction mixture is homogeneous as all of the reagents, including the monomer, are soluble in the dispersing medium. The reaction product is however not, resulting in the nucleation of NPs as soon as the growing polymer chains reach a critical chain length. To prevent newly formed NPs from aggregating, a suitable stabilizer is present in the reaction mixture, ensuring a monodispersed end product.

In emulsion polymerization the monomer possesses only restricted solubility in the dispersing medium and thus arranges itself into large isolated droplets, preserved by surfactant, coexisting with empty or monomer-swollen micelles. As the polymer reaction initiates, water-soluble initiator forms oligoradicals with slightly water-soluble monomer units diffusing throughout the dispersing medium. Once the propagating chains reach a certain threshold of hydrophobicity, they enter the micelles or nucleate particles in the dispersing medium. Through the application of shear by stirring and presence of surfactant, stabilization is maintained within the system. Concurrently with the polymerization reaction, monomer units will transfer from the large droplets into the micelles to ensure NP growth until the droplets reservoirs are completely depleted. This category of direct polymerization reactions usually yields conjugated polymer NPs with a diameter that exceeds 100 nm.

While the final NP does not resemble the primary emulsion droplet in emulsion polymerization, the complete opposite is true for the miniemulsion polymerization reaction. In this reaction, the NP end product is nearly an identical copy of the original droplet. This dissimilarity can be traced back to the inherent nature of both reactions. In emulsion polymerization kinetic processes like temperature, amount of initiator and nucleation rate, primarily determine the size of the NPs in contrast to miniemulsion polymerization where it is influenced by the dispersion process and droplet stability. In the miniemulsion method, applying high shear on the reaction mixture through methods such as ultrasonication forms nanoreactors. These nanodroplets remain stable throughout the whole polymerization process by virtue of surfactants.

The last dispersion subcategory is the microemulsion polymerization. Microemulsions are thermodynamically stable mixtures capable of existence in a particular composition regime for a given system of monomer, surfactant, dispersing medium, etc. They can be recognized by the progressive formation of a single transparent phase without the need for applying shear and are known for their dynamic nature, making the particle formation process more complex in comparison to the other direct methods.

However, it is the post-polymerization route, also known as secondary dispersion method, which is employed the most when it comes to the construction of conjugated polymer NPs. It relies on the use of preformed polymers with predefined interesting properties. With the commercially accessible polymers with established specifications, this route is widely spread as it does not require expertise in organic and polymer synthesis. There are two main reaction schemes that fall under this brand of polymerization method: the miniemulsion/solvent-evaporation and reprecipitation technique (Figure 1-3).

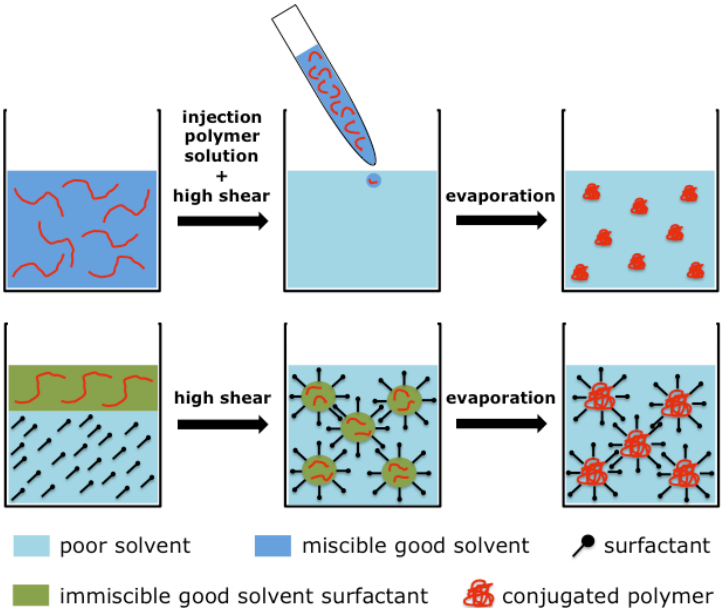

Figure 1—3: Preparation of conjugated polymer NPs using post-polymerization methods.

Schematic depiction of the two post-polymerization methods, namely the reprecipitation (top) and miniemulsion/solvent evaporation method (bottom).

The consolidation of the miniemulsion technique and solvent evaporation method for the construction of conjugated polymer NPs was demonstrated for the first time by Landfester and co-workers [29]. It involves the formation of nanodroplets through the application of ultrasonication that are comprised of the polymer dissolved in an organic solvent and are stabilized against coalescence by surfactants and against Ostwald ripening through the hydrophobic nature of the polymer itself. Following droplet formation, the organic solvent is evaporated, which leads to polymer chain precipitation and thus the formation of NPs with a size ranging between 40-500 nm.

The reprecipitation technique operates in a way similar to the "ouzo effect" [30, 31]. First, a hydrophobic conjugated polymer is dissolved in a good solvent like tetrahydrofuran (THF). Subsequently, the dilute solution is rapidly injected into an excess volume of poor solvent, in most cases water, that is miscible with the good solvent while simultaneously applying sonication or mechanical agitation in the form of high-speed stirring. The abrupt reduction in solvent quality results in precipitation of the polymer and after removal of the good solvent all that remains is a water-based dispersion of NPs with a diameter between 5-50 nm.

1.4 A brief history of poly(phenylene vinylene)-based nanoparticles

This dissertation will focus on PPV-based NPs. PPV and its derivatives (Figure 1-4) are a prominent class amongst conjugated polymers as they are one of the most thoroughly investigated semiconducting polymers to date [32]. They possess a bandgap of 2.2 eV, in case of plain-PPV, that can be tuned by the introduction of substituents on the aromatic core and tuning of the conjugation length. Throughout their existence they have been used in a large variety of advanced applications like organic light emitting diodes [33], organic photovoltaic cells [34], field effect transistors [35], biosensors [36] and more recently bioimaging as nanoparticle-based fluorophores.

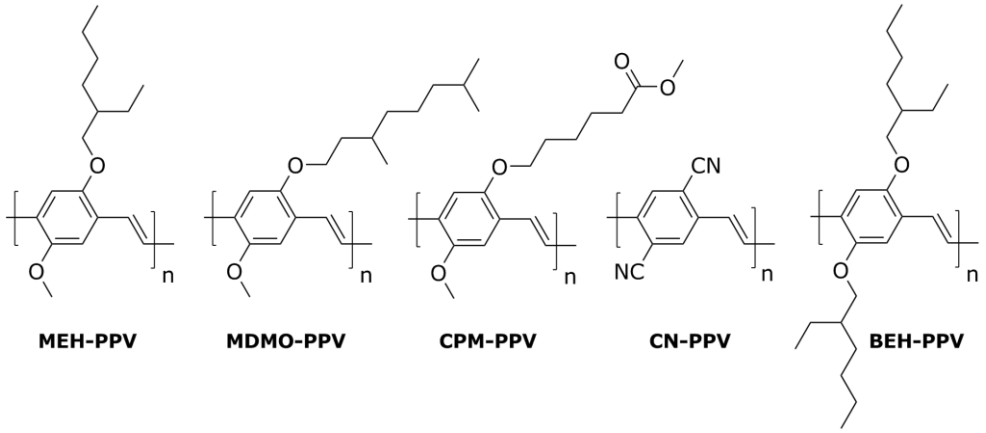

Figure 1—4: Chemical structures of PPV-derivatives.
Depiction of the chemical structures of the most commonly used PPV-derivatives, including MEH-PPV, MDMO-PPV, CPM-PPV, CN-PPV and BEH-PPV.

1.4.1 Synthesis of PPV polymers

Manufacturing of PPVs occurs primarily through step- or chain-growth methods [37]. Most PPVs are synthesized through the former, which produces PPV through a single reaction step. However, it often only allows for the synthesis of polymers with relatively low molecular weights and non-complex architectures as a result of limitations with regard to reactivity and purity of the monomers [38]. In addition to this, issues concerning the processability and solubility in common organic solvents are encountered. Examples of these direct methods are Horner [39], Knoevenagel [40], McMurry [41], Siegrist [40] and Wittig [39, 40] polycondensation reactions or palladium catalyzed Heck [42], Stille [43] and Suzuki [44] coupling reactions.

Chain growth polymerization methods for PPV manufacturing mainly involves the ring opening metathesis polymerization [45-47] and precursor routes [38]. The former converts unsaturated cyclic olefins into polymeric materials. Its main advantage is that a vinylic bond is directly obtained in the main chain of the polymer via the olefin metathesis reaction, making the π-conjugated PPV structure directly available. However, the main drawback lies in the large synthetic effort that is required for the construction of the monomer. The latter forms a precursor polymer through *p*-quinodimethane species, which subsequently is thermally

converted into PPV. It overcomes the inherent drawbacks of the step-growth method, resulting in the fast, easy and cost-effective manufacturing of high-molecular weight polymers [38]. This makes it very interesting for large-scale production. In addition, it makes it easier to control the reaction and construct PPVs with complex architectures.

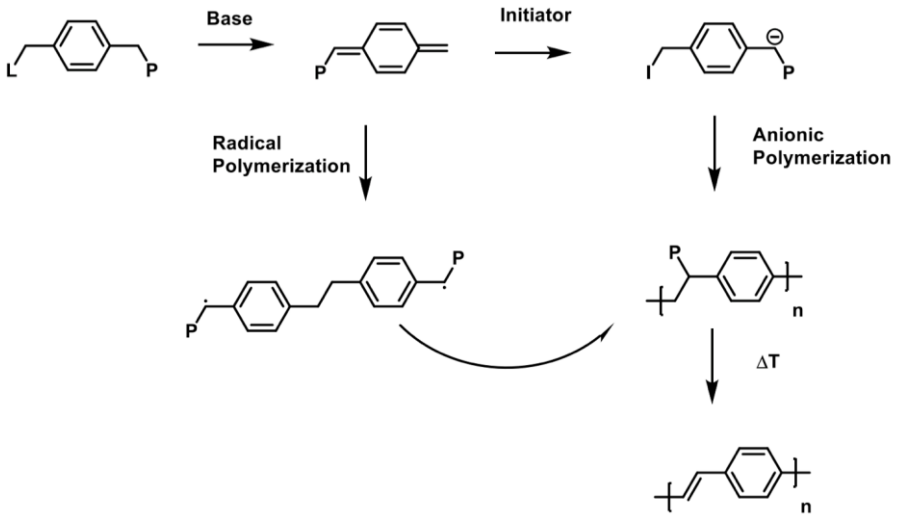

Figure 1—5: Reaction scheme of the sulfinyl precursor route

General reaction scheme of the sulfinyl precursor route *via* radical or anionic polymerization.

A precursor route that is of particular interest is the sulfinyl precursor one (Figure 1-5), as it decouples the polymerization reaction from the elimination step [48, 49]. It achieves this by starting from an asymmetric premonomer, in contrast to other routes like dithiocarbamate [50], Gilch [51], Wessling [52] and xanthate [53]. The mechanism behind the reaction can be either radical or anionic depending on the type of base and solvent employed during the reaction. The inherent division between polymerization and elimination drastically boosts control over the polymerization reaction and results in polymers with better photoluminescence [54, 55] and optoelectronic performances [38] due to a lower occurrence of defects. Furthermore, the design flexibility of this method was recently showcased with the construction of tailor-made functional PPVs [49, 56, 57].

1.4.2 MEH-PPV-based nanoparticles

The conjugated polymer poly(2-methoxy-5-(2-ethylhexyloxy)-1,4-phenylene-vinylene) (MEH-PPV) is the most extensively examined member of the PPV-derivatives family with regard to use in NP-based fluorophore constructs. It has transformed from being one of the first materials ever to be utilized as the main ingredient for bioimaging NP probes to one of the golden standards to which almost all other conjugated polymers are compared. Given the crucial impact it has had on the development of PPV-based bioimaging probes a short overview is given of the research performed so far.

Its primary use was to study the elementary characteristics of the system in various formats and under the influence of various parameters. McNeil and coworkers [9] were one of the first groups to design MEH-PPV NPs using the reprecipitation method. The NPs showcased a broad absorption band (300 – 550 nm), correlated to an unprecedented absorption cross section of the order of 10^{-13} cm^2. Although MEH-PPV's QY (2 %) is lower than other commonly used conjugated polymers (PFBT–7 %, PPE–12 %, PFO–40 %), its fluorescence brightness still easily outclasses many other fluorophores. The NPs exhibited remarkable photostability and fluorescent radiative rates, making a compelling case for their use in long-term imaging and tracking as well as high-speed applications. In addition to these outstanding photophysical properties, the NPs were taken up by cells, showed no cytotoxic effects and remained stable in cell growth medium. McNeil and coworkers [58] also demonstrated that MEH-PPV NPs are also capable of serving as fluorophores for multiphoton fluorescence microscopy, a very powerful technique that enables 3D imaging in biological systems, as they showcased an exceptionally high two-photon action cross-section in the order of 10^4 GM. It is this entirety of unrivaled properties that has made MEH-PPV such an interesting study object and catalyst for PPV-based bioimaging probe research.

Concurrently with these studies, McNeil's group implemented a method to synthesize single chain NPs and noticed that the QY and absorption cross-section appeared to be influenced by the NP size [9, 59]. An observation that was further explored by Grey *et al.* [60]. Size variations did not seem to alter the fingerprint

once the NP radius exceeded the threshold of 10 nm and mimicked that of bulk thin-films. Once the radius plunged below this border, a dual blue/red emission peak was observed as well as fluorescence intensity blinking as triplets and polarons injected by photo-oxidation can effectively quench single excitons. A more in depth look into single chain dynamics was provided by Masuo *et al.* [61], who demonstrated that exciton migration and annihilation processes are more efficient in single chain NPs. This feature makes the system a viable candidate for single-photon emission based applications, which even extends the field of bioimaging.

A study by Potai *et al.* [62] exposed the importance of the solvents employed during the reprecipitation route on the functioning of MEH-PPV NPs. By simply replacing the good solvent, the optical and physical properties were drastically altered due to a change in the chain conformation within the NPs. In case of THF the NPs consisted out of aggregates while with dichloromethane (DCM) they consisted mostly out of collapsed chains. Ghosh *et al.* [63] carried out an even more in depth investigation into the dynamics of NP formation and its implications on photophysical properties. Research conducted by the group of McNeil [64] confirmed the implications of altering chain conformation by purposely inducing swelling of the NPs. A lowering of the chromophore density consequently led to a decrease in quenching as exciton mobility to defects and various other quenching species as well as the existence of aggregated species diminished. This resulted in a blue shift of the emission spectrum and increase in QY and fluorescence lifetime. Kobayashi *et al.* [65] enforced the concept of the importance of chain conformations in the performance of MEH-PPV NPs. Instead of swelling, they applied pressure through the use of an AFM tip. The same spectral observations were made and were attributed to the creation of defects by the tip, resulting in a lowering of the conjugation length and affecting the energy transfer pathways. This is of special interest as mechanical strain and deformations are not uncommon in biological applications.

To remain into the subject of influence of the synthesis method, an intriguing question was asked by Clafton *et al.* [66] as to how it is possible for polymer chains that are hydrophobic in nature, such as MEH-PPV, to form stable NPs in

water using the reprecipitation method. They hypothesized and proved with infrared and X-ray photoelectron spectroscopy studies that chemical modification through oxidation of MEH-PPV ensued the formation of hydrophilic defects, which provide long-term colloidal stability.

Although various papers displayed MEH-PPV as a one-trick-pony when it comes to fluorescent fingerprint, Boa *et al.* [67] reversed this image by demonstrating a method to design multi-spectral MEH-PPV NPs with increased emission. Through temperature treatment of the MEH-PPV chains, the conjugation length is shortened. However, there is a limit as greater heat treatment does further blue shift the spectrum but reverses the initial boost in QY as a consequence of the appearance of carbonyl products and loss in vinylene type functions. A similar result was achieved by Jung *et al.* [68], as they tuned the emission color through pretreatment with a weak oxidant. In this case, controlled epoxidation rather than heat breaks the polymer backbone conjugation.

In addition to this wide array of studies that provide an insight into the working mechanisms of MEH-PPV bioimaging probes, Green *et al.* [69] established a novel synthesis route to synthesize MEH-PPV based NPs with, namely a reverse-micelle technique. A modification of the Landfester method, MEH-PPV is dissolved into DCM and subsequently added to a rapidly stirring solution of water/polyethylene glycol (PEG), which results with some additional processing steps into PEG-capped MEH-PPV NPs. This method usually yields NPs with an average size around 100 nm, but can be easily modified to produce small NPs of 2-5 nm [70]. No noticeable differences were observed in the photophysical properties when compared to the other synthesis routes. Follow-up studies demonstrated the versatility in choices of micelle materials by employing phospholipids [71] and executed a comparative test between miniemulsion synthesized MEH-PPV NPs covered with PEG and the phospholipid system of their behavior when exposed to different aqueous media [72]. The advantage of using a phospholipid system is the capability of attaching structures upon the surface, a higher QY and better stability in PBS. Not only phospholipids can be employed to encapsulate MEH-PPV NPs but also block copolymers, as was shown by Jung *et al.* [68].

A valid shortcoming addressed by several papers is the lack of capability to functionalize the MEH-PPV based NPs, severely limiting their applicability in biomedical experiments. A solution proposed by Wu *et al.* [31], Tan *et al.* [73] and Joshi *et al.* [74] was capturing MEH-PPV NPs in a silica shell through the condensation of active silica or alkoxysilanes. This grants easy functionalization as well as protection from photooxidation, without causing a detrimental impact on the optical properties. Another approach, namely embedding the MEH-PPV inside a PLGA matrix using the miniemulsion/solvent evaporation method, was presented by Li *et al.* [75]. However, a disadvantage when compared to the silica encapsulation method is the substantial size (300 nm) of the NPs.

MEH-PPV was not solely fit for researching the fundamental photophysical properties of conjugated polymer NPs, but has also seen a great deal of use within advanced systems designed for bioimaging purposes. These architectures often involve other complementary materials. For example, various groups have integrated MEH-PPV with near-infrared (NIR) dyes in order to circumvent the strong autofluorescence as well as scattering and absorption of high-energy light by living tissue when imaging *in vivo* [76-79]. Xiong *et al.* designed two models employing set NIR dyes for *in vivo* tumor imaging. The first model [76, 78] was a combination of the bioluminescence resonance energy transfer – fluorescence resonance energy transfer (BRET-FRET) system. The NP construct consisted of NIR dye encapsulated in a MEH-PPV NP, which in its turn was encapsulated by an amphiphilic polymer containing carboxylate groups. The latter was used as an anchoring point for a bioluminescent protein as well as targeting peptide. The bioluminescent protein serves as BRET donor, MEH-PPV as BRET acceptor and FRET donor and the NIR dye as FRET acceptor, resulting in a self-luminescent tumor tracking system. The second model [77] consisted of only MEH-PPV and a NIR dye. Palner *et al.* [79] also used this design and demonstrated that it was capable of emitting persistent luminescence with a 1 h lifetime after single excitation exposure to white light. This is a feature unique for PPV, as it can trap excitation energy within its semiconducting layer, and allows for a better separation from autofluorescence.

MEH-PPV NPs have also been paired up with photochromic dyes to generate photoswitches, a tool that is of particular interest for high-resolution applications. Harbron *et al.* [80] doped MEH-PPV NPs with the photochromic dye spirooxazine while Davis *et al.* [81] and Osakada *et al.* [82] used diarylethene derivative 1. These photochromic dyes undergo reversible structural changes when exposed to UV-irradiation, leading to quenching of the fluorescence through a FRET mechanism. PPV is an ideal core-material for photoswitches, as it does not undergo irreversible photobleaching in contrary to other conjugated polymers.

Apart from NIR dyes and photochromic dyes, photosensitizers are an appealing collaborator for MEH-PPV as they can be deployed to destroy malignant cells through photodynamic therapy while simultaneously providing the option of bioimaging. Zhang *et al.* [83] constructed such a system, which combined chemiluminescence resonant energy transfer (CRET) with FRET. The same scheme as for the NIR dye was employed, with the NIR dye being replaced by the photosensitizer m-tetra(hydroxyl-phenyl)chlorin and the NPs encapsulated in an amphiphilic Janus dendrimer that was covered with a targeting peptide and CRET catalyst. Haupt *et al.* [84, 85] used the same sensitizer but adhered it onto the exterior of the in lipid nanocoating encapsulated NPs. The advantage of the system is that the cell is not directly exposed to the sensitizer so a higher concentration can be used.

Another combination is MEH-PPV combined with other conjugated polymers to create blended NPs. McNeil and coworkers formulated various designs including combinations with polyfluorene derivatives [86] and poly((9,9-dioctylfluorenyl-2,7-diyl)-co-(1,4-benzo-(2,1’,3)-thiadiazole)) (PFBT) [87, 88]. These combinations utilize the extremely efficient FRET system to generate an enlarged Stokes shift and allow for the simultaneous excitation of multiple NPs with different emission wavelengths. The latter is of great use in applications where multiplexed fluorescence detection is required. In addition, the PFBT blends show great promise for super resolution imaging techniques, as they possess high-saturated emission rates at low excitation intensities and photoactivation phenomena owing to acceptor photobleaching. Kong *et al.* [89] also published a blend design of MEH-PPV with poly(9-vinyl carbazole).

Finally, in some cases, MEH-PPV is combined with superparamagnetic agents to generate bimodal NPs [90, 91]. These constructs are capable of complementary usage in multiple techniques like magnetic resonance and fluorescence imaging. In addition to this they can be physically manipulated by applying an external magnetic field and can now be functionalized to improve circulation time.

This overview accurately demonstrates the crucial role that MEH-PPV has played in the development of bioimaging probes based on conjugated polymers. From the endeavors to unravel their fundamental mechanics to the composition of state-of-the-art configuration, MEH-PPV has seen its use in all. However, various other important PPVs have also claimed their dividend in the field.

1.4.3 Other PPV-based nanoparticles

Another well-received member of the PPV-derivatives family is poly(2,5-di(hexyloxy)cyanoterephthalyidene) (CN-PPV). It can be converted into a NP formulation through a broad array of synthesis routes like in situ colloidal synthesis [92], microfluidics [93] and the reprecipitation [94] as well as micellar method [95]. Its primary selling point is its high QY (20-60 % depending on the synthesis route) in the red/NIR region, a valued trait that most other conjugated polymers lack. This opens up a whole new range of possibilities for *in vivo* bioimaging as CN-PPV NPs can overcome the photon-limiting interferences occurring in biological media, like autofluorescence, scattering and absorption. For example, Sehoon *et al.* [92] displayed the capability of CN-PPV NPs to be employed for lymph node mapping, while Penwell *et al.* [94] developed an approach to use them for the super-resolution technique STED. Because of its exquisite properties, CN-PPV is also regularly used in symbiotic designs with other materials. It has been encapsulated in biodegradable shells [93, 96] as well as silica [95] ones. However, it should be mentioned that cytotoxicity was already observed at a dose of 10 µg/mL for the silica encapsulated NPs. It has also been teamed up with NIR dyes [93, 97], photochromic molecules [98], photosensitizers [84, 85], other conjugated polymers [99] and L-tyrosine methyl ester [99]. A final favored architecture is a blend design with the polymer poly(styrene-alt-maleic acid) [97, 100-103], in order to generate carboxyl groups onto the NP surface that can subsequently be used for labeling. An additional observation that was

made is the fact that poly(styrene-alt-maleic acid) can cause photoblinking in CN-PPV NPs if certain conditions are met [102]. A feature required for super-resolution techniques like SOFI.

Other PPV derivatives that were adopted in the construction of conjugated polymer NPs for bioimaging are PPV-oligomers (OPVs) [104-107], poly(5-methoxy-2-(3-sulfo-propoxy)-1,4-phenylene-vinylene) (MPS-PPV) [108-110], poly((2-methoxy-5-(3',7',-dimethyloctyloxy))-1,4-phenylenevinylene) (MDMO-PPV) [111], various PPV-based block copolymers [81, 112-114], and PPV [115, 116]. This summary clearly highlights how truly versatile PPV-based nanostructures are as well as their vast potential to serve as state-of-the-art bioimaging probes. The remarkable productiveness within the field has unveiled the aptitude these probes show within the field of biomedicine. However, despite the fast progression much remains to be done to further polish PPV-based NPs into potent and consistent probes for day-to-day use by biomedical researchers.

1.5 Functional PPV-based fluorophores for bioimaging applications

Despite countless exemplary properties and fine-tuning over the past decade, some pivotal functionalities that could help advance PPV-based bioimaging probes to a whole new level remain absent. For example, when it comes to their adequacy to attach functional moieties onto the surfaces there is still room for improvement. This is an indispensable prerequisite when conducting biomedical research. One that can now be fulfilled solely through the addition of accessory materials using tedious post-synthesis methods or surface adsorbed molecules. Therefore, in an effort to counteract this shortcoming, a novel solution is offered in this dissertation. Tailor-made functional PPVs, manufactured via the sulfinyl precursor route, will be used to construct a brand new NP model with. The main research aim is to investigate whether this functional group bearing fluorophore can solve the aforementioned problem and is suitable to be utilized for biomedical research.

The next chapters of this dissertation are devoted to the following aspects: (i) the synthesis and investigation of the inherent traits of functional PPV-derivative based NP constructs, (ii) the examination of the consequences of changing the size of functional PPV-based NP constructs on their photophysical and biological properties, (iii) the study of the effect of PEGylation of functional PPV-based NP constructs on their photophysical and biological properties and (iv) the design of an advanced functional PPV-based NP construct for biomedical applications.

1.5.1 Synthesis and characterization of functional CPM-*co*-MDMO-PPV nanoparticles

Chapter 2 documents for the first time how NPs are constructed out of a functional statistical copolymer, synthesized via the sulfinyl precursor route. The employed copolymer is called 2-(5'-methoxy-carbonylpentyloxy)-5-methoxy-1,4-phenylenevinylene (CPM-PPV-*co*-MDMO-PPV, for simplicity henceforth named CPM-*co*-MDMO-PPV) and is formulated into a NP construct through the miniemulsion/solvent evaporation method. What makes CPM-*co*-MDMO-PPV so special is that it contains ester groups on its alkoxy side-chain. These can be easily converted into carboxylic acid groups that allow for the conjugation of biomolecules on request. As this is a brand new model, its innate optical (fluorescence fingerprint, QY, photostability, etc.) and biological (cytotoxicity, uptake, etc.) properties are assessed. The resulting values are compared to those of a construct synthesized out of the homopolymer MDMO-PPV to evaluate the potential repercussions of introducing functional groups via the PPV alkoxy side chain. This comparison is also extended to **chapters 3** and **4**.

For this dissertation, the premeditated choice was made to carry out the biological *in vitro* experiments on cell lines related to the central nervous system (CNS). As the biological mechanisms that underlie CNS diseases are often still shrouded in complexity, considerable interest remains present for potential new fluorophores that enable to study CNS disease related processes.

1.5.2 Implications of size variation on the inherent characteristics of functional CPM-*co*-MDMO-PPV nanoparticles

Modifying the dimensions of PPV-based NPs can exert influence on their photophysical and biological properties. However, for many biomedical applications different sizes are required to achieve a wide variety of goals. Therefore, in **chapter 3**, the size of CPM-*co*-MDMO-PPV based NPs is decreased in order to investigate whether size fluctuations affect the functioning of the fluorophore.

1.5.3 Implications of PEGylation on the inherent characteristics of functional CPM-*co*-MDMO-PPV nanoparticles

A highly requested functionality for fluorophores used in biomedical applications is stealth. Especially for difficult to reach locations in the body, such as the brain, it is of tremendous importance to increase the circulation time by remaining invisible for the body's immune system. PEG is a biocompatible and FDA approved polymer that is universally known for its capability to accomplish this daunting task. However, to date, the implications of grafting PEG onto the surface of CPM-*co*-MDMO-PPV based NPs are not yet explored. Therefore, in **chapter 4**, a more profound insight is offered on the PEGylation of CPM-*co*-MDMO-PPV NPs and any changes in the fluorophores behavior that might transpire.

1.5.4 Designing an advanced functional CPM-*co*-MDMO-PPV-based nanoparticle model for Multiple Sclerosis studies

Multiple sclerosis (MS) can be described as a chronic, inflammatory neurodegenerative disorder that causes demyelination within the CNS. Presumably, it finds its origin in an autoimmune process in which T-cells are considered to play a vital part. A cell population of particular interest for MS researchers is the $CD4^+CD28^-$ T-cell population as it undergoes an expansion in MS patients. These effector memory T-cells display pathogenic characteristics in a variety of immune disorders, including MS. Therefore, in **chapter 5**, an advanced NP construct is designed to study this intriguing cell population. The CPM-*co*-MDMO-PPV NPs are covered with the chemical moiety AZD8797, a known antagonist for the fractalkine receptor CX3CR1 expressed on various MS related cell populations, including $CD4^+CD28^-$ T-cells, converting them in a target specific

bioimaging probe. Its efficiency as a target molecule as well as antagonist is tested using a wide variety of techniques, like flow cytometry and chemotaxis assays, and blood-brain-barrier crossing capabilities are investigated *in vitro*. The inherent characteristics of the NP construct are monitored for any potential changes.

Chapter 2
Functional PPV-based conjugated polymer nanoparticles as a versatile bioimaging probe

This chapter is based on:

PPV-Based Conjugated Polymer Nanoparticles as a Versatile Bioimaging Probe: A Closer Look at the Inherent Optical Properties and Nanoparticle-Cell Interactions..

Peters M., Zaquen N., D'Olieslaeger L., Bové H., Vanderzande D., Hellings N., Junkers T., Ethirajan A.

Biomacromolecules. 2016;17(8):2562-71. IF(2016)=5.246.

Declaration of own contribution: Martijn Peters jointly designed the experiments. He synthesized the NP formulation consisting of MDMO-PPV and CPM-*co*-MDMO-PPV. He performed characterization of the inherent properties of the NP dispersions (except for TEM imaging) as well as their optical and biological characteristics. He also contributed in writing of the manuscript.

2.1 Abstract

Conjugated polymers have attracted significant interest in the bioimaging field due to their excellent optical properties and biocompatibility. Tailor-made poly(p-phenylene vinylene) (PPV) conjugated polymer nanoparticles (NPs) are in here described. Two different nanoparticle systems using poly[2-methoxy-5-(3',7'-dimethoxyoctyloxy)-1,4-phenylenevinylene] (MDMO-PPV) and a functional statistical copolymer 2-(5'-methoxycarbonylpentyloxy)-5-methoxy-1,4-phenylenevinylene (CPM-*co*-MDMO-PPV), containing ester groups on the alkoxy side chains, were synthesized by combining miniemulsion and solvent evaporation processes. The hydrolysis of ester groups into carboxylic acid groups on the CPM-*co*-MDMO-PPV NPs surface allows for biomolecule conjugation. The NPs exhibited excellent optical properties with a high fluorescent brightness and photostability. The NPs were *in vitro* tested as potential fluorescent nanoprobes for studying cell populations within the central nervous system. The cell studies demonstrated biocompatibility and surface charge dependent cellular uptake of the NPs. This study highlights that PPV-derivative based particles are a promising bioimaging probe and can cater potential applications in the field of nanomedicine.

2.2 Introduction

The tremendous efforts taken in understanding biological processes at the molecular and cellular level have led to great advances in the development of imaging tools as well as imaging probes in the last decades [117-119]. In this regard, optical imaging using fluorescence-based techniques has seen a steep rise in development leading to an unprecedented level of spatial resolution and temporal imaging that allows for investigation of biological activities such as protein transport, regulatory pathways and gene expression [120-123]. However, the potential of these advanced methods greatly depends on the characteristics of the fluorophore used as these significantly influence the detection limit, sensitivity and reproducibility of the employed technique.

Despite their extensive use, traditional probes like organic fluorophores, are hindered in high sensitivity cellular imaging applications owing to their low intensity, tendency to photobleach and a fast cellular clearance [9, 124]. Encapsulation in suitable inorganic/polymeric nanocarriers can counter some of these problems. However, problems associated with the physical characteristics of the employed materials and dye can lead to detrimental effects such as self-quenching as well as exclusion of the dye leading to erroneous interpretations and toxicity related issues [17, 18, 125]. Another prominent example under active development are colloidal inorganic semiconductor nanoparticles (NPs), also known as quantum dots, which in comparison hold several advantages such as resistance to photobleaching and a size and composition dependent narrow emission [21]. However, their potential as biological labels is still under debate due to *in vivo* degradation and both short as well as long-term cytotoxicity issues [22]. With the above-mentioned classes of materials, significant advances have been made whereby an exciting array of alternatives has become available. Yet, given the number of remaining limitations, the search for new *in vitro* and *in vivo* fluorescence probes remains ongoing.

In this regard, a very promising class of fluorescent nanoprobes is water-based luminescent nanoparticles formulated using conjugated polymers. With the inherent conjugated backbone, the latter have stipulated large interest outside the field of flexible electronics due to their excellent optical properties –

fluorescence brightness, ideal photostability, fast radiative rate and nonblinking behavior – together with biocompatibility for use in the bioimaging field [23, 126, 127]. Among the different polymers poly(*p*-phenylene vinylene) (PPV), a pioneer material for the first organic light emitting diode (oLED) and since then one of the most thoroughly studied conjugated polymers, is of great interest owing to its reliable synthesis routes in combination with design flexibility offered by the recent control methodologies for realizing tailor-made functional PPVs, simple scale up potential and their well-known photophysical properties [38, 49, 57].

Though PPV derivatives are highly interesting as a fluorophore, their interaction with biological environments and performance as bioimaging probe have not yet been fully explored to date, the research emphasis laying predominantly on synthesis routes and inherent material characteristics. Only the use of poly[2-methoxy-5-(2-ethylhexyloxy)-1,4-phenylenevinylene] (MEH-PPV) and poly[2,5-dicyano-*p*-phenylene vinylene] (CN-PPV) for biomedical applications has been studied more extensively, but these specific PPVs lack the functional groups necessary for surface modification when formulated for more advanced applications [128-131]. Functional moieties on the NP surface play an important role since they determine their biological identity [132, 133]. They are indispensable for attaching biomolecules to impart for instance target specificity or a stealth effect. Instead of being forced to use complex and tedious post-synthesis methods in a later stadium or surface adsorbed surfactant molecules [126], functionalized PPVs synthesized via the sulfinyl precursor route offer an elegant alternative to introduce surface functional groups. By employing such custom-made PPV-derivatives for the NP formulation, the synthetic identity of the NP based bioimaging probe can be fine-tuned to meet the set out conditions in the biological environment.

This study aims to shed light on the inherent characteristics of these yet unexplored PPV-based NPs, as compared with other established probes, and their interaction with biological systems resulting in a more profound insight in the use of conjugated polymer nanoparticles in biological sciences. The hydrophobic polymers are formulated into water-based NPs using the versatile miniemulsion technique in combination with the solvent evaporation method (Figure 2-1A) [24, 134]. Briefly, a two phase system is created consisting of a dispersed phase,

containing preformed conjugated polymer dissolved in chloroform, an easy to evaporate organic solvent and a continuous phase, containing surfactant in an aqueous solution [135]. After emulsification using high shear forces, stable nanodroplets are generated in which – after evaporation of the solvent – solid nanoparticles are formulated by precipitation of the conjugated polymer chains. In this way, a homogenous population of stable nanoparticles is created with a size range ideal for biomedical applications.[136, 137] In here, two separate nanoparticle systems are designed using poly[2-methoxy-5-(3',7'-dimethoxyoctyloxy)-1,4-phenylenevinylene] (MDMO-PPV) and a functional statistical copolymer 2-(5'-methoxycarbonylpentyloxy)-5-methoxy-1,4-phenylenevinylene (CPM-PPV-*co*-MDMO-PPV, for simplicity henceforth CPM-*co*-MDMO-PPV) containing ester groups on the alkoxy side chains (Figure 2-1B and C).

The ester groups present on the surface of the CPM-*co*-MDMO-PPV NPs can be conveniently converted into carboxylic acid groups through hydrolysis for the facile coupling of various biomolecules as per demand. As a proof-of-concept, in here gold-labeled antibodies (Ab) were attached to the NP surface. As finding therapies for central nervous system (CNS) diseases is often a stumbling block due to the complexity involved in the underlying biological processes, it is imperative to understand the biological activities occurring at the cellular level. Therefore, there is a significant interest for potential imaging probes for studying CNS processes [138]. In the present study, conjugated polymer nanoparticles as a suitable fluorescent nanoprobe for studying cell populations within the CNS was tested. To date and to the best of our knowledge such studies do not exist for PPV-based NPs and in general only very limited studies involving conjugated polymer NPs for such biological systems are available [139].

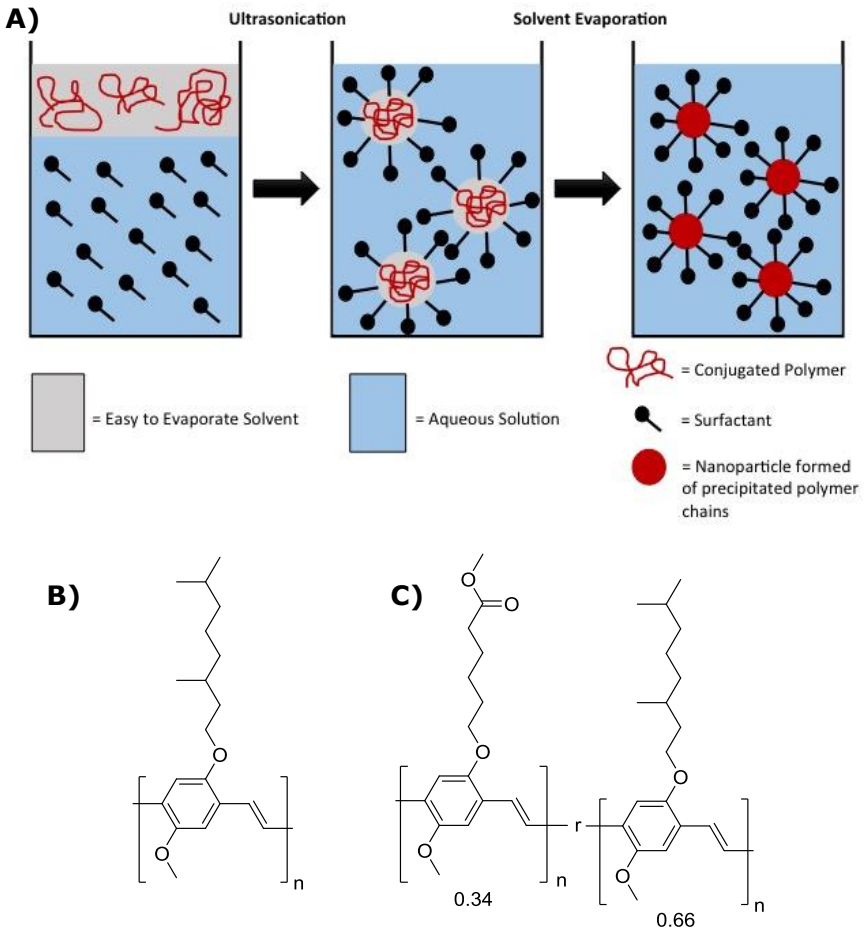

Figure 2—1: Miniemulsion/solvent evaporation method and chemical structure of employed PPV-derivatives.

Combination of the miniemulsion technique and solvent evaporation method for the synthesis of conjugated polymer NPs (A) and chemical structures of the used PPV-derivatives: MDMO-PPV (B) and CPM-*co*-MDMO-PPV (c).

2.3 Materials and methods

2.3.1 Materials and products

Sodium dodecyl sulfate (SDS), amicon ultra filter membrane tubes, 1-ethyl-3-(3-dimethylaminopropyl)carbodiimide (EDC) and sucrose were purchased from Merck (Overijse, Belgium). MDMO-PPV and CPM-*co*-MDMO-PPV were synthesized using the sulfinyl precursor route [56, 140]. The gold-labeled goat anti-mouse IgG(H+L) was purchased from KPL (Erembodegem, Belgium). Triton X-100 was purchased from Sigma-Aldrich (Diegem, Belgium) as well as tetrahydrofuran (THF), deuterated chloroform ($CDCl_3$), rhodamine 6G, rhodamine B, fluorescein isothiocyanate (FITC), hydrogen peroxide (H_2O_2), penicillin/streptomycin (P/S), hydrocortisone (HC), L-glutamine, trypsine and paraformaldehyde (PFA). Chloroform ($CHCl_3$) and sulfo-N-hydroxysulfosuccinimide (NHS) were bought at VWR (Leuven, Belgium). The square-mesh copper transmission electron microscopy (TEM) grids were bought from Electron Microscopy Sciences (Hatfield PA, US). MCDB 131 medium, Dulbecco's Modified Eagle Medium (DMEM) medium, Iscove's Modified Dulbecco's Medium (IMDM) medium, fetal calf serum (FCS), recombinant human epidermal growth factor (EGF), methylthiazolyldiphenyl-tetrazolium bromide (MTT), alamar blue, mouse monoclonal anti-α-tubulin antibody, Alexa Fluor® 488 Donkey Anti-Mouse IgG (H+L) antibody and 4',6-Diamidino-2-Phenylindole (DAPI) were purchased from Life Technologies (Ghent, Belgium). Bovine serum Albumin (BSA) was bought at USBiological (Swampscott MA, US). The culture plates and dark plates were obtained at Greiner Bio One (Vilvoorde, Belgium). The μ-Slide 8 Well plates were ordered at Ibidi. The 1x phosphate buffered saline (1xPBS) was bought at Lonza (Verviers, Belgium). HeLa (CCL-2), C8-D1A cell line (CRL-2541) and human microvascular endothelial cells (HMEC)-1 (CRL-3243) were purchased at ATCC (Molsheim, France). BV-2 cell line (ATL03001) was bought at ICLC (Genova, Italy). All chemicals were used as provided without further purification.

2.3.2 PPV-based NP preparation

Conjugated polymer nanoparticles using MDMO-PPV and the statistical copolymer CPM-*co*-MDMO-PPV were synthesized using the combination of miniemulsion and solvent evaporation method. Both PPV derivatives and their respective monomers were synthesized following literature procedures [56, 140]. A solution of MDMO sulfinyl premonomer (1.00 g, 2.05 mmol, 0.30 equiv.) and CPM sulfinyl premonomer (2.27 g, 4.77 mmol, 0.7 equiv.) in *sec*-butanol (14.8 mL) and a base solution of Na*t*BuO (0.256 g, 2.67 mmol, 1.3 equiv. to 1 equiv. premonomer blend) in *sec*-butanol (16.8 mL) were degassed three times at 30 °C using nitrogen. Equivalents (0.3 and 0.7) represent the theoretical ratio of the monomer units within the copolymer. In case of MDMO-PPV polymer synthesis only 1 equiv. of MDMO sulfinyl premonomer is taken. The base solution was added in one portion to the stirred monomer solution to start the reaction. After 1 h, the reaction was quenched with HCl (1 M, 50.0 mL). After extraction with CH_2Cl_2 (3 mL × 50 mL) and evaporation, synthesis towards the conjugated PPV was immediately followed. Precursor PPV (2.00 g) in toluene (200 mL) was degassed by purging for 15 min with nitrogen, after which the solution was heated to 110 °C and stirred for 3 h under nitrogen atmosphere. Subsequently, the reaction was cooled down to room temperature and precipitated in cold MeOH (40 mL) and filtered on a Teflon® filter. This enables to selectively isolate the desired high-molecular weight polymer product (gravimetric yield 75 %). The conjugated CPM-*co*-MDMO-PPV as well as the MDMO-PPV polymer were obtained as a red solid. The obtained MDMO-PPV polymer had a molecular weight (M_n) = 150 000 g·mol^{-1} with dispersity (*Đ)* = 2.7 and the CPM-*co*-MDMO-PPV polymer a M_n = 164 200 g·mol^{-1} with *Đ* = 2.7.

For the NP formulation, the continuous phase consisted of 16 g from a 72 mg SDS in 24 g ultrapure water solution. The dispersed phase contained 100 mg of the respective conjugated polymer in 6.625 g of $CHCl_3$. After adding the continuous phase to the dispersed one, the mixture was pre-emulsified for 1 hour at 1000 revolutions per minute (rpm) at room temperature. The pre-emulsification step was followed by ultrasonication under ice cooling using a Branson 450W digital sonifier (Soest, The Netherlands) with a 1/4”-tip for 3 min at 65 % amplitude using a 30 s pulse and 20 s pause regime. The resulting nanodroplet containing

emulsion was placed on a hotplate and the organic solvent was evaporated at 40 °C by stirring for 18 h at 500 rpm. The resulting red colored dispersion was passed through a paper filter (Whatman, pore size 4 – 7 μm) to remove any large aggregates. The excess SDS was washed using multiple centrifugation/redispersion steps with a Sigma 3-30K centrifuge (Suarlée, Belgium). First, 40 washing steps of 30 min at 2000 rpm were done with membrane tubes, followed by 3 steps at 14 000 rpm for 1 h with eppis. The washed sample, was stored in the dark and used as required. The nanoparticles samples were always sterilized with 30 Gy (= 3000 rad) using an IBL 437C type gamma radiator, Cis Bio International (Codolet, France), before usage in cell experiments.

For coupling gold-labeled Ab, CPM-*co*-MDMO-PPV NPs were diluted to a solid content of 0.005% with a total solution volume of 3 mL. A 1 mL solution containing 0.025 mg EDC and a 1 mL solution containing 0.014 mg sulfo-NHS were added to the NP solution. The resulting sample solution was stirred for 20 min at 750 rpm in the dark after which 200 μL of the gold labeled goat anti-mouse IgG solution was added. The sample was stirred for an additional 3 h at 750 rpm in the dark followed by washing using 3 cycles of centrifugation (14 000 rpm, 45 min) and redispersion steps.

2.3.3 Characterization methods

The molecular weight distribution of MDMO-PPV and CPM-*co*-MDMO-PPV were measured via a Tosoh EcoSEC (Tessenderlo, Belgium) system HLC-8320GPC, comprising an autosampler, PSS guard column SDV of 50 x 7.5 mm, followed by 3 PSS SDV analytical linear XL columns of 300 x 7.5 mm (5 μm) at 40 °C (column molecular weight range is 1 x 10^2 – 1 x 10^6 g·mol^{-1}) and a differential refractive index detector, Tosoh EcoSEC RI, using THF as eluent with a flow rate of 1 mL*min^{-1}. The used flow marker was toluene and calibration was performed using linear narrow polystyrene standards of 470 – 7.5 x 10^6 g·mol^{-1} obtained from PSS Laboratories (Valkenburg, The Netherlands) (MHKS for precursor (a = 0.67605 and k = 0.000142 ml·g-1) as well as conjugated MDMO-PPV (a = 0.809 and k = 0.00002 ml·g^{-1}) were applied for molecular weight analysis). To determine the copolymer composition of CPM-*co*-MDMO-PPV, ^{1}H-NMR spectra were recorded in

$CDCl_3$ on a Varian Inova 300 spectrometer (Chemnitz, Germany) (300 MHz and 75MHz respectively, 5 mm probe). ATR-IR spectra were collected with a Bruker (Brussels, Belgium) Tensor 27 FT-IR spectrophotometer.

The study of both size and morphology of the conjugated nanoparticles was performed with TEM on a Tecnai G2 spirit twin, FEI (Zaventem, Belgium), at an accelerating voltage of 120 keV. TEM images were processed with ImageJ software. The respective samples were drop casted and dried on copper grids. In parallel, the hydrodynamic diameter and polydispersity as well as zeta-potential were determined with dynamic light scattering using ZetaPALS equipment, Brookhaven Instrument Cooperation (Waddinxveen, The Netherlands). The solid content of all samples was determined by thermogravimetric analysis.

The optical fingerprint of both nanoparticles and molecularly dissolved polymers as well as the absorption integrity over a time period of 12 months was measured in 1 cm quartz cuvettes using the Cary 5000 UV-VIS-NIR spectrophotometer, Agilent Technologies (Diegem, Belgium), and the Jobin Yvon Fluorolog3 Tau fluorescence spectrophotometer, Horiba (Lier, Belgium). The emission spectra were corrected for the wavelength dependence of the throughput and sensitivity of the detection channel. The absorption extinction coefficient of the materials was calculated using the Beer-Lambert law by varying the concentration of nanoparticles in water or polymer in $CHCl_3$. The resulting extinction coefficients could be used to determine the absorption cross-section. The polymers and nanoparticles' quantum yield (QY) was measured using rhodamine 6G (in H_2O, QY = 0.95) as a fluorescence reference. Five dilutions were prepared for all samples (MDMO-PPV molecularly dissolved in $CHCl_3$, MDMO-PPV NPs in H_2O, CPM-*co*-MDMO-PPV molecularly dissolved in $CHCl_3$ and CPM-*co*-MDMO-PPV NPs in H_2O), as well as for the standard. The most concentrated one had an absorbance of 0.1 at 488 nm excitation for the NPs and 500 nm for the molecularly dissolved polymers, which were optically matched to the standard. Emission spectra were collected for all samples at their respective excitation wavelengths after which the absorption versus the integral of emission spectra for each dilution and sample were plotted and trend lines fitted. The resulting slope values (m) as well as the refractive indexes (η) of the liquids were used to determine the quantum yield of the sample according to the following formula.

$$QY_{SAMPLE} = QY_{STANDARD} \times \frac{mSAMPLE}{mSTANDARD} \times \frac{\eta SAMPLE^2}{\eta STANDARD^2}$$

The nanoparticle and reference dye lifetime was measured through fluorescence lifetime imaging microscopy (FLIM) using a commercial Zeiss LSM 510 META NLO scan head, Zeiss, mounted on an inverted laser scanning microscope Axiovert 200M equipped with a LD C-Apochromat 40x/1.1 W Korr UV-VIS-IR water immersion objective. Excitation was performed with a femtosecond pulsed titanium-sapphire MaiTai DeepSee laser, Spectra-Physics (Utrecht, The Netherlands), with an output wavelength of 970 nm (~5 mW average radiant power at the sample position). The emission light was detected using non-descanned detection: the fluorescence was directed using a dichroic mirror NFT 490 and the 480-520 nm band pass filter towards a photomultiplier tube (PMT), Hamamatsu 7422 (Mont-Saint-Guibert, Belgium). This PMT was connected to an SPC830 card, Becker and Hickl (Berlin, Germany), synchronized by the scan pulses from the confocal laser scanning microscope. The instrument response function was recorded using potassium dihydrogen phosphate micro-crystals, background subtracted and used in the analysis of the FLIM data. The data were obtained and exponentially fitted using SPCImage 2.9 data analysis software, Beckr and Hickl. An average lifetime of five independent measurements was taken. The same equipment was employed together with the Zeiss excitation fingerprinting macro window software for determining the two-photon excitation spectrum of both MDMO-PPV and CPM-*co*-MDMO-PPV NPs air-dried on microscope slides. Images were processed using AIM 4.2 software. The photobleaching kinetics were determined for both nanoparticle samples as well as reference dyes, with a fixed absorbance of 0.1 at their excitation λ_{max} (Table 2-1) The fluorescence intensity signal was collected at their respective emission λ_{max} on regular time intervals (10 s) for a time period of 3600 s with a constant excitation power at their excitation λ_{max} using the conventional fluorescence spectrophotometer set-up. The effect of oxidative stress on conjugated nanoparticles was evaluated by incubating the sample with 0.1 wt% of H_2O_2 and measuring the change in absorbance.

Table 2—1: Excitation and emission maxima of NP samples and reference dyes in H_2O.

Sample	$\lambda_{excitation\ (nm)}$	$\lambda_{emission\ (nm)}$
MDMO-PPV NPs	495	590
CPM-*co*-MDMO-PPV NPs	500	592
Rhodamine B	554	573
Rhodamine 6G	527	550
FITC	491	516

2.3.4 Cell culture

Cells were cultured with culture medium (Table 2-2) in a T25 flask stored at 37 °C in a 5 % CO_2 incubator (Sanyo, Japan) and were spliced after being 80 % confluent. For HMEC-1 cells, the medium needs to be refreshed after 3 days.

Table 2—2: Cell-lines and respective culture media.

Cell type	Medium	Supplements
HMEC-1	MCDB 131	10 % FCS 0.5 % P/S 500 ng EGF 50 μg HC 500 μmol L-Glutamine
BV-2	DMEM	1 % P/S 10 % FCS
C8-D1A	DMEM	1 % P/S 10 % FCS
HeLa	DMEM	1 % P/S 10 % FCS

2.3.5 Cytotoxicity assays

MTT assay. HeLa cells were seeded at a density of 10 000 cells per well, together with 100 μL of culture solution, in a 96-well flat bottom plate. After 24 h of incubation at 37 °C in a 5 % CO_2 incubator, the cells were washed with 1xPBS. A total of six wells per condition were taken and 100 μL of the reagents representing different required conditions were added to the respective wells: blank, 100 % cell death (1:9.1 dilution in IMDM culture solution of a 340 mM solution of SDS in ultrapure water), 100 μg/mL of NPs in IMDM culture solution (IMDM medium, 10 % FCS, 1 % P/S), 50 μg/mL, 10 μg/mL and 5 μg/mL. After the incubation period of 24h the cells were washed 3 times with 1xPBS. The MTT solution (10 μL MTT + 100 μL IMDM culture solution) was added to the wells and incubated for 4h at 37 °C, 5 % CO_2, after which 100 μL of SDS solution (1 g SDS in 10 mL of 0.01 M HCl) was added to each well and the plate was put back in the incubator for another 18 h. The solution was transferred to a dark plate and the absorbance was detected at λ_{ex} = 570 nm with a FLUOstar OPTIMA plate reader, BMG LABTECH. The experiment was performed in triplicate.

Alamar blue assay. HeLa, HMEC-1, BV-2 and C8-D1A cells were seeded in a 96-well flat bottom plate and left to grow to 80 % confluence at 37 °C in a 5 % CO_2 incubator. The desired sample concentration range (5, 10, 50 and 100 μg/mL) was obtained by diluting the sample with phenol red poor IMDM culture medium (replacing the medium solution of Table 2-2 in the culture medium) and 100 μL of each concentration was added to the wells after washing with 1xPBS (9 g/L NaCl, 0.795 g/L Na_2HPO_4 and 0.144 g/L KH_2PO_4). Also positive and negative control conditions were included. A total of six wells was taken per condition. After a 24 h at 37 °C, the conditions were removed and the cells were washed 3 times with 1xPBS. Then a 10 % alamar blue solution in IMDM culture medium was added and left to incubate for 24 h. The resulting solution was transferred to an opaque-walled dark 96-well culture plate and the fluorescence was measured at λ_{em} = 590 nm while excited at λ_{ex} = 570 nm, FLUOstar OPTIMA (BMG Labtech, Temse, Belgium). The experiment was performed in triplicate.

2.3.6 Uptake kinetics

HMEC-1 cells were seeded at a density of 100 000 cells per well in a 24-well plate and left to incubate for 24 h at 37 °C and 5 % CO_2. Subsequently, the cells were washed with 1xPBS and 500 μL of 75, 100, 150 and 200 μg/mL of NPs in culture solution was added to the cells which were then incubated for 2, 4, 6, 8, 24, 27 or 30 h at 37 °C with a CO_2 level of 5 %. The cells were washed 3 times with 1xPBS and harvested. The pellet was dispersed in 1 mL of 4 % PFA and left to incubate for 20 min at room temperature in the dark. The cells were then centrifuged in order to remove the PFA solution and washed 3 times using centrifugation with fluorescence-activated cell sorting (FACS) buffer (1xPBS and 2 % FCS). The resulting samples were measured and analyzed with the FACSCalibur, Becton Dickinson (Erembodegem, Belgium), using a 488 nm laser and an emission filter 585/42 nm. Unlabeled cells were used as a blank to gate the signal. For each sample 20 000 cells were counted in triplicate. The FACSCalibur software counted and calculated the amount of cells in the cell culture solution and measured in which cells fluorescent signal was detected. These calculations were converted to a percentage scale, with 100 % meaning that in all measured cells fluorescence, and thus NPs, was detected.

2.3.7 Confocal laser scanning microscopy

Live cell imaging. HMEC-1, BV-2 and C8-D1A cells were seeded in a μ-Slide 8-well plate (Ibidi) at a concentration of 50 000 cells per well and left to adhere and grow for 12 h at 37 °C. The cells were washed with 1xPBS after which 50 μg/mL of MDMO-PPV NPs and CPM-*co*-MDMO-PPV NPs in IMDM culture medium was added to each well and incubated for 20h. The cells were washed 3 times with 1xPBS and 100 μL of IMDM culture solution was added. All images were collected at 37 °C using a Zeiss (Zaventem, Belgium) LSM510 META NLO mounted on an inverted laser scanning microscope (Zeiss Axiovert 200 M) and a 40x/1.1 water immersion objective. Excitation of the nanoparticles was done at 488 nm (3 μW maximum radiant power at the sample) with the Argon-ion laser. Emission was detected using a band-pass filter of 565-615 nm. The resulting 1024x1024 images with a pixel size of 0.06 μm were recorded using a pixel dwell time of 14.2 μs. A fixed

pinhole size of 114 μm was used. Images were processed using AIM 4.2 and ImageJ software.

Fixated cell imaging. HeLa cells were seeded at 15 000 cells per well in a μ-Slide 8 well plate, Ibidi, and left to incubate for 24 h in a 5 % CO_2 incubator at 37 °C. The cells were washed with 1xPBS and incubated with 200 μL of 50 μg/mL of NPs in IMDM culture medium for another 24 h. As negative control IMDM culture medium was added. The cells were rinsed 3 times with 1xPBS at 37 °C. Next, 200 μL of fixation/extraction/permeabilization buffer (4 v/v % PFA supplemented with 0.3 v/v % triton x-100 and 5.0 w/v % sucrose) was added for 2 h at RT on a shaker at 50 rpm. The cells were washed 3 times with washing buffer (1xPBS containing 0.1 % triton x-100) after which 200 μL of blocking buffer (1xPBS containing 0.1 % triton x-100 and 2 % Bovine Serum Albumine) was added and the cells were put on a shaker for 1 h at 50 rpm on RT. Next the cells were incubated with 200 μL of primary antibody (mouse monoclonal anti-α-tubulin, 1:1000 in blocking buffer) for 1 h at RT on 50 rpm. The cells were rinsed 3 times using washing buffer for 5 min at 50 rpm. Next, the cells were incubated for 1 h with 200 μL of secondary Ab (donkey anti-mouse Alexa Fluor 488, 1:250 in blocking buffer) at 50 rpm, RT. The cells were washed with washing buffer for 5 min at 50 rpm and incubated with 200 μL of DAPI (1:25 in blocking buffer) for 1 h at RT. The cells were rinsed 3 times with washing buffer for 5 min at 50 rpm and covered with 2 drops of mounting medium to prevent photobleaching of the dyes. The cells were visualized at RT with the Zeiss LSM510 META NLO mounted on an inverted laser scanning microscope (Zeiss Axiovert 200 M) and a 40x/1.1 water immersion objective. Excitation of the nanoparticles and tubulin was done at 543 nm and 488 nm respectively (3 μW maximum radiant power at the sample) with an Argon-ion laser. Excitation of DAPI was done at 730 nm (~5 mW average radiant power at the sample position) with the femtosecond pulsed titanium-sapphire MaiTai DeepSee laser. Emission was detected using band-pass filters 565-615 (NPs), 390-465 nm (DAPI) and 500-550 nm (tubulin). The resulting 1024x1024 images with a pixel size of 0.06 μm were recorded using a pixel dwell time of 375 μs. A fixed pinhole size of 240 μm (tubulin), 600 μm (NPs) and 1000 μm (DAPI) was used. Images were processed using AIM 4.2 and ImageJ software.

2.4 Results and discussion

2.4.1 Synthesis of NPs using PPV-derivatives

Conjugated polymer nanoparticles were obtained from MDMO-PPV (M_n = 150 000 g·mol^{-1}) or statistical co-polymer CPM-*co*-MDMO-PPV (M_n = 164 200 g·mol^{-1}, 66:34 MDMO:CPM ratio as determined by ^{1}H NMR, FTIR peak of ester at 1730 cm^{-1}) [141] to serve as bioimaging probes (Figure 2-2 to 2-5). Both PPVs were synthesized *via* the so-called precursor sulfinyl route [56, 140]. Next to a very fast polymerization and high conversion being reached within a second to minute time scale, this specific route differs from others in its use of an unsymmetrical premonomer which results in better control over the regioregularity as compared to for instance, the Gilch route [140]. In addition to this, the sulfinyl precursor route enables the design of complex polar functionalized PPVs, as CPM-*co*-MDMO-PPV, in an easy manner. Subsequently, the polar group on the side chain can be substituted for a sheer unlimited number of chemical functionalities, such as propargyl groups that are highly interesting to perform orthogonal conjugation reactions (also known as "click reaction") using dicyclohexylcarbodiimide/4-dimethylaminopyridine (DCC/DMAP) post-polymerization functionalization [56, 141]. As the CPM-*co*-MDMO-PPV bears ester groups on the alkoxy side chain, the formulated NPs are expected to have the ester groups distributed within the volume and on the surface of NPs. The ester groups present on the surface of the CPM-*co*-MDMO-PPV NPs can be conveniently converted into carboxylic acid groups, using hydrolysis, which can subsequently be employed for the easy attachment of various biomolecules for incorporating different functional properties (*e.g.*, induce target specificity, enhanced circulation time, barrier crossing potential, or others). It should be noted that direct polymerization of an acid-functionalized monomer is impossible due to the basic nature of any precursor polymerization technique leading to PPVs.

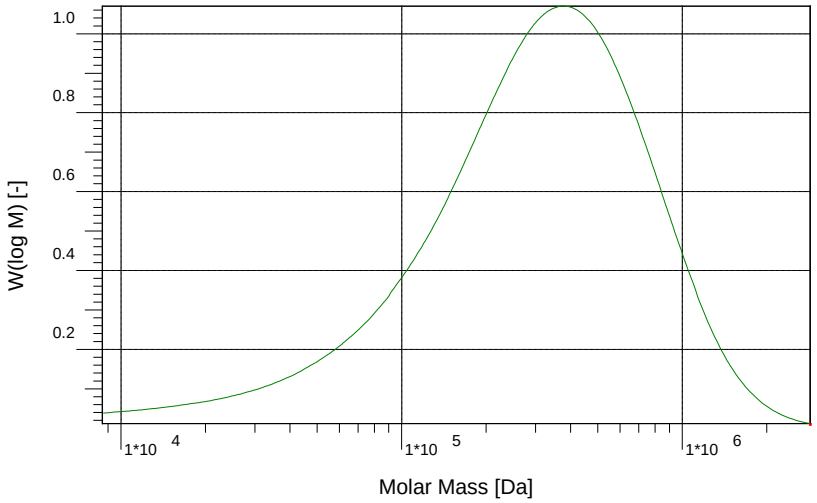

Figure 2—2: Molecular weight distribution of synthesized MDMO-PPV.

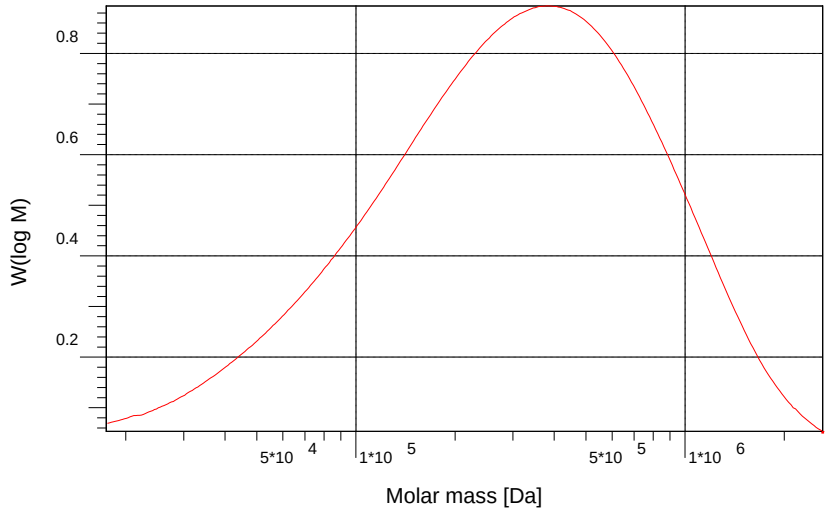

Figure 2—3: Molecular weight distribution of synthesized CPM-*co*-MDMO-PPV.

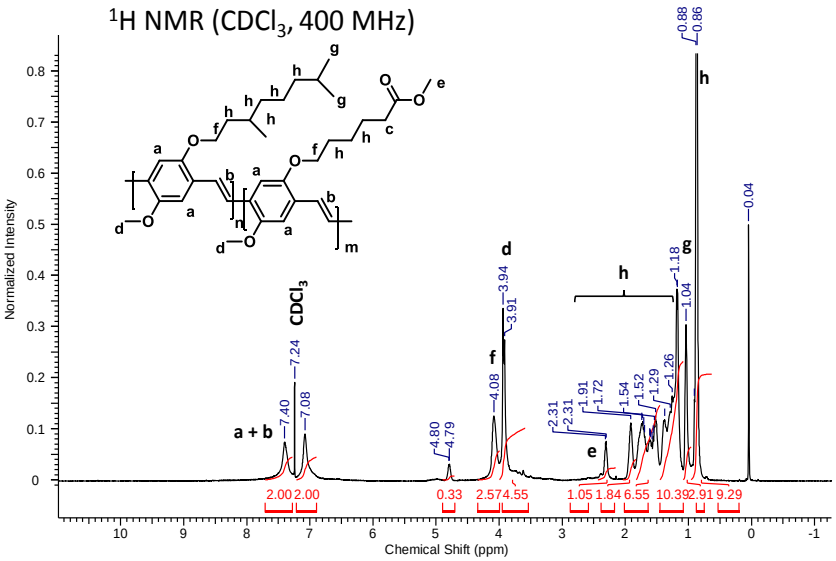

Figure 2—4: ^{1}H-NMR spectrum of CPM-*co*-MDMO-PPV.

^{1}H-NMR ($CDCl_3$): δ = 1.91 – 0.86 (m, 30H); 2.31 (t, 2H); 3.94 (s, 5H); 4.09 (s, 3H); 7.08 (m, 2H); 7.40 (m, 2H).

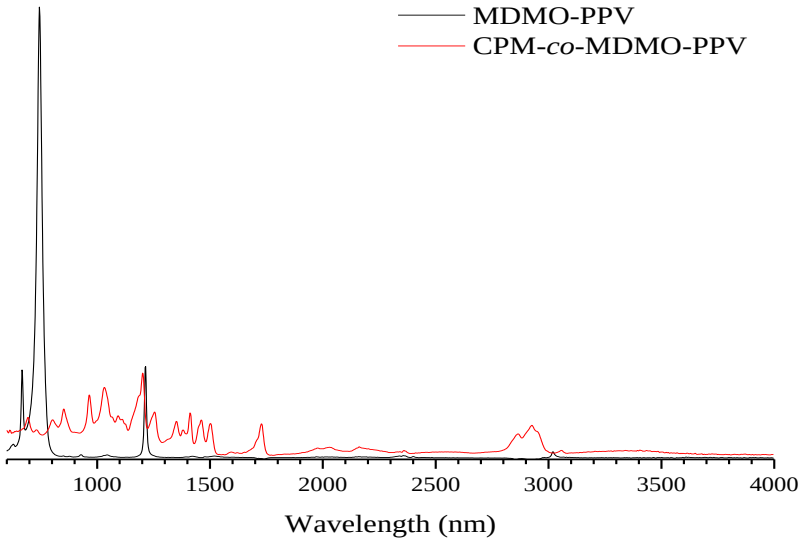

Figure 2—5: MDMO-PPV and CPM-*co*-MDMO-PPV infrared spectra.

Infrared spectra of MDMO-PPV (black line) and CPM-*co*-MDMO-PPV (red line).

The particle formulation using both preformed polymers was performed using a combination of the solvent evaporation and miniemulsion technique, which allows for generating NPs with tunable size, surface functionality and also dispersions with tunable solid content depending on the polymer amount used [134]. The characteristics of the two different particle systems are presented in Table 2-3.

Table 2—3: Characteristics of the synthesized PPV-based NPs.

Formulation	**Characteristics**			
	TEM (nm)	**DLS (nm)**	**Zeta potential (mV)**	**Solid content (%)**
(MDMO-PPV)	97 (±10.0)	116 (±1.8) (PDI = 0.060)	-29.8	1.1
(CPM-*co*-MDMO-PPV)	84 (± 11.7)	117 (±1.8) (PDI = 0.063)	-41.9	0.8

The solid content values reported here represent the values obtained immediately after synthesis and before the required washing steps to remove the excess of SDS. As it can be seen in Table 2-3, the obtained average hydrodynamic diameter values deduced from dynamic light scattering (DLS) are in the same range with narrow polydispersity indices (PDI) for both NPs. As the size of the particles does not vary, it can be inferred that the type and slight difference in MW of the used polymers does not significantly influence the particle formation in the present case. The more negative zeta potential value for the CPM-*co*-MDMO-PPV NPs (-41.9 mV) compared to the MDMO-PPV NPs (-29.8 mV) indicates that some of the ester groups have already been hydrolyzed during the washing steps to form carboxylic acid groups. With transmission electron microscopy (TEM) the average size of the actual conjugated polymer core was determined. These results indicate slightly smaller diameters than DLS, as expected as the latter measures the hydrodynamic radius. The TEM image (Figure 2-6 and 2-7) also highlights the spherical morphology of the synthesized nanoparticles. Further, it is also shown that after extensive washing, a colloidally stable colored dispersion is obtained (Figure 2-6).

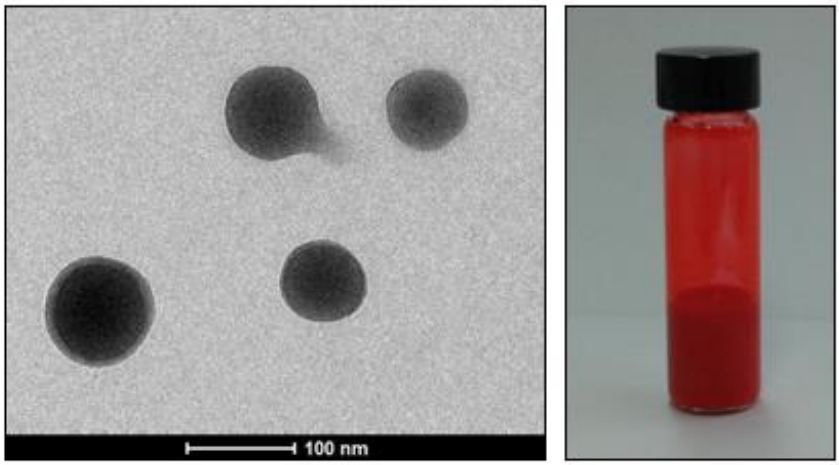

Figure 2—6: CPM-*co*-MDMO-PPV NPs TEM image and colloidal dispersion.
TEM image of CPM-*co*-MDMO-PPV NPs (left image) and a photograph of stable water-based NP dispersion (right image).

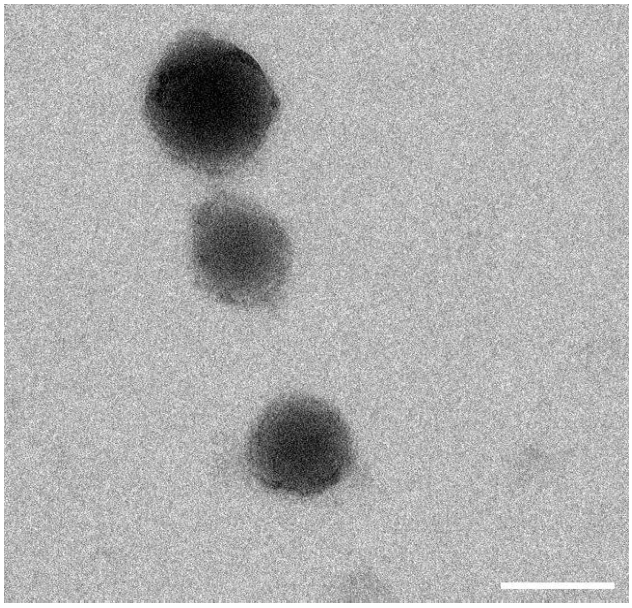

Figure 2—7: MDMO-PPV NPs TEM image.
TEM image of MDMO-PPV NPs. Scale bar represents a distance of 50 nm.

As previously mentioned, surface functionalization of NPs is an inevitable requirement in nanomedicine. Therefore, as a proof of concept to demonstrate the ease of attaching biological moieties onto the surface when using the surface carboxylic acid containing CPM-*co*-MDMO-PPV NPs, gold-labeled goat anti-mouse IgG Ab were attached using EDC-coupling [142]. The complementary amine group is abundantly present on the Ab, which may impact its activity due to covalent attachment to the surface in a random orientation. The presence of these gold-labeled Ab was proven visually using TEM imaging and confirmed using energy-dispersive x-ray (EDX) (Figure 2-8 and 2-9). The difference in contrast due to the higher electron density of the gold NPs as compared to the polymer particles, clearly enables to visualize the presence of gold-labeled Ab. It can be seen that multiple darker spots (gold NPs) are present on the polymer particle after washing steps thereby confirming the former's firm covalent attachment. Since a multiple centrifugation and dispersion protocol, involving mechanical forces, was adopted for washing the NPs after the coupling reaction, some of the gold-labeled Ab were detached as is also seen in the TEM image. EDX analysis shows characteristic peaks of gold (2.1 and 9.7 keV), while the peaks of copper can be attributed to the grid on which the sample is placed [143].

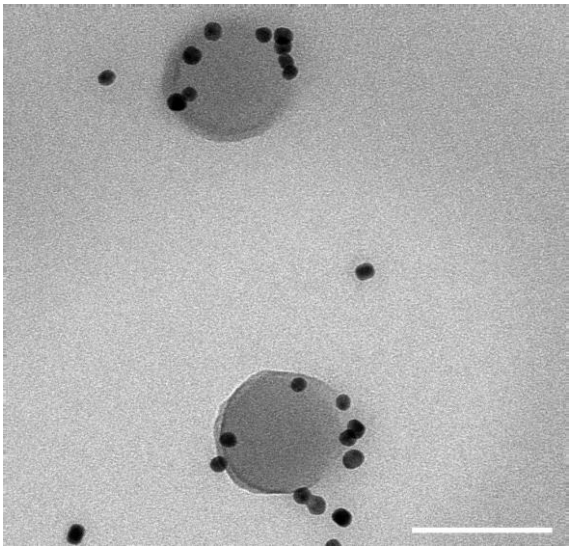

Figure 2—8: Functionalized CPM-*co*-MDMO-PPV NPs TEM image.
TEM image of CPM-*co*-MDMO-PPV NPs functionalized with gold labeled Abs. The scale bar represents a distance of 100 nm.

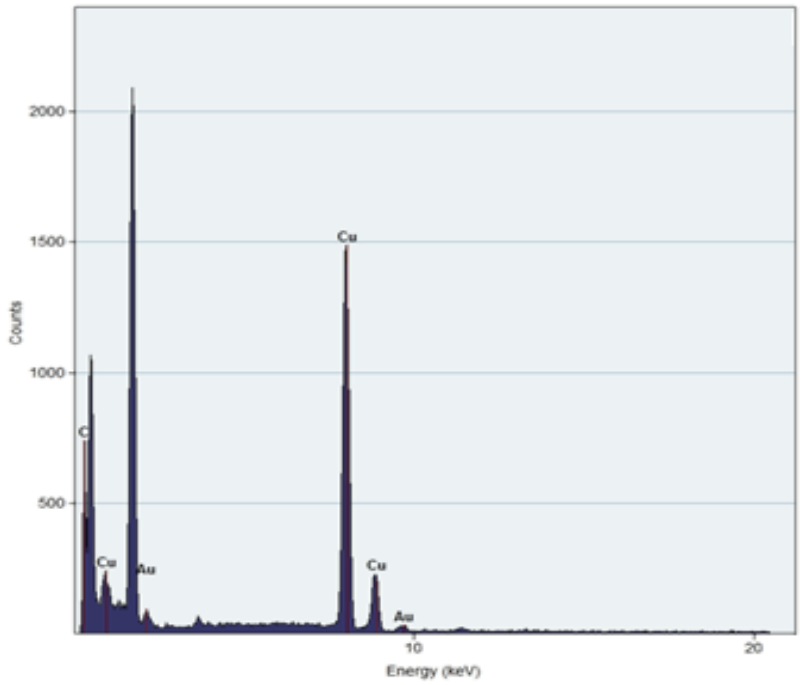

Figure 2—9: Functionalized CPM-*co*-MDMO-PPV NPs EDX spectrum.
EDX spectrum of CPM-*co*-MDMO-PPV NPs functionalized with gold labeled Abs. C = carbon, Cu = cupper and Au = gold.

2.4.2 Optical characteristics of PPV-based NPs

The optical properties of the NPs were studied in detail using different optical spectroscopic techniques. UV-VIS and fluorescence spectroscopy were used to measure the absorbance and emission spectrum of both molecularly dissolved MDMO-PPV and CPM-*co*-MDMO-PPV chains in chloroform and their respective NPs in water (Figure 2-10). A feature characteristic of conjugated polymer nanoparticles is their broad absorption band ranging from 350 to 600 nm. This large wavelength range is ideal for applications like fluorescence microscopy. The absorption spectra of the nanoparticles are broadened as compared to that of the free chains, caused by the torsion, kinking and bending of the polymer backbone [144]. Also a clear shift in the emission maximum peak was observed from 550 to 590 nm when going from molecularly dissolved chains to NP configuration. This can be attributed to the change from intrachain emission to interchain emission when the conjugated polymers aggregate, during the evaporation of the solvent,

into nanoparticles [144]. The occurring red shift is caused by overlap of π-orbitals during aggregation, which leads to a delocalization of the π-electrons across several chains causing the formation of new electronic species with lower band gaps [71, 144]. Also, a lower energy shoulder becomes visible, corresponding to the relaxation of π-electrons through a ground state energy level [145].

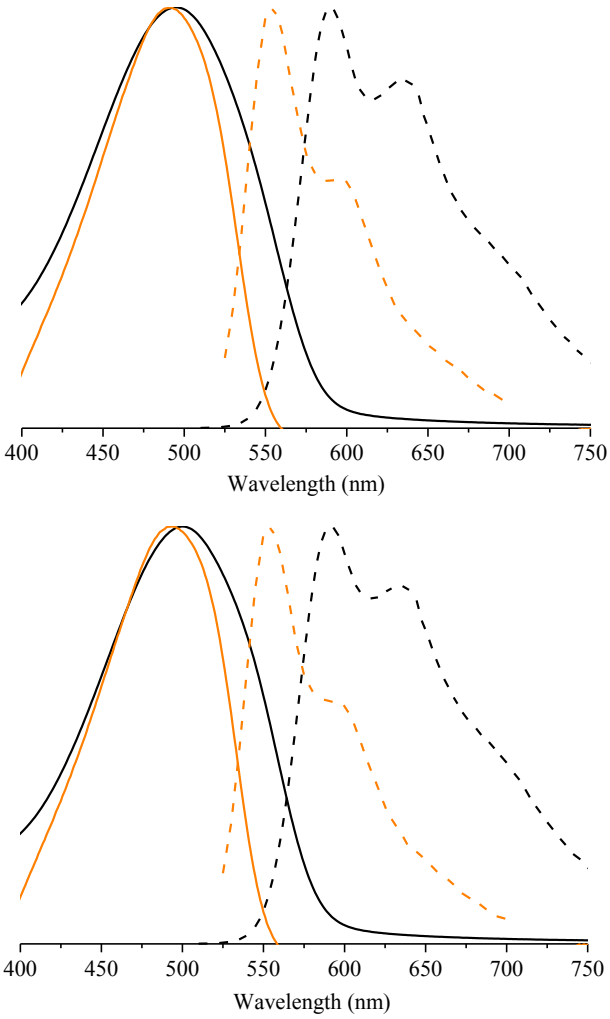

Figure 2—10: Fingerprint of MDMO-PPV and CPM-*co*-MDMO-PPV NPs and free chains.

Optical spectra (solid line reflects the absorbance and dashed line the emission) of MDMO-PPV (top) and CPM-*co*-MDMO-PPV (bottom) in different forms: molecularly dissolved polymer in chloroform (orange color) and NP water-based dispersion (black color).

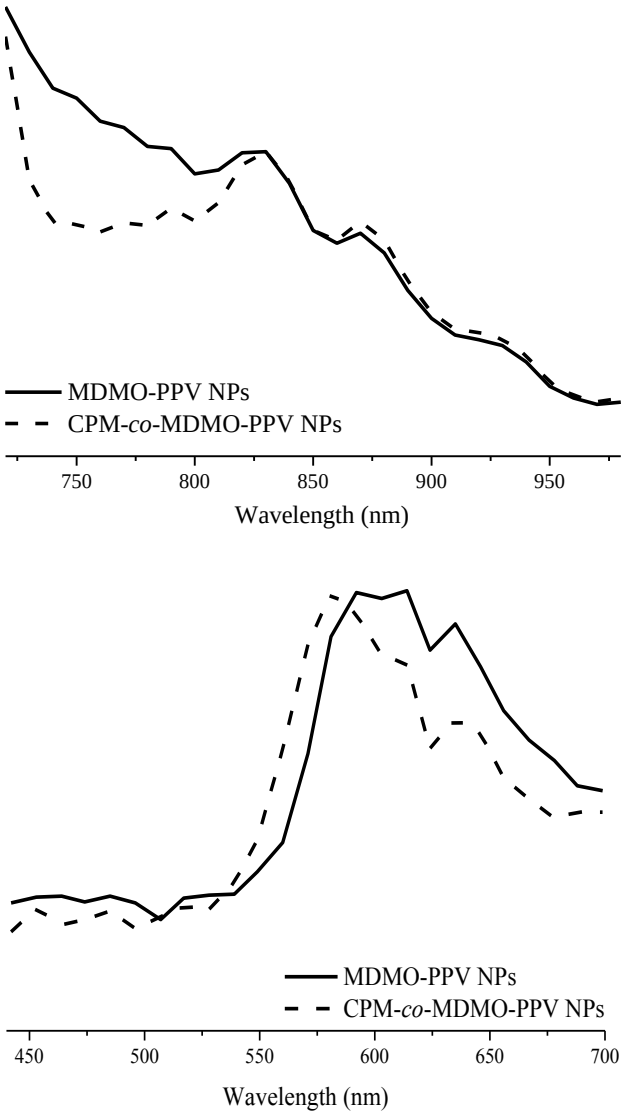

Figure 2—11: Two-photon fingerprint of MDMO-PPV and CPM-*co*-MDMO-PPV NPs. Two-photon fingerprint of MDMO-PPV (solid line) and CPM-*co*-MDMO-PPV NPs (dashed line) with the respective absorbance (top) and emission spectra (bottom).

Recently multiphoton microscopy has emerged as a powerful technique for 3D imaging in biological systems [58, 146]. In two-photon fluorescence, two photons are absorbed simultaneously by the imaging probe under investigation to promote an electron to its excited state. When the electron relaxes back to its ground state level, it emits a photon identical to one-photon absorption and fluorescence. In this manner a highly localized excitation and improved spatial resolution is generated caused by the nonlinear dependence of excitation probability on light intensity [146]. In addition, the background signal caused by autofluorescence and fluorescence outside the focal plane is greatly reduced by the small effective excitation volume [146]. The ability to employ near-IR wavelengths during excitation reduces the photodamage to the sample as well as photobleaching to the probe, facilitates deep tissue imaging (up to 1 mm) resulting from the near-transparency of a wide range of tissues and biological water in the used spectral range and enables an enhanced image quality due to a decrease in light scattering by for example cells [146]. It has been demonstrated that conjugated polymers possess a larger efficiency when it comes to multiphoton absorption as compared to conventional dyes [58, 147]. Therefore, the two-photon excitation and emission characteristics of the constructed PPV-based NPs were also studied (Figure 2-11). For both MDMO-PPV NPs and CPM-*co*-MDMO-PPV NPs the excitation maximum was located at a wavelength of 830 nm. The emission spectra after two-photon excitation shows features similar to the ones obtained after one-photon excitation as expected with a maximum around 580 nm for the CPM-*co*-MDMO-PPV NPs and 590 nm for the MDMO-PPV NPs.

Table 2-4 summarizes several inherent optical characteristics of both nanoparticle systems. A decrease in quantum yield for both NP types was observed as compared to their molecularly dissolved counterparts: from 33 % to 3 % for the MDMO-PPV NPs and from 22 % to 3 % for the CPM-*co*-MDMO-PPV NPs. It has been reported that the nanoparticle formation causes a lowering in quantum yield because of quenching, following chain confinement in the condensed phase [144]. Through the aggregation formed between the conjugated chains, exciton migration becomes more effective, resulting in excitations reaching quenching sites more easily. Therefore, this becomes a more effective relaxation path leading to a reduction in fluorescence efficiency. The NP quantum yields determined are

better than the previously reported values of other PPV-based NPs, like MEH-PPV NPs of a similar size with a yield of 1 % [9, 67, 71]. Although the quantum yield of the constructed conjugated NPs is lower than those of quantum dots (0.1-0.8) and organic dyes (0.5 - 1.0), their molar extinction coefficients are considerably higher [8, 10]. For both NP models the value is in the order of 10^6 $M^{-1}{\cdot}cm^{-1}$, while that of organic dyes and quantum dots is in the order of 10^5 $M^{-1}{\cdot}cm^{-1}$ [8, 10]. Consequently, the fluorescence brightness, thus the product of the quantum yield and molar extinction coefficient – in the end the determining factor for a successful imaging probe – is high. Even though not strictly required, the quantum yield can in principle be further increased through chemical structure adaptation of the conjugated polymer [100, 128].

Table 2—4: Optical characteristics of the synthesized NPs

	MDMO-PPV NPs	**CPM-*co*-MDMO-PPV NPs**
λ_{max} excitation (nm)	494	499
λ_{max} emission (nm)	590	590
Quantum Yield (φ_F)	3 %	3 %
Molar Extinction Coefficient (ε, $M^{-1}*cm^{-1}$)	$9.4*10^6$	$9.1*10^6$
Absorption Cross Section (σ, cm^2)	$3.60*10^{-14}$	$3.47*10^{-14}$
Lifetime (τ, ps)	518.6	418.5
Fluorescence radiative rates (K_R, s^{-1})	$6.7*10^7$	$4.8*10^7$

Fluorescence lifetime imaging microscopy (FLIM) measurements of the NPs resulted in lifetime values around 0.4 - 0.5 ns, similar to other PPV-based NPs but lower than organic dyes (1 - 10 ns) and quantum dots (10 - 100 ns) (Figure 2-12) [8-10]. This lifetime value is of particular importance in high-speed application like flow cytometry and high-speed tracking since it determines the fluorescence radiative rate together with the quantum yield ($\varphi = K_R/(K_R+K_{NR})$ and $\tau = (K_R+K_{NR})^{-1}$) [10]. The values coincide with those reported in literature and are in the range

of 10^7 s^{-1}, which is lower than the reported values of standard organic dyes (10^8 s^{-1}) and higher than those of quantum dots (10^6 s^{-1}) [9].

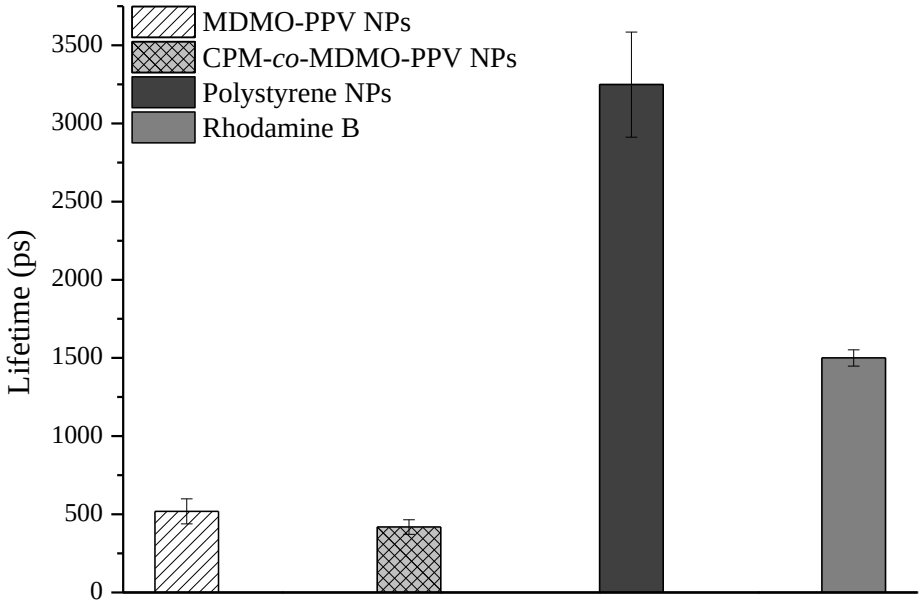

Figure 2—12: Lifetime of MDMO-PPV and CPM-*co*-MDMO-PPV NPs

Lifetime values of MDMO-PPV and CPM-*co*-MDMO-PPV NPs in comparison to reference samples polystyrene and Rhodamine B. Data are expressed as mean ± SD.

Another important property is the photostability of the synthesized NPs, especially if the application involves long-term imaging and tracking of NPs. After an exposure time of 1 hour the fluorescence intensity was still at 90 % integrity for the MDMO-PPV NPs and 85 % for the CPM-*co*-MDMO-PPV NPs as compared to commonly used stable organic dyes (Figure 2-13). The PPV-derivative NPs undergo little to no photobleaching.

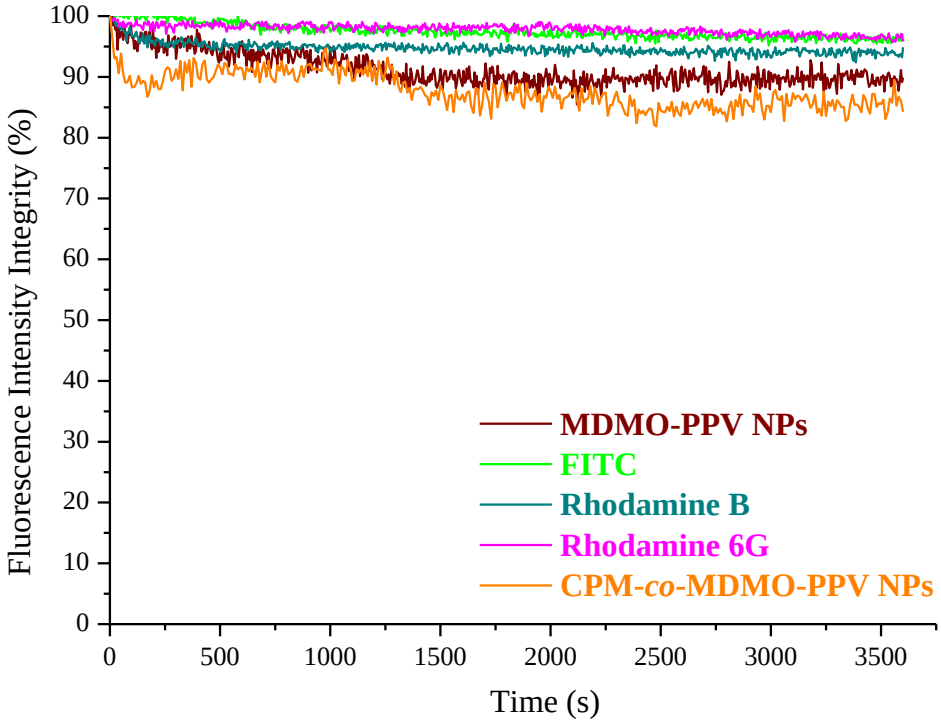

Figure 2—13: Photobleaching profile of MDMO-PPV and CPM-*co*-MDMO-PPV NPs. Photobleaching curves of MDMO-PPV and CPM-co-MDMO-PPV NPs in comparison to reference dyes FITC, Rhodamine B and Rhodamine 6G when exposed to their respective emission λ_{max} for a time period of 3600 s. Fluorescence intensity signal was collected every 10 s.

As photodegradation is a concern in such conjugated systems [148], the NPs produced as aqueous dispersions were monitored for their optical properties over a time period of 12 months by determining the absorption integrity at different time points (Figure 2-14). No decrease in absorbance integrity below 90 % was observed for both MDMO-PPV and CPM-*co*-MDMO-PPV NPs as compared to the sample directly measured after synthesis and washing procedures, indicating an excellent shelf-life time of these bioimaging probes. In addition, the chemical stability was tested by measuring the integrity of absorbance after exposure to a 0.1 wt % of H_2O_2 solution, a stable and common reactive oxygen species in cells. A difference of only 0.6 % compared to the control was monitored after 24 h of exposure to this physiological environment (Figure 2-15).

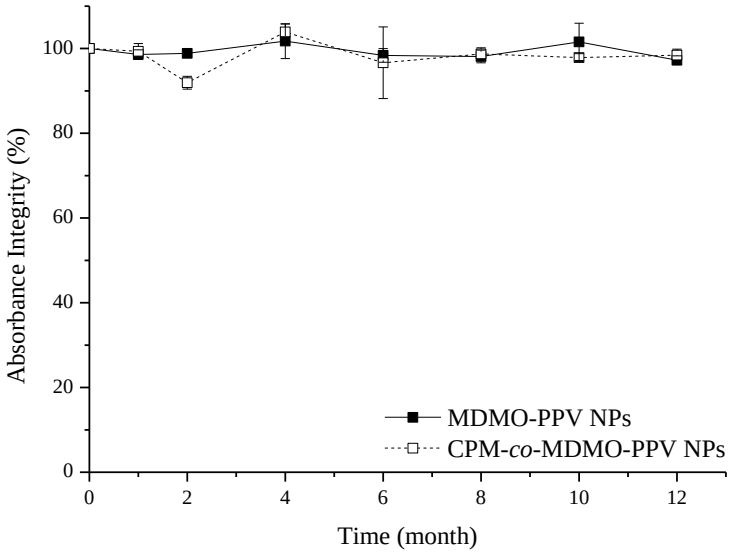

Figure 2—14: Absorbance integrity of MDMO-PPV and CPM-*co*-MDMO-PPV NPs over a 12 month period.

Absorbance integrity measurement of MDMO-PPV (solid line) and CPM-co-MDMO-PPV (dashed line) NPs over a time period of 12 months measured after synthesis and washing. A reference sample was included to correct for the lifetime of the lamp.

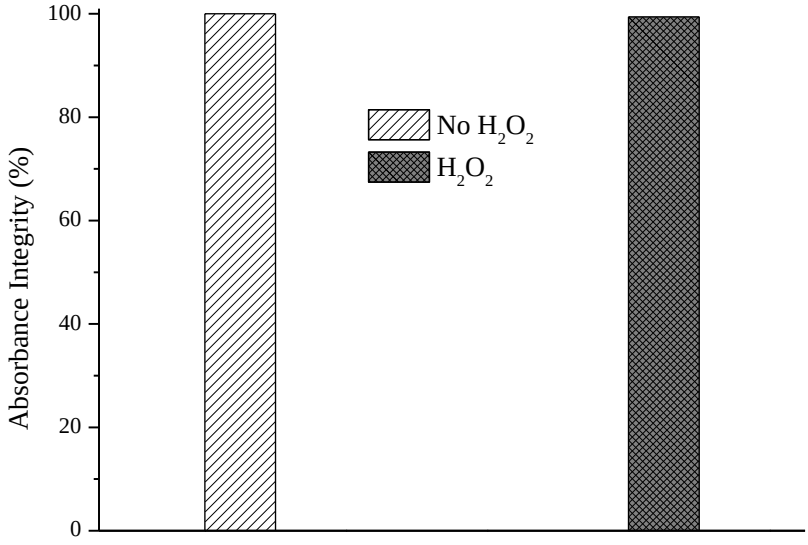

Figure 2—15: Absorbance integrity measurement of MDMO-PPV NPs before and after 24 h of exposure to 0.1 wt% H_2O_2 solution.

2.4.3 Monitoring the cytotoxic behavior of PPV-based NPs

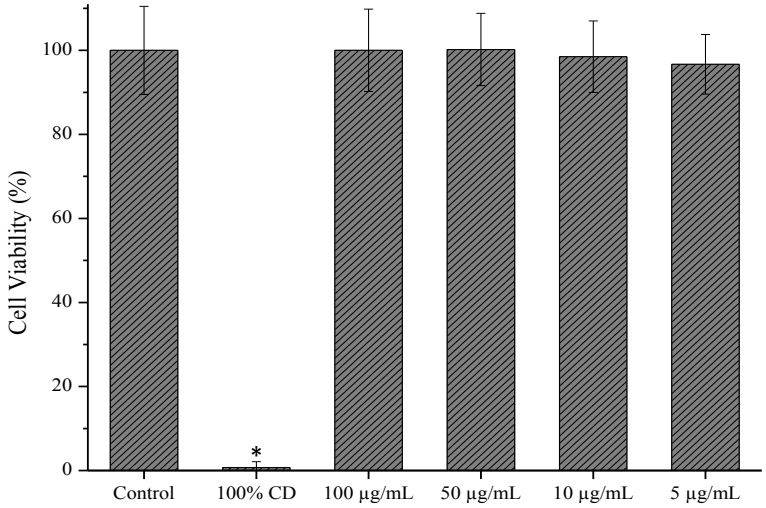

Figure 2—16: MTT assay dose-dependent cytotoxicity of MDMO-PPV NPs after 24 h of exposure.

Measurement of dose-dependent cytotoxicity of MDMO-PPV NPs in HeLa cells using the MTT assay. Data are expressed as percent of control mean ± SD (N=3). CD = cell death.

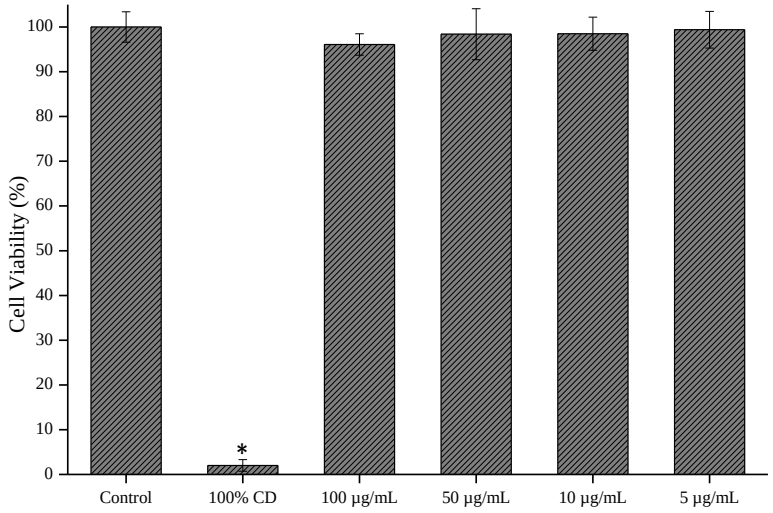

Figure 2—17: Alamar blue assay dose-dependent cytotoxicity of MDMO-PPV NPs after 24 h of exposure.

Measurement of dose-dependent cytotoxicity of MDMO-PPV NPs in HeLa cells using the alamar blue assay. Data are expressed as percent of control mean ± SD (N=3). CD = cell death.

Cytotoxicity of NPs is no issue for *ex vivo* applications like immunoassays, but is of great relevance for *in vitro* and especially *in vivo* applications. Therefore, the biocompatibility of MDMO-PPV and CPM-*co*-MDMO-PPV NPs was evaluated. The results of MTT and alamar blue assays on HeLa cells showed no significant reduction ($p < 0.05$) in cell viability for any concentration of MDMO-PPV NPs as compared to the control (Figure 2-16 and 2-17). No concentration effect was visible ($p < 0.05$) and the observed trends were consistent between both assays. Therefore, all subsequent experiments were executed with the alamar blue assay, which is more homogenous and has a higher sensitivity than the MTT assay.

As indicated earlier a high demand is present for bioimaging probes that can be employed for unraveling neurological diseases. Hence, the PPV-derived NPs were tested for their cytotoxicity towards different neurological cell lines associated to the brain. The viability of three different cell types incubated with increasing amounts of MDMO-PPV or CPM-*co*-MDMO-PPV NPs was assessed using the alamar blue assay (Figure 2-18 and 2-19). The endothelial cell line (HMEC-1) was chosen to mimic the blood brain barrier (BBB) comprised of blood vessels which the nanoparticles have to pass, the astrocyte (C8-D1A) and microglia (BV-2) cell line were chosen as representatives for the cell populations present inside the brain which the NPs could encounter.

For all three cell lines and both NP models the cell viability never went below 90 % after an exposure period of 24 h when compared to the untreated control. The HMEC-1 cell line showed a slightly lower viability in comparison to the other cell lines under investigation, which can be attributed to its inherent slower proliferation rate. No statistical difference was observed between the control group and different concentrations and between the concentrations tested (one-way ANOVA $p < 0.05$). Both PPV-derivative NP systems show no significant cytotoxicity on the tested cell lines. Therefore, it can be concluded that the NPs have no discernible impact on the cell viability and no dose dependent response is present in the used concentration range.

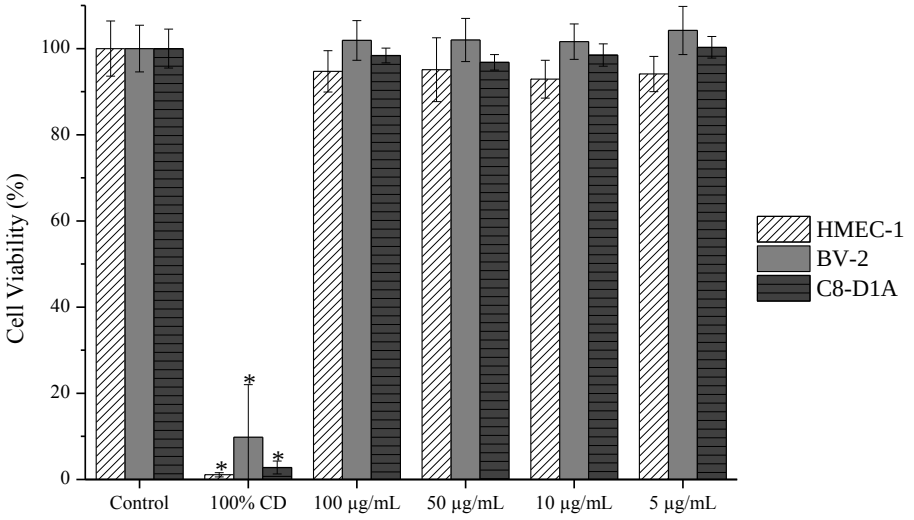

Figure 2—18: Dose-dependent cytotoxicity of MDMO-PPV NPs after 24 h of exposure in CNS related cell lines.

Measurement of dose-dependent cytotoxicity of MDMO-PPV NPs in HMEC-1, BV-2 and C8-D1A cells using the alamar blue assay. Data are expressed as percent of control mean ± SD (N=3). CD = cell death.

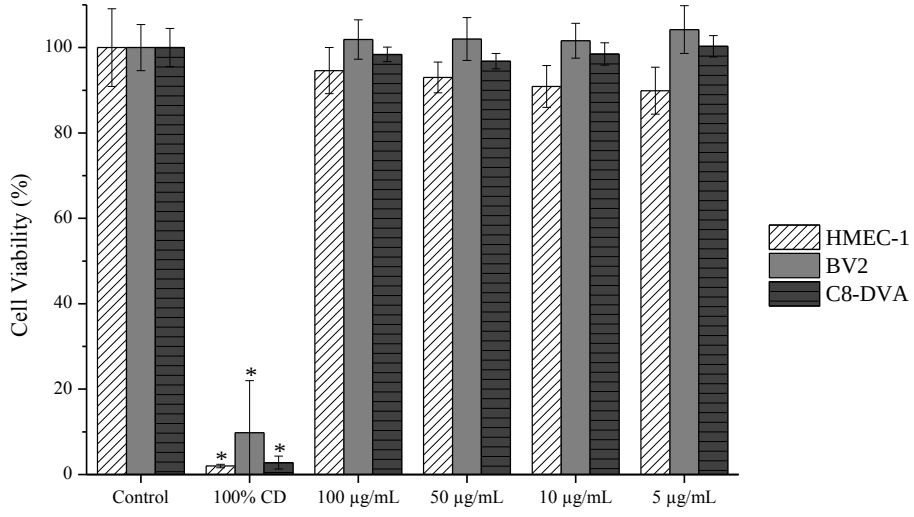

Figure 2—19: Dose-dependent cytotoxicity of CPM-*co*-MDMO-PPV NPs after 24 h of exposure in CNS related cell lines.

Measurement of dose-dependent cytotoxicity of CPM-*co*-MDMO-PPV NPs in HMEC-1, BV-2 and C8-D1A cells using the alamar blue assay. Data are expressed as percent of control mean ± SD (N=3). CD = cell death.

2.4.4 Cellular uptake of PPV-based NPs

Uptake by cells as a function of time for different concentrations was studied using flow cytometry. The uptake kinetics of PPV-derivative NPs over a time period of 30 h is shown in Figure 2-20. The fluorescence radiative rates of the constructed NPs described earlier are high enough to be detected with flow cytometry. HMEC-1 cells of the CNS were chosen since endothelial cells make up blood vessels and are thus one of the first ones to encounter injected NPs.

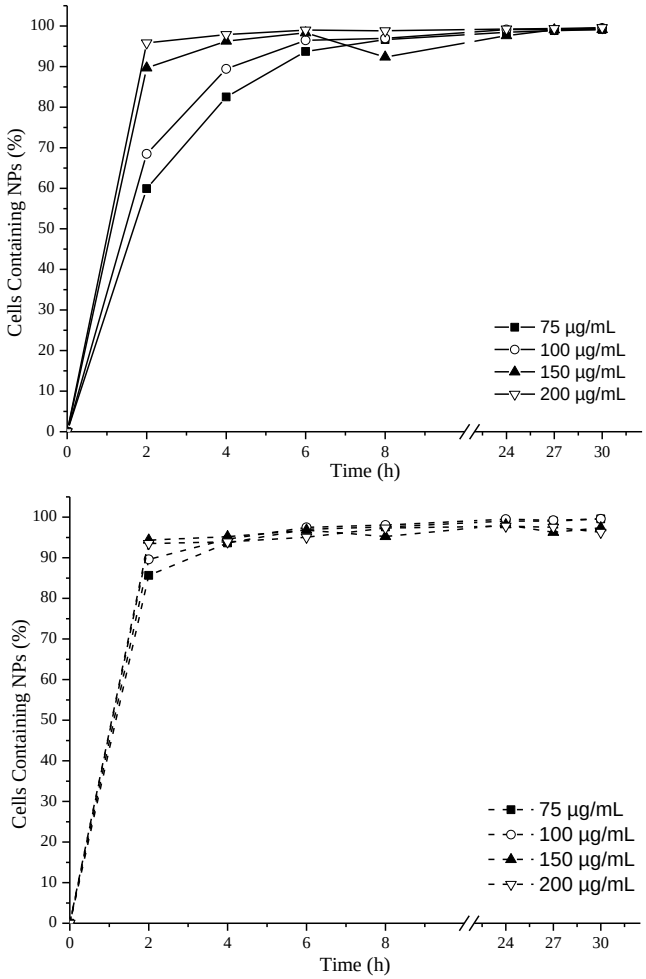

Figure 2—20: Kinetics of MDMO-PPV and CPM-*co*-MDMO-PPV NP uptake.
Kinetics of the internalization of MDMO-PPV (top) and CPM-co-MDMO-PPV (bottom) NPs by HMEC-1 cells over a time period of 30h for concentrations ranging from 75 to 200 μg/mL.

A clear difference is visible between the uptake of CPM-*co*-MDMO-PPV and MDMO-PPV NPs in the early hours. Approximately 85 % of the cells have taken up NPs after 2 hours for the lowest concentration of CPM-*co*-MDMO-PPV NPs, while this is only 60 % for MDMO-PPV NPs. When the incubation time extends, the difference fades between the two NP configurations and saturation is reached after approximately 6 to 8 h, meaning that all cells have taken up NPs. For high concentrations, 150 and 200 μg/mL, the discrepancy at short time periods is less pronounced. Standard deviations are not visible since they do not exceed 1.0 %. Although both particle types carry residual anionic surfactant after washing, the difference in uptake between the two configurations at lower concentrations, could be related to the presence of increased negative surface charge on the CPM-*co*-MDMO-PPV NPs due to partial hydrolysis, which occurred during the washing steps. NPs with a charge present on the surface are known to be taken up faster than NPs with no surface charge, aside from the one caused by the physically adsorbed surfactant [149].

The uptake was also confirmed visually using confocal laser scanning microscopy (Figure 2-21 and 2-22) for living HMEC-1, BV-2 and C8-D1A cells. The fluorescent NPs show to remain stable in cell culture medium and all three cell lines are taking up nanoparticles within the incubation period without any detrimental effect on the cell morphological integrity, confirming the results of the cytotoxicity measurements. In accordance with the FACS results, all cells demonstrated an increased uptake of CPM-*co*-MDMO-PPV NPs, especially BV-2 cells. The small discrepancy between the cell lines as well as individual BV-2 cells is most likely the result of activated phagocytic cells showing a high rate of uptake for anionic NPs.

The astrocytes show rather flat polygonal fibroblast-like cell bodies (type 1) instead of central neuron-like bodies with long thing protrusions (type 2) (Figure 2-23) [150]. This is not due to the NP incubation but because C8-D1A cell lines belong to the type 1 astrocytes subcategory, as most culture cell lines do [151]. The C8-D1A cell line was chosen since it is used most frequently to study *in vitro* the astrocyte properties and are more associated with the blood brain barrier than other types of astrocytes, thus having a higher probability of encountering the incorporated nanoparticles [151].

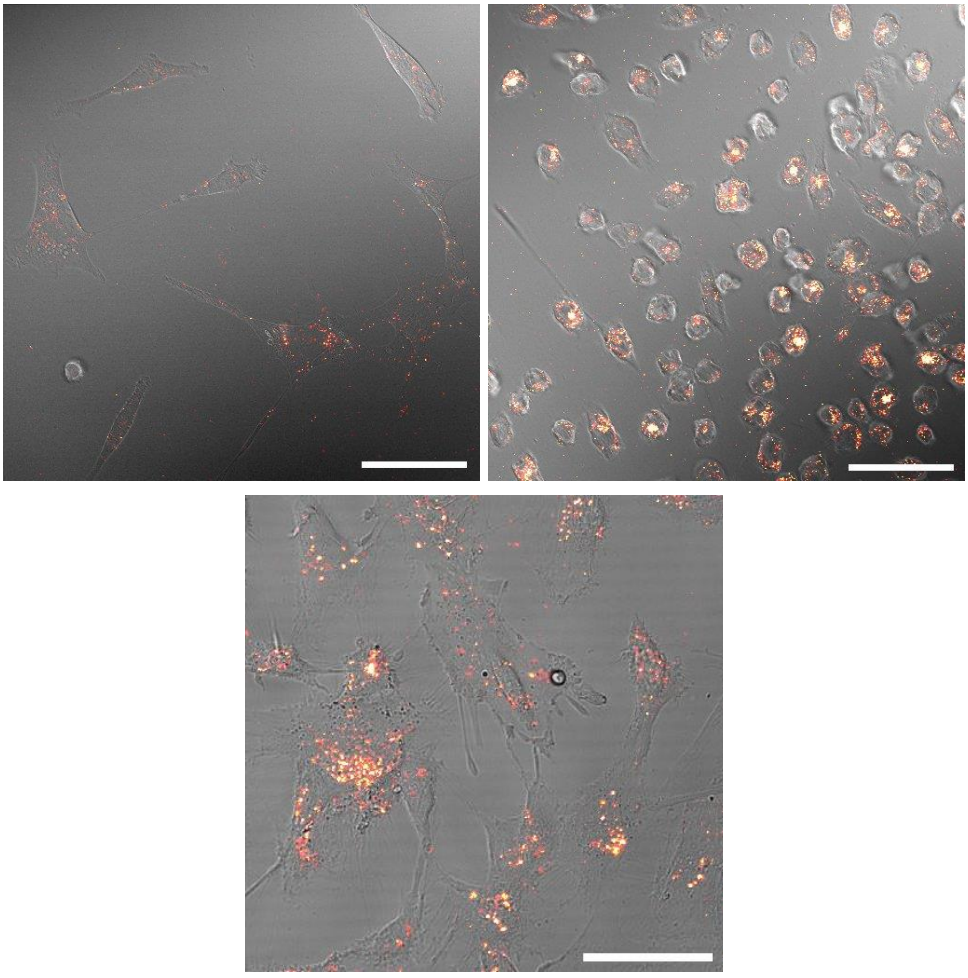

Figure 2—21: Confocal microscope image of CNS related cell lines treated with MDMO-PPV NPs.

Confocal microscope images of C8-D1A (left), BV-2 (right) and HMEC-1 (bottom) cells treated with MDMO-PPV NPs (red color) for a time period of 20 h. Scale bars represent 50 μm.

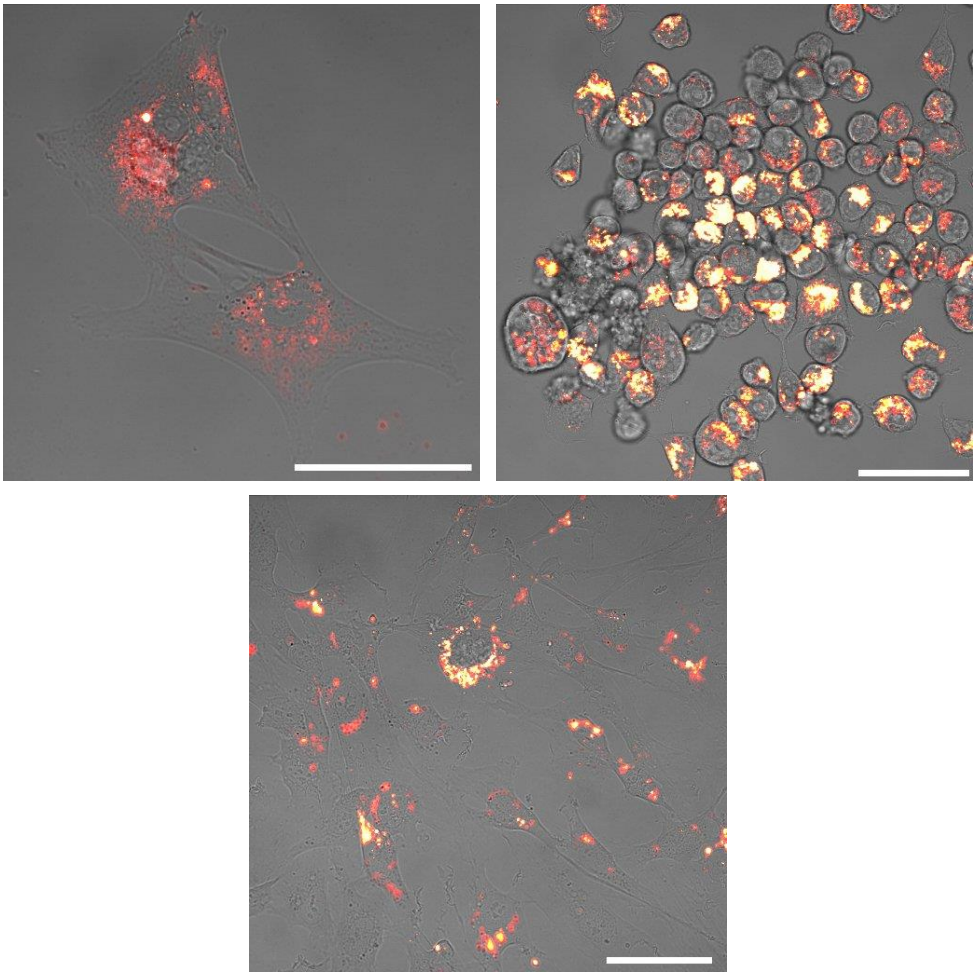

Figure 2—22: Confocal microscope image of CNS related cell lines treated with CPM-*co*-MDMO-PPV NPs.

Confocal microscope images of C8-D1A (left), BV-2 (right) and HMEC-1 (bottom) cells treated with CPM-*co*-MDMO-PPV NPs (red color) for a time period of 20 h. Scale bars represent 50 μm.

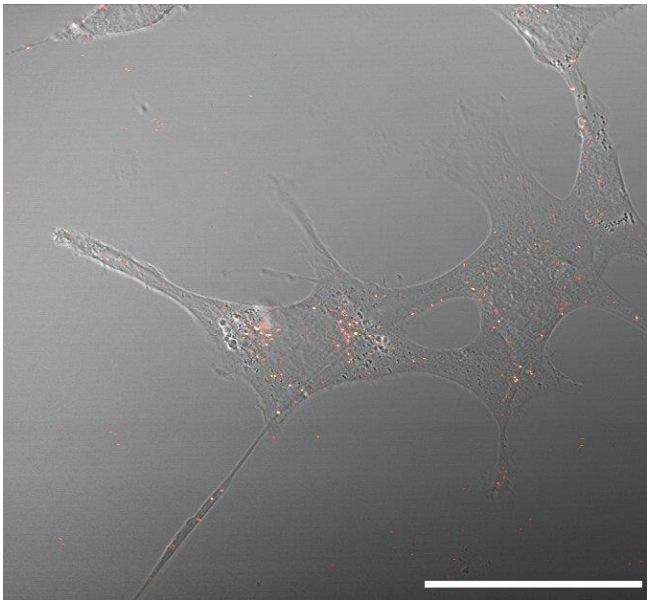

Figure 2—23: Confocal microscope image of MDMO-PPV NPs internalized by C8-D1A cells.

Confocal microscope image of MDMO-PPV NPs (red color) taken up by C8-D1A cells after a 24 h incubation period. Scale bar represents 50 μm.

A larger uptake of NPs is seen in the BV-2 cells compared to the HMEC-1 and C8-D1A cells, which can be explained by the nature of the cells. The murine BV-2 cell line is made through infecting primary microglial cell cultures with a v-raf/v-mvc recombinant retrovirus, exhibiting phenotypic as well as functional properties of active microglial cells and is widely employed in neuroscience research [152]. Microglial cells are immunocompetent macrophage-like cells, comprising 20 % of the total glial cell population, that are forming the core of the immune system inside the central nervous system [153]. Their role is to form the first line of defense for the brain against invasions of foreign microorganisms, thus they are most likely the first ones to respond to NPs [154]. Normally they have a ramified structure with small protrusions, but when activated this changes to an amoeboid-like appearance in order to migrate to the required site and phagocytize the intruders [155]. The larger uptake is thus correlated to the uptake mechanism of this specialized cell which is phagocytosis [149]. No ramified structure was seen on the confocal images, but it is documented that microglial cells do not have this

feature *in vitro* and show rather heterogeneous shapes like spindles, rods or even round which is the case in the confocal images [156]. Since the NPs are not covered with any biological agents, which could provide stealth, they activate and are taken up in large numbers by the microglia, hence explaining the uptake difference with HMEC-1 and C8-D1A cells. Amoeboid-like appearances as well as pseudopodia used to engulf and take up the nanoparticles can be visualized in Figure 2-24. It should be noted that the BV-2 cells were not stimulated by pharmacological agents, like macrophage colony stimulating factor (rM-CSF), used to induce phagocytosis or micropinocytosis [157]. All observations of the behavior of the cells regarding NP uptake in physiological conditions can thus be regarded as spontaneous. Apart from the neurological cell lines, HeLa cells also showed uptake of NPs as can be seen in Figure 2-25. Internalization of the NPs was confirmed by z-stacks throughout the cells (see video of image series acquired for HeLa cell after 24 h incubation).

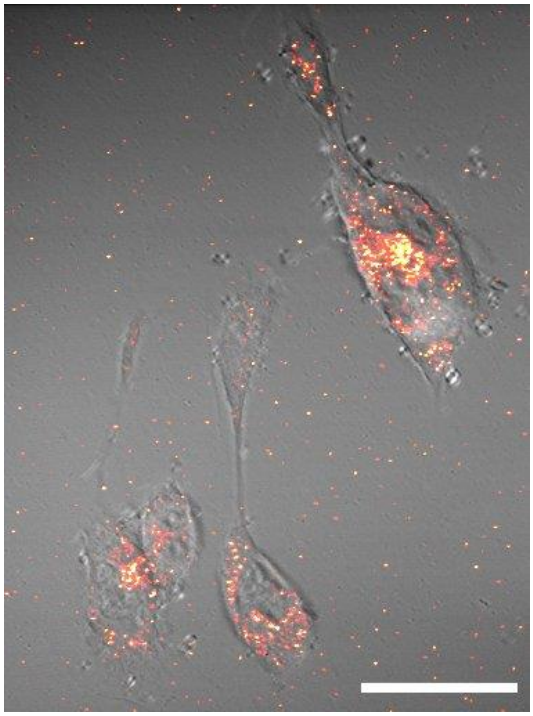

Figure 2—24: Confocal microscope image of MDMO-PPV NPs taken up by BV-2 cells
Confocal microscope image of MDMO-PPV NPs (red color) taken up by C8-D1A cells after a 24 h incubation period. Scale bar represents 25 μm.

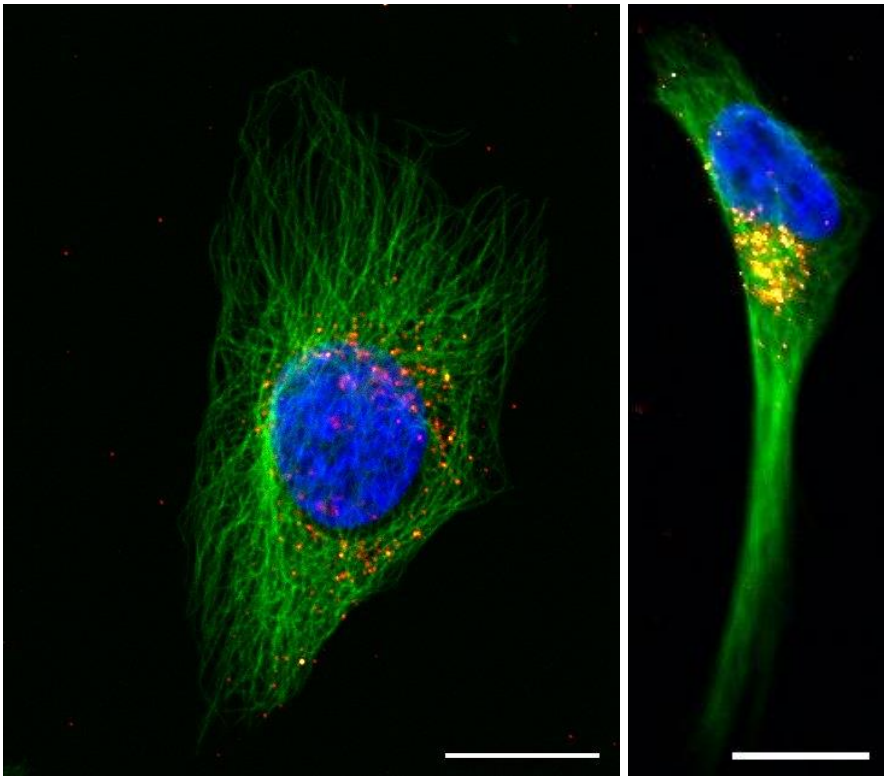

Figure 2—25: Confocal microscope images of MDMO-PPV NPs taken up by HeLa cells.

Confocal microscope images of MDMO-PPV NPs (red color) taken up by HeLa cells after a 24 h incubation period. Additional staining of the cell nucleus (blue) and tubulin (green) was performed. Scale bar represents 15 μm.

2.5 Conclusion

MDMO-PPV and CPM-*co*-MDMO-PPV NPs with a 100 nm size range were synthesized using the combination of miniemulsion and solvent-evaporation method. A more negative zeta potential was observed for the CPM-*co*-MDMO-PPV NPs, caused by carboxylic acid groups on the alkyl side chain. The latter renders the NP surface with functional groups that can be used for biomolecule conjugation. As a proof of principle, gold-labeled Ab were successfully attached to the NP surface. The study of optical properties revealed that the polymer in the nanoparticle configuration exhibited different characteristics as compared to their respective molecularly dissolved counterparts. Optical properties studies of the NPs determined a fingerprint of 500/590 nm. A clear shift from 550 to 590 nm in the emission maximum was observed for the NPs. This can be attributed to the characteristic switch from intrachain emission to interchain emission. Both NPs exhibit excellent photostability as no photobleaching occurred after 1 h of continuous exposure, compared to reference dyes. A quantum yield of 2-3 % was observed combined with a high molar extinction coefficient of $9*10^6$ $M^{-1}\cdot cm^{-1}$, resulting in a high fluorescence brightness. The NPs excited state lifetime reached around 500 ps, ideal for fast-imaging applications. The cell studies demonstrated that the NPs do not lower the cell viability below 90 % and can be internalized by different neurological cell types. A clear difference was observed between the uptake of MDMO-PPV NPs and CPM-*co*-MDMO-PPV NPs, the latter one being faster due to the surface charge of the carboxylic acid groups indicating the profound effect of an additional surface charge. As the results with the neurological cell lines are very encouraging, these NP systems apart from serving as a useful bioimaging probe will certainly spur new avenues for understanding some of the complex processes at the cellular level within the CNS. The results presented highlight that PPV-derivative based NPs are excellent candidates for bioimaging applications due to their interesting optical properties, design flexibility for surface functionalization, and benign biological characteristics.

Chapter 3
Size-dependent properties of functional PPV-based conjugated polymer nanoparticles

This chapter is based on:
Size-Dependent Properties of Functional PPV-based Conjugated Polymer Nanoparticles for Bioimaging.
Peters M., Seneca S., Hellings N., Junkers T., Ethirajan A
Manuscript submitted

Declaration of own contribution: Martijn Peters jointly designed the experiments. He performed all experiments, except for TEM imaging. He also participated in writing the manuscript.

3.1 Abstract

Conjugated polymer nanoparticle (NP) constructs have gained significant momentum in the bioimaging field on account of their accomplished biocompatibility and outstanding spectroscopic properties. Recently, new control procedures have spawned custom-built functional poly(*p*-phenylene vinylene) (PPV). These facilitate the one-pot synthesis of semiconducting polymer NPs with incorporated surface functional groups, an essential feature for advanced biomedical applications. In this work, NPs of different sizes are synthesized consisting of the statistical copolymer with monomer units 2-(5'-methoxycarbonylpentyloxy)-5-methoxy-1,4-phenylenevinylene and poly(2-methoxy-5-(3',7'-dimethoxyoctyloxy)-1,4-phenylenevinylene) (CPM-*co*-MDMO-PPV). To monitor potential implications of switching from a commonly used homopolymer to copolymer system, MDMO-PPV NPs were constructed as a control. The versatile combination of the miniemulsion and solvent evaporation method allowed for an easy adaptation of the NP size. Decreasing the diameter of functional PPV-based NPs up to 20 nm did not significantly affect their optical properties nor the biocompatibility of the bioimaging probe, as cell viability never dropped below 90 %. The quantum yield and molar extinction coefficient remained stable at values of 1-2 % and 10^6 $M^{-1}\cdot cm^{-1}$ respectively, indicating an excellent fluorescence brightness. However, a threshold was observed to which the size could be lowered without causing irreversible changes to the system. Cell uptake varied drastically depended on size and material choice, as switching from homo- to copolymer system and lowering the size significantly increased NP uptake. These results clearly demonstrate that adjusting the size of functional PPV-based NPs can be achieved easily to a lower limit of 20 nm and does not adversely affect their performance in bioimaging applications.

3.2 Introduction

Immense endeavors have been made during the last decennia to visualize and gain a more thorough insight into the extensive array of biological activities in living systems on the molecular and cellular level [3, 119, 120, 158]. Fluorescence imaging is a technique that allows researchers to bring about this ambition by providing a high temporal and spatial resolution in combination with an excellent signal-to-noise ratio. The adoption of conventional fluorescent visualization agents, including organic fluorophores as well as fluorescent nanoparticles (NPs) such as quantum dots and dye-doped silica colloids, have culminated in considerable advances in the biomedical field. Regardless of this impressive feature, each material system still has its own deficiencies and intrinsic restraints [8, 17-19, 21, 22, 159, 160]. For instance, the long established low molecular weight organic dyes are often plagued by a poor photostability and rapid cellular efflux. These obstacles can be surmounted by encapsulating them in NPs or by shifting to other options like quantum dots and nanodiamond. Nevertheless, these systems face other obstacles. NPs with encapsulated dyes often encounter pigment leakage or self-quenching and the use of quantum dots is still under debate given their short- and long-term cytotoxicity issues as well as *in vivo* degradation. Albeit nanodiamonds solve most of the aforementioned problems, dispersing them into single nanoparticles without causing contamination is a demanding task [161].

Due to the remaining shortcomings of the preceding material classes, water-based colloidal dispersions consisting of fluorescent conjugated polymers have gained great acclaim within the bioimaging field [10, 23, 111, 113, 162-165]. The reason for this is their ultra-bright photoluminescence, owing to their π-conjugated backbone, in conjunction with an excellent biocompatibility. A prominent example amongst semiconducting polymers is poly(*p*-phenylene vinylene) (PPV), which is mostly known for being the pioneer material in the first organic light emitting diode constructs and has since been exploited in a wide variety of applications like biological sensors, solar cells and various other optoelectronic devices. Its acclaim can be ascribed to its well-known photophysical properties and dependable synthesis routes, like the sulfinyl precursor route, that can be used to devise state-

of-the-art custom-made functional PPVs while being simple to scale up [38, 49, 56, 57, 140]. These complex functionalized PPVs grant an easy and elegant way to generate NPs with functional groups distributed on the surface that can be employed for the on demand attachment of various nature- or man-made entities [165]. This has tremendous potential in the biomedical field where there is a never-ending appeal for the incorporation of different functional properties (stealth effect, barrier crossing potential, etc.) to permit control over biological and chemical traits.

Alongside surface alteration, NP size is one of the most critical concerns for biomedical applications as it has been identified to play a key role in biological processes like cellular uptake, biodistribution and cytotoxicity [166, 167]. Effective internalization by cells is essential to achieve the successful application of NPs for bioimaging objectives. In addition, adjusting the size can have an influence on the optical properties of conjugated polymer NPs [60]. Here, we probe for the first time the potential consequences of lowering the size of functional PPV-based NPs on the optical and biological characteristics of a conjugated system specifically designed for bioimaging purposes. The NP construct's core material consists of the functional statistical copolymer with monomer units 2-(5'-methoxycarbonylpentyloxy)-5-methoxy-1,4-phenylene-vinylene and poly(2-methoxy-5-(3',7'-dimethoxyoctyloxy)-1,4-phenylene-vinylene) (CPM-PPV-*co*-MDMO-PPV, for simplicity henceforth called CPM-*co*-MDMO-PPV). The ester groups available at the CPM-*co*-MDMO-PPV NPs surface are of particular significance as they can be conveniently converted into carboxylic acid groups, enabling facile coupling of various biomolecules on demand. Since most PPV-based NP studies only focus on homopolymers, MDMO-PPV NPs were included to demonstrate the potential consequences of transitioning from this system to a statistical copolymer type. Size adaptation was achieved by implementing subtle changes in the synthesis method, a combination of the miniemulsion and solvent evaporation method [164, 165, 168]. Subsequently, the effects of varying the size on the colloidal, optical and biological properties of the water-based bioimaging agent were studied in detail.

3.3 Materials and methods

3.3.1 Materials and products

Rhodamine 6G, penicillin/streptomycin (P/S), hydrocortisone (HC), L-glutamine, trypsine, paraformaldehyde (PFA), triton X-100 were purchased at Sigma-Aldrich (Diegem, Belgium). Human microvascular endothelial cells (HMEC)-1 (CRL-3243) were bought at ATCC (Molsheim, France). MCDB 131 medium, fetal calf serum (FCS), recombinant human epidermal growth factor (EGF), iscove's modified dulbecco's medium (IMDM) medium and alamar blue were obtained from Life Technologies (Ghent, Belgium). All culture and dark plates were bought at Greiner Bio One (Vilvoorde, Belgium). The 1x phosphate buffered saline (1xPBS) was purchased at Lonza (Verviers, Belgium). Sodium dodecyl sulfate (SDS) was bought at GE Healthcare Life Sciences (Diegem, Belgium). Spectrum™ Spectra/Por 3 Regenerated Cellulose Dialysis Membrane Tubing (3.5 kD, 45 mm flat width) were bought at Fisher Scientific (Merelbeke, Belgium). All chemicals were used as provided without further purification.

3.3.2 PPV-based NPs of various sizes: synthesis procedure

The synthesis procedure of the conjugated polymer and NPs was performed as described elsewhere [165]. NPs consisting of either MDMO-PPV (Mn = 150 000 $g \cdot mol^{-1}$) or the copolymer CPM-*co*-MDMO-PPV (Mn = 164 200 $g \cdot mol^{-1}$, 66:34 MDMO:PPV ratio as determined by ^{1}H NMR) were constructed employing a combination of the miniemulsion and solvent evaporation method. In order to generate different sizes of NPs various amounts of polymer (50, 25, 10, 5, 2.5 and 1 mg) were used in the synthesis procedure and the surfactant SDS was increased to 100 mg in 24 g of ultrapure water solution. The continuous phase, consisting of SDS and ultrapure water, and dispersed phase, consisting of the conjugated polymer in $CHCl_3$, are mixed together to pre-emulsify. This mixing step is followed by ultrasonication (1/4”-tip, 3 min, 65 % amplitude, 30 s pulse and 20 s pause regime) under ice cooling to generate nanodroplets of which the organic solvent is evaporated at 40 °C overnight. This results in a colored dispersion of PPV-based NPs in water after filtration (Whatman, pore size 4–7 μm) of the sample to remove any large aggregates present.

3.3.3 PPV-based NPs of various sizes: washing, reconcentration and characterization

After synthesis, the NPs underwent 40 washing steps of 1 hour employing Spectrum™ Spectra/Por 3 Regenerated Cellulose Dialysis Membrane Tubing (3.5 kD, 45 mm flat width) at 500 rpm with ultrapure water. Subsequently, the samples were reconcentrated through evaporation at 40 °C with 500 rpm stirring. The reconcentrated NP samples were sterilized using an IBL 437C type gamma radiator (Cis Bio International, Codolet, France) at 30 Gy (= 3000 rad) after which they were stored in the dark.

The hydrodynamic diameter, polydispersity and zeta potential were determined using dynamic light scattering with Brookhaven Instrument Cooperation ZetaPALS equipment (Waddinxveen, The Netherlands). In parallel, the study of size and morphology of the NPs was performed with TEM at an accelerating voltage of 120 keV using a FEI Tecnai G2 spirit twin (Zaventem, Belgium), after drop casting and drying the respective samples on copper grids. TEM data are represented as means ± standard deviation after measuring 25 NPs per sample using ImageJ software, which was also used to process the images. As the solutions were dilute, the solid contents were obtained by determining the amount of conjugated polymer in a given volume from their measured absorbance using the Agilent Technologies Cary 5000 UV-VIS-NIR spectrophotometer (Diegem, Belgium). For this, a calibration curve of the absorbance of various conjugated polymer concentrations (10, 25, 50, 100, 250, 500, 1000, 2500 μg/mL) for MDMO-PPV and CPM-*co*-MDMO-PPV in $CHCl_3$ was constructed. The respective NP samples were dried and redissolved in $CHCl_3$ after which the absorbance was measured and used to calculate the solid content.

3.3.4 Influence of NP size on optical characteristics of PPV-based NPs

The optical fingerprint of PPV-based NPs of different sizes and PPVs were measured in a 1 cm quartz cuvette with the Cary 5000 UV-VIS-NIR spectrophotometer and Horiba Jobin Yvon Fluorolog3 Tau fluorescence spectrophotometer (Lier, Belgium). The wavelength dependence of the throughput and sensitivity of the detection channel were corrected for the emission spectra.

A comparison was made between the different NP sizes for the molar extinction coefficient, absorption cross-section and quantum yield (QY). The Beer-Lambert Law was used to calculate the molar extinction coefficient of the NPs, by varying their concentration in water, and subsequently used to determine the absorption cross-section. The QY was determined with rhodamine 6G as fluorescence reference (QY = 0.95, in H_2O). Five dilutions were prepared for all samples and reference, the absorbance of the most concentrated one reaching a value of 0.1 at 490 nm excitation to which the standard was optically matched. For each of these sample dilutions the emission spectrum correlated to the respective excitation wavelength was measured and the absorption versus integral of emission spectrum was plotted. The obtained slope value (m) of the fitted trend line and refractive indexes (η) of the liquids were inserted into the following formula to obtain the QY.

$$QY_{SAMPLE} = QY_{STANDARD} \times \frac{m_{SAMPLE}}{m_{STANDARD}} \times \frac{\eta^2_{SAMPLE}}{\eta^2_{STANDARD}}$$

Subsequently, the fluorescence brightness of the NPs (B_{NP}) was determined through multiplication of the quantum yield and molar extinction coefficient.

3.3.5 Influence of NP size on biological characteristics of PPV-based NPs

Cell Culture. The HMEC-1 cell line was maintained in a T25 flask in culture medium (MCDB 131 medium supplemented with 10 % FCS, 0.5 % P/S, 500 ng EGF, 50 μg HC, 500 μmol L-Glutamine) stored at 37 °C in a 5 % CO_2 incubator (Sanyo, Japan). The medium needed to be refreshed after 3 days and the cell line was spliced after reaching 80 % confluence.

Cytotoxicity assay. HMEC-1 cells were seeded and left to grow to 80 % confluence at 37 °C in a 5 % CO_2 incubator in a 96-well flat bottom plate. The NP samples were diluted to a defined concentration range (5, 10, 25, 50 μg/mL), starting from a stock solution of 197 μg/mL, in phenol red poor IMDM culture medium (MCDB 131 medium replaced by IMDM medium). Before adding 100 μL of each concentration to the cells, the latter were washed with 1xPBS (9 g/L NaCl, 0.795 g/L Na_2HPO_4, 0.144 g/L KH_2PO_4). A total of six wells per condition was taken and positive as well as negative control conditions were included. After an incubation

period in the incubator of 24 h, the cells were washed 3 times with 1xPBS and a 10 % alamar blue solution in IMDM culture medium was added. After another 24 h, the resulting solution was transferred to an opaque-walled dark 96-well culture plate and the fluorescence was measured using a BMG Labtech FLUOstar OPTIMA (Temse, Belgium) at 590 nm with an excitation at 570 nm. The experiment was performed in triplicate. Data are represented as means ± standard deviation after analyzing with the commercially available software JMP Pro 12 (SAS Institute Inc., USA). Analysis of linear mixed model followed by a post-test Dunnett for multiple comparisons ($p < 0.05$) were performed.

Uptake Kinetics. HMEC-1 cells were seeded, employing a density of 100 000 cells per well, in a 24-well plate and left to grow for a 24 h period in a 5 % CO_2 atmosphere at 37 °C. First the cells were washed with 1xPBS after which 500 μL of 25 μg/mL of NPs in IMDM culture medium solution was added to the cells for a specific incubation period (5 min, 15 min, 30 min, 1 h, 2 h, 4 h, 6 h, 24 h and 30 h) at 37 °C with a CO_2 level of 5 %. After this period, the cells were washed 3 times with 1xPBS and harvested. Subsequently, the pellet was redispersed in 4 % PFA and left to incubate in the dark for 20 min at room temperature (RT). In order to remove the PFA, the cells were centrifuged 3 times after which the pellet was redispersed in fluoresence-activated cell sorting (FACS) buffer (1xPBS and 2 % FCS). The resulting samples were measured and analyzed with the Becton Dickinson LSR Fortessa (Erembodegem, Belgium). A 488 nm laser and 530/30 nm emission filter were employed and unlabeled cells were used as a blank to gate the signal. For each sample 20 000 cells were counted in triplicate. The number of cells that contained a fluorescent signal corresponding to NP uptake were converted to a percent scale from 0 – 100 % with 100 % meaning that in all cells fluorescence was detected and thus NPs were present.

Confocal Laser Scanning Microscopy. HMEC-1 cells were left to adhere and grow for 24 h at 37 °C with a starting concentration of 20 000 cells per well in a μ-Slide 8-well plate (Ibidi). Subsequently, the cells were washed 3 times with 1xPBS after which 400 μL of 25 μg/mL of NPs in IMDM culture medium was added and left to incubate for a period of 24 h. The cells were washed 3 times with 1xPBS after which they were fixated with 4 % PFA for 20 min at RT in the dark. After this, the PFA solution was removed and the cells were washed an additional 3 times with

1xPBS. The images were collected at RT with a Zeiss (Zaventem, Belgium) LSM510 META NLO mounted on an inverted laser scanning microscope (Zeiss Axiovert 200 M) and a water immersion 40x/1.1 objective. Nanoparticle excitation was performed with an Argon-ion laser at 488 nm (3 μW maximum radiant power at the sample) and the emission was detected with a band-pass filter of 565-615 nm. The resulting 1024x1024 images were recorded using a pixel dwell time of 14.2 μs with a pixel size of 0.06 μm. The images were processed using ImageJ and AIM 4.2 software.

.

3.4 Results and discussion

3.4.1 Synthesis of PPV-based NPs of different sizes

The particle formulation of PPV-based NPs of different sizes was performed using a combination of the miniemulsion technique and solvent evaporation approach. This process allows for a tunable NP diameter, surface functionality and solid content [134, 169]. Two types of preformed PPVs were employed, namely the homopolymer MDMO-PPV and statistical co-polymer CPM-*co*-MDMO-PPV. The latter is a polar functionalized PPV carrying an ester group on the alkoxy side chain that can be functionalized either by saponification or transesterification. The resulting formulated NPs are expected to bear ester groups distributed on the surface and within the volume of the NPs, whereby the surface groups can be easily converted through hydrolysis into carboxylic acid groups. These chemical moieties are of particular interest as they can be employed for the straightforward incorporation of numerous functional attributes. The negatively charged low molecular weight surfactant SDS was selected as the surfactant for the stabilization of the droplets (size tunable between 30 and 500 nm) [23].

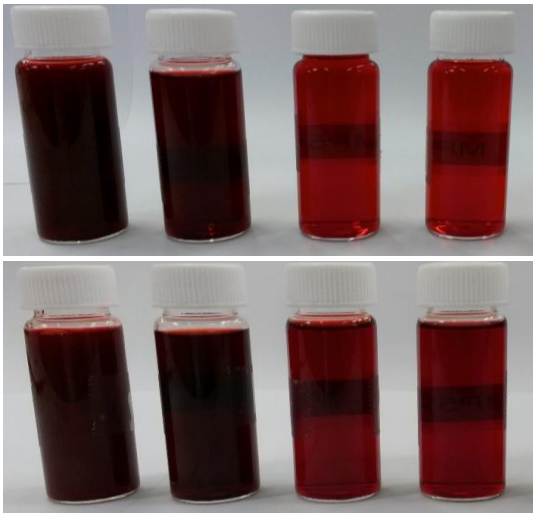

Figure 3—1: CPM-*co*-MDMO-PPV and MDMO-PPV NP dispersions with different sizes.

Water-based formulations of CPM-*co*-MDMO-PPV (top) and MDMO-PPV (bottom) NPs with different sizes created by varying starting amount of PPV (amounts of polymer used during synthesis are 50, 25, 10 and 5 mg from left to right).

To diminish the diameter of the PPV-based NPs, the polymer load used during preparation was scaled down [170]. The resulting characteristics of the red-colored water-based dispersion of PPV-based NPs (Figure 3-1) are summarized in Table 3-1. Decreasing the amount of polymer from 50 mg to 5 mg led to a reduction in the hydrodynamic diameter from 51.1 nm to 16.7 nm for the CPM-*co*-MDMO-PPV NPs as shown by DLS as well as TEM (Figure 3-2). The same effect was monitored for the MDMO-PPV NPs. However, it was observed that the polydispersity value of the nanoparticle formulations rose as the amount of polymer decreased. It has already been demonstrated that the employed synthesis method has the inherent characteristic of generating colloidal dispersion with a large size distribution [169]. In addition, for the same amount of the dispersed phase solvent, a larger amount of hydrophobic polymer within the emulsion droplets can also serve as an osmotic control agent, thereby leading to a reduced size distribution for NPs of a bigger size.

Table 3—1: Formulation and characteristics of the synthesized PPV-based NPs

Sample	Formulation	Polymer (mg)	DLS (nm)	TEM (nm)
1a	CPM-*co*-MDMO-PPV	50	51.1 (±12,6) (PDI = 0.102)	53.0 (±13.0)
2a	CPM-*co*-MDMO-PPV	25	34.2 (±9.8) (PDI = 0.132)	30.7 (±7.1)
3a	CPM-*co*-MDMO-PPV	10	20.9 (±7.5) (PDI = 0.204)	29.6 (±3.6)
4a	CPM-*co*-MDMO-PPV	5	16.7 (±6.3) (PDI = 0.226)	22.0 (±4.5)

1b	MDMO-PPV	50	50.9 (±13.0) (PDI =0.108)	54.3 (±8.8)
2b	MDMO-PPV	25	28.2 (±9.5) (PDI =0.179)	33.5 (±7.2)
3b	MDMO-PPV	10	23.0 (±7.6) (PDI =0.174)	26.5 (±4.6)
4b	MDMO-PPV	5	17.0 (±6.9) (PDI =0.267)	22.6 (±2.6)

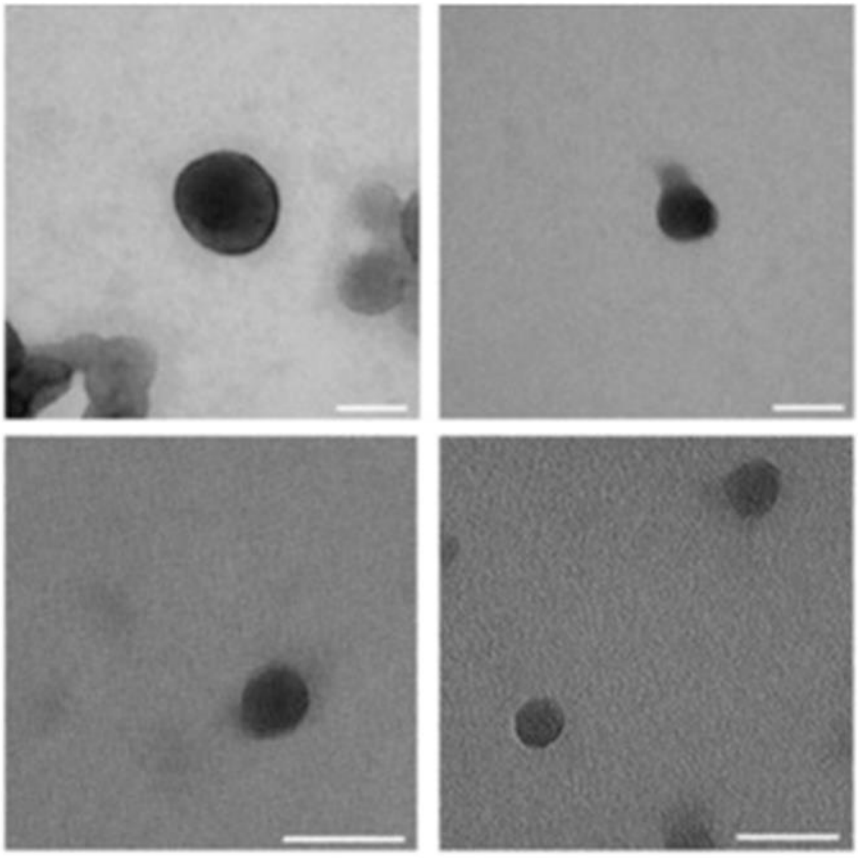

Figure 3—2: TEM image of CPM-*co*-MDMO-PPV NPs with different sizes.

TEM image of CPM-*co*-MDMO-PPV samples 1a (top left), 2a (top right), 3a (bottom left) and 4a (bottom right). Scale bar represent 50 nm.

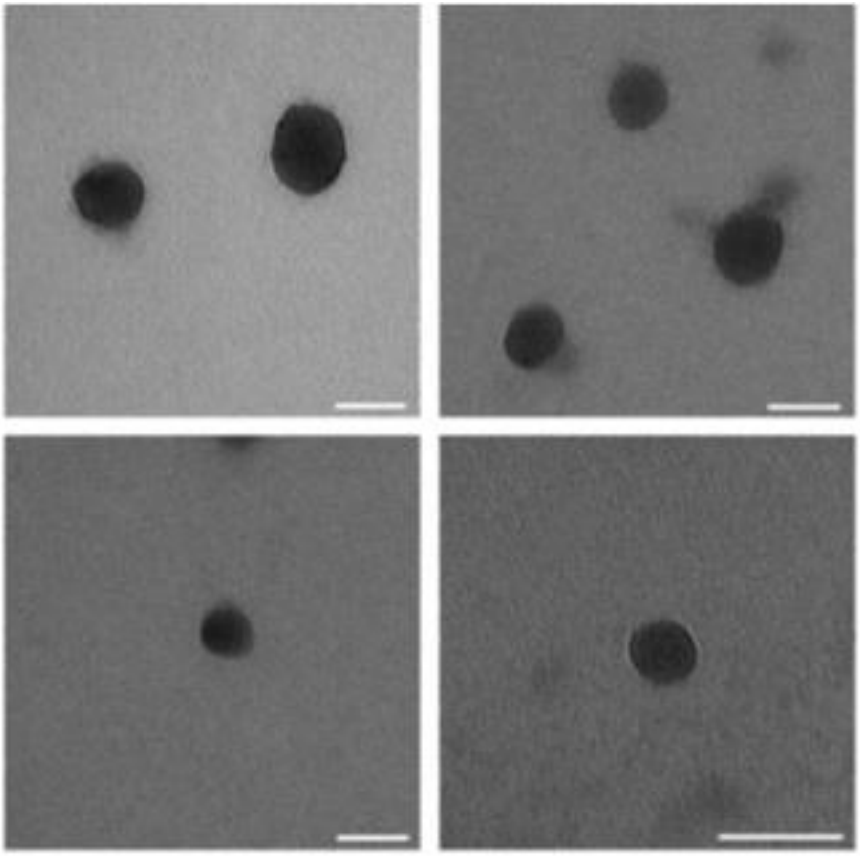

Figure 3—3: TEM image of MDMO-PPV NPs with different sizes.
TEM image of MDMO-PPV samples 1b (top left), 2b (top right), 3b (bottom left) and 4b (bottom right). Scale bar represent 50 nm.

Another consequence of synthesizing NPs through lowering the polymer content is that it was required to reconcentrate the sample in order to be suitable to operate as a bioimaging probe without causing dilution induced effects. The resulting solid content was determined through UV-VIS-spectrophotometry rather than thermogravimetrically due to dilute samples (Figure 3-4). Given the excess of SDS that is extracted during the extensive washing steps, as demonstrated by earlier research [165], the remaining NPs only consist out of their respective PPV-derivative and some residual traces of SDS. Following washing and reconcentrating, the samples' solid content ranged from 1427 to 88 μg/mL for CPM-*co*-MDMO-PPV NPs and 907 to 197 μg/mL for MDMO-PPV NPs.

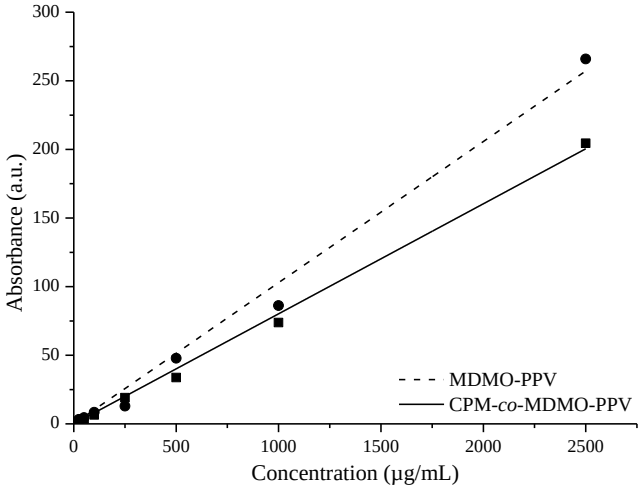

Sample	1a	2a	3a	4a	1b	2b	3b	4b
Solid content (µg/mL)	1427	670	199	88	907	637	208	197

Figure 3—4: UV-VIS-spectrophotometric determination of NP solid content.
Determination of the NP samples' solid content using UV-VIS-spectrophotometry with the respective calibration curve (top) and solid content values (bottom).

3.4.2 Influence of NP size on optical characteristics of PPV-based NPs

Subsequently, the influence of size reduction on the optical attributes of the NPs was studied in detail employing different optical spectroscopic techniques. The absorbance and emission spectrum were assessed using UV-VIS and fluorescence spectroscopy (Figure 3-5 and 3-6). Decreasing NP size did not alter their characteristic broad adsorption band, ranging from 350 to 600 nm. The same implies for the emission spectrum, exhibiting its characteristic vibronic structure (0-0, 0-1 and 0-2 emission bands at 590, 640 and 660 nm respectively), where no distinct difference was observed. This is in line with previous findings by Barbara et al., who showed that MEH-PPV based NPs are spectroscopically indistinguishable from each other and bulk thin films when their radius exceeds the size of 10 nm [60]. There is however a noticeable difference in the spectrum between the MDMO-PPV and CPM-*co*-MDMO-PPV NPs.

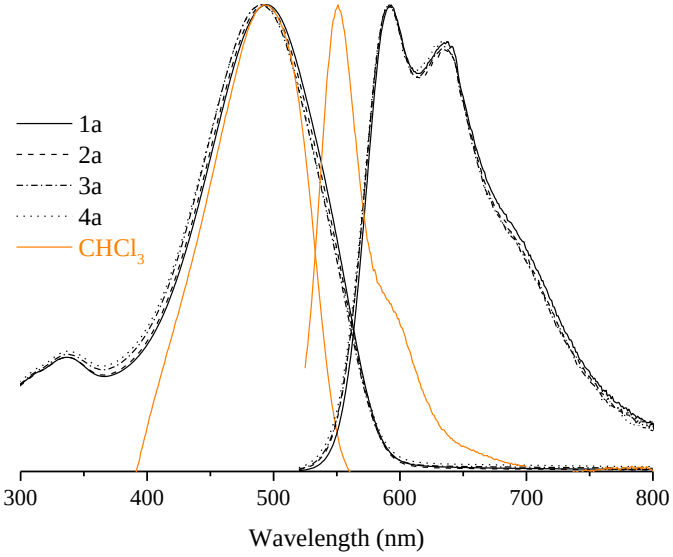

Figure 3—5: Size-dependent fingerprint of CPM-*co*-MDMO-PPV NPs.
Absorbance (left) and emission (right) profile of CPM-*co*-MDMO-PPV NPs of various sizes (black) as well as the molecularly dissolved polymer in chloroform (orange).

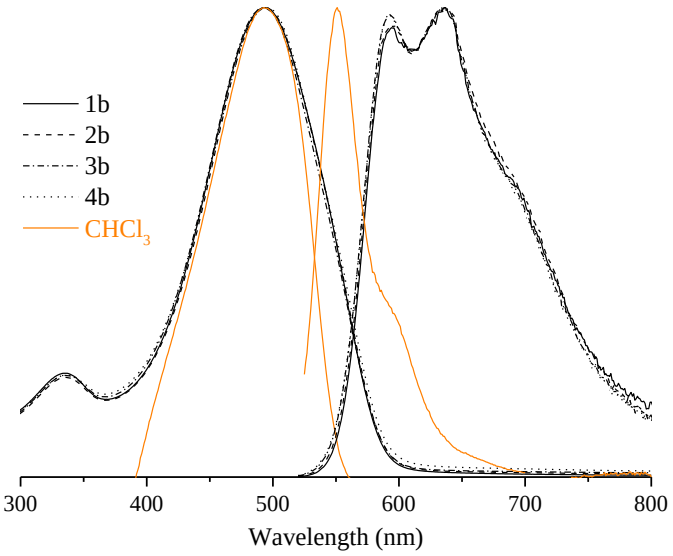

Figure 3—6: Size-dependent fingerprint of MDMO-PPV NPs.
Absorbance (left) and emission (right) profile of MDMO-PPV NPs of various sizes (black) as well as the molecularly dissolved polymer in chloroform (orange).

A total red-shift of the whole vibronic structure from single polymer chains to NPs is expected as the dipole of the PPVs excited state interacts more strongly, in the highly polarizable environment of a NP construct, with its surroundings. This is observed for both PPV constructs as their emission shifts from 550 to 580 upon turning into NP conformation. However, a difference is noted in the relative height of the vibronic peaks between the two PPVs. For MDMO-PPV based NPs, a more substantial boost of the two low-energy red peaks occurs when compared to CPM-*co*-MDMO-PPV NPs. This observation can be correlated to the difference of the NPs' side chain, as that of CPM-*co*-MDMO-PPV is more polar. It is likely that this affects the chromophore packing during NP formation as well as the interactions of the exterior chains with the surrounding solvent. MDMO-PPV lacks these polar side chain groups and is therefore more prone to strong hydrophobic attraction between chains and large interfacial surface tension between the polymer and water. It encounters a larger drop in solvent quality as compared to CPM-*co*-MDMO-PPV, resulting in more kinking and bending of the polymer backbones and the subsequent stronger interchain interaction [130]. Therefore, CPM-*co*-MDMO-PPV NPs' main peak is the 0-0 band at 590 nm, while for MDMO-PPV NPs this shifts to the 0-1 band at 640 nm with an additional increase in the 0-2 band [64, 145]. The switch in the main peak location of small MDMO-PPV NPs can be attributed to the chain becoming more hydrophilic during the NP synthesis process. It was shown that when working with small amounts of PPV, chemical defects might be more likely to occur during the synthesis process [66].

Several other inherent optical characteristics, besides the NP fingerprint, are summarized in Table 3-2. Variation of NP size or polymer showed no distinct difference with regard to quantum yield as it retained its value of 1-2 % [130]. The molar extinction coefficient lowered as the number of chromophores per NP decreases when the size becomes smaller, but remained in the order of 10^6 $M^{-1} \cdot cm^{-1}$ [130]. The size variation did not have detrimental ramifications on the fluorescence brightness, the product of the quantum yield and the molar extinction coefficient, which is one of the determining factors for a successful imaging probe.

Table 3—2: Optical characteristics of the synthesized PPV-based NPs.

	$\lambda_{max,ex}$ (nm)	$\lambda_{max,em}$ (nm)	Quantum Yield (φ_F, %)	Molar extinction coefficient (ε, $M^{-1} \cdot cm^{-1}$)	Absorption cross section (σ, cm^2)
1a	494	593	2	13.1×10^6	5.00×10^{-14}
2a	493	591	2	10.2×10^6	3.91×10^{-14}
3a	490	591	2	$9{,}9 \times 10^6$	3.80×10^{-14}
4a	490	592	1	9.7×10^6	3.71×10^{-14}
1b	494	636	2	11.7×10^6	4.47×10^{-14}
2b	494	638	1	9.5×10^6	3.65×10^{-14}
3b	492	636	1	9.5×10^6	3.62×10^{-14}
4b	495	592	1	6.4×10^6	2.46×10^{-14}

In order to investigate the limit of lowering the amount of PPV to synthesize smaller NPs with the employed synthesis method, an additional sample was made using only 1 mg of the respective polymers (Figure 3-7 and 3-8). For both constructs, a transformation in the colloidal dispersion color from red to orange (MDMO-PPV) and yellow (CPM-*co*-MDMO-PPV) was observed. In addition, the CPM-*co*-MDMO-PPV NPs absorbance intensity lowered and both constructs demonstrated a blue shift in the excitation as well as emission spectrum. This latter feature signifies a shortening in the average conjugation length of the conjugated polymer [145].

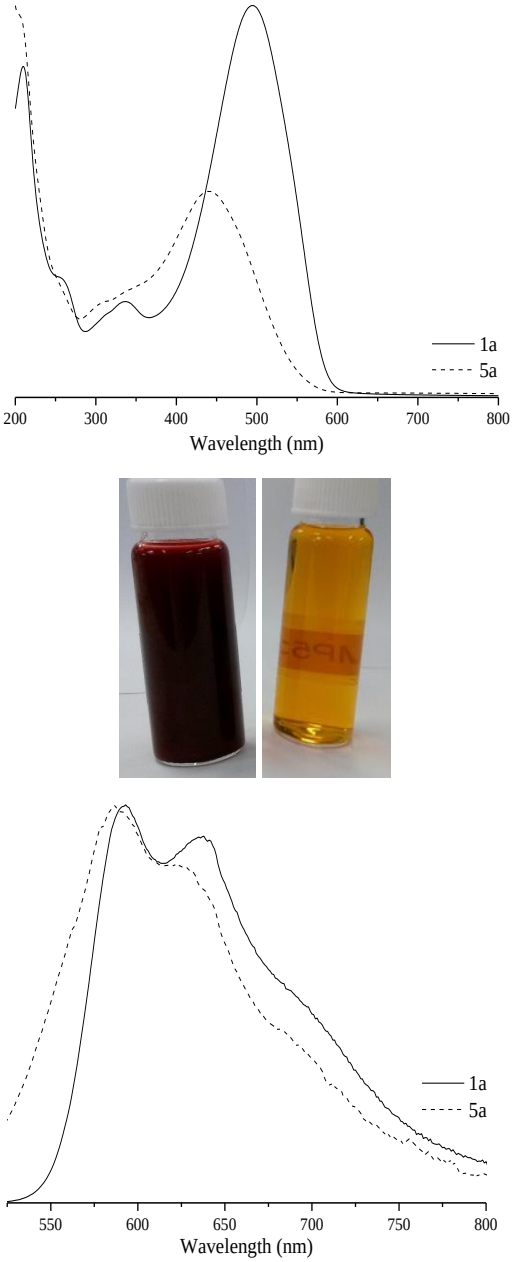

Figure 3—7: Fingerprint of CPM-*co*-MDMO-PPV NPs with low and high starting polymer concentration.

Absorbance (top) and emission (bottom) profile of CPM-*co*-MDMO-PPV NPs with a low starting polymer amount (sample 5a, 1 mg, right vial) and high starting polymer amount (sample 1a, 50 mg, left vial).

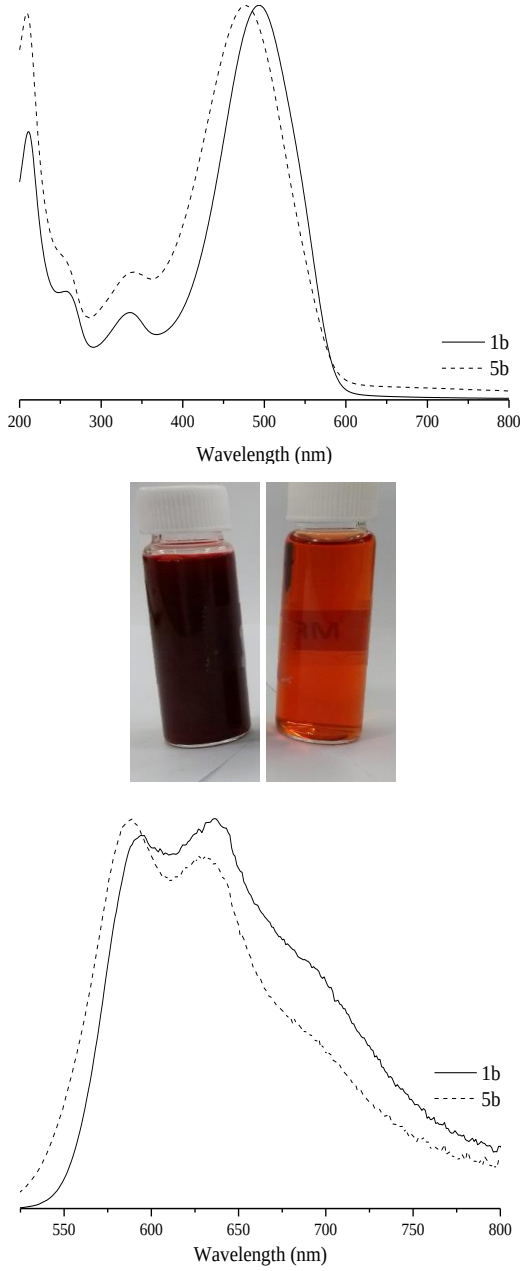

Figure 3—8: Fingerprint of MDMO-PPV NPs with low and high starting polymer concentration.

Absorbance (top) and emission (bottom) profile of MDMO-PPV NPs with a low starting polymer amount (sample 5b, 1 mg, right vial) and high starting polymer amount (sample 1b, 50 mg, left vial).

In order to determine if the conjugation length shortening was a temporary or permanent issue CPM-*co*-MDMO-PPV NPs were redissolved in $CHCl_3$ and the fingerprints of the free molecular chains measured (Figure 3-9). If the blue shift was caused by a reversible effect, such as torsion of the polymer backbone, no difference should be observed between the spectra of both samples. Sample 1a exhibited the innate behavior of the system when dissolved in $CHCl_3$, namely an alteration in the emission maximum to 550 nm and a narrowing of the absorbance spectrum peak due to the disappearance of aggregates [165]. However, sample 5a displayed a blue shift in absorbance maximum to 417 nm, loss of the vibronic structure and the appearance of a blue shoulder in the emission spectrum. This clearly demonstrates that the change in conjugation length is a permanent feature.

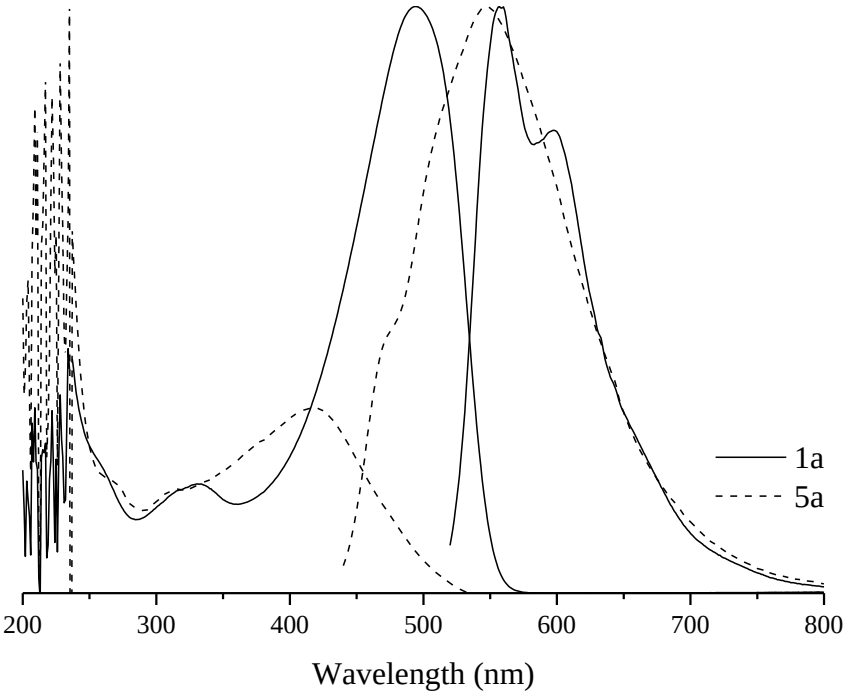

Figure 3—9: Fingerprint of in $CHCl_3$ dissolved CPM-*co*-MDMO-PPV NPs with low and high starting polymer concentration.

Fingerprint of molecular chains of redissolved CPM-*co*-MDMO-PPV NPs in CHCl3 of low (sample 1a, 1 mg, solid line) and high (sample 5a, 50 mg, dashed line) starting polymer concentration.

It is well documented that the double bonds between the aryl units in PPVs are prone to photo-oxidation, a process which potentially can disrupt the π-conjugation [171]. Because the 5a NPs consist of only a few polymer chains as compared to variants 1a – 4a, resulting in a higher surface-to-volume ratio, it is probable that the chains in the configuration are more exposed to photoinduced oxidation, chain scission and opening of the conjugated system, as these processes are much more severe at the surface where solar irradiation takes place [66, 172]. The difference between CPM-*co*-MDMO-PPV NPs and MDMO-PPV NPs can be attributed to the hydrophilic side chains of the former. Swelling behavior at the interface might induce extra void space between the chain coils, allowing for oxygen to diffuse more readily to the photoexcited regions and resulting in an increase of the rate at which damage occurs [145]. In addition, chain degradation can also occur due to exposure to ultrasonication [71].

3.4.3 Influence of NP size on biological characteristics of PPV-based NPs

As it has been established that the size of nanoparticles plays a pivotal role in the interplay with their biological surroundings, the influence of size modification on the biological characteristics was studied. Although it was shown earlier that CPM-*co*-MDMO-PPV and MDMO-PPV based NPs of 100 nm size are not cytotoxic [165], reducing the diameter can have a detrimental effect on the biocompatibility [173-175]. Therefore, it is of importance to re-evaluate the cytotoxicity of PPV-based NPs of various sizes. Cytotoxicity experiments were conducted on HMEC-1 cells as endothelial cells make up the blood vessels and are therefore one of the first cell-types that NPs will encounter upon being administered.

The alamar blue assay results showed that size did influence the biocompatibility of PPV-based NPs (Figure 3-10 and 3-11). For the higher concentrations there was a slight statistically significant reduction on viability independent of size. However, cell viability never dropped below 90 % after an exposure period of 24 h, which is in agreement with previous results [165]. Accordingly, it can be concluded that varying the size of PPV-based NPs does not have a discernible impact on cell viability. Sample 4a was excluded from the cytotoxicity and uptake studies, given the concentration was too low to conduct the biomedical experiments with.

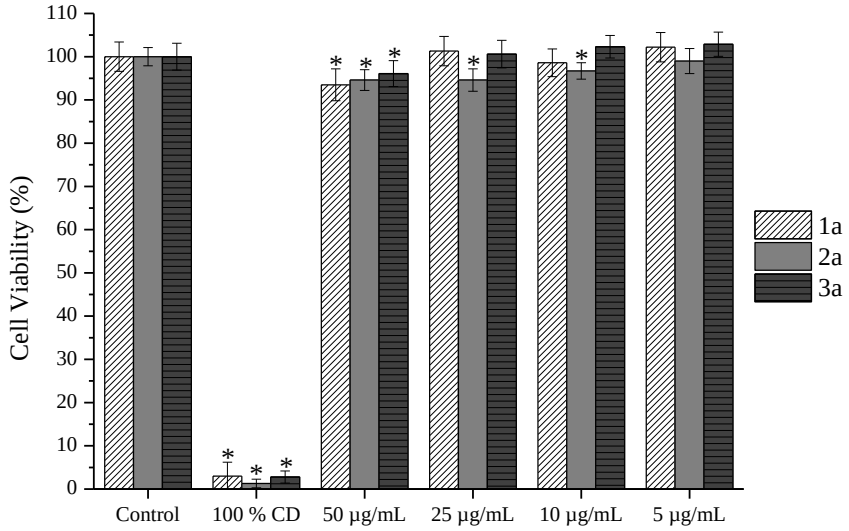

Figure 3—10: Dose-dependent cytotoxicity of CPM-*co*-MDMO-PPV NPs of different sizes.

Dose-dependent cytotoxicity of CPM-*co*-MDMO-PPV NPs of different sizes (sample 1a – 3a) in HMEC-1 cells after 24 h, tested with the alamar blue assay. Data are expressed as percentage of control mean ± SD (N =3).

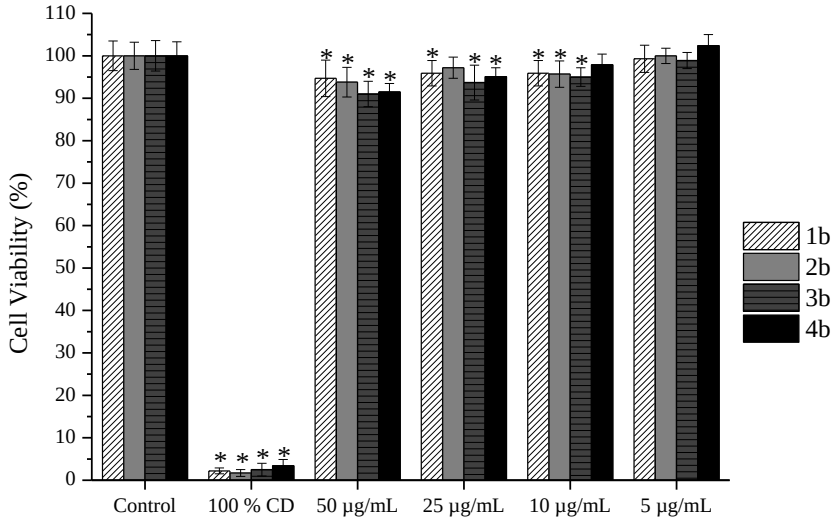

Figure 3—11: Dose-dependent cytotoxicity of MDMO-PPV NPs of different sizes.

Dose-dependent cytotoxicity of MDMO-PPV NPs of different sizes (sample 1b – 4b) in HMEC-1 cells after 24 h, tested with the alamar blue assay. Data are expressed as percentage of control mean ± SD (N =3).

In addition to this, the uptake by cells as a function of time for the different NP sizes was monitored using flow cytometry (Figure 3-12) and confocal microscopy (Figure 3-13 and 3-14). A clear difference is visible in the uptake profiles of NPs of different sizes. For MDMO-PPV NPs, decreasing the size lead to a clear increase in the rate of uptake, while for CPM-*co*-MDMO-PPV NPs this effect was less pronounced. After 30 h of incubation with a concentration of 25 μg/mL the amount of cells that have taken up NPs is almost double for MDMO-PPV NPs when comparing the smallest and biggest constructed NPs. This difference between the NP constructs can be attributed to the already fast uptake of CPM-*co*-MDMO-PPV NPs due to an increased negative surface charge [165]. As stated earlier we previously showed [165] that after washing a zeta potential difference is observable between CPM-*co*-MDMO-PPV NPs and MDMO-PPV NPs due to hydrolysis of ester group, which increases uptake.

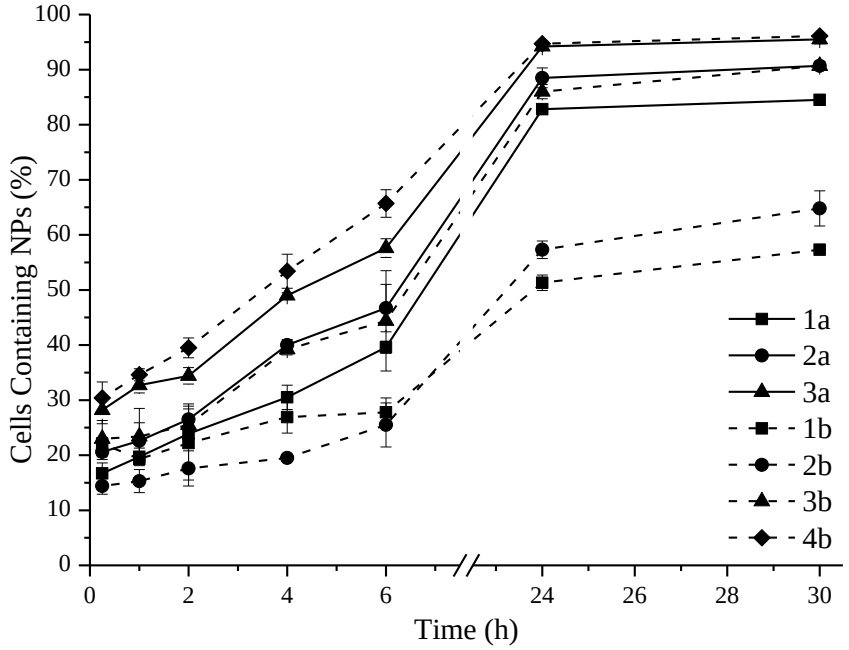

Figure 3—12: Kinetics of MDMO-PPV and CPM-*co*-MDMO-PPV NP uptake of different sizes.

Kinetics of the internalization of MDMO-PPV (dashed line) and CPM-co-MDMO-PPV (solid line) NPs by HMEC-1 cells over a time period of 30 h for different sizes (sample 1a – 3a and 1b – 4b).

A size related pattern in the amount of uptake was also observed visually using confocal laser scanning microscopy. The fluorescent NPs remained stable in cell culture medium and were indeed taken up by the HMEC-1 cells within the set incubation period, without causing any inimical effects on the integrity of cell morphology. A boost in uptake for both NP constructs was visible when the size of the NPs was lowered. This feature allows for the construction of a system that can be easily modified to have the right size and functionality to achieve a set biomedical target.

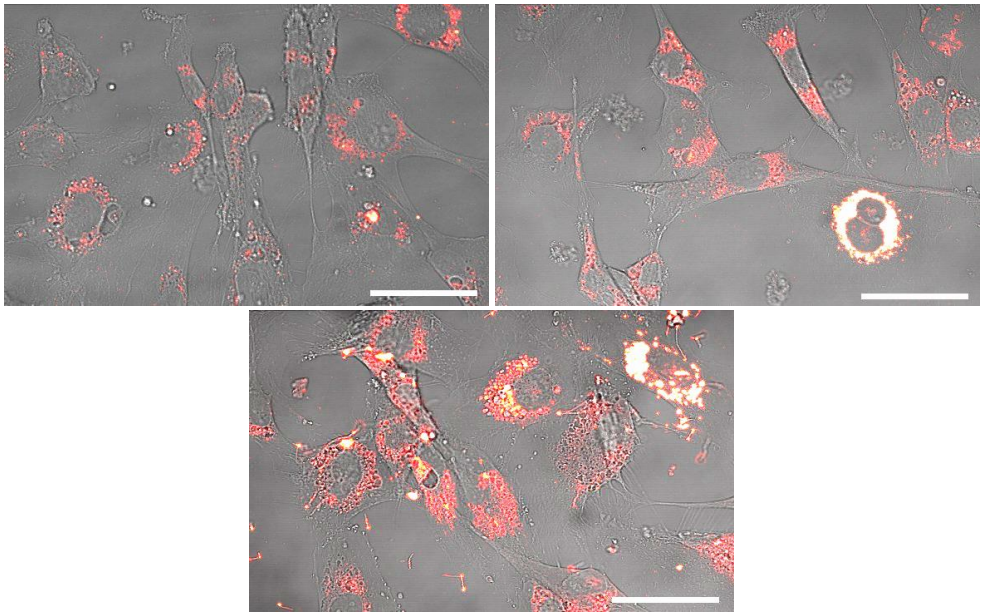

Figure 3—13: Confocal microscope image of HMEC-1 cells treated with CPM-*co*-MDMO-PPV NPs of different sizes.

Confocal microscope image of HMEC-1 cells incubated with CPM-*co*-MDMO-PPV NPs (red color) of different sizes (1a – left, 2a – right, 3a – bottom) for 24 h. Scale bars represent 50 μm.

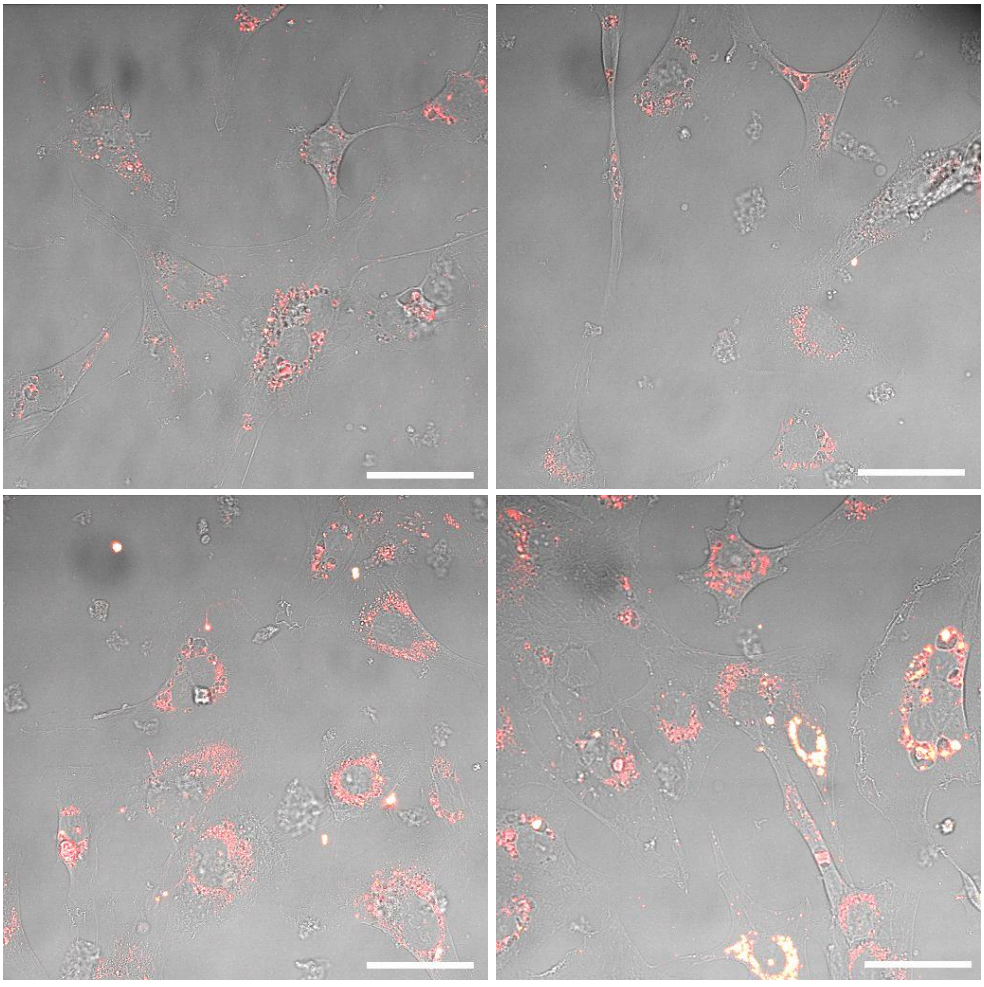

Figure 3—14: Confocal microscope image of HMEC-1 cells treated with MDMO-PPV NPs of different sizes.

Confocal microscope image of HMEC-1 cells incubated with MDMO-PPV NPs (red color) of different sizes (1b – top left, 2b – top right, 3b – bottom left, 4b – bottom right) for 24 h. Scale bars represent 50 μm.

3.5 Conclusion

MDMO-PPV and CPM-*co*-MDMO-PPV NPs of various sizes were successfully synthesized through the combination of the miniemulsion and solvent-evaporation method by lowering the amount of polymer systematically in the formulation. By curtailing the amount of polymer used during the synthesis process from 50 to 5 mg, the size of the NPs could be decreased from 50 to 17 nm for both constructs. However, the combination of employing the miniemulsion and solvent evaporation technique and lowering the hydrophobic polymer content has the inherent drawback of increasing the polydispersity of the colloidal solution. An investigation of the optical properties revealed that size did not have an influence on the optical properties of the PPV-base NP configurations within the tested range. The fingerprint of both MDMO-PPV and CPM-*co*-MDMO-PPV NPs showed the characteristic vibronic structure with 0-0, 0-1 and 0-2 emission bands at 590, 640 and 660 nm. A difference between the two PPV constructs was observed, namely MDMO-PPV having its main peak shifted from 590 to 640 nm, which can be attributed to the lack of a hydrophilic group in its side-chain. No substantial changes were observed in the fluorescent brightness of the NPs, determined by the quantum yield and molar extinction coefficient, as well. However, for very small NPs constructed by lowering the amount of polymer below 5 mg, a permanent change in the conjugation length was observed. This observed phenomenon could be attributed to photoinduced oxidation, a well-known hurdle of PPVs. Cell studies demonstrated that decreasing the size of the NPs does not lower the cell viability below 90 % but does influence the rate and amount of uptake. An effect that is even more pronounced for the MDMO-PPV variant, which is taken up more slowly due to the lack of an additional surface charge compared to CPM-*co*-MDMO-PPV. The results presented highlight that PPV-based NPs are an excellent candidate for bioimaging applications owing to their high design flexibility, which does not show adverse effects on their interesting optical properties or benign biological characteristics.

Chapter 4
PEGylation of functional PPV-based conjugated polymer nanoparticles

This chapter is based on:

PEGylation of functional PPV-based conjugated polymer nanoparticles: implications on the synthetic and biological identity.

Peters M., Desta D., Reekmans G., Adriaensens P., Noben J-P., Hellings N., Junkers T., Ethirajan A.

Manuscript submitted

Declaration of own contribution: Martijn Peters jointly designed the experiments. He executed the synthesis and most of the characterization of the nanoparticle constructs. He also participated in writing of the manuscript.

4.1 Abstract

Conjugated polymers nanoparticles (NPs) have attracted considerable attention in the bioimaging field owing to their excellent optical properties and biocompatibility. Recently, novel control methodologies have generated tailor-made functional poly(p-phenylene vinylene) (PPV), which enable one-pot synthesis of NPs containing functional surface groups. Here, NPs consisting of statistical copolymer 2-(5'-methoxycarbonylpentyloxy)-5-methoxy-1,4-phenylenevinylene and poly(2-methoxy-5-(3',7'-dimethoxyoctyloxy)-1,4-phenylenevinylene) (CPM-*co*-MDMO-PPV) are described. The surface carboxylic acid groups were used to covalently attach amine-terminated polyethylene glycol (PEG) – an established stealth molecule – of different molecular weight (MW) onto the surface. PEGylation had no detrimental influence on the NPs' optical properties or biocompatibility, enforcing their potential in the nanomedicine field as inducing stealth is a highly desired feature. A significant decrease in protein corona formation and uptake in central nervous system cell lines, dependent on PEG chain length, was observed. These results clearly show that introducing new stealth functionalities onto NPs does not affect their role as excellent aspirant for bioimaging applications.

4.2 Introduction

In the past decades, fluorescence-based biotechnology has stipulated ample attention in the bioimaging field as it provided various powerful research tools that have led to a more profound understanding of biological processes at the molecular and cellular level [118-120]. Traditional fluorescent probes include organic fluorophores and fluorescent nanoparticles (NPs), such as quantum dots (QDs) and dye-doped silica colloids or latex spheres, which both have instigated significant advances in the biomedical sciences [8, 21, 176, 177]. Despite the fact that fluorescent NPs are superior towards conventional dyes in terms of optical properties and possess a lower susceptibility to cellular efflux mechanisms, they still cannot overcome certain limitations [8, 9, 124]. Examples are short- and long-term cytotoxicity issues and *in vivo* degradation, in case of QDs, and self-quenching combined with erroneous interpretations and toxicity due to exclusion of the dye in case of dye-loaded NPs [17-19, 22].

Given the remaining shortcomings of the above-mentioned classes of materials, the search for alternatives remains ongoing. In this regard, water-based conjugated polymer nanoparticles have rapidly grown into a rising star [10, 23, 69, 113, 126, 127]. This can be attributed to their excellent biocompatibility and inherent π-conjugated backbone structure, which gives rise to ultra-bright photoluminescence and fast emission rates. One prominent example is poly(*p*-phenylene vinylene) (PPV), a pioneer material for the first organic light emitting diode (oLED) that quickly transcended to a wide variety of applications such as solar cells, biological sensors and other optoelectronic devices [38]. This has led it to become one of the most thoroughly studied semiconducting polymers. Its large appeal can be correlated to reliable synthesis routes combined with simple scale up potential, well known photophysical properties and particularly the design flexibility offered by novel control methodologies for constructing custom-made functional PPVs [38, 49, 57]. More specifically, the sulfinyl precursor route offers a very fast and elegant way to construct complex polar functionalized PPVs that can be employed to generate NPs with functional groups distributed within the volume and on the surface [140]. The latter can be conveniently employed for the easy attachment of various functionalities as per demand in order to incorporate different functional properties (e.g., barrier crossing potential, stealth effect,

target specificity, or others). Surface modification is indispensable when NPs are formulated for advanced biomedical applications, as it not only permits the control over chemical but also biological key characteristics to meet the setout conditions of different environments [132, 133].

Since its identification, polyethylene glycol (PEG) has become the most widely used nanoparticle surface coating [179]. A PEG ligand – a hydrophilic polymer chain with a high exclusion volume resulting from its high conformational entropy – provides colloidal stability through steric repulsion. It drastically lowers levels of protein adsorption as well as nonspecific NP-cell membrane interactions, is biocompatible and has been FDA-approved since its introduction [180]. Furthermore, it has been demonstrated that protein adsorption and cellular uptake can be tweaked by simply varying the PEG chain length [181, 182]. However, to date the consequences of grafting PEG chains onto the surface of functional PPV-based NPs are not fully explored. Therefore, the aim of this study is to generate a more profound insight into the various ways in which PEG, with different chain lengths, can affect this particular type of bioimaging probe.

Here, a NP system is designed of which the core material consists of a functional statistical hydrophobic copolymer. This copolymer comprises of the randomly repeating monomer units 2-(5'-methoxycarbonylpentyloxy)-5-methoxy-1,4-phenylenevinylene and poly[2-methoxy-5-(3',7'-dimethoxyoctyloxy)-1,4-phenylenevinylene] (CPM-PPV-*co*-MDMO-PPV, for simplicity henceforth called CPM-*co*-MDMO-PPV). The NPs are synthesized using a combination of the versatile miniemulsion technique and solvent evaporation method, which results in a water-based dispersion of a homogeneous NP population with a size range ideal for biomedical applications and ester functionalities on the surface [24, 134, 136]. The latter can be easily converted into carboxylic acid groups through hydrolysis, which are then used to covalently attach amine terminated PEG chains with various molecular weights onto the surface. Subsequently, the ramifications of PEGylation on the colloidal, optical and biological characteristics of the bioimaging probe were assessed in detail. For the cell-NP interaction studies, cell lines representative for cell populations of the central nervous system (CNS) were selected. The reasoning behind this is the fact that the exact etiology for many CNS diseases remains unknown, resulting in an extensive demand for bioimaging

tools that allow the study of disease processes at the subcellular level [138]. To date, only few studies have addressed the use of conjugated polymer NPs for such biological systems and since PEGylation is a proven method to increase blood-brain-barrier (BBB) transport and decrease nonspecific cellular uptake by neural cell populations, studying its effect on this novel bioimaging probe is of great importance [183, 184].

4.3 Materials and methods

4.3.1 Materials and products

Sodium hydroxide (NaOH), 1-ethyl-3-(3-dimethylaminopropyl)carbodiimide (EDC), hydrochloric acid (HCl), 30 % acrylamide/0.8 % bisacrylamide and amicon ultra filter membrane tubes were purchased at Merck (Overijse, Belgium). Sulfo-N-hydroxysulfosuccinimide (sulfo-NHS) was bought at VWR (Leuven, Belgium). Hydroxyl-polyethylene glycol-amine with MW of 2000 (OH-PEG2000-NH_2) and 5000 (OH-PEG5000-NH_2) was bought at JenKem Technology (Plano TX, US). Deuterated chloroform ($CDCl_3$), dibromomethane, rhodamine 6G, penicillin/streptomycin (P/S), hydrocortisone (HC), L-glutamine, trypsine, paraformaldehyde (PFA), triton X-100, 2-mercaptoethanol and ProteoSilver™ Silver Stain Kit were purchased at Sigma-Aldrich (Diegem, Belgium). Human microvascular endothelial cells (HMEC)-1 (CRL-3243), HeLa (CCL-2) and C8-D1A cell line (CRL-2541) were bought at ATCC (Molsheim, France). MCDB 131 medium, dulbecco's modified eagle medium (DMEM) medium, fetal calf serum (FCS), recombinant human epidermal growth factor (EGF), iscove's modified dulbecco's medium (IMDM) medium, alamar blue, mouse monoclonal anti-α-tubulin antibody, alexa fluor® 488 donkey anti-mouse IgG (H+L) antibody and 4',6-diamidino-2-phenylindole (DAPI) were obtained from Life Technologies (Ghent, Belgium). BV-2 cell line (ATL03001) was purchased from ICLC (Genova, Italy). All culture and dark plates were bought at Greiner Bio One (Vilvoorde, Belgium). The 1x phosphate buffered saline (1xPBS; 9 g/L NaCl, 0.795 g/L Na_2HPO_4, 0.144 g/L KH_2PO_4) was purchased at Lonza (Verviers, Belgium) and the μ-Slide 8 well plates were ordered at Proxylab (Beloeil, Belgium). Bovine serum Albumin (BSA) was purchased from USBiological (Swampscott MA, US). Tris-base, glycerol 87 %, sodium dodecyl sulfate (SDS), bromophenol blue, ammonium persulfate (APS), tetramethylethylenediamine (TEMED), glycine, dithiothreitol (DTT) and iodoactemide (C_2H_4INO) were bought at GE Healthcare Life Sciences (Diegem, Belgium). Precision Plus Protein™ Dual Color Standard was purchased from Bio-Rad (Hercules, CA, USA). Formic acid (CH_2O_2) and ammonium bicarbonate (NH_4CO_3) were bought at Fisher Scientific (Merelbeke, Belgium). Acetonitrile (C_2H_3N) was purchased from Biosolve BV (Valkenswaard, The Netherlands). All chemicals were used as provided without further purification.

4.3.2 Surface functionalized PPV-based NPs: synthesis and preparation

Nanoparticle Synthesis. Synthesis of the conjugated polymer and NPs was performed as described elsewhere [165]. In summary, CPM-*co*-MDMO-PPV NPs were formulated using a combination of the miniemulsion and solvent evaporation method. In this synthesis route, a continuous phase, consisting of sodium dodecyl sulfate (SDS, 100 mg instead of 72 mg) and ultrapure water, and dispersed phase, consisting of the respective conjugated polymer in $CHCl_3$, are mixed together during a pre-emulsification step, followed by ultrasonication (1/4"-tip, 3 min, 65 % amplitude, 30 s pulse and 20 s pause regime) under ice cooling. This generates nanodroplets of which the organic solvent is subsequently evaporated, resulting in colored dispersion of CPM-*co*-MDMO-PPV NPs in water. This dispersion was passed through a filter paper (Whatman, pore size 4–7 μm) to remove any large aggregates. The solid content of all samples was determined by thermogravimetric analysis. Finally, the NPs were hydrolyzed and washed.

Nanoparticle Hydrolysis. CPM-*co*-MDMO-PPV NPs were incubated on an Intelli-Mixer RM-2L shaker at 10 rpm for different time points (1 h, 2 h, 4 h, 6 h, 20 h and 24 h) in a 0.5 M NaOH solution with a resulting solid content of 0.5 %. The surface charge evolution was studied using zeta potential measurements using ZetaPALS equipment (Brookhaven Instrument Cooperation, Waddinxveen, The Netherlands).

Nanoparticle Washing. After a 24h hydrolysis period CPM-*co*-MDMO-PPV NPs underwent multiple centrifugation/redispersion steps with a Sigma 3-30K centrifuge (Suarlée, Belgium). First, 4 washing steps of 1 h at 14 000 rpm were done with eppis to remove the NaOH solution. Subsequently, the NPs were washed 40 times in amicon ultra filter membrane tubes (30 kD) for 30 min at 2000 rpm, followed by 2 steps at 14 000 rpm for 1 h with eppis. The resulting NP samples were sterilized with 30 Gy (= 3000 rad) using an IBL 437C type gamma radiator (Cis Bio International, Codolet, France) and stored in the dark.

Evolution Size and Zetapotential at different pH. Hydrolyzed/washed and non-hydrolyzed (untreated) CPM-*co*-MDMO-PPV NPs were incubated with different pH solutions of 2, 4, 7 and 10. The resulting size and zetapotential values were measured using the ZetaPALS equipment.

4.3.3 Surface functionalized PPV-based NPs: PEGylation

PEGylation. CPM-*co*-MDMO-PPV NPs were diluted to a 3mL solution with solid content of 0,01 % in ultrapure water, after which 0,050 mg of EDC and 0,029 mg of sulfo-NHS, both in 1mL ultrapure water were added. The resulting solution was stirred for 20 min at 750 rpm in the dark, followed by the addition of 5 mg of OH-PEG2000-NH_2 or OH-PEG5000-NH_2 and another 3 h of stirring. The PEGylated NPs were subsequently washed by multiple centrifugation (1 h at 14 000 rpm) and redispersion steps using the Sigma 3-30K centrifuge (Suarlée, Belgium).

Characterization. PEG functionalization was characterized using size, zetapotential, infrared spectroscopy and nuclear magnetic resonance (NMR) spectroscopy measurements. The hydrodynamic diameter and zetapotential were collected using dynamic light scattering (DLS) with the ZetaPALS equipment (Brookhaven Instrument Cooperation, Waddinxveen, The Netherlands). Attenuated total reflection infrared (ATR-IR) spectra were obtained with a Tensor 27 FT-IR spectrophotometer (Bruker, Brussels, Belgium). PEGylation was also confirmed visually through AFM microscopy. Non-PEGylated as well as PEGylated CPM-*co*-MDMO-PPV NPs were drop casted onto cleaned silicon wafers, placed on a ramp and allowed to air dry in order to support the particle monolayer formation onto the substrate. The topographic height and phase images of the film were studied with an NX10 AFM microscope (Park Systems, Suwon, Korea) in non-contact mode. The AFM tip was an n-type silicon probe with a 13-77 N/m spring constant and tip radius lower than 10 nm.

The total nanoparticle PEG content was determined by ^{1}H NMR using a 400 MHz Varian Inova NMR spectrometer (Agilent Technologies Inc., Santa Clara, CA, USA) using a 5 mm OneNMR Pulsed-Field-Gradient (PFG) probe. Control ^{1}H NMR experiments were performed on SDS, NH_2-PEG2000-OH, the polymer CPM-*co*-MDMO-PPV and non-PEGylated NPs. The chemical shift scale (δ; in ppm) was calibrated relatively to $CHCl_3$ (7.24 ppm). The dried NPs were weighted and dissolved in $CDCl_3$, containing 0.035 v/v % dibromomethane as an internal standard (peak integration area was kept constant). The PEG surface content was determined by comparing to a PEG calibration curve calculated from ^{1}H NMR spectra of solutions with known PEG concentrations. The same was performed for

CPM-*co*-MDMO-PPV. All spectra were acquired with a 90° pulse of 6.9 μs, a spectral width of 6.5 kHz, an acquisition time of 4 s, a preparation delay of 45 s and 32 accumulations. A line-broadening of 0.2 Hz was applied prior to Fourier transformation to the frequency domain. The surface PEG density (Γ, PEG molecules/m^2) was calculated through the following formula and derived to the number of PEG molecules/100 nm^2 surface area of the NPs.

$$\Gamma = \frac{\#\ \text{PEG molecules}}{\#\ \text{NPs}} \text{ / Surface NP } = \frac{n_{PEG} \times N_A}{(m_{NP}/\rho_{NP})/(0.75\pi\ (d/2)^3)} \text{ / } 4\pi\ (d/2)^2$$

Where n_{PEG} is the total PEG content in mole, N_A Avogadro's number, m_{NP} the total mass of NPs, d the diameter determined by DLS and ρ_{NP} the density of the NPs. The density of the NP is assumed to be equal to that of CPM-*co*-MDMO-PPV, namely $1.0*10^6$ g/m^3. Subsequently, the full surface mushroom coverage (Γ*), the number of unconstrained PEG molecules per 100 nm^2, was calculated using the following formula assuming random-walk statistics where M is the molecular weight of the respective PEG chain.

$$\Gamma^* = \frac{100\ \text{nm}^2}{\pi * (\frac{0.76 M^{0.5} * \text{Å}}{2})^2}$$

Subsequently, the ratio (Γ)/(Γ*) can be calculated, which reflects how densely the PEG is packed on the surface of the NPs. If the ratio is lower than 1, it indicates that the PEG chains are in a mushroom conformation due to their low density. If the ratio has a higher value than 1, the PEG chains are in a brush conformation given their high density.

4.3.4 Influence of PEGylation on optical characteristics of PPV-based NPs

The optical fingerprint of PEGylated and non-PEGylated CPM-*co*-MDMO-PPV NPs was measured using the Cary 5000 UV-VIS-NIR spectrophotometer (Agilent Technologies, Diegem, Belgium), and Jobin Yvon Fluorolog3 Tau fluorescence spectrophotometer (Horiba, Lier, Belgium) in a 1 cm quartz cuvette. A correction was made for the emission spectra for the wavelength dependence of the throughput and sensitivity of the detection channel. Also the quantum yield (QY) was measured.

The molar extinction coefficient of the NPs was calculated using Beer-Lambert Law by varying the concentration of NPs in water. The resulting coefficients could be used to determine the absorption cross-section. The QY of the NPs was measured using the fluorescence reference rhodamine 6G (in H_2O, QY = 0.95). For all samples (CPM-*co*-MDMO-PPV NPs before hydrolyzing, CPM-*co*-MDMO-PPV NPs after hydrolyzing, CPM-*co*-MDMO-PPV NPs with PEG2000 and CPM-*co*-MDMO-PPV NPs with PEG5000), five dilutions were prepared as well as for the reference. The absorbance of the most concentrated one reached a value of 0.1 at 485 nm excitation to which the standard was matched. The emission spectrum was collected for each sample at its respective excitation wavelength. Subsequently, the absorption versus integral of emission spectrum for each dilution and sample was plotted and the trend lines fitted. The obtained slope value (m) as well as refractive indexes (η) of the liquids were used to calculate the quantum yield of the sample according to the following formula.

$$QY_{SAMPLE} = QY_{STANDARD} \times \frac{mSAMPLE}{mSTANDARD} \times \frac{\eta SAMPLE^2}{\eta STANDARD^2}$$

The fluorescence brightness of the NPs (B_{NP}) was determined by multiplying the quantum yield with the molar extinction coefficient.

4.3.5 Influence of PEGylation on biological characteristics of PPV-based NPs

Cell Culture. The cells were cultured with culture medium (Table 4-1) in a T25 flask stored in a 5 % CO_2 incubator (Sanyo, Japan) at 37 °C. For HMEC-1 cells, the medium needs to be refreshed after 3 days and both cell-lines were spliced after being 80 % confluent.

Cytotoxicity assay. HeLa and HMEC-1 cells were seeded and left to grow to 80 % confluence in a 96-well flat bottom plate at 37 °C in a 5 % CO_2 incubator (Sanyo, Japan). HeLa cells were chosen next to neural cell lines, given they are a widely used cell line and can therefore be employed as a comparative control towards other studies. The NPs were diluted to the desired concentration range (5, 10, 50 and 100 μg/mL) with phenol red poor IMDM culture medium. Subsequently, 100 μL of each concentration was added after washing with 1xPBS. Positive and negative control conditions were included, with a total of six wells per condition,

and the experiment was performed in triplicate. Following 24 h of incubation at 37 °C, the cells were washed another 3 times after which a 10 % alamar blue solution in IMDM culture medium was added. The cells were left to incubate for 24 h and the resulting solution was transferred to an opaque-walled dark 96-well culture plate. Fluorescence was measured at λ_{em} = 590 nm while excited at λ_{ex} = 570 nm, FLUOstar OPTIMA (BMG Labtech, Temse, Belgium).

Table 4—1: Cell-lines and respective culture media.

Cell type	Medium	Supplements
HMEC-1	MCDB 131	10 % FCS 0.5% P/S 500 ng EGF 50 μg HC 500 μmol L-Glutamine
HeLa/BV-2/C8-D1A	DMEM	1 % P/S 10 % FCS

Protein Corona Determination. NPs were incubated for 2 min, 5 min, 30 min, 1 h and 2 h at 37 °C with a 10x excess of FCS giving a final concentration of 50 μg/mL. After the incubation, the samples were washed 3 times for 2 h at 14 000 rpm in 1xPBS. The pellet of the final washing step was eluted in reduced sample buffer (3.55 mL ultrapure water, 1.25 mL 0.5 M Tris-HCl with pH 6.8, 25 v/v% glycerol, 2 v/v% 10 % SDS solution, 0.1 mL 1% bromophenol blue solution) at 95 °C for 5 min. The eluted samples were separated, with a protein standard, on 4 % stacking gel (6.1 mL ultrapure water, 1.3 mL 30 % acrylamide/0.8 % bisacrylamide, 2.5 mL 0.5 M Tris-HCl with pH 6.8, 0.1 mL 10 % SDS solution, 50 μL 10 % APS, 10 μL TEMED, 5 % v/v% 2-mercaptoethanol) and 12 % resolving gel (3.4 mL ultrapure water, 4 mL 30 % acrylamide/0.8 % bisacrylamide, 2.5 mL 1.5 M Tris-HCl with pH 8.8, 0.1 mL 10 % SDS solution, 50 μL 10 % APS, 5 μL TEMED) in 1xSDS electrophoresis buffer (25 mM Tris, 192 mM glycine, 1 w/v% SDS, pH 8.3) at 200 V for 35 min. Protein bands were visualized with a ProteoSilver™ Silver Stain Kit.

The spots were cut out and dehydrated with C_2H_3N after which the gel was dried in a 5301 concentrator vacuum centrifuge (Eppendorf, Rotselaar, Belgium). A solution of 10 mM dithiothreitol (DTT) in 100 mM of ammonium bicarbonate (NH_4HCO_3) was added to the gel spots to incubate for 1 h at 56 °C. Subsequently, the supernatant was removed after cooling to RT and replaced by a solution of 55 mM C_2H_4INO in 100 mM NH_4HCO_3. The spots were left to incubate for 45 min at RT in the dark after which the solution was replaced by a 100 mM NH_4HCO_3 solution for 10 min followed by incubation with C_2H_3N for another 10 min. This was repeated 2 times. Afterwards, the gel was dried in the vacuum centrifuge followed by a 4 h incubation step with 10 μL digestion buffer (62,6 v/v% of 20 μg/mL trypsine solution in NH_4HCO_3) on ice. The supernatant was removed and 50 mM NH_4HCO_3 was added and left to incubate overnight at 37 °C. The supernatant was replaced by 20 mM NH_4HCO_3 and the samples were sonicated for 20 min. Next, 50 μL of a 5 % CH_2O_2 in 50 % C_2H_3N was added to the gels followed by 20 min sonication 3 times in a row. After the final step, the supernatant was taken and kept at -18 °C until mass spectrometry during which the extract was evaporated and replaced by 20 μL of cortisone working solution.

An Easy-nLC 1000 liquid chromatograph (Thermo Scientific, Gent, Belgium) was on-line coupled to a mass calibrated LTQ-Orbitrap Velos Pro (Thermo Scientific, Gent, Belgium) via a Nanospray Flex ion source (Thermo Scientific, Gent, Belgium) using sleeved 30 μm ID stainless steel emitters (spray voltage +2.3 kV, capillary temperature: 200 °C). The SpeedVac (Thermo Scientific, Gent, Belgium) dried tryptic peptide mixture was dissolved in 20 μl buffer A (0.1 v/v% CH_2O_2 in ultrapure water) of which half was loaded, concentrated and desalted on a trapping pre-column (Acclaim PepMap 100 C18, 75 μm ID × 2 cm nanoViper, 3 μm, 100 Å, Thermo Scientific) at a buffer A flow rate of 5 μL/min for 5 minutes. The peptide mixture was separated on an NS-AC-16-C18 BioSphere 5 μm 120 Å 50 μm ID x 20 cm (NanoSeparations, Nieuwkoop The Netherlands) at a flow rate of 250 nL/min with a linear gradient in 40 minutes of 0 to 70 % buffer B (0.1 v/v% CH_2O_2 in C_2H_3N) in buffer A.

Mass spectrometry data were acquired in a data-dependent mode under direct control of the Xcalibur software (version 2.2.SP1.48), selecting the fragmentation events based on the top six precursor abundances in the survey scan (350 – 2000 Th). The resolution of the full scan was 30000 at 400 Th with a target value of $1x10^6$ ions and one microscan. CID MS/MS spectra were acquired with a target value of 10000 and the maximum injection time was 100 ms. Dynamic exclusion was 30 s and early expiration was disabled. The isolation window for MS/MS fragmentation was set to 2 Th and the normalized collision energy, Q-value and activation time were 30 %, 0.25 and 10 ms, respectively. Helium was used as the collision gas.

The analysis of the mass spectrometric raw data was carried out using Proteome Discoverer software v.1.4 (Thermo Scientific) with build-in Sequest v.1.4.0.288 and interfaced with an in-house Mascot v.2.5 server (Matrix Science). MS/MS spectra were searched against the Bos taurus protein collection extracted from NCBI database (query 'Bos taurus' on October 27th 2015; 31850 entries) and peptide scoring for identification was based on following search criteria: enzyme trypsin, maximum missed cleavages 2, precursor mass tolerance 10 ppm and fragment mass tolerance 0.5 Da. Carbamidomethylation of cysteine and oxidation of methionine were set as fixed and dynamic modifications, respectively. Result files of both search engines were uploaded and automatically evaluated in Scaffold v.4.4.1.1 (Proteome Software) using the Peptide Prophet and Protein Prophet algorithm with a preset minimal peptide and protein identification probability of 95 % and 99 %, respectively.

Uptake Kinetics. HMEC-1 cells were seeded in a 24-well plate at a density of 100 000 cells and left to incubate for 24 h at 37 °C in a 5 % CO_2 atmosphere. After washing the cells with 1xPBS, 500 μL of 25, 75, 100 and 150 μg/mL of NPs in culture solution was added to the cells. Incubation periods of 2, 4, 6, 8, 24, 27 or 30 h at 37 °C with a CO_2 level of 5 % were taken after which the cells were washed 3 times with 1xPBS and harvested. The pellet was redispersed in 1 mL of 4 % paraformaldehyde (PFA) and left to incubate for 20 min at room temperature (RT) in the dark. The cells were then centrifuged to remove the PFA and washed 3 times using centrifugation with fluorescence-activated cell sorting (FACS) buffer (1xPBS and 2 % FCS). The obtained samples were measured and analyzed with

the FACSCalibur (Becton Dickinson, Erembodegem, Belgium), using a 488 nm laser and 585/42 nm emission filter. Unlabeled cells were used as a blank to gate the signal and for each sample 20 000 cells were counted in triplicate. The FACSCalibur software counted the amount of cells and in parallel determined in which a fluorescent signal was detected. These calculations were converted to a percent scale from 0 – 100 % with 100 % meaning that in all cells fluorescence was detected and thus NPs were present.

Confocal Laser Scanning Microscopy. For live cell imaging, HMEC-1, C8-D1A and BV-2 cells were seeded at respective densities of 10 000, 50 000 and 1000 cells in a μ-Slide 8-well plate and left to grow for 24 h at 37 °C. The cells were subsequently washed with 1xPBS after which 50 μg/mL of NPs in IMDM culture medium was added and incubated for 24 h. After the incubation period, the cells were washed 3 times with 1xPBS and 200 μL of IMDM culture solution was added. The images were collected at 37 °C using a Zeiss (Zaventem, Belgium) LSM510 META NLO mounted on an inverted laser scanning microscope (Zeiss Axiovert 200 M) and a 40x/1.1 water immersion objective. NP excitation was performed at 488 nm (maximum radiant power at the sample of 3 μW) with the Argon-ion laser. Emission was detected using a band-pass filter of 565-615 nm. The resulting 1024x1024 images with a pixel size of 0.06 μm were recorded using a pixel dwell time of 14.2 μs and a fixed pinhole size of 114 μm. Images were processed using AIM 4.2 and ImageJ software.

For fixated cell imaging, HMEC-1 cells were seeded at 20 000 cells per well in a μ-Slide 8 well plate and left to incubate in a 5 % CO_2 incubator at 37 °C. After 24 h, the cells were rinsed with 1xPBS followed by the addition of 400 μL of 75 μg/mL of NPs in IMDM culture medium for another 24 h. The cells were then washed 3 times with 1xPBS at 37 °C after which 400 μL of fixation/extraction/ permeabilization buffer (4 v/v % PFA supplemented with 0.3 v/v % triton x-100) was added for 20 min on ice at 4 °C. Subsequently, the cells were washed 3x with washing buffer (1xPBS containing 0.1 % triton x-100) after which they were incubated for 1h at 4 °C in 400 μL of a 0.3 v/v % triton x-100 in 1xPBS solution. The cells were again washed 3 times with washing buffer. Next, 400 μL of blocking buffer (1xPBS containing 0.1 % triton x-100 and 2 % BSA) was added for 1 h on 50 rpm at RT after which the cells were incubated with 200 μL of primary antibody

(mouse monoclonal anti-α-tubulin, 1:1000 in blocking buffer) on 50 rpm overnight at 4 °C. The cells were washed 3 times with washing buffer at 50 rpm for 5 min and incubated with 400 μL of secondary Ab (donkey anti-mouse Alexa Fluor 488, 1:250 in blocking buffer) for 20 min at RT on 50 rpm. After another rinsing step, 400 μL of DAPI (1:25 in blocking buffer) was added for 1 h at RT. The cells were washed a final time and covered with 2 drops of mounting medium to prevent photobleaching of the dyes. The cells were visualized at RT with the Zeiss LSM510 META NLO (Zaventem, Belgium) mounted on an inverted laser scanning microscope (Zeiss Axiovert 200 M) and a 40x/1.1 water immersion objective. Excitation of the tubulin and NPs was done with an Argon-ion laser at 488 nm and 543 nm respectively (3 μW maximum radiant power at the sample). Excitation of DAPI was done at 730 nm (average radiant power of ~5 mW at the sample position) with a femtosecond pulsed titanium-sapphire MaiTai DeepSee laser. Emission was detected using band-pass filters 500-550 nm (tubulin), 565-615 (NPs) and 390-465 nm (DAPI). The resulting 1024x1024 images with a pixel size of 0.06 μm were recorded using a pixel dwell time of 375 μs and a fixed pinhole size of 240 μm (tubulin), 600 μm (NPs) and 1000 μm (DAPI). Images were processed using AIM 4.2 and ImageJ software.

4.4 Results

4.4.1 Surface functionalized PPV-based NPs: preparation

In order to obtain optimal surface functional group coverage on the PPV-based NPs, all ester groups on the surface need to be converted to carboxylic acid groups through hydrolysis. The conversion process was monitored using zetapotential measurements, as the appearance of carboxylic acid groups induces a more negative surface charge (Figure 4-1). A steep rise from -38 mV to -55 mV was observed in the first 6 h after which stabilization occurred. As an additional characterization step, the pH-dependent evolution of the zetapotential and size of NPs before and after the hydrolysis/washing process was studied (Figure 4-2). A significant difference was observed when the pH was lowered to a value of 4. For the hydrolyzed/washed NPs the zetapotential dropped from -55 to -20 mV, while their size increased from 125 (polydispersity, PD = 0.097) to 190 nm (PD = 0.194). The values of the untreated sample were however unaffected by the pH variation and remained stable at -55 mV and 112 nm for the zetapotential and size respectively.

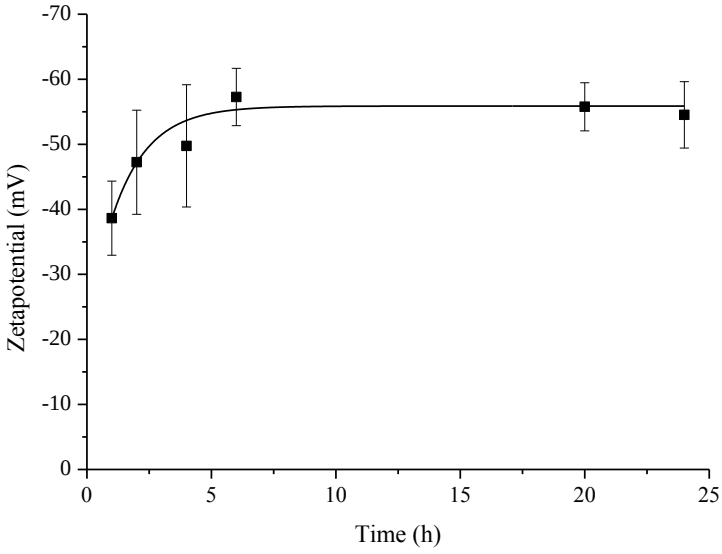

Figure 4—1: Zetapotential evolution of the CPM-*co*-MDMO-PPV NP surface over time.

Evolution of the zetapotential of CPM-*co*-MDMO-PPV NPs over a time period of 24 h when exposed to a 0.5 M NaOH solution (pH 13.7).

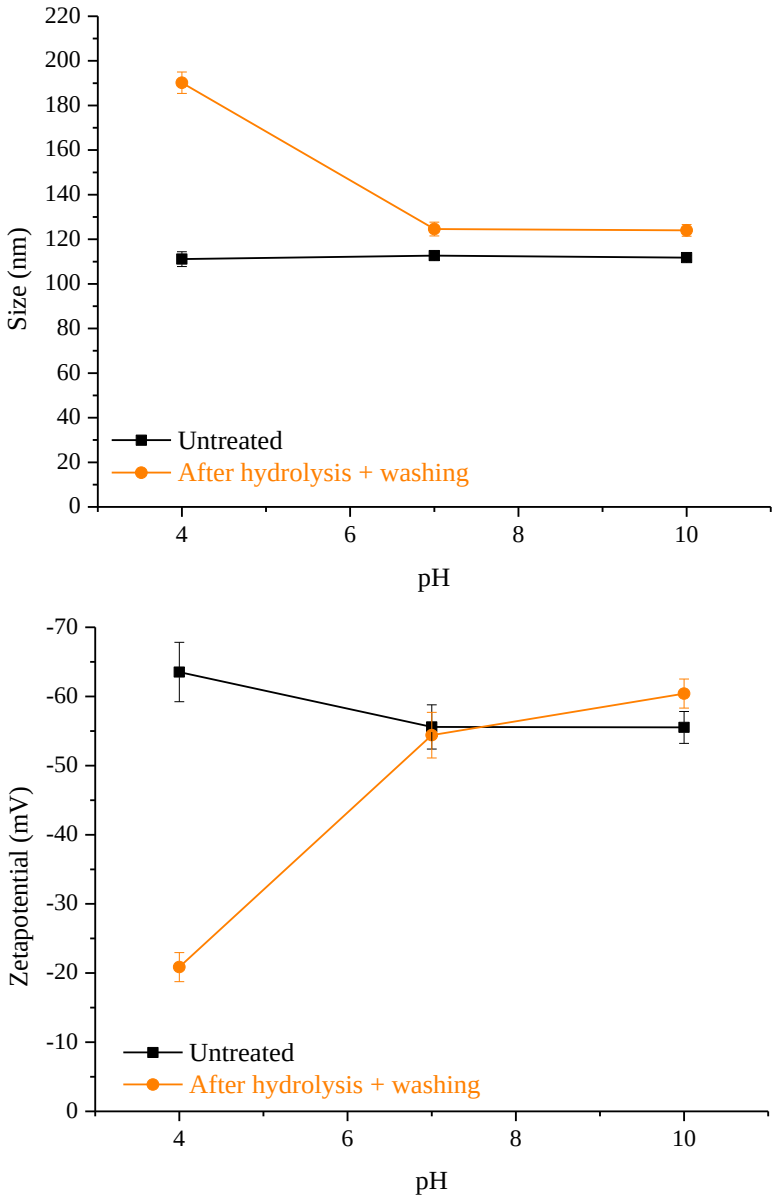

Figure 4—2: pH-dependent evolution of CPM-*co*-MDMO-PPV NP size and zetapotential.

Evolution of the size (top) and zetapotential (bottom) of non-hydrolyzed (black line) and hydrolyzed/washed (orange line) CPM-*co*-MDMO-PPV NPs when exposed to solutions with different pH values.

4.4.2 Surface functionalized PPV-based NPs: PEGylation

Following PEGylation, the effect on the colloidal properties was characterized. An increase in the hydrodynamic radius from 113 to 121 nm for PEG2000 and to 126 nm for PEG5000 was observed (Table 4-2). The zetapotential dropped from -44 to -27 mV for PEG2000 and to -30 mV for PEG5000.

Table 4—2: Size, zetapotential and ratio of PEG density to full surface coverage (Γ/Γ*) before and after PEGylation.

Sample	Size (nm)	Zetapotential (mV)	Γ/Γ*
CPM-*co*-MDMO-PPV-Hydrolyzed NP	113.4 (+/- 1.8), PD = 0.081	-43.50 (+/- 3.11)	/
CPM-*co*-MDMO-PPV-PEG2000 NP	120.8 (+/- 1.3), PD = 0.091	-26.70 (+/- 3.06)	1,83
CPM-*co*-MDMO-PPV-PEG5000 NP	125.9 (+/- 3.8), PD = 0.094	-29.53 (+/- 2.33)	1,91

To determine if PEG was grafted covalently onto the NP surface, infrared spectroscopy was used (Figure 4-3 to 4-7). Following PEG grafting, the C=O band at 1730 cm^{-1} decreased in intensity, while the R-O-R peak at 1100 cm^{-1}, amide I peak at 1640 cm^{-1}, amide II peak at 1590 cm^{-1}, amide III peak at 1280 cm^{-1} and CH_2 peak at 1340 cm^{-1} increased.

To determine the amount of coupled PEG chains and ratio of their density to full surface coverage, ^1H NMR was employed. Using the specific PEG peak at 3.65 ppm, not present in the spectra of CPM-*co*-MDMO-PPV, SDS or hydrolyzed NPs (Figure 4-8 to 4-11), the exact amount of PEG could be deduced. This was performed by taking the integral value (peak area) of this peak in the spectra of the PEGylated NPs (Figure 4-12 and 4-13) and comparing it to the respective calibration curves (Figure 4-14 and 4-15). For PEG2000, 20.2 PEG molecules/100 nm^2 were present and for PEG5000, 8.4 PEG molecules/100 nm^2, which gives a [Γ/Γ*] ratio >1 for both samples. PEGylation was also confirmed visually through AFM microscopy (Figure 4-16). In the phase images, non-PEGylated NPs exhibit a homogenous surface composition while PEGylated NPs show an inhomogeneous surface structure consisting of two phases.

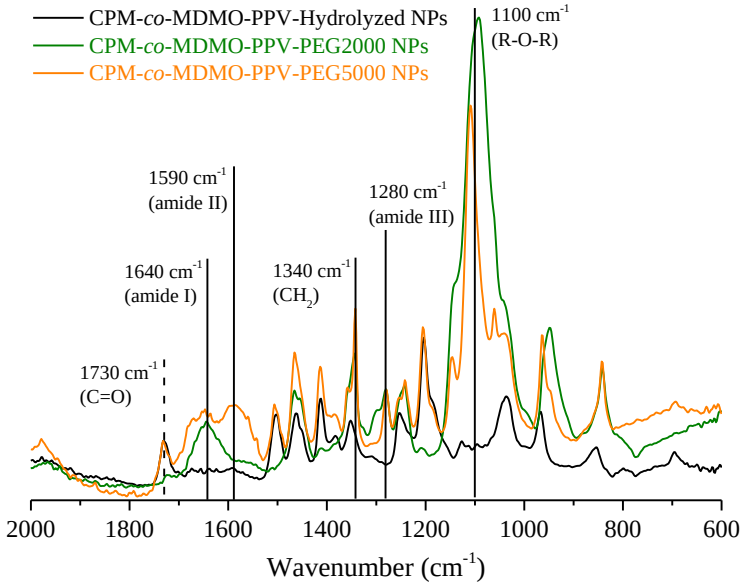

Figure 4—3: Infrared spectra of hydrolyzed and PEGylated CPM-*co*-MDMO-PPV NPs.

Infrared spectra of hydrolyzed (black line), PEG2000 (green line) and PEG5000 (orange line) covered CPM-*co*-MDMO-PPV NPs.

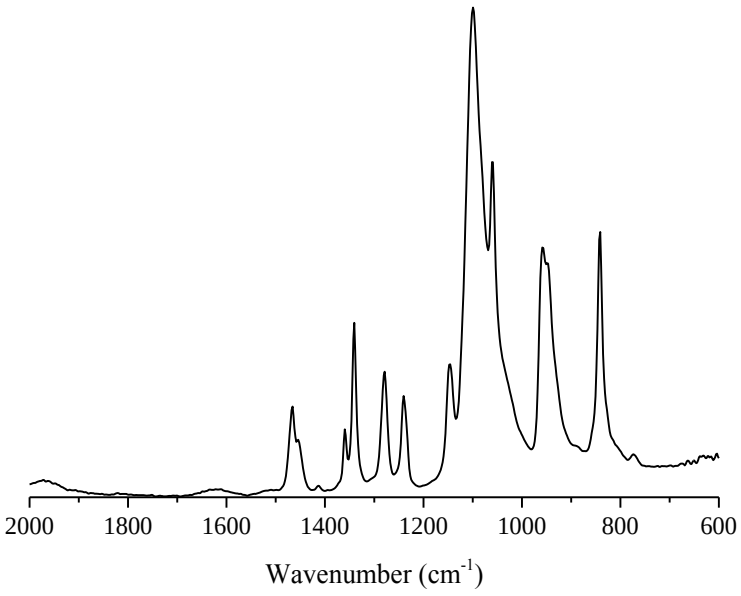

Figure 4—4: Infrared spectrum of NH_2-PEG2000-OH.

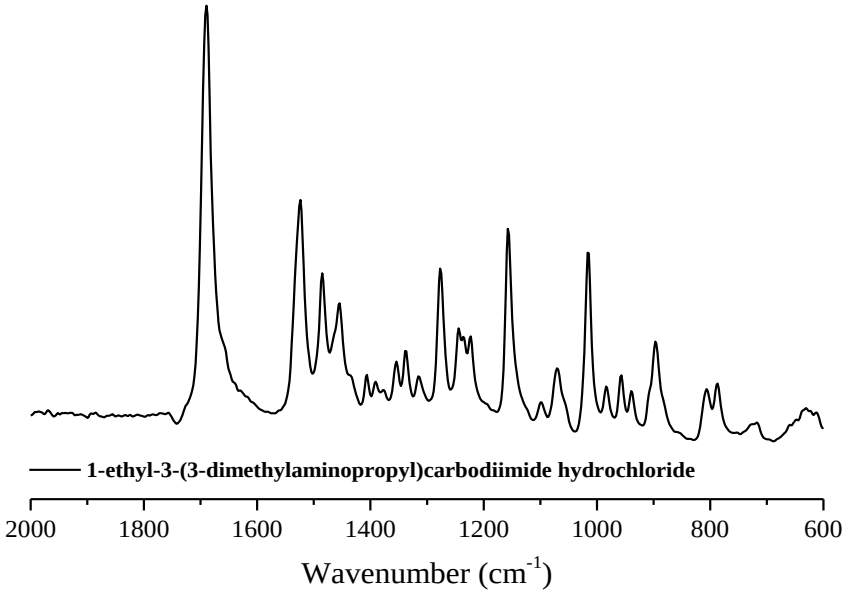

Figure 4—5: Infrared spectrum of 1-ethyl-3-(3-dimethyl-amino-propyl)carbodiimide.

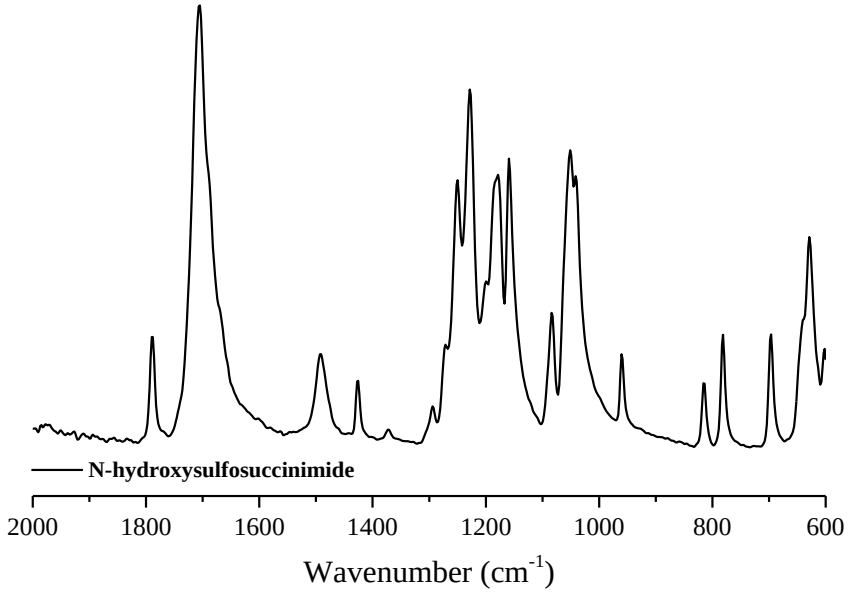

Figure 4—6: Infrared spectrum of sulfo-N-hydroxysulfosuccinimide.

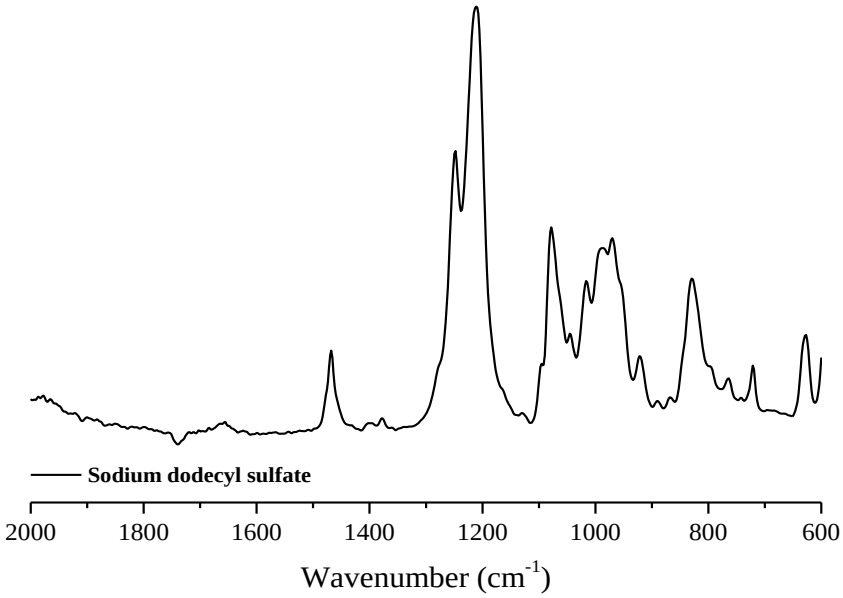

Figure 4—7: Infrared spectrum of sodium dodecyl sulfate.

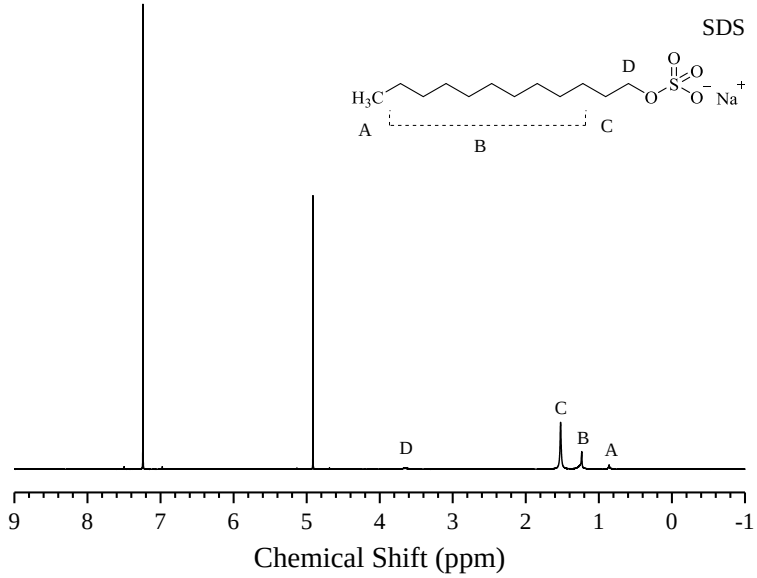

Figure 4—8: ^{1}H NMR spectrum of SDS in $CDCl_3$.

^{1}H NMR spectrum of SDS in $CDCl_3$.(7.24 ppm) with 0.035 v/v% dibromomethane (4.95 ppm) as an internal standard. Signal C also contains a contribution from H_2O.

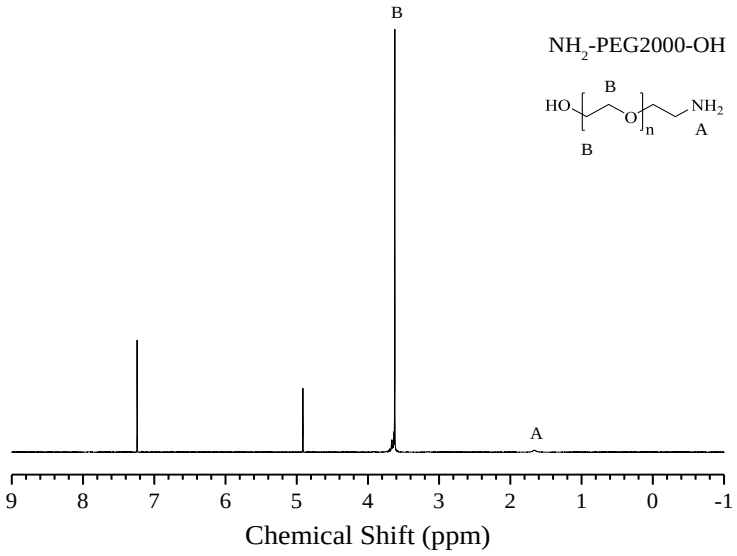

Figure 4—9: ^{1}H NMR spectrum of NH_2-PEG2000-OH.

^{1}H NMR spectrum of NH_2-PEG2000-OH in $CDCl_3$ (7.24 ppm) with 0.035 v/v % dibromomethane (4.95 ppm) as an internal standard. Signal A contains a contribution from H_2O.

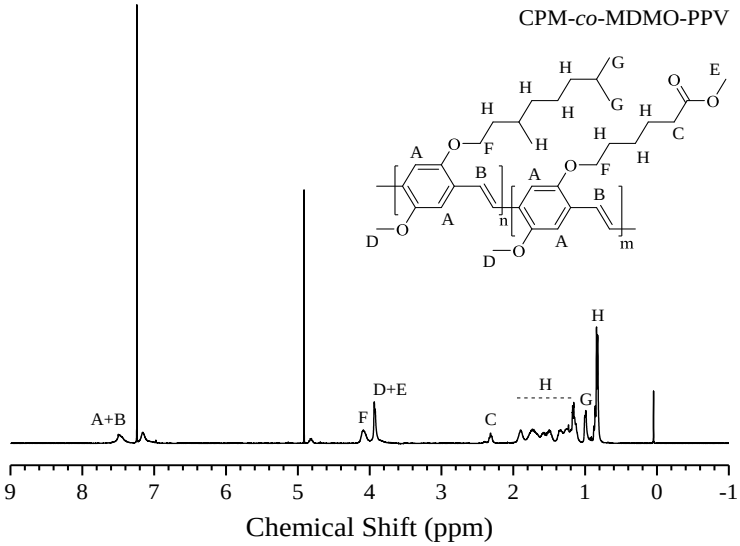

Figure 4—10: ^{1}H NMR spectrum of CPM-*co*-MDMO-PPV.

^{1}H NMR spectrum of CPM-*co*-MDMO-PPV in $CDCl_3$ (7.24 ppm) with 0.035 v/v % dibromomethane (4.95 ppm) as an internal standard.

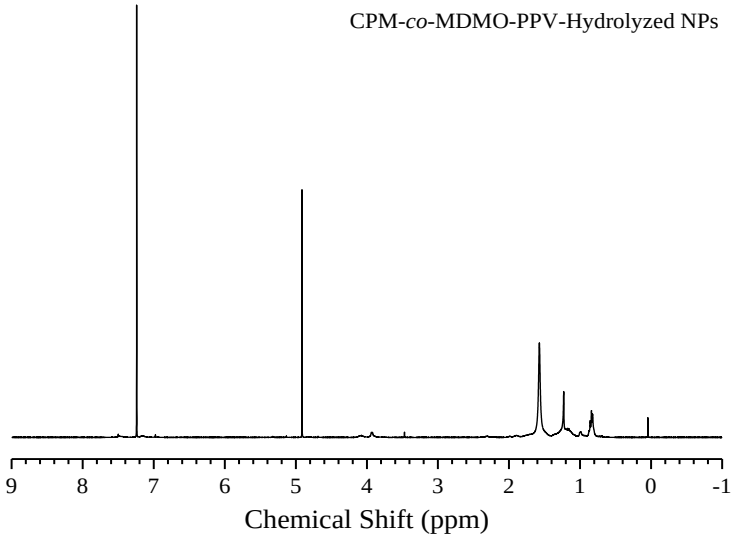

Figure 4—11: ^{1}H NMR spectrum of dried CPM-*co*-MDMO-PPV-Hydrolyzed NPs redissolved in $CDCl_3$.

^{1}H NMR spectrum of dried CPM-*co*-MDMO-PPV-Hydrolyzed NPs redissolved in $CDCl_3$. (7.24 ppm) with 0.035 v/v % dibromomethane (4.95 ppm) as an internal standard.

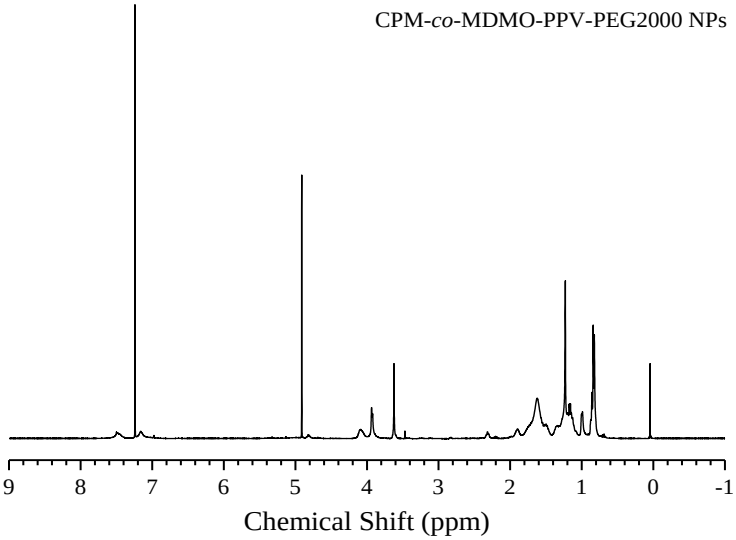

Figure 4—12: ^{1}H NMR spectrum of dried CPM-*co*-MDMO-PPV-PEG2000 NPs redissolved in $CDCl_3$.

^{1}H NMR spectrum of dried CPM-*co*-MDMO-PPV-PEG2000 NPs redissolved in $CDCl_3$. (7.24 ppm) with 0.035 v/v % dibromomethane (4.95 ppm) as an internal standard.

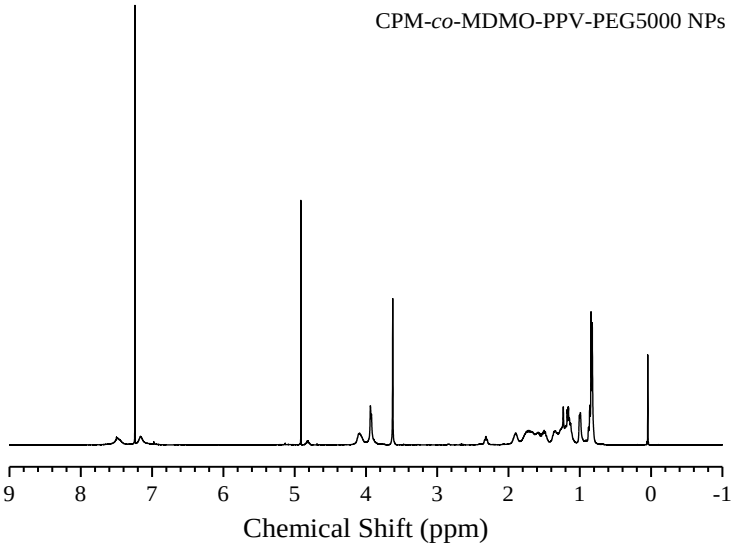

Figure 4—13: ^{1}H NMR spectrum of dried CPM-*co*-MDMO-PPV-PEG5000 NPs redissolved in CDCl3.

^{1}H NMR spectrum of dried CPM-*co*-MDMO-PPV-PEG5000 NPs redissolved in CDCl3. (7.24 ppm) with 0.035 v/v % dibromomethane (4.95 ppm) as an internal standard.

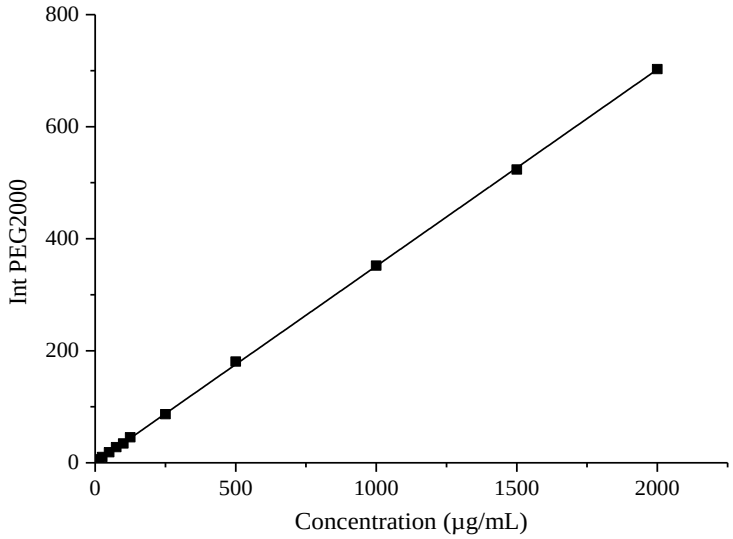

Figure 4—14: ^{1}H NMR calibration curve for PEG2000.

^{1}H NMR calibration curve for PEG2000 dissolved in $CDCl_3$ containing 0.035 v/v % dibromomethane as internal standard, on the basis of the peak area (integration) of the signal at 3.65 ppm.

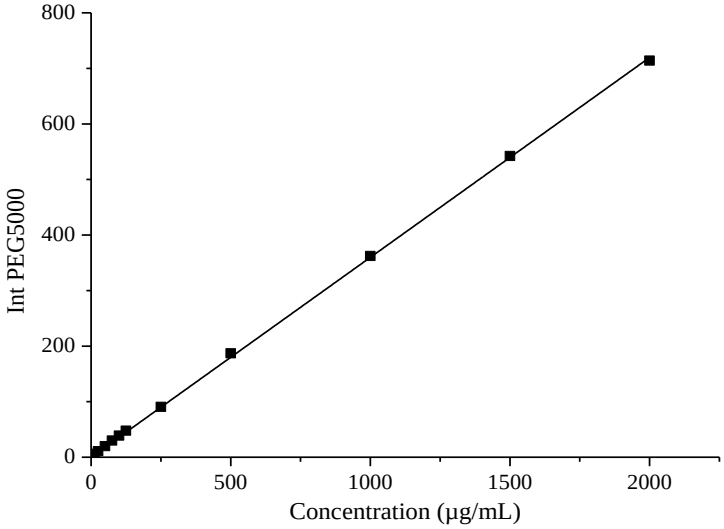

Figure 4—15: ^{1}H NMR calibration curve for PEG5000.

^{1}H NMR calibration curve for PEG5000 dissolved in $CDCl_3$ containing 0.035 v/v % dibromomethane as internal standard, on the basis of the peak area (integration) of the signal at 3.65 ppm.

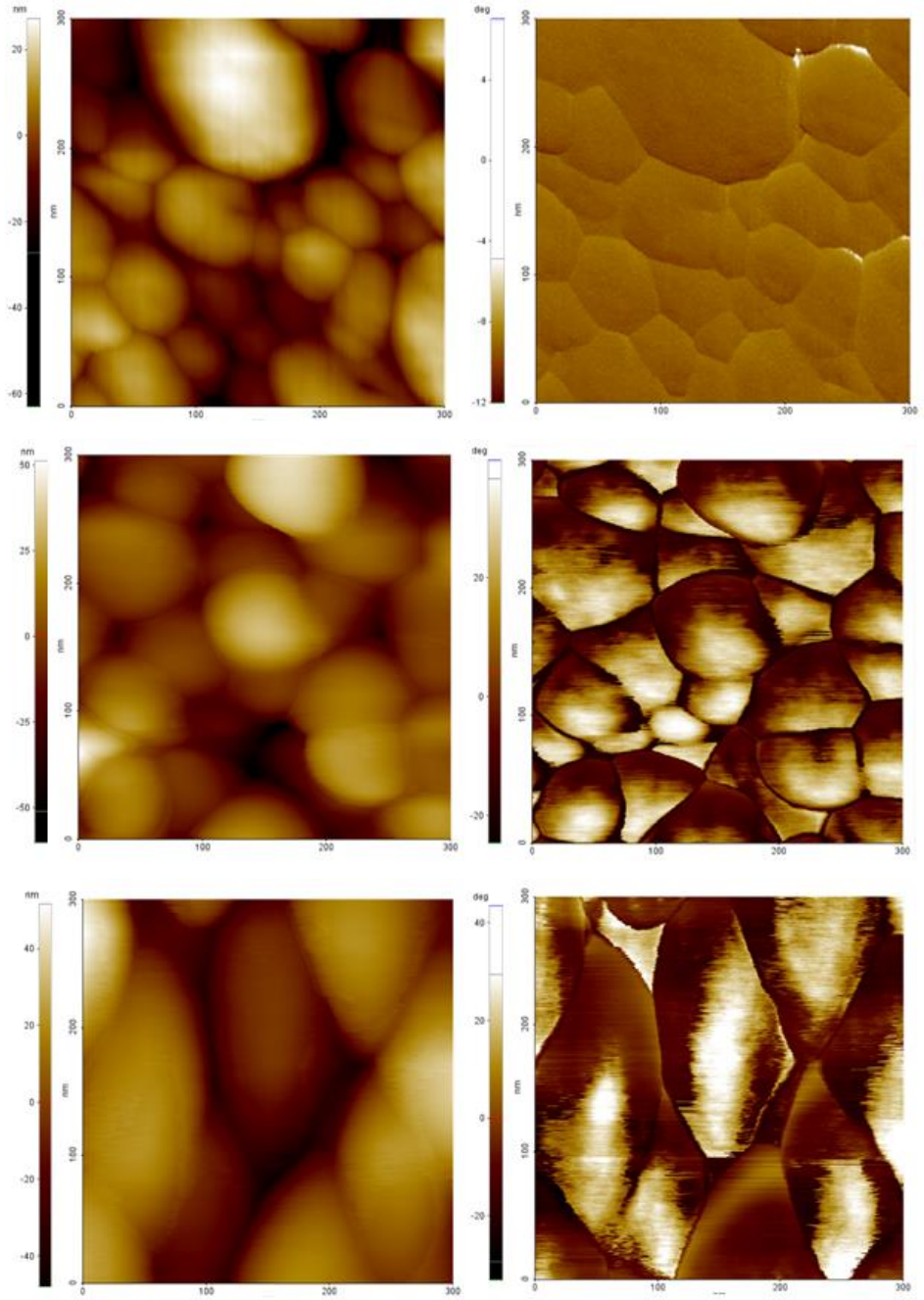

Figure 4—16: AFM height and phase images of non-PEGylated and PEGylated CPM-*co*-MDMO-PPV NPs.

AFM height (left) and phase (right) images of non-PEGylated (top) and PEGylated (middle – PEG2000, bottom – PEG5000) CPM-*co*-MDMO-PPV NPs deposited on a silicon wafer.

4.4.3 Influence of PEGylation on optical characteristics of PPV-based NPs

As coupling proved to be successful, its possible effect on the optical properties was investigated. Fingerprint measurements showed that grafting did not have a detrimental effect on excitation or emission maxima (Figure 4-17). However, surface hydrolysis appears to lower NP fluorescent brightness (B_{NP}), the product of the QY and molar extinction coefficient, with a factor 3.5 following hydrolysis which reverses back to almost its original value after PEGylation for both PEG2000 and 5000 (Table 4-3).

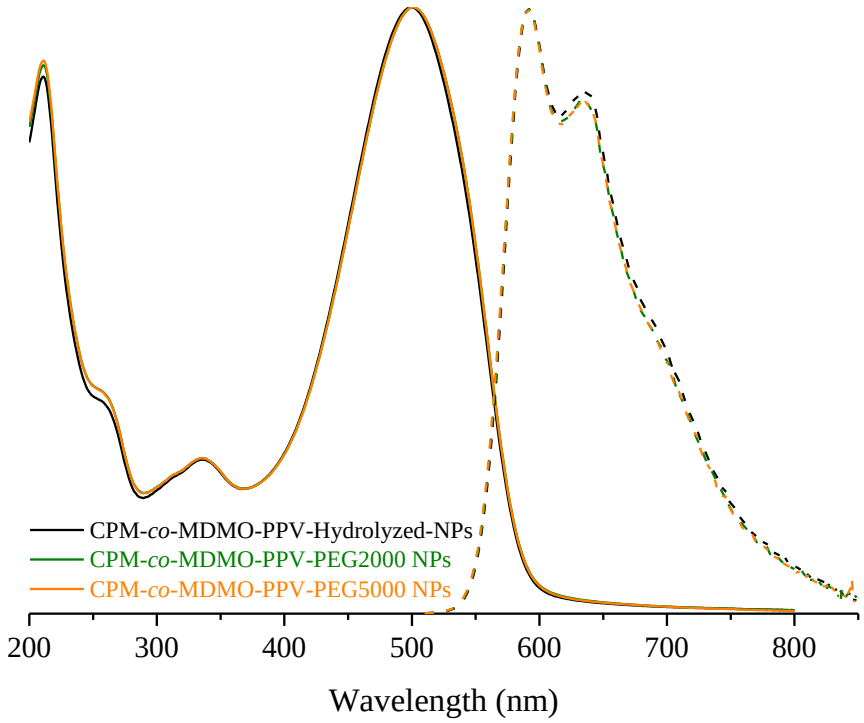

Figure 4—17: Fingerprint of hydrolyzed and PEGylated CPM-*co*-MDMO-PPV NPs. Optical Spectra (absorbance solid and emission dashed line) of CPM-*co*-MDMO-PPV NPs of which the surface is hydrolyzed (black) and covered with either PEG2000 (green) or PEG5000 (orange).

Table 4—3: Quantum yield values of non-treated, hydrolyzed, and PEGylated CPM-*co*-MDMO-PPV NPs

	Untreated	Hydrolyzed	PEG2000	PEG5000
quantum yield (φ_F)	3 %	2 %	3 %	2 %
molar extinction coefficient (ε, $M^{-1} \bullet cm^{-1}$)	9.7 x 10^6 (± 0.4 x 10^6)	5.2 x 10^6 (± 0.4 x 10^6)	9.7 x 10^6 (± 0.7 x 10^6)	11.8 x 10^6 (± 1.9 x 10^6)
absorption cross section (σ, cm^2)	3.7 x 10^{-14} (± 0.1 x 10^{-14})	2.0 x 10^{-14} (± 0.2 x 10^{-14})	3.7 x 10^{-14} (± 0.3 x 10^{-14})	4.5 x 10^{-14} (± 0.7 x 10^{-14})
fluorescence brightness (B_{NP}, $M^{-1} \bullet cm^{-1}$)	3,4 x 10^5	9,7 x 10^4	2,7 x 10^5	2,5 x 10^5

4.4.4 Influence of PEGylation on biological characteristics of PPV-based NPs

The biocompatibility of a bioimaging probe is of great relevance when conducting *in vitro* and *in vivo* experiments. Therefore, the effect of PEGylation on this key characteristic was studied using a dose-dependent alamar blue cytotoxicity test (Figure 4-18 and 4-19). The test showed that after PEGylation cell viability of HMEC-1 as well as HeLa cell lines, a widely used non-CNS cell line, did not drop below 97 % in comparison to an untreated control after 24 h incubation. No significant statistical difference was observed within the tested concentration range (linear mixed model followed by post-test Dunnett for multiple comparisons, $p < 0.05$), except for the 100 μg/mL concentration of PEG5000 covered NPs. The NPs remained stable in cell culture medium.

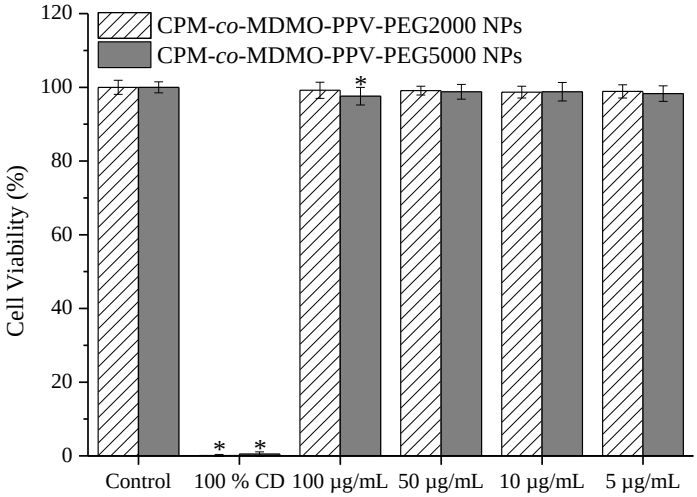

Figure 4—18: Dose-dependent cytotoxicity of CPM-*co*-MDMO-PPV-PEG2000 and PEG5000 NPs in HMEC-1 cells.

Dose-dependent cytotoxicity of CPM-*co*-MDMO-PPV-PEG2000 and PEG5000 NPs determined by the alamar blue assay in HMEC-1 cells after 24 h of exposure. CD stands for cell death. Data are presented as percent of control mean ± SD (N = 3).

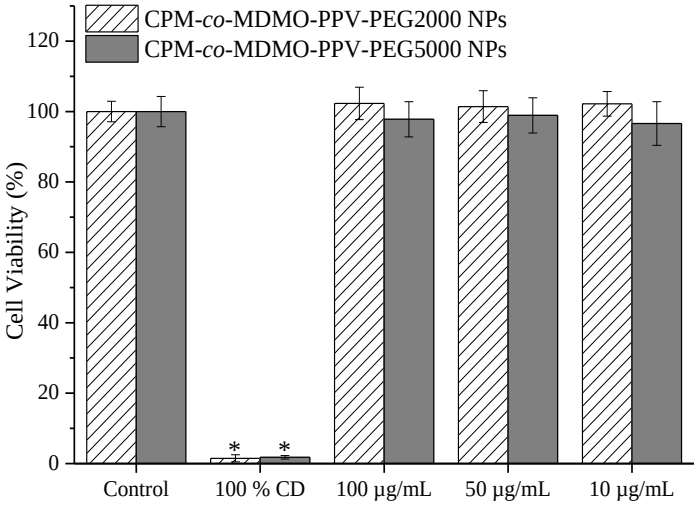

Figure 4—19: Dose-dependent cytotoxicity of CPM-*co*-MDMO-PPV-PEG2000 and PEG5000 NPs in HeLa cells.

Dose-dependent cytotoxicity of CPM-*co*-MDMO-PPV-PEG2000 and PEG5000 NPs determined by the alamar blue assay in HeLa cells after 24 h of exposure. CD stands for cell death. Data are presented as percent of control mean ± SD (N = 3).

In addition to the cytotoxicity, the hard protein corona that remains after the washing steps, which remove weakly and unbound (soft corona) proteins, was analyzed using SDS-page gel electrophoresis and mass spectrometry. This was performed for MDMO-PPV NPs (Figure 4-20), hydrolyzed CPM-*co*-MDMO-PPV NPs (Figure 4-21) and PEGylated constructs (Figure 4-22 and 4-23). The corona was almost identical for the two ungrafted NPs, except for antithrombin-III in case of MDMO-PPV NPs and alpha-1B-glycoprotein for CPM-*co*-MDMO-PPV NPs. A time-dependent increase in band-intensity was observed for the alpha-2-macroglobulin precursor band, while those of serotransferrin, albumin, alpha-1-antiproteinase, alpha-2-HS-glycoprotein and apolipoprotein A-I (only for CPM-*co*-MDMO-PPV NPs) decreased. PEGylation resulted in an almost complete disappearance of the corona, except for some traces of albumin.

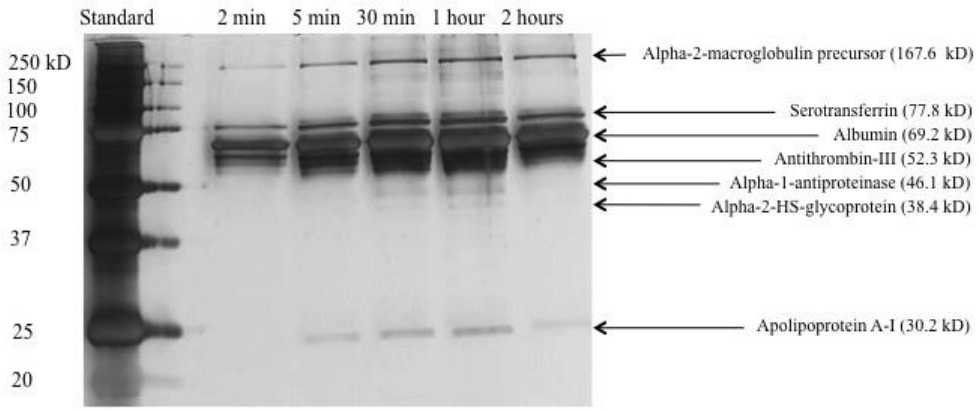

Figure 4—20: SDS-page blot of MDMO-PPV NPs after incubation with FCS for different time periods.

MDMO-PPV NPs incubated with FCS for different time periods and subjected to SDS-PAGE. Corona-derived proteins were visualized using highly sensitive silver staining. Proteomic profiling was done using mass spectrometry.

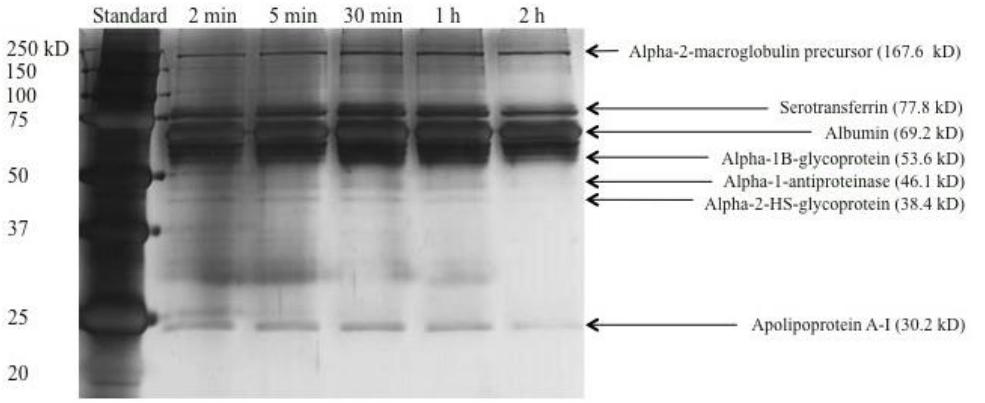

Figure 4—21: SDS-page blot of CPM-*co*-MDMO-PPV NPs after incubation with FCS for different time periods.

CPM-*co*-MDMO-PPV NPs incubated with FCS for different time periods and subjected to SDS-PAGE. Corona-derived proteins were visualized using highly sensitive silver staining. Proteomic profiling was done using mass spectrometry.

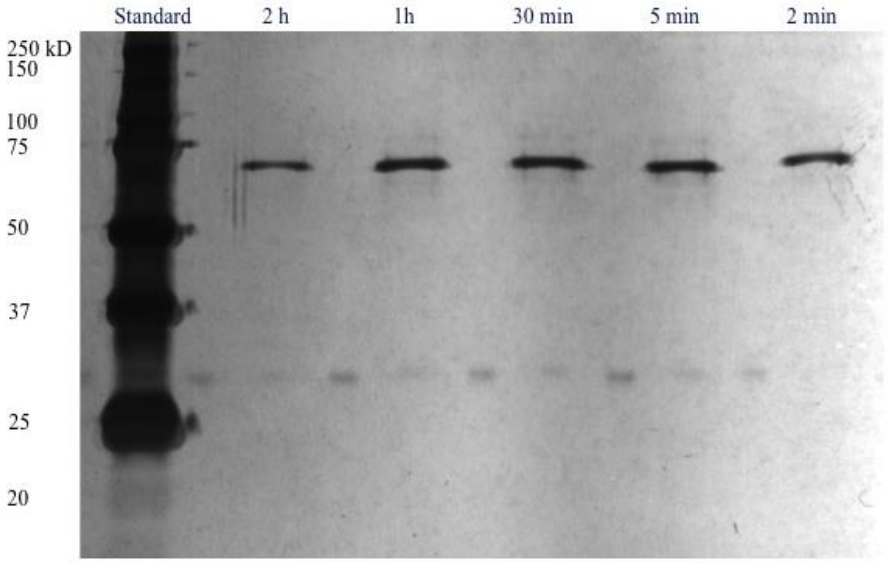

Figure 4—22: SDS-page blot of CPM-*co*-MDMO-PPV-PEG2000 NPs after incubation with FCS for different time periods.

CPM-*co*-MDMO-PPV-PEG2000 NPs incubated with FCS for different time periods and subjected to SDS-PAGE. Corona-derived proteins were visualized using highly sensitive silver staining. Proteomic profiling was done using mass spectrometry.

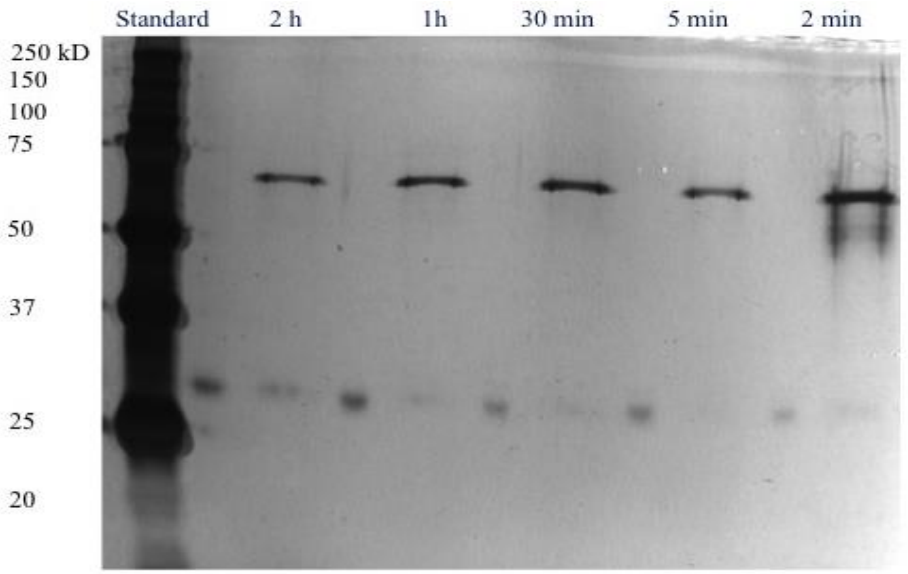

Figure 4—23: SDS-page blot of CPM-*co*-MDMO-PPV-PEG5000 NPs after incubation with FCS for different time periods.

CPM-*co*-MDMO-PPV-PEG5000 NPs incubated with FCS for different time periods and subjected to SDS-PAGE. Corona-derived proteins were visualized using highly sensitive silver staining. Proteomic profiling was done using mass spectrometry.

Next, dose-dependent NP uptake kinetics by HMEC-1 cells, as a function of time, were studied using flow cytometry for a time period of 30 h (Figure 4-24). A clear difference was observed between the NP constructs. The different concentrations of hydrolyzed NPs always reached the 100 % saturation level within the provided timeframe, meaning every cell has engulfed NPs, which is in agreement with our previous work [165], while this is never the case for PEGylated NPs. Also, a significant difference between the PEGylated NPs was visible. In case of PEG2000 the highest level of uptake achieved was 86 % after 30 h, while PEG5000 NPs only reached 36 %. In the early phase, PEG2000 NPs uptake increases during the first 8 h with approximately 20 % / 2 h compared to a 2-3 % / 2 h increase for PEG5000 NPs. Standard deviations are displayed but not observable since they do not exceed 1 %.

Additionally, NP uptake was confirmed visually for living and fixated HMEC-1 cells (Figure 4-25 and 4-26) using confocal laser scanning microscopy. Uptake by other CNS cell lines, namely BV-2 and C8-D1A cells, was also imaged and the results are present in the SI (Figure 4-27 and 4-28). All three cell lines are internalizing the different NP constructs within the incubation period, as was also confirmed by z-stacks throughout fixated HMEC-1 cells. Also, no changes in the morphological integrity of the cell were monitored. For all tested cell lines, a drastic decrease in NP uptake was visible after PEGylation.

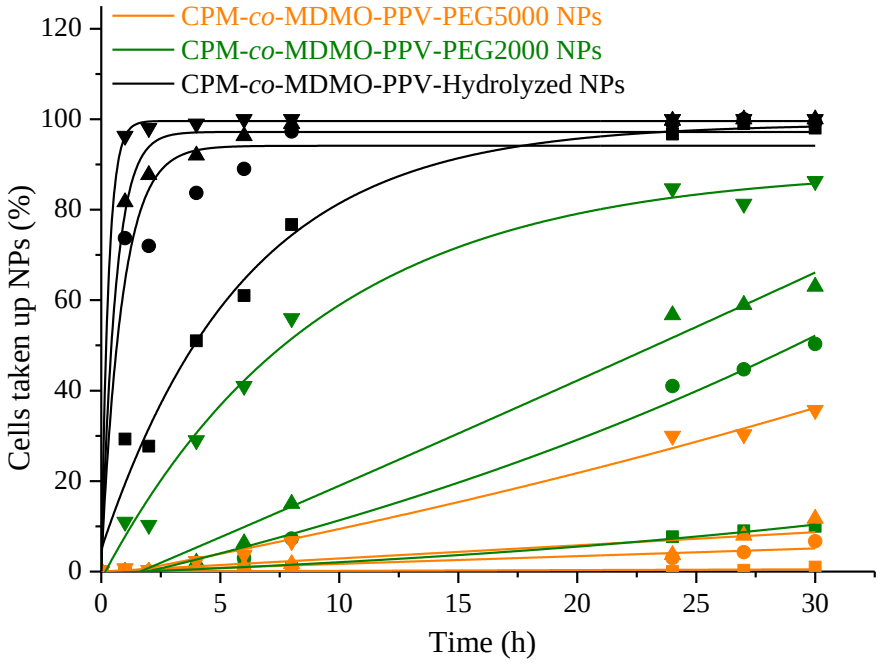

Figure 4—24: Kinetics of hydrolyzed and PEGylated CPM-*co*-MDMO-PPV NP uptake. Kinetics of the internalization of CPM-*co*-MDMO-PPV hydrolyzed (black) and PEG2000 (green) and PEG5000 (orange) covered NPs by HMEC-1 cells over a time period of 30 h for concentrations of 25 (square), 75 (circle), 100 (triangle) and 150 (reverse triangle) μg/mL.

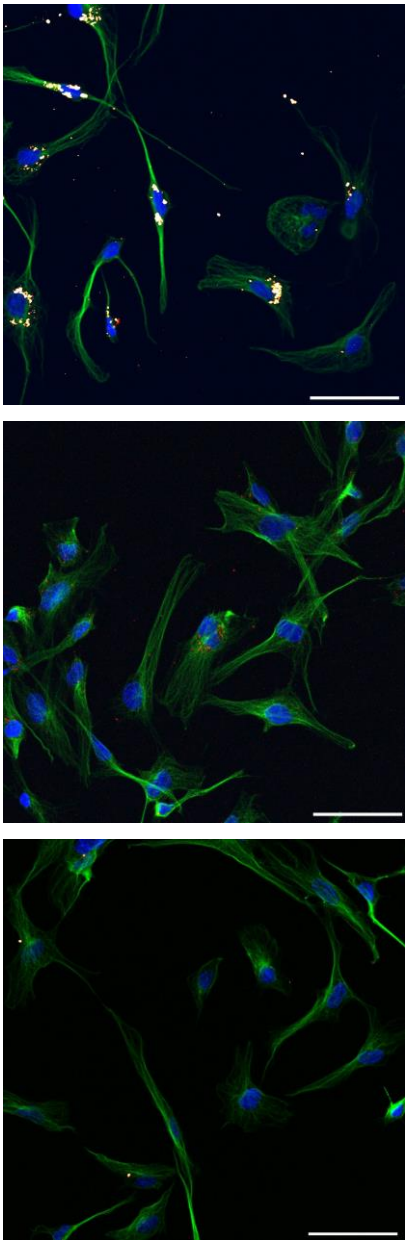

Figure 4—25: Confocal microscope images of fixated HMEC-1 cells treated with hydrolyzed and PEGylated CPM-*co*-MDMO-PPV NPs.

Confocal microscope images of HMEC-1 cells incubated with CPM-*co*-MDMO-PPV hydrolyzed and PEGylated NPs (top) and PEG2000 (middle) and PEG5000 (bottom) covered NPs (red) for a time period of 24 h with additional staining of cell nucleus (blue) and tubulin (green). Scale bar represents 50 μm.

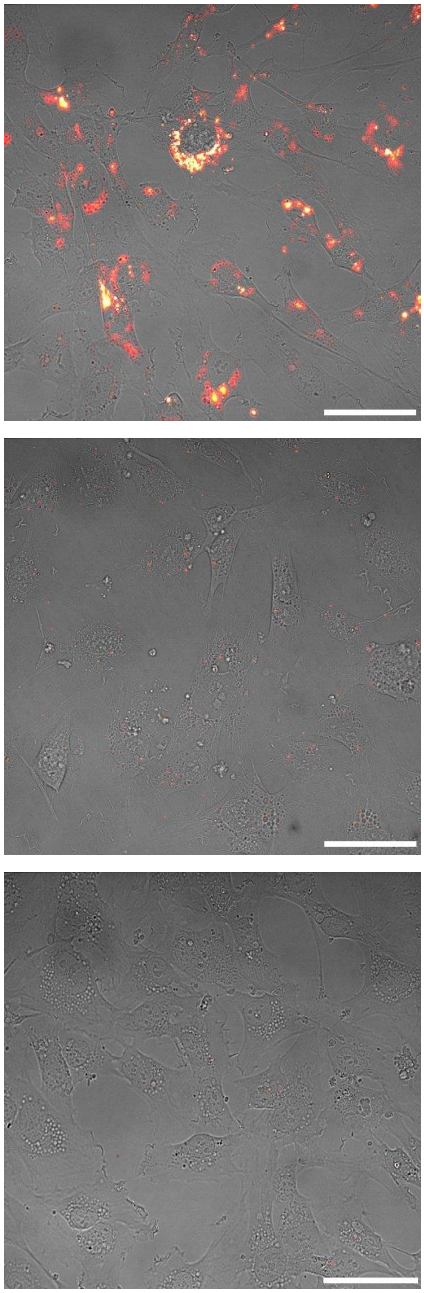

Figure 4—26: Confocal microscope images of living HMEC-1 cells treated with hydrolyzed and PEGylated CPM-*co*-MDMO-PPV NPs.

Confocal microscope images of HMEC-1 cells incubated with CPM-*co*-MDMO-PPV hydrolyzed and PEGylated NPs (top) and PEG2000 (middle) and PEG5000 (bottom) covered NPs (red) for a time period of 24 h. Scale bar represents 50 μm.

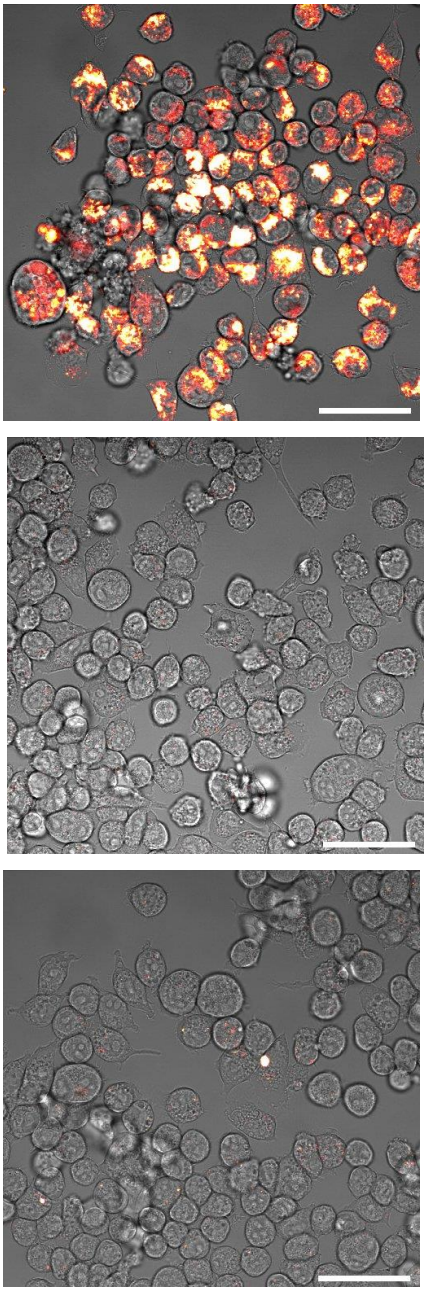

Figure 4—27: Confocal microscope images of living BV-2 cells treated with hydrolyzed and PEGylated CPM-*co*-MDMO-PPV NPs.

Confocal microscope images of BV-2 cells incubated with CPM-*co*-MDMO-PPV hydrolyzed and PEGylated NPs (top) and PEG2000 (middle) and PEG5000 (bottom) covered NPs (red) for a time period of 24 h. Scale bar represents 50 μm.

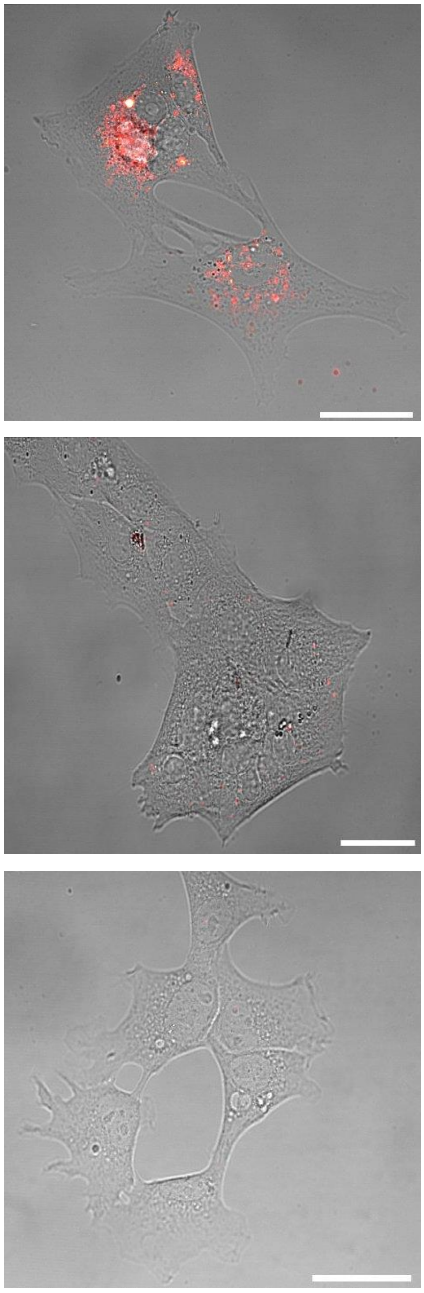

Figure 4—28: Confocal microscope images of living C8-D1A cells treated with hydrolyzed and PEGylated CPM-*co*-MDMO-PPV NPs.

Confocal microscope images of C8-D1A cells incubated with CPM-*co*-MDMO-PPV hydrolyzed and PEGylated NPs (top) and PEG2000 (middle) and PEG5000 (bottom) covered NPs (red) for a time period of 24h. Scale bar represents 30 μm.

4.5 Discussion

4.5.1 Surface functionalized PPV-based NPs: preparation

Successful conversion of ester groups into carboxylic acids was achieved within a 6 h hydrolysis period (Figure 4-1). The pH dependent variations in size and zetapotential can be correlated to the presence of carboxylic acid groups on the NPs, as these play a crucial role in aggregation kinetics (Figure 4-2). At neutral and basic pH the carboxylic acid groups impart stability to the colloidal solution through electrostatic repulsion. When an acidic pH value of 4 is reached, they are neutralized through protonation due to their pKa value of 4.7. The resulting reduction in surface charge leads to NP aggregation as a consequence of the now dominant van der Waals forces [185]. As the untreated NPs are stabilized by the anionic surfactant SDS, with a pKa value of 1.9, no aggregation behavior occurs [186]. This demonstrates that not only the hydrolysis process was successful but the presence of carboxyl groups also aids in the removal of excess surfactant during the washing steps.

4.5.2 Surface functionalized PPV-based NPs: PEGylation

PEGylation was confirmed by the decrease in zetapotential to approximately -30 mV upon functionalization, caused by the shift from carboxylic acid groups to the hydroxyl terminus of the PEG chain (Table 4-2). Also, the hydrodynamic radius underwent an increase of 7 nm for PEG2000 and 12 nm for PEG5000 which is in accordance to research by Schöttler *et al* [187]. The covalent immobilization of PEG through the formation of an amide bond was demonstrated using infrared spectroscopy (Figure 4-3). The depletion of carboxylic acids was proven by the decrease in the C=O band. This was not the case for the PEG5000 construct, which can be attributed to the fact that fewer chains are bound resulting in a larger remainder of carboxylic acids. The amide bond formation was confirmed given the appearance of the amide I, II and III band. The amide I band is governed by stretching vibrations of the C=O group (80 %), the amide II band corresponds to N-H bending (60 %) as well as C-N stretching vibrations (40 %) and the amide III band correlates to C-N stretching vibrations (40 %) and N-H bending (30 %) [188]. Additionally, the intensity of the CH_2 and R-O-R peak, linked to the PEG chains themselves (Figure 4-4), increased substantially. The peaks were not

linked to any of the reaction products involved (Figure 4-5 to 4-7). The effective amount of PEG chains was determined by ^{1}H NMR, after showing that SDS and CPM-*co*-MDMO-PPV did not interfere with the characteristic PEG peak at 3.65 ppm (Figure 4-8 to 4-15). The number of PEG molecules on the surface decreased as the molecular weight (MW) of the polymer increased. However, the ratio [Γ/Γ*] is approximately the same for both constructs and larger than 1, indicating PEG is present as a dense brush like coating [189]. Induced variations in the NP surface were evaluated through AFM measurements (Figure 4-16). The appearance of a second phase in the AFM phase images confirmed PEGylation, as this inhomogeneity is caused by the presence of PEG on the surface [190].

4.5.3 Influence of PEGylation on optical characteristics of PPV-based NPs

For the optical properties, no change occurred in the NPs' fingerprint following PEGylation (Figure 4-17). The introduction of carboxylic acid groups through hydrolysis proved to be detrimental for the fluorescence brightness (Table 4-3), a feature already documented in literature [191]. The introduction of hydrophilic side chain moieties interferes with the association strength among various portions of the hydrophobic PPV chain or between different chains, affecting the NPs' internal structure (stacking of chains close to the aqueous interface) and compactness. An increase in solvation can occur at the interface as a consequence of newly introduced ionic groups, which might be correlated to the observed reduction in fluorescence brightness. PEGylation via covalent attachment of amine functionalized PEG chains reverses this effect by converting a large amount of carboxylic acid groups into amide bonds during EDC/sulfo-NHS coupling. As a result, the interactions of hydrophobic polymer chains within the NPs and with the environment are altered, and eventually reverses the reduction in fluorescence brightness.

4.5.4 Influence of PEGylation on biological characteristics of PPV-based NPs

One of the most important biological properties is the biocompatibility of a novel bioimaging probe. There are cases documented in literature where PEGylation increases NP cytotoxicity [192], therefore the biocompatibility of PPV-based NPs

was reevaluated (Figure 4-18 and 4-19). As no dose-dependent effect or significant reduction ($p < 0.05$) in cell viability was observed after 24 h, it can be concluded that PEGylation has no discernible impact on the biocompatibility.

The main determinant for the biological fate of NPs is the adsorption of proteins from physiological fluids on the surface, defined as the protein corona [193]. Therefore, generating knowledge about the fundamental interactions of PPV-based NPs with the biological environment is a key objective. A 2 h time limit was chosen for the corona study as endocytosis occurs primarily in a one-to-four hour period following NP administration. The corona formation of three PPV-based NP systems was tested: namely MDMO-PPV NPs and hydrolyzed as well as PEGylated CPM-*co*-MDMO-PPV NPs (Figure 4-20 to 4-23). As most PPV-based NP studies only employ homopolymers, MDMO-PPV NPs were included to demonstrate the potential consequences of transitioning from such a system to a statistical copolymer type on the formation of a protein corona. For both homo- and copolymer NPs the protein corona are homologous, except for a small population of unique proteins. This is in line with other studies that showed that introducing a change in the NP surface charge, in this case caused through the introduction of carboxylic acid groups in the side chain, are able to cause small alterations in the protein corona buildup [194, 195]. The protein corona for both systems consisted of albumin, apolipoprotein A-I, alpha-2HS-glycoprotein, serotransferrin, alpha-1-antiproteinase and alpha-2-macroglobulin precursor.

The main component of the overlapping profile is albumin, a dysopsonin that can be recovered from a wide variety of NPs [196]. The difference in surface charge does not affect its adsorption but does change the thermodynamic process of adsorption [197]. Apolipoproteins, like apolipoprotein A-I, are the main type of proteins adsorbing onto hydrophobic polymer NPs. They are involved in the transportation of lipids and cholesterol and affect intracellular NP trafficking [195, 198]. Also alpha-2HS-glycoprotein, involved in endocytosis, and serotransferrin, an important protein in transport and trafficking, are known to attach to hydrophobic polymer NPs [196, 199]. Alpha-1-antiproteinase is involved in blood coagulation and the alpha-2-macroglobulin precursor is known to inhibit proteinases [196]. The proteins alpha-1B-glycoprotein for CPM-*co*-MDMO-PPV NPs and antithrombin-III for MDMO-PPV NPs were unique to both constructs. Alpha-

1B-glycoprotein can be found on NPs with different surface charges but has a strong affinity for negatively charged NPs [196, 200]. Antithrombin III on the other hand is associated with NPs that have a more neutral surface charge [195]. The observed time-dependent competitive adsorption of proteins can be divided into different phases. First, a corona forms consisting of the proteins that are most abundant in FCS such as albumin, alpha-2-HS-glycoprotein, alpha-1-antiproteinase and serotransferrin. This occurs despite their low affinity for the NP surface [201]. However, over time these proteins are replaced by high affinity proteins as was demonstrated by the gradual increase of apolipoprotein A-I on the hydrophobic MDMO-PPV NPs. The collective effects behind these dynamic changes in protein corona composition are known as the "Vroman effect" [202].

PEGylation is one of the most efficient anti-opsonization strategies [203]. The grafted linear chains create a thermodynamic shield against protein diffusion by using steric hindrance to block protein binding-sites, thereby reducing protein adsorption [204]. This is especially the case for grafted PEG chains, which have a higher surface coverage compared to multiblock copolymer NPs, consisting of PEG, despite having a lower total PEG content [205]. The reduced adsorption was clearly seen for PEGylated NPs as solely a "weak" corona, consisting of traces of albumin, was detected (Figure 4-22 and 4-23). Recently, it was demonstrated that SDS can also increase the binding enthalpy and number of interacting proteins [206]. Despite the fact that the NPs underwent rigorous washing steps, still some residual traces of SDS remain as was shown in the ^{1}H NMR spectra (Figure 4-8). After PEGylation, however, this residual SDS disappears (Figure 4-12 and 4-13) as PEG takes over the stabilizing role, further decreasing the amount of proteins present.

In order to correlate the protein corona findings to cell-NP interactions, uptake studies using flow cytometry were performed. Previous studies have proven that the fluorescence radiative rates are high enough to detect PPV-based NPs in such set-up [165]. A profound decrease in the percentage of cells exhibiting PPV-based NP labeling was observed after PEGylation and by a factor 2 when the PEG chain MW was increased (Figure 4-24), which is in accordance to literature [181, 182]. These results are consistent as confocal laser scanning microscopy showed the same pattern (Figure 4-25 and 4-26). It is a clear demonstration that PEG

provides a 'steric-repulsive barrier' against cellular uptake for PPV-based NPs [187, 207]. It does not only achieve the latter by reducing interactions with serum proteins but also by reducing surface charge density and increasing colloidal stability through steric hindrance caused by the flexible and hydrated PEG chains. These results nicely demonstrate the flexibility of the system, as the degree of stealth can be adapted to fit the needs by simply varying the PEG chain length on the surface.

The MW-dependent reduction in uptake was not limited to one cell type, but was observed in various brain-related cell lines (Figure 4-27 and 4-28). The endothelial cell line (HMEC-1) was chosen to mimic the blood brain barrier (BBB) while microglia (BV-2) and astrocyte (C8-D1A) cell lines were chosen to represent the cell population residing inside the brain. PEGylation proved to be a valid method to evade engulfment by microglia, the resident immune cells of the brain, which are known to drastically limit NP bioavailability through massive uptake. No activation of microglia was observed for PEGylated samples, in sharp contrast with the ungrafted samples where transformation to amoeboid-like appearances and employment of pseudopodia occurred in line with our previous findings [165]. The protection that PEG offers against microglial clearance promotes the bioavailability and retention of PPV-based NPs in the extracellular space, enhancing their use as a bioimaging probe overall. This reduction in uptake is not only specific for immune cells as HMEC-1 and C8-D1A cell lines also show similar results. This highlights how PEGylation offers non-specific cellular evasion from brain cell populations, of which the extent can be tuned through modification of the PEG chain MW, even further prolonging bioavailability within the CNS parenchyma. These observations are in agreement with work by Jenkins *et al* [184] where it was shown that PEGylated nanoparticles evade major brain cell populations.

4.6 Conclusion

To conclude, this study highlights the advantage of using functional PPVs as a core material for NPs designed for bioimaging. The alkoxy side chain moieties present on the NP surface were conveniently tuned for high density surface grafting with PEG stealth groups. PEGylation proved to be compatible with PPV-based NPs as it only slightly increased the hydrodynamic radius and had no significant detrimental effect on the optical fingerprint or fluorescence brightness. It did not alter the intrinsic biocompatibility of PPV-based NPs, clearly decreased protein corona formation and induced non-specific cellular evasion that was dependent on the MW of the PEG chain. This paper clearly presented the various implications of PEGylating PPV-based NPs and shows that introducing stealth groups does not affect their inherent characteristic of being excellent candidates for bioimaging applications.

.

Chapter 5
CX_3CR1^+ cell targeting functional PPV-based conjugated polymer nanoparticles

This chapter is based on:

AZD8797 covered functional PPV-based conjugated polymer nanoparticles for targeted bioimaging of CX_3CR1^+ cells.

Peters M., Broux B., Seneca S., Hellings N., Junkers T., Ethirajan A.

Manuscript in preparation.

Declaration of own contribution: Martijn Peters jointly designed and performed the synthesis and characterization of the nanoparticle constructs. Special thanks to Bieke Broux for the assistance in the biological characterization experiments. He also contributed in writing the manuscript.

5.1 Abstract

Multiple sclerosis (MS) is a disabling chronic illness affecting the central nervous system (CNS) of millions of patients across the globe. However, to date, its exact etiology still remains partly understood. Therefore, lots of efforts are being undertaken to develop new research tools that help to gain a better understanding of disease processes underlying MS. Here, nanoparticles (NPs) constructed out of statistical functional copolymer 2-(5'-methoxycarbonylpentyloxy)-5-methoxy-1,4-phenylenevinylene and poly(2-methoxy-5-(3',7'-dimethoxyoctyloxy)-1,4-phenylenevinylene) (CPM-*co*-MDMO-PPV) are used for the design of a bioimaging probe directed against CX_3CR1. CX_3CR1 is the receptor for the chemokine fractalkine (CX_3CL1) and is expressed on immune and glial cells that participate in the development of MS disease. Tailor-made functional poly(p-phenylene vinylene) (PPV) possesses outstanding optical properties, non-cytotoxicity and the ability to enable one-pot synthesis of NPs with functional surface moieties. These moieties were employed for covalent attachment of CX_3CR1 antagonist AZD8797. Functionalization had no detrimental influence on fluorophore quality and led to uptake by CX_3CR1^+ cells within the peripheral blood mononuclear cell (PBMC) population. This provides researchers with the opportunity to investigate the specific role of CX_3CR1 bearing cells in diseases such as MS. Additionally, the small molecule kept its antagonistic features when anchored onto the NP surface, shown by reduced migration towards fractalkine in a chemotaxis assay. Lastly, the NPs were able to migrate over an *in vitro* blood-brain-barrier (BBB), making them usable to image disease processes behind a closed BBB. These results clearly demonstrate the vast potential functional PPVs possess for use in advanced biomedical applications.

5.2 Introduction

Multiple sclerosis (MS) is a chronic disabling disease that wreaks havoc inside the central nervous system (CNS). It affects genetically predisposed persons following a trigger with a still unknown origin. Although its exact etiology has yet to be unraveled, most genes associated with susceptibility to MS allude to a strong involvement of the adaptive immune system when it comes to disease predisposition. It is the combination of this immunological/genetic susceptibility with the possibility to bring about an MS-like disease in animal models through adoptive transfer of myelin-reactive T-cells that showcases the major role T-cells appear to play in the pathogenesis of MS [208, 209].

T-cell infiltration into the CNS of MS patients is potentiated by a collection of upregulated chemokines [210]. One of these chemokines is of particular interest, namely fractalkine (CX_3CL1) as its levels are elevated in the cerebrospinal fluid (CSF) and serum of people suffering from MS [211]. It is the sole member of the CX_3C-chemokine family and can fulfill both the role of adhesion molecule [212], when membrane bound, and chemoattractant [213] when in solution. Its receptor can be found on various other cells in addition to T-cells [214-216], such as monocytes [215], dendritic cells [217] and natural killer cells [215] in circulation and astrocytes [218] and microglia [219-221] inside the brain. It is therefore of particular interest as it provides an opportunity to specifically study these cell populations and their role in MS.

One of the T-cell sub-populations that has received significant attention in the past years due to its correlation with immune disorders is a population of T helper cells which have lost the expression of the costimulatory molecule CD28. These $CD4^+CD28^-$ T-cells are memory-type effector T-cells, which can infiltrate the brain, accumulate within MS lesions and display cytotoxic features [214, 222-225]. This accurately illustrates the involvement of $CD4^+CD28^-$ T-cells in the initial disease-related inflammatory processes inside the brain of certain MS patients. A means to distinguish these cells from their $CD4^+CD28^+$ counterpart is the expression of the aforementioned fractalkine receptor CX_3CR1 [214]. A bioimaging probe targeting this receptor could therefore help to further unravel the association between $CD4^+CD28^-$ T-cells, as well as other CX_3CR1 bearing cells, and MS.

During the preceding decades, major headway has been made in the expansion of visualization tools and bioimaging agents in order to accelerate our understanding of biological processes occurring at the cellular and molecular level [118, 120]. Especially fluorescence-based techniques have seen a sharp rise in development [158]. This has led to an extraordinary level of spatial resolution and temporal imaging. Over the past years, various new imaging probes have been manufactured that all have their own benefits and drawbacks. Although they have seen extensive service, fluorophores such as organic dyes are obstructed for use in high sensitivity applications as a consequence of their tendency to photobleach, their fast cellular clearance and low intensity [9, 124]. Fluorescent nanoparticles (NPs), like dye-loaded silica colloids/latex spheres or quantum dots (QDs), provide an interesting alternative given their superiority towards the traditional organic dyes when it comes to optical properties [8, 21, 226]. However, they are still plagued by inherent limitations such as short- and long-term cytotoxicity issues and *in vivo* degradation for QDs [22] and self-quenching as well as toxicity caused by dye exclusion in case of dye-doped NPs [17-19]. Although significant progress has been made with the abovementioned fluorophores, the continuous quest for new imaging agents remains ongoing.

Water-based colloidal dispersions comprised of conjugated polymers have recently received a lot of attention and praise for their use as a fluorophore. They possess an excellent biocompatibility as well as ultra-bright fluorescent signal, on account of their inherent π-conjugated backbone structure [10, 23, 26, 127]. One of the most thoroughly investigated conjugated polymers is poly(*p*-phenylenevinylene) (PPV). It owes its excellent reputation to its reliable synthesis routes, simple scale up potential, well-known photophysical properties and design flexibility offered by novel control methodologies [38, 49, 57]. This last feature allows for the manufacturing of custom-made PPVs, like complex polar functionalized PPVs that are synthesized via the sulfinyl precursor route [48, 56, 141]. These functional PPVs open the door to the manufacturing of NPs with functional moieties spread within the volume as well as on the NP surface [165]. The latter can be employed for the fast and elegant attachment of various requested functionalities onto the surface in order to incorporate specific characteristics essential for biomedical applications such as target specificity.

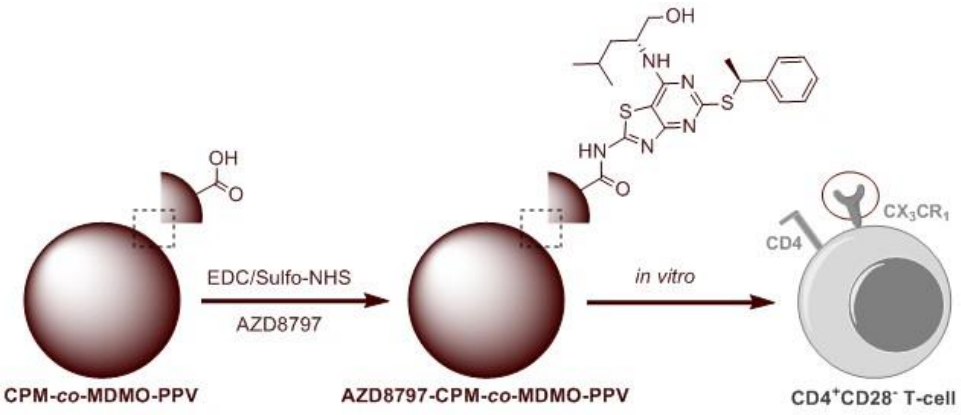

Figure 5—1: Synthesis scheme of AZD8797-CPM-*co*-MDMO-PPV NPs for CX_3CR1^+ cell staining.

Synthesis scheme depicting the EDC/Sulfo-NHS coupling of AZD8797 onto the surface of CPM-*co*-MDMO-PPV NPs, after which they are administered to CX_3CR1 bearing cells like $CD4^+CD28^-$ T-cells.

Here, a NP construct is designed comprised of the functional statistical copolymer that consists of the randomly repeating monomer units 2-(5'-methoxycarbonylpentyloxy)-5-methoxy-1,4-phenylenevinylene and poly(2-methoxy-5-(3',7'-dimethoxyoctyloxy)-1,4-phenylenevinylene) (CPM-PPV-*co*-MDMO-PPV, for simplicity henceforth called CPM-*co*-MDMO-PPV). The NPs are synthesized by employing the versatile combination of the miniemulsion and solvent evaporation method [165]. Subsequently, the resulting fluorescent NPs' surface functionalities are used to secure AZD8797, an allosteric non-competitive modulator of CX_3CR1 [227-229], onto the surface through EDC/sulfo-NHS coupling. This in order to obtain a bioimaging probe directed at CX_3CR1 carrying cells (Figure 5-1). It will allow researchers to gain a more profound insight into the working mechanisms of these cell populations in MS and other autoimmune diseases as well as the potential implications for the development of future therapies.

5.3 Materials and methods

5.3.1 Study subjects

Peripheral blood samples (Li-Heparin coated tubes) were collected from 3 healthy donors in collaboration with the University Biobank Limburg (UBiLim). Ethical approval was obtained from the medical ethical committee of Hasselt University and Jessa Ziekenhuis, and informed consent was obtained from each donor.

5.3.2 Materials and products

Non-essential amino acids, penicillin, streptomycin and sodium pyruvate were purchased from Life Technologies (Ghent, Belgium). The 96-well U bottom plates and 24-well cell culture insert with 3.0 μm pores were bought at Greiner Bio One (Vilvoorde, Belgium). The 1x phosphate buffered saline (1xPBS), microvascular endothelial cell growth (EGM-2-MV) medium and endothelial cell basal (EBM-2) medium were obtained from Lonza (Verviers, Belgium). Sodium dodecyl sulfate (SDS) and HyClone™ Fetal Bovine Serum (FBS) were purchased at GE Healthcare Life Sciences (Diegem, Belgium). Spectrum™ Spectra/Por 3 Regenerated Cellulose Dialysis Membrane Tubing (3.5 kD, 45 mm flat width) were bought from Fisher Scientific (Merelbeke, Belgium). Chloroform ($CHCl_3$), Filtropur S 0.2 filter, sulfo-N-hydroxysulfosuccinimide (sulfo-NHS) and dimethyl sulfoxide (DMSO) were purchased at VWR (Leuven, Belgium). The square-mesh copper transmission electron microscopy (TEM) grids were ordered at Electron Microscopy Sciences (Hatfield PA, US). Bovine serum albumin (BSA) was purchased at USBiological (Swampscott MA, US). The poly-L-lysine coated µ-Slide 8 well plates were bought at Proxylab (Beloeil, Belgium). Sodium hydroxide (NaOH) and 1-ethyl-3-(3-dimethyl-amino-propyl)carbodiimide (EDC) were ordered at Merck (Overijse, Belgium). AZD8797 was purchased from Axon Medchem (Groningen, The Netherlands). CD4 FITC and CD28 APC were bought at BD Biosciences (Franklin Lakes, USA). CX3CL1 was bought from Peprotech (Rocky Hill, USA). Roswell Park Memorial Institute (RPMI)-1640 medium and Cascade Blue-Dextran (10 kDa) were purchased at Thermo Fisher Scientific (Merelbeke, Belgium). Type I rat tail collagen, the chemotaxis transwell system (pore size 5.0 μm) and trypsine were bought at Sigma-Aldrich (Diegem, Belgium). All chemicals were used as provided without further purification.

5.3.3 AZD8797 functionalized PPV-based NPs: synthesis and preparation

Nanoparticle Synthesis. The construction method of CPM-*co*-MDMO-PPV based NPs, a combination of the miniemulsion and solvent evaporation method, was executed as published elsewhere [165]. The amount of copolymer was lowered to 25 mg and surfactant SDS increased to 100 mg in 24 g of ultrapure water. The amount of chloroform was kept the same. After a 1 h pre-emulsification step of the continuous and dispersed phase at 1000 rpm, the mixture was ultrasonicated on ice (1/4"-tip, 3 min, 65 % amplitude, 30 s pulse and 20 s pause regime). This generated nanodroplets of which the organic solvent was subsequently evaporated at 40 °C for 24 h at 500 rpm, resulting in a colored water-based dispersion of CPM-*co*-MDMO-PPV NPs after filtration (Whatman, pore size 4–7 μm) to remove any large aggregates if present. The solid content was determined through thermogravimetric analysis.

Nanoparticle Hydrolysis and washing. The synthesized NPs were incubated for 24 h with 0.5 M NaOH at 10 rpm using an Intelli-Mixer RM-2L shaker, with a resulting solid content of 0.5 %. Following the 24h incubation period, the hydrolyzed CPM-*co*-MDMO-PPV NPs were washed multiple times through centrifugation and redispersion using a Sigma 3-30K centrifuge (Suarlée, Belgium). The first 3 washing steps of 1 h at 14 000 rpm in eps were executed in order to remove the NaOH solution. Following the NaOH extraction, the NPs were washed 40 times for 30 min at 500 rpm with Spectrum™ Spectra/Por 3 Regenerated Cellulose Dialysis Membrane Tubing (3.5 kD, 45 mm flat width) in ultrapure water. The washed sample was filtered through a Filtropur S 0.2 filter.

5.3.4 AZD8797 functionalized PPV-based NPs: functionalization

Stability Test. The CPM-*co*-MDMO-PPV NPs were incubated in various volume fractions of DMSO in H_2O (v/v %: 0.00 %, 3.33 %, 16.67 %, 33.33 %, 66.67 %). The stability was monitored using dynamic light scattering (DLS) with the zetapals equipment (Brookhaven Instrument Cooperation, Waddinxveen, The Netherlands).

EDC/Sulfo-NHS Coupling Reaction. The CPM-*co*-MDMO-PPV NPs were diluted to a solid content of 0.05 % in DMSO/H_2O mixture with a 16.67 v/v % fraction of DMSO and a total volume of 1.5 mL. Subsequently, 2 mixtures with identical volume fractions and total volume of 0.5 mL, one containing 125 *μ*g of EDC and the other 72.5 *μ*g of sulfo-NHS, were added to the NP solution. This colloidal dispersion was incubated for 30 min in the dark at 500 rpm at room temperature after which 1.52 *μ*mol of AZD8797 was added to the dispersion, followed by another 6 h of incubation. The samples were washed with a Spectrum™ Spectra/Por 3 Regenerated Cellulose Dialysis Membrane Tubing (3.5 kD, 45 mm flat width) for 2 days at 500 rpm in the DMSO/H_2O mixture followed by 3 days in H_2O. The solvent was changed every 4 h. The washed NP dispersion was sterilized using an IBL 437C type gamma radiator (Cis Bio International, Codolet, France) at 30 Gy (= 3000 rad) and stored in the dark.

Characterization. The system was characterized before and after functionalization with AZD8797 through DLS, transmission electron microscopy (TEM) and infrared spectroscopy measurements. Size and zetapotential values were determined using DLS. In addition the size and morphology were visualized, drop-casting/drying NPs on copper grids, through TEM at an accelerating voltage of 120 keV using a FEI Tecnai G2 spirit twin (Zaventem, Belgium). TEM data are represented as means ± standard deviation after measuring 150 NPs per sample with ImageJ software. Attenuated total reflection infrared (ATR-IR) spectra were collected using a Tensor 27 FT-IR spectrophotometer (Bruker, Brussels, Belgium). The optical fingerprint was measured in a 1 cm quartz cuvette using the Cary 5000 UV-VIS-NIR spectrophotometer (Agilent Technologies, Diegem, Belgium) and the Jobin Yvon Fluorolog3 Tau fluorescence spectrophotometer (Horiba, Lier, Belgium). The emission spectra were corrected for the wavelength dependence of the throughput and sensitivity of the detection channel.

5.3.5 Influence of AZD8797 NP functionalization on NP uptake by PBMCs

Flow cytometry. Peripheral blood mononuclear cells (PBMC) were isolated from whole blood of healthy donors by density gradient centrifugation (Histopaque; Sigma–Aldrich, St. Louis, MO, USA). Uptake studies of AZD8797-CPM-*co*-MDMO-PPV were performed on PBMCs. Cells were seeded at a density of 2×10^5 cells per well in a 96-well U bottom plate. The following conditions were tested: 75 μg/mL AZD8797-CPM-*co*-MDMO-PPV NPs in culture medium (RPMI-1640, 1 % non-essential amino acids, 1 % sodium pyruvate, 10 % FBS, 50 U/ml penicillin, 50 mg/ml streptomycin), AZD8797-CPM-*co*-MDMO-PPV NPs with cells that underwent a pretreatment with 100 ng/mL fractalkine and AZD8797-CPM-*co*-MDMO-PPV NPs with cells pretreated with 100 ng/mL AZD8797. The pretreatment blocking was performed for 12 h at 37 °C in a 5% CO_2 incubator (Sanyo, Japan). Subsequently the cells were centrifuged for 5 min at 3000 rpm after which 20 μL of the NP solution was added to the cells, which were left to incubate for 4 h in the incubator. The PBMCs were doubled stained 15 min before the end of the incubation period with anti-human CD4 FITC and CD28 APC. Based on these markers, $CD4^+CD28^-$ T cells can be distinguished from $CD4^+CD28^+$ T cells. Monocytes can be distinguished from lymphocytes using their forward and side-scatter characteristics. To remove all unbound fluorophores, the cells were centrifuged 3 times and the pellet was resuspended in fluoresence-activated cell sorting (FACS) buffer (1xPBS and 2 % FCS). The resulting samples were measured and analyzed with the Becton Dickinson LSR Fortessa (Erembodegem, Belgium). A 488 nm laser and 710/50 nm (NPs) as well as 530/30 nm (FITC) emission filter were employed. In addition, a 640 laser and 670/14 (APC) emission filter were used and unlabeled cells were employed as a blank to gate the signal. The amount of cells that contained a fluorescent signal attributed to NP uptake were converted to a percent scale from 0 – 100 %, with 100 % indicating that all cells emitted a fluorescent signal corresponding to NP uptake.

Confocal microscopy. PBMCs were incubated with 75 μg/mL AZD8797-CPM-*co*-MDMO-PPV NPs in culture medium for 4 h at 37 °C and 5 % CO_2. Subsequently, the cells were washed 3 times with 1xPBS at 2000 rpm for 5 min after which they were seeded a poly-L-lysine coated μ-Slide 8-well plate (Ibidi) at a concentration of 5×10^4 cells per well and left to settle for 1 h in the incubator before imaging.

All images were collected using a Zeiss (Zaventem, Belgium) LSM510 META NLO mounted on an inverted laser scanning microscope (Zeiss Axiovert 200 M) and a 40x/1.1 water immersion objective. Excitation of the NPs was performed with a 30 mW air-cooled Argon ion laser (LASOS Lasertechnik GmbH, Germany) emitting at 488 nm (~3 mW maximum radiant power at the sample). Emission was detected using a band-pass filter of 565-615 nm. $CD28^+$ cells were visualized using a 5 mW Helium Neon laser (LASOS Lasertechnik GmbH, Germany) at 633 nm (~3 mW maximum radiant power at the sample) and a band-pass filter of 650-710 nm. The resulting 512x512 images were recorded using a pixel dwell time of 3.20 μs. A fixed pinhole size of 1000 μm was used. Images were processed using AIM 4.2 and ImageJ software.

5.3.6 Influence of AZD8797 NP functionalization on $CD4^+CD28^-$ T-cell migration

PBMCs were stained with anti-human CD4 FITC and CD28 APC, after which $CD4^+$ T-cells were sorted using the FACSAria II (BD Biosciences, Erembodegem, Belgium) with a purity that was routinely higher than 95 %. For the migration assay, a costar transwell system (pore size 5.0 μm) was used. The bottom compartment contained the chemokine fractalkine (CX_3CL1) in chemotaxis buffer (0.5 % BSA/RPMI-1640) at a concentration of 10 ng/mL. In each insert 5×10^5 $CD4^+$ T-cells were seeded and left to migrate for 4 h at 37 °C in 5 % CO_2. The cells were exposed to the following conditions: no pretreatment, pretreatment for 12 h with 75 μg/mL AZD8797-CPM-*co*-MDMO-PPV NPs, with 100 ng/mL AZD8797 and with 100 ng/mL fractalkine. After this 4 h migration period, the total number of cells that migrated to the bottom compartment was counted. Through flow cytometry measurements on the Becton Dickinson LSR Fortessa the percentage of $CD4^+CD28^-$ T-cells in the migrated fraction for each condition was determined. The experiment was performed in duplicate with 1 donor. The chemotactic index of both $CD28^-$ and $CD28^+$ cell populations was calculated as follows: (number of migrated cells with fractalkine)/(number of migrated cells without fractalkine).

5.3.7 Influence of AZD8797 NP functionalization on *in vitro* BBB passage

Construction in vitro blood-brain-barrier. First, the membrane (pore size 3.0 μm) was coated with collagen I by adding 50 μL of 0.01 % working solution to the transwell upper side for 2 h at 37 °C. After this incubation period, the coating solution was removed, the surface was rinsed two times with 1xPBS and the inserts were transferred to a 24-well plate filled with 600 μL of EGM-2-MV culture medium (EBM-2^+ medium supplemented with hydrocortisone, ascorbic acid, vascular endothelial growth factor, human basic fibroblast growth factor, recombinant human insulin-like growth factor-1, human epidermal growth factor, gentamicin, amphotericin-B, and 2.5 % FCS as recommended by the manufacturer). Next, hCMEC/D3 cells (Tébu-Bio, Le Perray-en-Yvelines, France) were harvested with trypsine-EDTA at 37 °C and subsequently washed with 1xPBS. The cell suspension was centrifuged at 1000 g for 10 min and the pellet resuspended in EGM-2-MV culture medium. Cells were counted and 8250 hCMEC/D3 cells in a volume of 50 μL were administered to the upper side of the insert. The cells were left to adhere for 20 min after which 200 μL of EGM-2-MV culture medium was added to the upper compartment and the cultures were grown for 10 - 14 days. From day 3 on the *in vitro* blood-brain-barrier (BBB) cultures were cultivated in EBM-2^+ medium, which was replaced every 3 days.

Characterization in vitro blood-brain-barrier. During the culture period (4, 7, 9 and 10 days), the transendothelial electrical resistance (TEER) was determined using the EVOM-2 voltohmmeter with STX electrodes (World Precision Instruments, Hitchin, Hertfordshire, United Kingdom) to test the integrity of the tight junction dynamics. The measurements were performed in septuplicate and the final TEER value (Ωcm^2) was obtained by subtracting the TEER background signal collected using an empty insert from the mean TEER value measured across the hCMEC/D3 monolayers. To assess the permeability of the in vitro blood-brain-barrier a Cascade Blue-Dextran permeability assay was conducted on day 10. A volume of 250 μL EBM-2^+ medium with a Cascade Blue-Dextran (10 kDa) concentration of 50 μg/mL was added to the upper compartment and the fluorescence recovery in the lower chamber was monitored after 120, 180 and 240 min using the FLUOstar OPTIMA (BMG Labtech, Temse, Belgium) and

expressed as the percentage of fluorescence recovery when compared to the signal of the original concentration. The experiment was performed in triplicate.

Nanoparticle migration over in vitro blood-brain-barrier. To investigate NP migration over the *in vitro* BBB, 25 *μ*g/mL of AZD8797-CPM-*co*-MDMO-PPV NPs in EBM-2^+ medium was added to the upper compartment after 10 days of BBB culture and left to incubate for 24 h. After the incubation period the medium in the bottom compartment was collected and the fluorescent signal measured using the FLUOstar OPTIMA. The NP concentration of the lower compartment was determined using a calibration curve and used to calculate the percentage of NP migration over the *in vitro* BBB.

5.4 Results and discussion

5.4.1 AZD8797 functionalized PPV-based NPs: synthesis, preparation and functionalization

The goal of this study was to design a novel bioimaging probe that could be employed for the labeling of cells that have the fractalkine receptor CX_3CR1 located on their surface and are thought to be crucial in MS disease. Therefore, the exterior of CPM-*co*-MDMO-PPV NPs was functionalized with AZD8797, a selective small-molecule that functions as an allosteric non-competitive modulator of the human CX_3CR1 receptor [227, 229]. AZD8797 has been demonstrated to successfully block the migration of leukocytes in experimental autoimmune encephalomyelitis, an animal model for MS, resulting in reduced inflammation, paralysis and degeneration in the CNS [228]. In addition, the molecule's chemical structure possesses an amine group that allows covalent coupling with the carboxylic acid groups on the surface of the NPs through the EDC/sulfo-NHS technique (Figure 5-1). The amine provides a viable anchoring point as the affinity and selectivity of the molecule is specifically attributed to the eucinol moiety attached to the core-structure in the 7-position together with *a*-methyl branched benzyl derivatives in the 5-position [227].

Most of the time, EDC/sulfo-NHS couplings are performed in water or buffer. However, AZD8797 has very limited to no solubility in solvents other than DMSO. As DMSO is a water-miscible organic solvent and can be used in EDC/sulfo-NHS coupling reactions mixtures, the reaction was executed in a DMSO/H_2O mixture. An additional advantage of using DMSO is that the reaction compounds are much less likely to hydrolyze than when solely dissolved in water. Although the statistical CPM-*co*-MDMO-PPV copolymer is not soluble in DMSO, given its monomer ratios, the stability of the NP system in DMSO/H_2O needed to be evaluated [230]. Therefore, non-functionalized NPs were dispersed in various DMSO/H_2O mixtures and their stability was monitored through DLS measurements (Table 5-1).

Table 5—1: CPM-*co*-MDMO-PPV NP stability in different volume fractions of DMSO in H_2O

DMSO/H_2O	0.00 %	3.33 %	16.67 %	33.33 %	66.67 %
Size (nm)	48.7 (± 10.4) (PDI = 0.080)	55.8 (± 9.6) (PDI = 0.058)	56.0 (± 12.5) (PDI = 0.086)	67.9 (± 17.6) (PDI = 0.111)	100.5 (± 27.1) (PDI = 0.119)

The system remained stable up until 33.33 v/v% of DMSO in H_2O, as indicated by the steady hydrodynamic radius values and low polydispersity index (PDI). Once this threshold was reached, the NP size and PDI values started increasing, indicating system destabilization. Therefore, the coupling reaction was performed with a 33.33 v/v% DMSO/H_2O mixture, given the stability of the CPM-*co*-MDMO-PPV NPs. An additional advantage of employing this v/v% mixture is the fact that it has a pH value of 7.4, making it ideal for the EDC/sulfo-NHS reaction [231].

Following functionalization with AZD8797, the effect on the colloidal properties was characterized (Table 5-2). The NP constructs upheld their stability throughout the coupling reaction and subsequent washing steps, as demonstrated by the obtained DLS and TEM values (Figure 5-2 and 5-3). The TEM images also highlight that the integrity of the spherical morphology was kept intact. The NP aggregation is due to surface dewetting and the 'coffee-ring effect', which occur after drop-casting the NP sample onto the TEM grid. The optical fingerprint remained unaltered after functionalization except for the occurrence of a small blue shift in both the absorption and emission maximum (Figure 5-4). The presence of AZD8797 on the NP surface was confirmed by a drop in zetapotential from -53 to -36 mV upon functionalization, a consequence of the disappearance of the negatively charged carboxylic acid groups.

Table 5—2: CPM-*co*-MDMO-PPV and AZD8797-CPM-*co*-MDMO-PPV NP characteristics

	Size (nm)	Zeta (mV)	λ_{ex} (nm)	λ_{em} (nm)
CPM-*co*-MDMO-PPV	41.5 (± 11.5)	-52.92	483	588
AZD8797-CPM-*co*-MDMO-PPV	43.9 (± 20.3)	-36.02	475	585

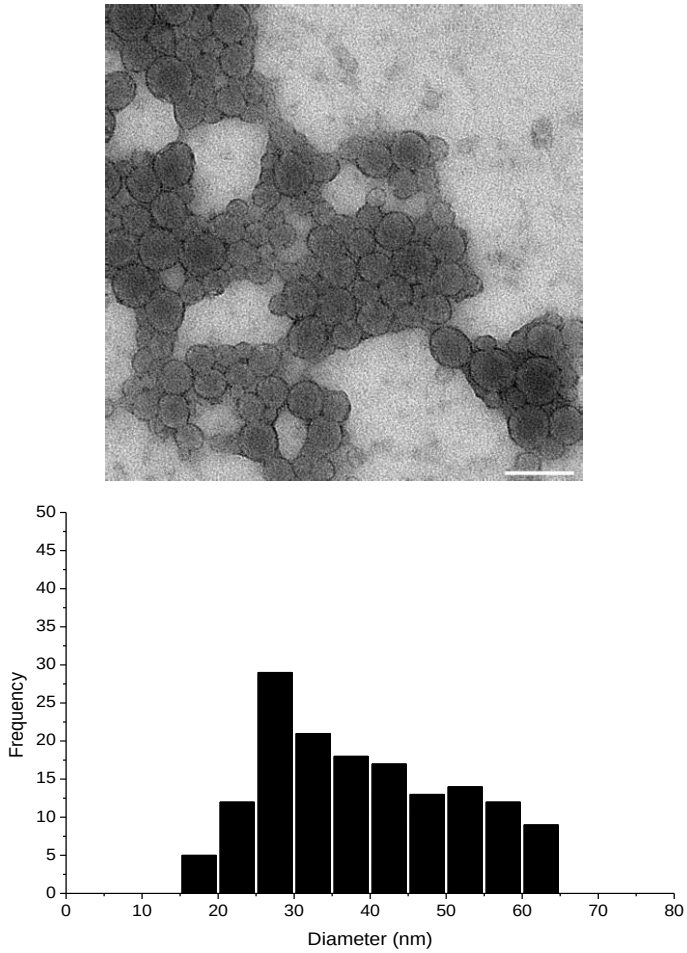

Figure 5—2: TEM image of CPM-*co*-MDMO-PPV NPs and its respective size distribution.

TEM image of CPM-*co*-MDMO-PPV NPs (top, scale bar represents 100 nm) and its respective size distribution (bottom, data obtained by measuring 150 NPs).

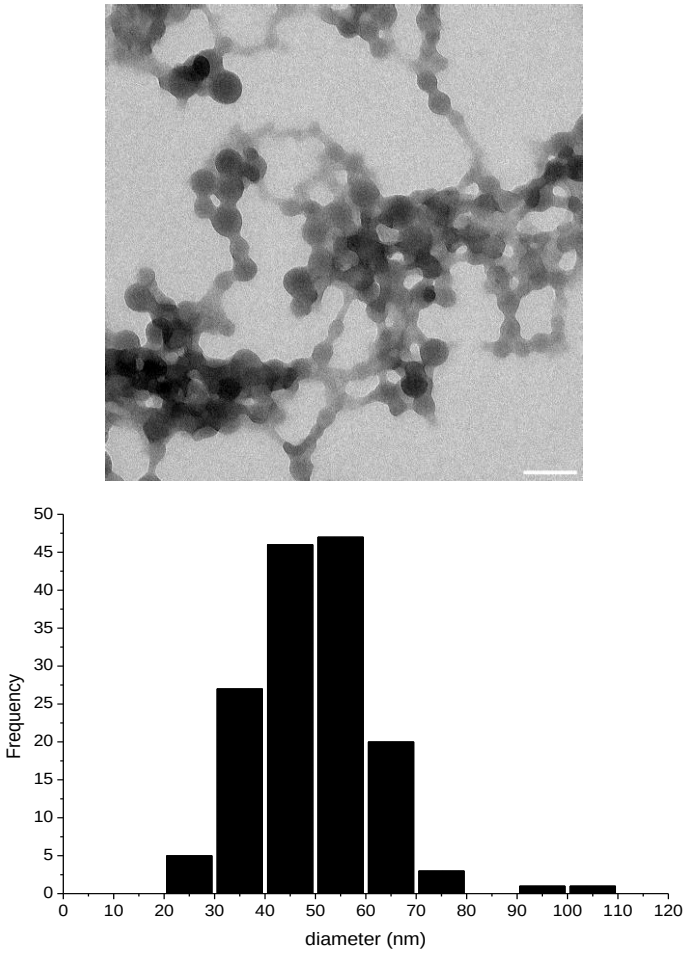

Figure 5—3: TEM image of AZD8797-CPM-*co*-MDMO-PPV NPs and its respective size distribution.

TEM image of AZD8797-CPM-*co*-MDMO-PPV NPs (top, scale bar represents 100 nm) and its respective size distribution (bottom, data obtained by measuring 150 NPs).

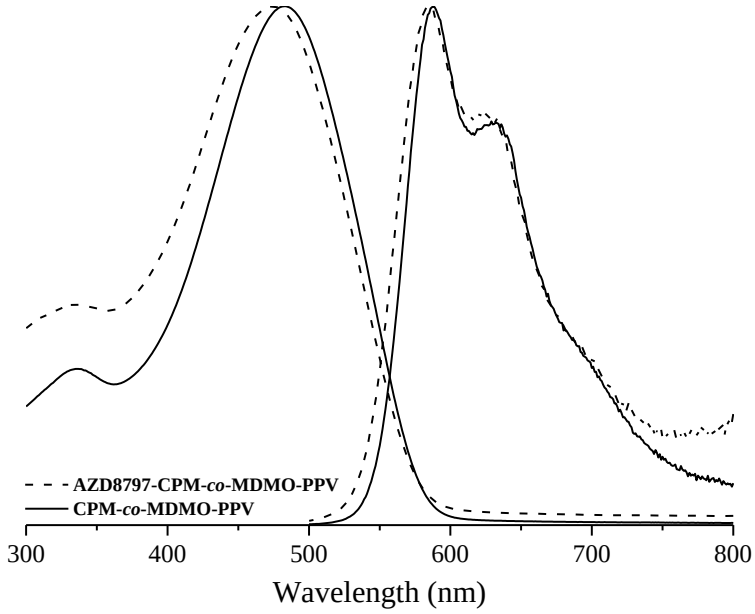

Figure 5—4: Fingerprint of CPM-*co*-MDMO-PPV and AZD8797-CPM-*co*-MDMO-PPV NPs.

Optical spectra of absorbance (left) and emission (right) CPM-*co*-MDMO-PPV (solid line) and AZD8797-CPM-*co*-MDMO-PPV (dashed line) water-based NP dispersions.

To further demonstrate that the covalent immobilization of AZD8797 onto the NP surface was successful, infrared spectroscopy was performed (Figure 5-5). Following grafting, the C-O stretching peak of carboxylic acid at 1240 cm^{-1} disappeared almost completely, although the presence of the C=O band at 1730 cm^{-1} indicates that there is still a remainder of carboxylic acids left on the surface [232]. The amide I peak at 1640 cm^{-1} and amide II shoulder at 1590 cm^{-1} increased in intensity, confirming the formation of amide bonds. The amide I band corresponds to the stretching vibrations of C=O (80 %), while the amide II band is correlated to N-H bending (60 %) and C-N stretching vibrations (40 %) [188]. In addition to amide bond formation, the increase in intensity of several other peaks demonstrates the presence of AZD8797 on the surface of the CPM-*co*-MDMO-PPV NPs. The peak at 1470 cm^{-1} can be correlated to the asymmetrical bending vibration of the methyl group of AZD8797 and the peak at 1380 cm^{-1} to its symmetrical bending vibration [232]. The increase in both peaks is also caused by the isopropyl group, which has a symmetric deformation doublet at 1380 and

1360 cm^{-1} and asymmetrical deformation at 1470 cm^{-1} [233]. The increase in the intensity of the peak at 1080 cm^{-1} is the C-N stretching band of the secondary amine, which also contributes to the amide peak shoulder due its N–H bending band at 1615 cm^{-1} [232]. None of these peaks showed overlap with the reaction components EDC and sulfo-NHS or with the surfactant SDS (Figure 4-5 to 4-7).

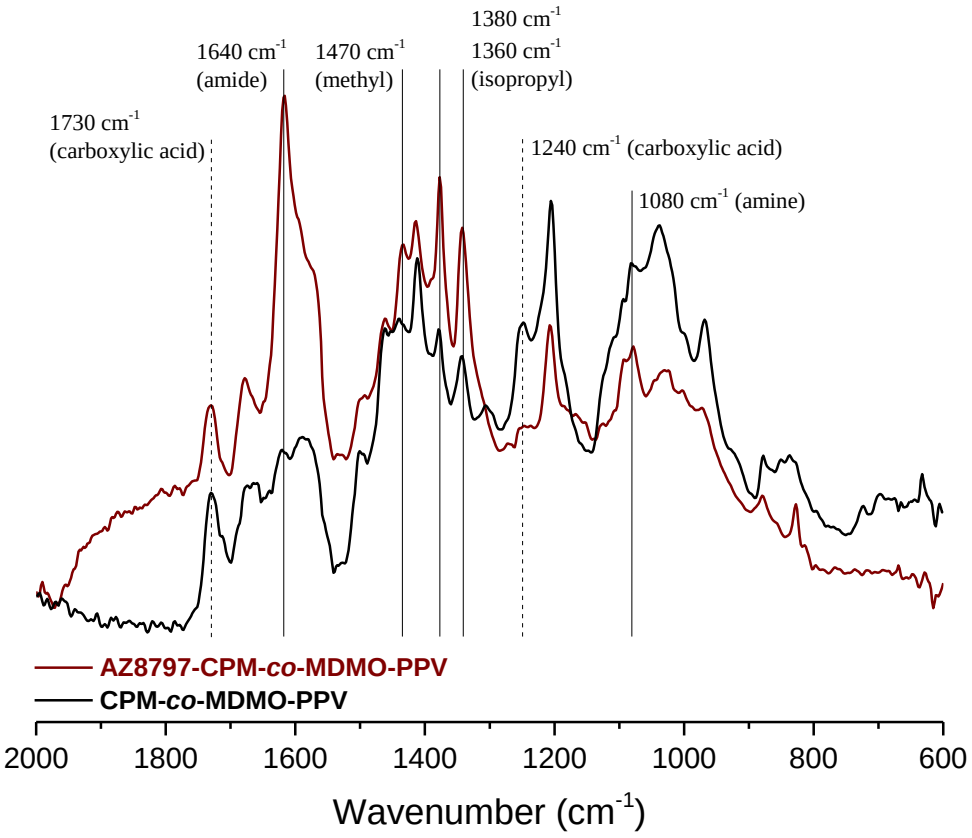

Figure 5—5: FTIR spectrum of CPM-*co*-MDMO-PPV and AZD8797-CPM-*co*-MDMO-PPV NPs.

FTIR spectrum of CPM-*co*-MDMO-PPV (black) and AZD8797-CPM-*co*-MDMO-PPV (red) nanoparticles.

5.4.2 Influence of AZD8797 NP functionalization on NP uptake by PBMCs

As the coupling of AZD8797 proved to be successful, its potential as a bioimaging probe for CX_3CR1^+ cells was investigated. For this, the NP uptake after an incubation period of 4 h was monitored in PBMCs (Figure 5-6). The human PBMC population mainly consists of lymphocytes (70 - 90 %), monocytes (10 - 30 %) and dendritic cells (1 - 2 %) [234]. The lymphocytes can be subdivided into $CD3^+$ T-cells (70 - 85 %), B-cells (5 - 10 %) and NK-cells (5 - 20 %). The $CD3^+$ T-cells are composed of $CD4^+$ and $CD8^+$ T-cells. For the uptake experiments three cell types from the PBMC population were monitored, namely $CD4^+CD28^-$ T-cells, $CD4^+CD28^+$ T-cells and monocytes. Both monocytes and $CD4^+CD28^-$ T-cells possess CX_3CR1, while $CD4^+CD28^+$ T-cells only have a very low expression of the receptor. The difference between the former two lays in the rate of uptake, as monocytes take up NPs more easily than T-cells [235].

Through the use of these cell types, it can be demonstrated that functionalization with AZD8797 evokes NP uptake in CX_3CR1^+ cells. For the $CD4^+$ T-cells a difference in uptake was monitored between the CX_3CR1^- and CX_3CR1^+ population, namely 1.2 (± 0.5) and 4.8 (± 3.9) % respectively. Given the extensive washing steps and lack of NP fluorescent signal on the exterior of the cells in confocal images (Figure 5-7) it can be concluded that the NPs are most likely internalized rather than bound onto the cell surface. The low uptake of NPs can be attributed to the inherent nature of T-cells [235]. No significant difference was observed for the mean values between the different cell population conditions, yet a trend of decrease is visible when blocking with AZD8797 or fractalkine. The former is due to the high variation between the initial uptake percentages of the different donors (ranging between 2.2 and 9.2 %). When looking at the normalized donor values individually (Figure 5-6), uptake through CX_3CR1^+ is showcased more clearly as a 25 % decrease was observed for donor 2 and 50 % decrease for donor 1 and 3 after blocking with AZD8797. The same pattern was observed for donor 1 when blocking with fractalkine but not for donors 2 and 3, which only experienced a lowering of 4–10 %. A similar drop of approximately 50 % was observed when incubating at 4 °C, indicating that the uptake occurs through an energy-dependent active process as these are inhibited at low temperature [236]. For $CD28^+$ cells

blocking appeared to have no effect at all as the uptake remained 1 % for all conditions.

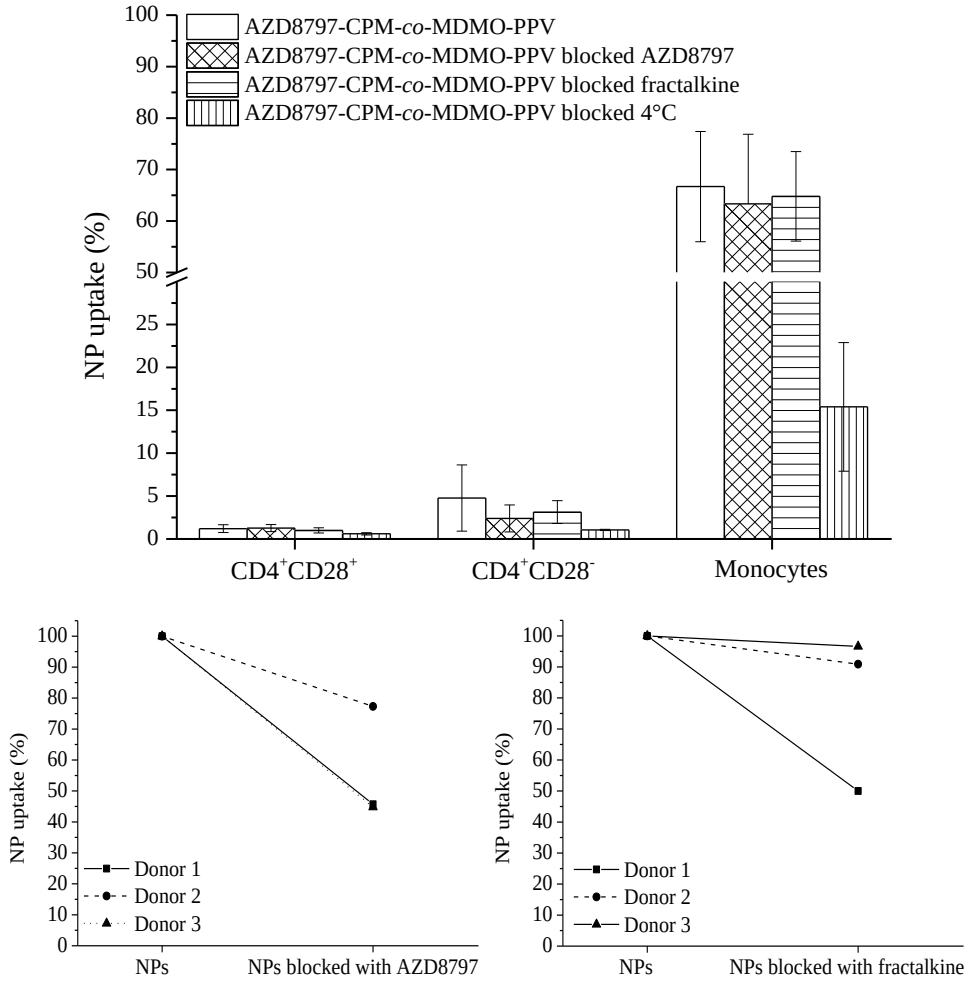

Figure 5—6: Internalization of AZD8797-CPM-*co*-MDMO-PPV NPs by PBMCs.

Internalization of 75 μg/mL AZD8797-CPM-*co*-MDMO-PPV NPs by the PBMC population over a time period of 4 h with and without blocking by AZD8797 and fractalkine (top): Data are expressed as percent of control mean ± SD (N = 3) with % being the number of cells that contain nanoparticles. Normalized internalization of 75 μg/mL AZD8797-CPM-*co*-MDMO-PPV NPs by $CD4^+CD28^-$ T-cells (bottom) over a time period of 4 h with and without AZD8797 (left) and fractalkine (right) blocking for individual donors.

Monocytes showed 66.7 (± 10.7) % uptake of AZD8797-CPM-*co*-MDMO-PPV NPs, which decreases with approximately 3.0 – 3.5 % after the inhibition pretreatment. This demonstrates that both cell types take up AZD8797 functionalized NPs at least partly through the fractalkine receptor. However, where uptake appeared to take largely place *via* this pathway for $CD28^-$ T-cells, this is not the case for monocytes. Internalization can also be attributed to the monocytes natural endocytotic activities, resulting in them being very efficient at NP internalization. Given their reputation as professional phagocytes [237], NPs are taken up through various other routes. Additional functionalization with for example stealth molecules like polyethylene glycol might prove useful to block the internalization routes other than that of the fractalkine receptor or endocytosis could be blocked to truly create a target specific bioimaging probe. Also here, NP internalization at 4 °C showed a drastic decrease in uptake. This experiment nicely demonstrates that functionalizing CPM-*co*-MDMO-PPV NPs with AZD8797 enables uptake by CX_3CR1^+ cells. This was also confirmed visually through confocal microscopy, which clearly showcases the uptake of NPs by the CX_3CR1^+ $CD28^-$ cells (Figure 5-7).

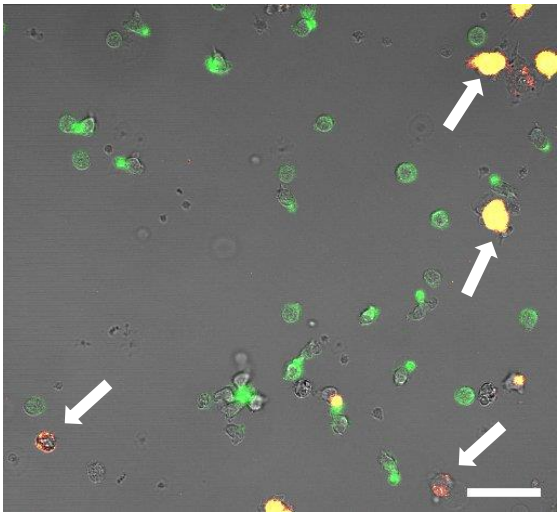

Figure 5—7: Confocal microscopy image of AZD8797-CPM-*co*-MDMO-PPV NPs uptake by PBMCs.

Confocal microscopy image of AZD8797-CPM-*co*-MDMO-PPV NPs (red) uptake (arrow) by PBMCs after a 4 h incubation period, with additional staining of $CD28^+$ cells (green, CX_3CR1^- cells). The scale bar represents 30 μm.

5.4.3 Influence of AZD8797 NP functionalization on $CD4^+CD28^-$ T-cell migration

In order to investigate whether AZD8797-CPM-*co*-MDMO-PPV NPs are not functional bioimaging probes but also retain their antagonist features, a chemotaxis assay was executed on $CD4^+$ T-cells with the focus lying on the CX_3CR1^+ $CD4^+CD28^-$ cells (Figure 5-8).

When no fractalkine is present in the bottom compartment a baseline migration of approximately 1.6 (± 0.1) % of $CD4^+CD28^-$ cells occurs in a time period of 4 h. However, when the chemokine is added, the cells are attracted and migration undergoes a twelvefold increase to 19.5 (± 0.4) %. When the cells are pretreated overnight with the designed NP construct, an 82 % drop in fractalkine-induced migration occurs to 3.6 (± 0.2) %.

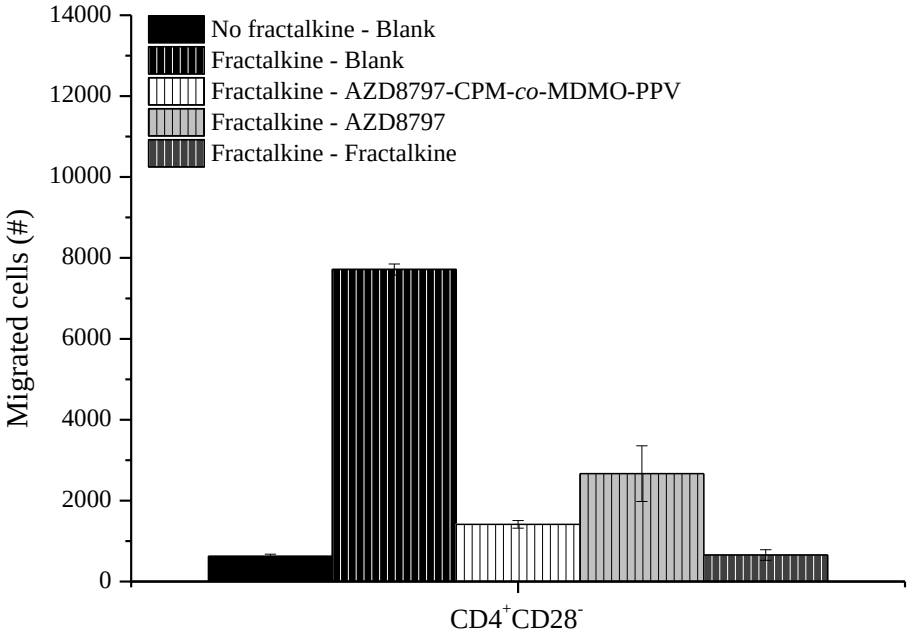

Figure 5—8: Chemotaxis assay of $CD4^+CD28-$ T-cells exposed to various conditions. Chemotaxis assay of $CD4^+CD28-$ T-cells with and without pre-incubation with AZD8797-CPM-*co*-MDMO-PPV NPs, AZD8797 and fractalkine for a time period of 12 h.

This is also reflected in the chemotactic index, which is the number of migrated cells with fractalkine in the bottom compartment divided by the number of

migrated cells without fractalkine [214]. For cells that only express CX_3CR1 in very low quantities like $CD28^+$ T-cells the chemotactic index almost did not change from 2.6 (± 0.6) to 1.2 (± 0.1). Values around 1 indicate a lack of difference in the migration of the cell population regardless of the presence of a fractalkine gradient. For $CD28^-$ cells, which show a high expression of the receptor, a significant drop in the chemotactic index from 12.4 (± 0.8) to 3.3 (± 0.0) was observed. This clearly demonstrates the theranostic potential of the NP construct as it co-delivers therapeutic and imaging functions without reducing efficacy. It allows for visualization to occur not only before or after treatment regimen but also during, providing an additional benefit compared to the sole use of the antagonist as it enables a rapid evaluation of the treatment method.

The same effect was observed when the cells were pretreated with fractalkine or AZD8797, though the effect appears to be more pronounced for fractalkine. This can be attributed to the fact that the agonist only binds to the high-affinity active conformation of the receptor while the antagonist binds to both the inactive low-affinity and active high-affinity forms, therefore diluting its effect [229].

5.4.4 Influence of AZD8797 NP functionalization on *in vitro* BBB passage

Various CX_3CR1^+ cell populations of interest, like microglia, reside within the CNS. In order to target these the AZD8797-CPM-*co*-MDMO-PPV NP construct needs to be able to cross the impermeable BBB, which protective role enables the neural microenvironment that is crucial for healthy brain functioning. Therefore, the transport capacity of the NPs through the BBB was investigated using the well-established hCMEC/D3 *in vitro* BBB model with transwell inserts. To assess the barrier integrity of the constructed *in vitro* BBB, TEER measurements were performed (Figure 5-9) [238].

TEER is conducted by measuring the electrical resistance across the formed cellular monolayer and has gained the reputation of being a very reliable and sensitive method to assess the integrity as well as permeability of the *in vitro BBB*. It reflects the ionic conductance of the paracellular pathway and pore size of the tight junctions in the epithelial monolayer. During the growth of the *in vitro* BBB the TEER value gradually increased up until day 9 where it reached a plateau

around 25 Ωcm^2, which is in accordance to literature for static culture conditions and indicates the model being confluent [239, 240].

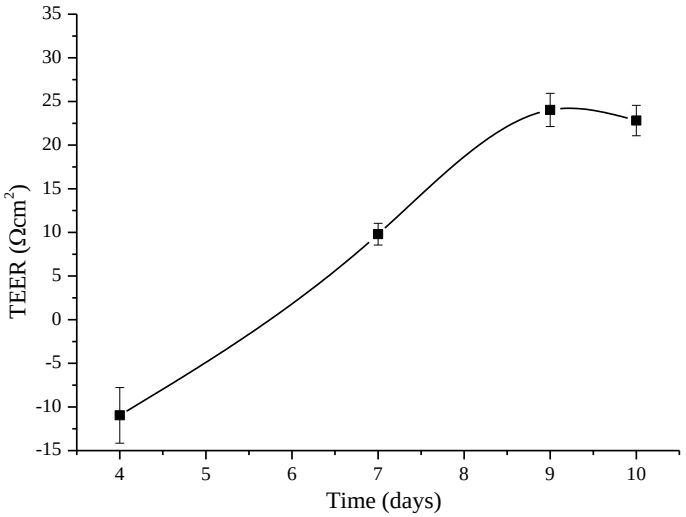

Figure 5—9: Time-dependent evolution of the TEER value of *in vitro* BBB.

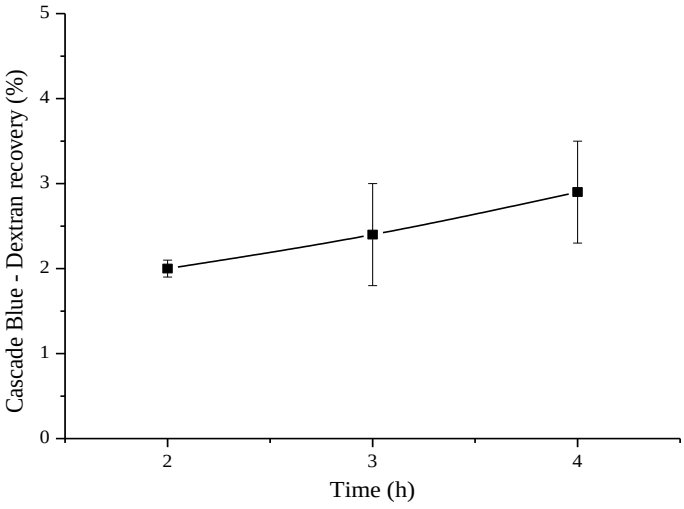

Figure 5—10: Time-dependent Cascade Blue-Dextran transport over the *in vitro* BBB.

Time dependent Cascade Blue-Dextran transport over the *in vitro* BB with data expressed as the percentage of Cascade Blue-Dextran recovery.

To confirm the poor paracellular permeability of external constructs through the barrier the tracer molecule Cascade Blue-Dextran (10 kDa) was used (Figure 5-10). For a healthy BBB a low value of around 2 % of dextran transport is expected, as was the case for the constructed *in vitro* BBB [239]. The combination of these two methods validates the use of this model to study the migration of NPs across the BBB through transcellular pathways.

Subsequently, the *in vitro* BBB was exposed to NPs for a 24h duration, after which the migration of NPs was measured. Of the starting amount of AZD8797-CPM-*co*-MDMO-PPV NPs, on average 20 (± 16.6) % was transported across the *in vitro* BBB. It shows that the constructed NPs are passing through the cells and excreted onto the other side of the barrier. Taken together, these data clearly demonstrate the applicability of AZD8797 functionalized CPM-*co*-MDMO-PPV NPs for the specific imaging of CX_3CR1^+ cells, even when they are residing inside the CNS behind a closed BBB.

5.5 Conclusion

In this study functional CPM-*co*-MDMO-PPV NPs with a 40 nm size range were successfully functionalized with the allosteric non-competitive CX_3CR1 modulator AZD8797. This feature was achieved by taking advantage of the alkoxy side chain moieties present on the NP surface for an EDC/sulfo-NHS coupling reaction, generating a bioimaging probe capable of targeting CX_3CR1^+ cells. Surface grafting did not seem to alter the inherent characteristics of the fluorophore, as it only slightly increased the hydrodynamic radius and had no significant adverse effects on its optical fingerprint. The NPs demonstrated uptake by the CX_3CR1^+ cells within the PBMC population, namely $CD4^+CD28^-$ T-cells and monocytes. This was confirmed by a trend of a decrease in uptake, especially for the T-cells when looking at the different donors separately, through the CX_3CR1 pathway by pre-incubation with blocking agents fractalkine and AZD8797. It should be noted that the NPs also underwent non-specific uptake through other active processes, which was most pronounced for monocytes given their innate phagocytosis behavior. A characteristic that was confirmed by the partial inhibition of NP uptake through energy-dependent pathways at 4 °C. Confocal microscopy provided an additional visual conformation of NP uptake by the CX_3CR1^+ $CD28^-$ cells of the PBMC population. Not only is this NP construct a viable candidate for targeting cell populations as a bioimaging probe, the antagonistic functioning of AZD8797 was kept intact as demonstrated by the chemotaxis assay. Incubation of $CD4^+CD28^-$ T-cells drastically diminished their migration response towards the chemokine fractalkine. In addition the ability of AZD8797 functionalized NPs to cross the BBB to potentially target CX_3CR1^+ cells residing in our brain was investigated using an *in vitro* BBB model. After an incubation period of 24 h, 20 % of the NPs were able to migrate through the barrier using transcellular pathways. This study highlights the potential of functional PPV-derivatives for the design of advanced NP constructs for biomedical applications.

Additional research can further strengthen the results described above. A better insight into the amount of antagonist present on the surface will provide more information on the efficiency of the coupling as well as antagonistic properties of the probe. Also, additional functionalization with PEG might prove useful for blocking NP uptake through unwanted routes, making the probe truly target-

specific. With regard to uptake, the selective inhibition of uptake routes can result in a better understanding of the pathways through which the NPs are internalized. For the uptake and chemotaxis assays, more repetitions are needed given high donor variation. Also, additional *in vitro* BBB experiments, namely more repetitions as well as tests on an inflamed BBB, will result in a better understanding of the potential of this novel bioimaging probe.

Chapter 6
General summary and outlook

Disclaimer: The summary provided in this chapter gives a general overview of the work described in this dissertation for people outside of the field. Technical abstracts of the experimental work can be found at the beginning of each individual chapter.

6.1 Can a PPV-based bioimaging probe with inherent surface functionalities be designed

As a scientist, we possess a deep-seeded insatiable desire to explore and expand our knowledge of everything that revolves around our pale blue dot. However, in order to navigate in uncharted territories, the right contraptions are required. One particular novelty, called fluorescence microscopy, has bestowed researchers with a new set of eyes to observe biological entities with. It has truly revolutionized our understanding of the subtle nuances that occur at the cellular level and their implications on our daily lives.

A key component of the technique, which dictates its effectiveness, is the fluorophore. During the preceding decades, numerous innovative designs have been conceived that have pushed the applicability of fluorescence microscopy to unprecedented levels. From organic dyes and fluorescent proteins to NP constructs such as dye loaded nanospheres and quantum dots, each system carries its own advantages and drawbacks (*vide supra*, chapter 1).

Science has showcased on countless occasions that it is a process that cultivates continuous innovation. On its never-ending quest to push the boundaries of human knowledge, conjugated polymer NPs were introduced as a novel fluorescent probes. They quickly rose through the ranks as they featured various prominent characteristics, such as an outstanding fluorescent signal and non-toxicological behavior. As a result this state-of-the-art bioimaging probe has been highly requested to serve as an imaging tool for advanced biomedical applications.

Amongst the wide array of conjugated polymers, PPV has been revered ever since it first synthesis. It is placed in high regard, which has led to its status of being one of the most thoroughly investigated conjugated polymers to date, both in- and outside of the bioimaging field. Thanks to this excellent reputation, PPV and its derivatives have been exploited to investigate the working mechanisms of conjugated polymer NPs. They even became the model system to which all other conjugated polymer NPs are compared as well as one of the preferred materials to create advance architectures with.

Nonetheless, when carefully examining literature, it became clear that despite extensive research within the field, an essential feature is still lacking in the design of PPV-based NPs. This critical flaw is the absence of inherent surface groups that could serve as an anchoring point for functional moieties, which are essential when executing complex undertakings in the field of biomedical sciences. In order to close this crucial gap, this dissertation focused on the research question if functional group bearing PPV-based fluorophores can be generated *in situ*, striving to make the current need for tedious post-synthesis modifications and surface adsorbed molecules a deficit of the past.

6.2 The strength of interdisciplinary research

To confront the aforesaid daunting research question, the boundaries of conventional disciplines needed to be obliterated as only highly interdisciplinary research can provide a resolution. Hence, this dissertation is the outcome of a fruitful collaboration between various research groups at Hasselt University and a '*shining*' example of how interdisciplinary research pays off.

As detailed in chapter 2, for the first time ever, a 100 nm-sized fluorophore that contains functional groups on its surface was constructed using the miniemulsion and solvent evaporation method. More specifically, preexisting in-house knowledge regarding the synthesis of complex PPV-architectures was utilized to construct a high-MW functional PPV-copolymer, namely CPM-*co*-MDMO-PPV, which served as the core material. Its unique selling point is the polar group present on the alkoxy side chain, which allows for the *in situ* manufacturing of fluorescent NPs that bear functional groups on their surface. These functional groups provide the opportunity to attach biological or chemical moieties onto the NPs, as demonstrated in chapter 2 by the successful coupling of antibodies. In chapter 4 and 5, this feature received an in-depth investigation. Given the contemporary nature of the design, a homopolymer NP system consisting of MDMO-PPV was synthesized to serve as a point of comparison, a *modus operandi* that was also extended to chapter 3 and 4.

An extensive look at the optical properties of the newfangled fluorophore in chapter 2 disclosed that the functional copolymer system behaves in a matter similar to that of the homopolymer and other PPV-based NPs. The characteristic red shift that occurs upon NP formulation resulted in a fluorescence fingerprint with 500 nm and 590 nm excitation and emission maxima, respectively. The fluorophore also exhibited a distinctive fluorescence brightness as well as excellent photostability.

As the field still resides in its juvenescent stage, not much data is readily available about the interaction between PPV-based NPs and their biological environment. Moreover, this is even non-existent for functional PPVs. Until this day, the research emphasis has predominantly lain on the development of various synthesis routes and investigation of inherent material characteristics. Therefore, chapter 2 did not only focus on the optimization of the NP synthesis process and study of photophysical properties but also on the yet unexplored biological characteristics of PPV-based bioimaging probes. Given the vast interest for fluorophores that are capable to counter the epidemic of neurodegenerative diseases, all cell studies in the dissertation were conducted on cells lines correlated to the central nervous system (CNS). No cytotoxicity was observed and cells took up the NPs successfully, with the rate depending on their surface charge. The results presented in chapter 2 nicely highlight that functional PPVs are excellent applicants to serve as a core material of fluorophores.

6.3 Decreasing the size of functional PPV-based NPs does not diminish their strength as a fluorophore

A decisive feature that requires to be taken into consideration when designing NP bioimaging probes for biomedical goals is their size. The dimension of a fluorophore can affect its photophysical properties and play a key role in various mechanisms like cellular uptake, biodistribution, crossing barriers and cytotoxicity. Therefore, chapter 3 concentrated on the potential implication of size adaptations in functional PPV-based NPs.

The NP diameter was conveniently lowered by a systematic reduction of the polymer content from 50 to 5 mg in the formulation process. By curtailing the amount of CPM-*co*-MDMO-PPV the size could be cut down to 20 nm, showcasing the versatility of the employed synthesis method. The scaling down process did not appear to have an adverse effect on the optical properties overall, except for the anticipated lowering of the molar extinction coefficient. However, a threshold for this method was documented with regard to the photophysical properties, as decreasing the amount of polymer below 5 mg induced irreversible changes in the polymer backbone conjugation length. No upsurge in cytotoxicity was documented for smaller NPs, yet they did cause a transition in the rate and amount of NP uptake. With these conclusions, chapter 3 established the flexibility of the synthesis process of functional PPV-based NPs as well as their robustness when exposed to dimensional adjustments that are required for various biomedical applications.

6.4 Functional PPV-based NPs can be made invisible

Already in chapter 2, gold-labeled antibodies were coupled onto the NP surface. However, an in-depth understanding of the many nuances of the coupling process or its implications was still lacking. Therefore, chapter 4 focused on the modification of the surface with PEG-chains of different MW, in order to provide answers for these uncertainties. PEG was selected in virtue of its excellent reputation as a FDA-approved stealth molecule. Coverage of the NPs with PEG allows for them to become invisible, resulting in more NP reaching their target site.

The coupling operation was preceded by the optimization of the hydrolysis procedure. In only 6 h, all ester groups were converted to carboxylic acids, required for the EDC/sulfo-NHS coupling with amine-terminated PEG chains. High density grafting was achieved and resulted in successful blocking of protein corona formation and cellular uptake. No unfavorable side effects were observed upon surface coverage concerning the intrinsic properties of the fluorophore. With these results, chapter 4 reinforced and permanently cemented the position of *in situ* generated functional PPV-based NPs within the bioimaging field.

6.5 A functional PPV-based fluorophore designed for MS research

Within chapter 2 to 4, the potential of functional PPVs to construct NP bioimaging probes has been firmly established. Therefore, in the final chapter, the novel fluorophore was put to the test.

Chapter 5 revolved around the manufacturing of a bioimaging probe that can aid in unraveling the working mechanisms of multiple sclerosis (MS). The functional moieties of 50 nm sized CPM-*co*-MDMO-PPV NPs were used to firmly anchor the fractalkine receptor (CX3CR1) antagonist AZD8797 onto their surface. This brought about a fluorophore-directed against $CX3CR1^+$ cells, like $CD4^+CD28^-$ T-cells, which have been associated with the progression of MS.

Using this probe, $CX3CR1^+$ cells were successfully targeted within the peripheral blood mononuclear cell population. In addition to this, the antagonistic behavior of the attached molecule remained intact as migration of $CD4^+CD28^-$ T-cells towards a fractalkine gradient was severely inhibited when treated with NPs. The NPs also showcased their potential for crossing the formidable blood-brain-barrier using transcellular pathways. This allows for the labeling of $CX3CR1^+$ cells within the CNS, such as microglia, if required. With this final chapter no doubt remains that functional PPVs are an excellent choice to serve as advanced bioimaging probes designed for biomedical research.

6.6 Always question, always wonder

When your 4 years are over, every PhD student wonders: Have I made an impact, are there things that I could have done better or what would I still like to do if there was more time left on the clock? During my journey I was able to labor in the amazing, brand-new field of conjugated polymer NPs designed for bioimaging. When I hit the road, a major hurdle for conjugated polymers NPs was the lack of functional groups available on their surface. Therefore the aim of my dissertation was to pioneer a new area in order to solve this problem. We designed a state-of-the art bioimaging probe based on a functional PPV-copolymer, thereby overcoming this hurdle. But the past is a place of reference and not a place of residence. As scientist we need to look forward, journey on the road ahead.

Gandalf the white once said "End? No, the journey does not end here". Therefore, the following section will illustrate on how this road ahead might look like.

In chapter 2 to 4, the aptitude of using functional PPV-copolymer as the groundwork for a nano-sized bioimaging probe was demonstrated and subsequently culminated in chapter 5 in the target specific fluorophore for MS research. However, a concern that can be raised when working with PPVs is their position compared to other, more recently developed, conjugated polymers when it comes to optical performance. Though they still outclass most standard fluorophores, they could indeed benefit from an increased quantum yield and emission in the (near/far) infrared (NIR) region. One way to achieve this for functional PPVs is to switch the monomer units used to construct the polymer backbone with. Instead of MDMO-PPV, a copolymer system could be manufactured with CN-PPV, which possesses the requested high quantum yield and NIR emission. As acknowledged in chapter 1, CN-PPV has already been employed for high-end imaging applications like *in vivo* visualization and super resolution microscopy. Currently, research within the group is being conducted on the design of this copolymer system as well as others, which could be tested in the future. A second solution could be to combine the functional PPV-copolymer with other materials and create blended nanoparticles. This popular approach has already seen extensive use in the bioimaging field to increase quantum yield and generate NIR emission. With these resolutions, the stated setbacks can be easily overcome without much effort.

It was already briefly touched upon in chapter 2, but it could be interesting to test different PPVs with a wide variety of side chain moieties. Through dicyclohexylcarbodiimide/4-dimethyl-aminopyridine post-polymerization functionalization, the side chain ester moiety can be easily exchanged for another polar group. For example, propargyl groups provide a very interesting alternative as they grant the ability to perform orthogonal conjugation reactions, also known as click reactions. Not only would this open up doors to an exciting new range of functionalities, it would also help us gain more insight into how the functional side chain moiety influences the fluorophore. In chapter 3 the observation was already made that the hydrophilic nature of the copolymer can influence its chain packing during NP formation. In addition to this, another colleague working on poly(p-

phenylene ethynylene) based NPs discovered monitored the influence of the side chain on the photophysical properties.

To stay on the topic of photophysical properties, although great efforts have been made over the last decades to document the various properties of PPV-based systems, those of functional PPV-copolymers still remain a large mystery. With chapter 2 to 4 we boldly went where no scientist had gone before. However, a more thorough investigation into matter such as the exciton dynamics for these NPs and packing conformation would be interesting. The obtained data could then be taken into consideration when designing new functional PPVs NPs.

Chapter 5 proved to be a nice closure for this thesis as it showcased that the possibilities with functional PPVs are only limited by our own imagination. However, despite all the excellent results of the pilot study for the designed MS bioimaging probe, there is still some room left for improvement. A first point of consideration would be to get rid of the non-receptor induced uptake, which was especially apparent in phagocytic cells. This could prove to be problematic when our immune system comes into play. A possible solution was already revealed in chapter 4, as PEGylation induces a stealth effect. A bifunctional PEG-chain could be employed to cover the surface and simultaneously bind to the antagonist. Researchers often use this strategy, but instead in those cases PEG is used as a surfactant rather than covalently anchored to the surface. With this novel design, a follow-up study that takes a closer look at various *in vitro* (such as cytotoxicity, immunogenicity, BBB passage and cell specific targeting in murine brain slice cultures and post mortem MS material) and *in vivo* properties (like plasma stability, biodistribution and selective cell targeting in the CNS) would be interesting. A second concern is the antagonistic property of the targeting molecule. The probe could provide a better understanding into how fractalkine induced behavior plays a role in the development of MS for these cell populations, but cannot be used to study normal behavior in a living environment. Also, with the current design no differentiation can be made between different CX_3CR1 bearing cells (namely microglia versus $CD4^+CD28^-$ T-cells). Co-localization with other immunofluorescent dyes that target major CNS cell type populations (Iba-1: microglia, CC1: oligodendrocytes, GFAP: astrocytes and CD4/CX3CR1: cytotoxic CD4 T cells) could provide a solution. However, publications are released

every day and given the design flexibility of the system, a switch to a newly discovered molecule or more selective marker can be easily made. For example, another interesting avenue to monitor disease activity in the CNS is to visualize pathogenic phagocytes involved in MS disease, which can be targeted through sialoadhesin (CD169) by functionalization with a sialic acid like N-acetylneuraminic acid.

What makes a system as created in this dissertation so interesting for studying diseases such as MS is that it can be employed behind a closed BBB. Most imaging techniques used are only valuable during the early active stages of the disease when the BBB is leaky. In addition, a functional PPV-based bioimaging probe can also significantly contribute to a better and more accurate understanding of progressive MS, which remains to date a still largely untreated subpopulation. In case of a low BBB penetration co-functionalization with peptides (TAT, angiopeps), endogenous molecules (apolipoprotein A, transferrin) or certain surfactants (polysorbate-80) can provide a solution.

With this last outlook I would like to conclude my dissertation. It has been an exciting and intensive 4 years with lots of scientific discoveries and I am truly looking forward to the novelties that lie ahead for this field.

"And now we take the first step, and move forward"

Nederlandse samenvatting

Wetenschappers bezitten een diepgewortelde en onverzadigbare drang naar het vergaren van nieuwe inzichten over alles wat er rondom ons afspeelt op onze kleine blauwe stip. Echter enkel wanneer ze over de juiste wetenschappelijk uitrusting beschikken kunnen ze hun vele ontdekkingstochten tot een goed einde brengen. Een bewonderenswaardig voorbeeld van zo een werktuig is de fluorescentie microscoop, een innovatieve visualisatietechniek wat er eigenhandig voor heeft gezorgd dat we de wereld vanuit een nieuwe invalshoek kunnen bewonderen.

Een sleutelcomponent die essentieel is voor een efficiënte werking van de techniek is de fluorofoor. Hierdoor zijn er in de afgelopen decennia vele verwoede pogingen ondernomen om de perfecte visualisatiesonde te creëren. Gaande van organische kleurstoffen en fluorescente proteïnes tot nanostructuren, alle hebben ze op hun manier ervoor gezorgd dat fluorescentiemicroscopie telkens naar een nieuw niveau werd getild. De cultuur van continue innovatie en stimulatie in wetenschap heeft er recent voor gezorgd dat een nieuw lid is toegevoegd aan de groep van nanostructuren, de geconjugeerde polymere nanodeeltjes. Dit fluorofoor is snel door de rangen gerezen omwille van een uitmuntend fluorescent signaal en goede biocompatibiliteit en wordt op regelmatige basis aangewend voor geavanceerd biomedisch onderzoek.

Geconjugeerde polymeren zijn in grote getalen aanwezig, maar één van de bekendste en meest grondig onderzochte - tot nog toe - is de poly(p-fenyleen vinyleen) (PPV)-familie. PPV en zijn derivaten zijn voornamelijk gebruikt geweest voor het bestuderen van de fundamentele eigenschappen van geconjugeerde polymere nanodeeltjes en zijn hierdoor uitgegroeid tot de maatstaf waartegen alle nieuwe ontwerpen vergeleken worden. Toch werd het, na een diepgaande doorlichting van de literatuur, snel duidelijk dat ondanks het omvangrijke onderzoek er een essentiële eigenschap ontbreekt in het ontwerp van PPV-gebaseerde nanodeeltjes. Ze beschikken namelijk niet over de nodige aanhechtingspunten welke noodzakelijk zijn voor het verkrijgen van bepaalde functionaliteiten door koppeling, zoals bijvoorbeeld een doelgerichte visualisatie. De centrale onderzoeksvraag van dit interdisciplinair doctoraatsonderzoek is daarom als volgt geformuleerd: Kan de hierboven besproken hindernis overwonnen worden zonder gebruik te maken van de huidige postsynthese

modificaties of op het oppervlak geabsorbeerde moleculen en kan dit nieuwe fluorofoor aangewend worden voor biomedische onderzoek.

Het eerste deel van deze vraag werd beantwoord in hoofdstuk 2, waar voor de eerste keer ooit een PPV-gebaseerd fluorofoor gesynthetiseerd werd met functionele groepen op het oppervlak. Dit werd gerealiseerd door gebruik te maken van een complexe functionele PPV-constructie, namelijk het copolymeer CPM-*co*-MDMO-PPV. Dit polymeer beschikt over een polaire groep op zijn alkoxyzijketen, wat de mogelijkheid biedt om biologische of chemische structuren op het oppervlak van de nanodeeltjes vast te hechten. Uitgebreid onderzoek toonde aan dat het nieuwe copolymeersysteem zich op optisch vlak gelijkaardig gedraagt als de reeds beschreven homopolymeersystemen. Gezien het jonge karakter van de discipline werd er ook uitvoerig gekeken naar de interactie van nanodeeltjes met hun biologische omgeving, aangezien hier nog weinig over bekend was. Er werd geen toxiciteit vastgesteld en de opname van de nanodeeltjes door cellen gerelateerd aan het centrale zenuwstelsel bleek succesvol.

Vervolgens werd er in hoofdstuk 3 gekeken of de diameter van de nanodeeltjes kleiner kon gemaakt worden dan de 100 nm geproduceerd in hoofdstuk 2. De beweegreden hierachter is het feit dat afhankelijk van de biomedische toepassing een andere grootte vereist is. De diameter kon vlot gereduceerd worden tot 20 nm door de dosis aan polymeer te verlagen tijdens het syntheseproces. Er werden geen nadelige effecten geobserveerd voor de optische karakteristieken. Echter bleek er wel een drempel te zijn tot welke de hoeveelheid copolymeer kon verlaagd worden zonder permanente beschadigingen in de polymeerketen te induceren. Ook de biologische effecten dat het systeem teweeg brengt werden niet beïnvloedt door de grootte van de nanodeeltjes, met uitzondering van de verwachte toename in snelheid alsook hoeveelheid in opname door cellen bij een daling van de diameter.

In hoofdstuk 4 werd er dieper ingegaan op de functionele groepen aanwezig op de oppervlakte van de deeltjes en of deze geschikt zijn voor het aanhechten van structuren. Polyethyleenglycol (PEG) werd gekozen voor verankering op het oppervlak, omdat het de nanodeeltjes zogenaamd onzichtbaar kan maken voor

het immuunsysteem. In slechts 6 uur kon de oppervlakte geprepareerd worden voor de PEG aanhechting en een hoge bedekkingsgraad werd gerealiseerd voor PEG-kettingen met een verschillend moleculair gewicht. Bedekking van het oppervlak met PEG verhinderde de vorming van een proteïnecorona en opname door cellen, zowel voor de immuun- als reguliere cellen van het centrale zenuwstelsel, zonder de optische eigenschappen te beïnvloeden.

Finaal werd in hoofdstuk 5 de proef op de som genomen om het laatste deel van de onderzoeksvraag van dit doctoraatsonderzoek te beantwoorden en werd er een op CPM-*co*-MDMO-PPV nanodeeltjes model ontworpen voor onderzoek naar het ontstaan van MS. Om dit te verwezenlijken werd de fractalkinereceptor antagonist AZD8797 vastgehecht op het oppervlak van de deeltjes. Dit resulteerde in de creatie van een fluorofoor dat specifiek cellen kon visualiseren die de fractalkinereceptor bezaten, zoals $CD4^+CD28^-$ T-cellen, welke geassocieerd zijn met de progressie van MS. Ook belemmerden de nanodeeltjes de migratie van deze T-celpopulatie naar een fratalkinegradiënt, een bewijs dat aantoont dat de antagonistische werking van het molecuul zelfs na binding behouden blijft. Daarnaast toonde de nanodeeltjes ook dat ze zich over de normaal ondoordringbare bloed-brein-barrière konden manoeuvreren. Dit biedt de mogelijkheid om relevante cellen, zoals microglia, te visualiseren in het centraal zenuwstelsel.

De resultaten gepresenteerd in deze thesis demonstreren dat het mogelijk is om een PPV-gebaseerd fluorofoor *in situ* te synthetiseren welke functionele oppervlaktegroepen bezit. Uit de experimenten bleek dat functionele PPVs excellente kandidaten zijn om fluorescerende nanodeeltjes mee te vormen voor biomedische toepassingen. Hun buitengewone optische en biologische karakteristieke en uitzonderlijke flexibiliteit op vlak van design-mogelijkheden hebben ervoor gezorgd dat deze een permanente plaats verzilverd hebben in het veld van de biovisualisatie.

References

1. Bianconi E*, et al.* An estimation of the number of cells in the human body. *Annals of human biology*. **2013**;40(6):463-71.

2. Stokes GG. On the Change of Refrangibility of Light. *Philosophical Transactions of the Royal Society of London*. **1852**;142:463-562.

3. Lichtman JW*, et al.* Fluorescence microscopy. *Nature methods*. **2005**;2(12):910-9.

4. Conchello J-A*, et al.* Optical sectioning microscopy. *Nat Methods*. **2005**;2(12):920-31.

5. Huang B*, et al.* Super-resolution fluorescence microscopy. *Annual review of biochemistry*. **2009**;78:993-1016.

6. Schermelleh L*, et al.* A guide to super-resolution fluorescence microscopy. *The Journal of cell biology*. **2010**;190(2):165-75.

7. Ng KK*, et al.* Molecular interactions in organic nanoparticles for phototheranostic applications. *Chem Rev*. **2015**;115(19):11012-42.

8. Resch-Genger U*, et al.* Quantum dots versus organic dyes as fluorescent labels. *Nat Methods*. **2008**;5(9):763-75.

9. Wu C*, et al.* Multicolor Conjugated Polymer Dots for Biological Fluorescence Imaging. *ACS Nano*. **2008**;2(11):2415-23.

10. Wu C*, et al.* Highly Fluorescent Semiconducting Polymer Dots for Biology and Medicine. *Angew Chem, Int Ed*. **2013**;52(11):3086-109.

11. Shimomura O*, et al.* Extraction, purification and properties of aequorin, a bioluminescent protein from the luminous hydromedusan, Aequorea. *Journal of Cellular Physiology*. **1962**;59(3):223-39.

12. Tsien RY. The green fluorescent protein. Annual Reviews 4139 El Camino Way, PO Box 10139, Palo Alto, CA 94303-0139, USA; 1998.

13. Shaner NC*, et al.* A guide to choosing fluorescent proteins. *Nature methods*. **2005**;2(12):905.

14. Commision recommendation of 18 October 2011 on the definition of nanomaterials (2011/696/EU). *Official Journal of the European Union*. **2011**:38-40.

15. Roduner E. Size matters: why nanomaterials are different. *Chem Soc Rev*. **2006**;35(7):583-92.

16. Wang L*, et al.* Watching silica nanoparticles glow in the biological world. ACS Publications; 2006.

17. Penjweini R*, et al.* Intracellular localization and dynamics of Hypericin loaded PLLA nanocarriers by image correlation spectroscopy. *J Controlled Release*. **2015**;218:82-93.

18. Hofmann D*, et al.* Drug delivery without nanoparticle uptake: delivery by a kiss-and-run mechanism on the cell membrane. *Chem Commun*. **2014**;50(11):1369-71.

19. Alford R*, et al.* Toxicity of organic fluorophores used in molecular imaging: literature review. *Molecular imaging*. **2009**;8(6):7290.2009. 00031.

20. Moras JD*, et al.* Semiconductor clusters, nanocrystals, and quantum dots. *Science*. **1996**;271:933.

21. Michalet X*, et al.* Quantum Dots for Live Cells, in Vivo Imaging, and Diagnostics. *Science*. **2005**;307(5709):538-44.

22. Bradburne CE*, et al.* Cytotoxicity of Quantum Dots Used for In Vitro Cellular Labeling: Role of QD Surface Ligand, Delivery Modality, Cell Type, and Direct Comparison to Organic Fluorophores. *Bioconjugate Chem*. **2013**;24(9):1570-83.

23. Tuncel D*, et al.* Conjugated polymer nanoparticles. *Nanoscale*. **2010**;2(4):484-94.

24. Pecher J*, et al.* Nanoparticles of conjugated polymers. *Chem Rev*. **2010**;110(10):6260-79.

25. Chan YH*, et al.* Semiconducting polymer nanoparticles as fluorescent probes for biological imaging and sensing. *Particle & Particle Systems Characterization*. **2015**;32(1):11-28.

26. Yu J*, et al.* Recent Advances in the Development of Highly Luminescent Semiconducting Polymer Dots and Nanoparticles for Biological Imaging and Medicine. *Analytical Chemistry*. **2017**;89(1):42-56.

27. Chiang CK*, et al.* Electrical conductivity in doped polyacetylene. *Physical review letters*. **1977**;39(17):1098.

28. Rohatgi-Mukherjee K. Fundamentals of photochemistry: *New Age International*; **1978**.

29. Landfester K*, et al.* Semiconducting polymer nanospheres in aqueous dispersion prepared by a miniemulsion process. *Adv Mater*. **2002**;14(9):651-5.

30. Vitale SA*, et al.* Liquid droplet dispersions formed by homogeneous liquid–liquid nucleation:"The ouzo effect". *Langmuir*. **2003**;19(10):4105-10.

31. Wu C*, et al.* Preparation and encapsulation of highly fluorescent conjugated polymer nanoparticles. *Langmuir*. **2006**;22(7):2956-60.

32. Kulkarni AP*, et al.* Electron transport materials for organic light-emitting diodes. *Chem Mater*. **2004**;16(23):4556-73.

33. Grimsdale AC*, et al.* Synthesis of light-emitting conjugated polymers for applications in electroluminescent devices. *Chem Rev*. **2009**;109(3):897-1091.

34. Günes S*, et al.* Conjugated polymer-based organic solar cells. *Chem Rev*. **2007**;107(4):1324-38.

35. Horowitz G. Organic field-effect transistors. *Adv Mater*. **1998**;10(5):365-77.

36. Kraft A*, et al.* Electroluminescent conjugated polymersÐseeing polymers in a new light. *Angew Chem Int End Engl*. **1998**;37:402-28.

37. Akagi K*, et al.* Conjugated polymers: a practical guide to synthesis: *Royal Society of Chemistry*; **2013**.

38. Junkers T*, et al.* Synthesis of poly(p-phenylene vinylene) materials via the precursor routes. *Polym Chem*. **2012**;3(2):275-85.

39. Davey AP*, et al.* Synthesis and optical properties of phenylene-vinylene copolymers. *Synthetic Metals*. **1999**;103(1):2478-9.

40. Koßmehl G. Semiconductive Conjugated Polymers. *Berichte der Bunsengesellschaft für physikalische Chemie*. **1979**;83(4):417-26.

41. Feast WJ*, et al.* Optical absorption and luminescence in poly(4,4′-diphenylenediphenylvinylene). *Synthetic Metals*. **1985**;10(3):181-91.

42. Bao Z*, et al.* Conjugated liquid-crystalline polymers - soluble and fusible poly(phenylenevinylene) by the Heck coupling reaction. *Macromolecules*. **1993**;26(20):5281-6.

43. Babudri F*, et al.* Synthesis, characterization and properties of a soluble polymer with a poly(phenylenevinylene) structure. *Macromol Rapid Commun*. **1996**;17(12):905-11.

44. Koch F*, et al.* Soluble poly(1,4-phenylenevinylene)s and poly(1,4-phenyleneethynylene)s via suzuki coupling. *Macromol Chem Phys*. **1997**;198(5):1531-44.

45. Conticello VP*, et al.* Ring-opening metathesis polymerization of substituted bicyclo[2.2.2]octadienes: a new precursor route to poly(1,4-phenylenevinylene). *J Am Chem Soc*. **1992**;114(24):9708-10.

46. Miao Y-J*, et al.* Paracyclophene Route to Poly(p-phenylenevinylene). *J Am Chem Soc*. **1994**;116(20):9379-80.

47. Son S*, et al.* Luminescence enhancement by the introduction of disorder into poly (p-phenylene vinylene). *SCIENCE-NEW YORK THEN WASHINGTON-*. **1995**:376-.

48. Louwet F*, et al.* A new synthetic route to a soluble high molecular weight precursor for poly (p-phenylenevinylene) derivatives. *Macromolecules*. **1995**;28(4):1330-1.

49. van Breemen AJJM*, et al.* Highly Selective Route for Producing Unsymmetrically Substituted Monomers toward Synthesis of Conjugated Polymers Derived from Poly(p-phenylene vinylene). *J Org Chem*. **1999**;64(9):3106-12.

50. Henckens A*, et al.* Synthesis of poly (p-phenylene vinylene) and derivatives via a new precursor route, the dithiocarbamate route. *Polymer*. **2006**;47(1):123-31.

51. Gilch H*, et al.* Polymerization of α- halogenated p- xylenes with base. *J Polym Sci, Part A: Polym Chem*. **1966**;4(6):1337-49.

52. Denton FR*, et al.* Para-Xylylenes and analogues by base-induced elimination from 1,4-bis-(dialkylsulfoniomethyl)arene salts in poly(1,4-arylene vinylene) synthesis by the wessling soluble precursor method. *J Polym Sci, Part A: Polym Chem*. **1992**;30(10):2233-40.

53. Kesters E*, et al.* Polymerization Behavior of Xanthate-Containing Monomers toward PPV Precursor Polymers: Study of the Elimination Behavior of Precursor Polymers and Oligomers with in-Situ FT-IR and UV−Vis Analytical Techniques. *Macromolecules*. **2002**;35(21):7902-10.

54. Hu D*, et al.* Spatial Confinement of Exciton Transfer and the Role of Conformational Order in Organic Nanoparticles. *Nano Lett*. **2002**;2(10):1121-4.

55. Traiphol R*, et al.* Solvent-induced photoemissions of high-energy chromophores of conjugated Polymer MEH-PPV: Role of conformational disorder. *Macromolecular Research*. **2008**;16(3):224-30.

56. Duchateau J*, et al.* Versatile post-polymerization functionalization of poly(p-phenylene vinylene) copolymers containing carboxylic acid substituents: development of a universal method towards functional conjugated copolymers. *Polym Chem*. **2010**;1(8):1313-22.

57. Vandenbergh J*, et al.* Controlled synthesis of MDMO-PPV and block copolymers made thereof. *Polym Chem*. **2012**;3(7):1722-5.

58. Wu C*, et al.* Conjugated Polymer Dots for Multiphoton Fluorescence Imaging. *J Am Chem Soc*. **2007**;129(43):12904-5.

59. Szymanski C*, et al.* Single Molecule Nanoparticles of the Conjugated Polymer MEH−PPV, Preparation and Characterization by Near-Field Scanning Optical Microscopy. *J Phys Chem B*. **2005**;109(18):8543-6.

60. Grey JK*, et al.* Size-Dependent Spectroscopic Properties of Conjugated Polymer Nanoparticles. *J Phys Chem B*. **2006**;110(51):25568-72.

61. Masuo S*, et al.* Single-photon emission from a single nanoparticle consisting of a single conjugated polymer chain. *Synthetic Metals*. **2009**;159(9):805-8.

62. Potai R*, et al.* Controlling chain organization and photophysical properties of conjugated polymer nanoparticles prepared by reprecipitation method: The effect of initial solvent. *Journal of colloid and interface science*. **2013**;403:58-66.

63. Ghosh A*, et al.* Exciton Dynamics and Formation Mechanism of MEH-PPV Polymer -Based Nanostructures. *The Journal of Physical Chemistry C*. **2017**.

64. Groff LC*, et al.* Effect of Swelling on Multiple Energy Transfer in Conjugated Polymer Nanoparticles. *The Journal of Physical Chemistry C*. **2017**;121(13):7549-57.

65. Kobayashi H*, et al.* Mechanical manipulation of photophysical properties of single conjugated polymer nanoparticles. *The Journal of Physical Chemistry Letters*. **2013**;4(15):2591-6.

66. Clafton SN*, et al.* Chemical defects in the highly fluorescent conjugated polymer dots. *Langmuir*. **2010**;26(23):17785-9.

67. Bao B*, et al.* A controllable approach to development of multi-spectral conjugated polymer nanoparticles with increased emission for cell imaging. *Chem Commun*. **2013**;49(90):10623-5.

68. Jung Y*, et al.* Encapsulating light-emitting polymers in block copolymer micelles. *Langmuir*. **2010**;26(10):7540-3.

69. Green M*, et al.*, editors. Simple conjugated polymer nanoparticles as biological labels. Proceedings of the Royal Society of London A: Mathematical, Physical and Engineering Sciences; 2009: The Royal Society.

70. Hashim Z*, et al.* Luminescent quantum-dot-sized conjugated polymer nanoparticles—nanoparticle formation in a miniemulsion system. *Journal of Materials Chemistry*. **2011**;21(6):1797-803.

71. Howes P*, et al.* Phospholipid Encapsulated Semiconducting Polymer Nanoparticles: Their Use in Cell Imaging and Protein Attachment. *J Am Chem Soc*. **2010**;132(11):3989-96.

72. Howes P*, et al.* Colloidal and optical stability of PEG-capped and phospholipid-encapsulated semiconducting polymer nanospheres in different aqueous media. *Photochemical & Photobiological Sciences*. **2010**;9(8):1159-66.

73. Tan H*, et al.* Silica-shell cross-linked micelles encapsulating fluorescent conjugated polymers for targeted cellular imaging. *Biomaterials*. **2012**;33(1):237-46.

74. Joshi PB*, et al.* Facile capture of conjugated polymer nanodots in silica nanoparticles to facilitate surface modification. *J Mater Sci*. **2015**;50(10):3597-603.

75. Li K*, et al.* Generic strategy of preparing fluorescent conjugated-polymer- loaded poly (dl- lactide- co- glycolide) nanoparticles for targeted cell imaging. *Advanced Functional Materials*. **2009**;19(22):3535-42.

76. Xiong L*, et al.* Self-luminescing BRET-FRET near infrared dots for in vivo lymph node mapping and tumor imaging. *Nature communications*. **2012**;3:1193.

77. Xiong L*, et al.* Long-term-stable near-infrared polymer dots with ultrasmall size and narrow-band emission for imaging tumor vasculature in vivo. *Bioconjugate Chem*. **2015**;26(5):817-21.

78. Xiong L*, et al.* Highly luminescent and photostable near-infrared fluorescent polymer dots for long-term tumor cell tracking in vivo. *Journal of Materials Chemistry B*. **2016**;4(2):202-6.

79. Palner M*, et al.* Semiconducting Polymer Nanoparticles with Persistent Near- Infrared Luminescence for In Vivo Optical Imaging. *Angewandte Chemie*. **2015**;127(39):11639-42.

80. Harbron EJ*, et al.* Photochromic dye-doped conjugated polymer nanoparticles: photomodulated emission and nanoenvironmental characterization. *The Journal of Physical Chemistry C*. **2009**;113(31):13707-14.

81. Davis CM*, et al.* Ensemble and single-particle fluorescence photomodulation in diarylethene-doped conjugated polymer nanoparticles. *The Journal of Physical Chemistry C*. **2011**;115(39):19065-73.

82. Osakada Y*, et al.* Live cell imaging using photoswitchable diarylethene doped fluorescent polymer dots. *Chemistry–An Asian Journal*.

83. Zhang Y*, et al.* Small molecule-initiated light-activated semiconducting polymer dots: an integrated nanoplatform for targeted photodynamic therapy and imaging of cancer cells. *Analytical chemistry*. **2014**;86(6):3092-9.

84. Haupt S*, et al.* Pdots, a new type of nanoparticle, bind to m THPC via their lipid modified surface and exhibit very high FRET efficiency between the core and the sensitizer. *Physical Chemistry Chemical Physics*. **2015**;17(17):11412-22.

85. Haupt S*, et al.* FRET energy transfer via Pdots improves the efficiency of photodynamic therapy and leads to rapid cell death. *Journal of Photochemistry and Photobiology B: Biology*. **2016**;164:123-31.

86. Wu C*, et al.* Energy transfer mediated fluorescence from blended conjugated polymer nanoparticles. *J Phys Chem B*. **2006**;110(29):14148-54.

87. Wang X*, et al.* Photoactivation and saturated emission in blended conjugated polymer nanoparticles. *Langmuir*. **2013**;29(45):13925-31.

88. Wang X*, et al.* Multiple energy transfer dynamics in blended conjugated polymer nanoparticles. *The Journal of Physical Chemistry C*. **2014**;118(44):25731-9.

89. Kong F*, et al.* Tunable emission from composite polymer nanoparticles based on resonance energy transfer. *Thin Solid Films*. **2008**;516(18):6287-92.

90. Howes P*, et al.* Magnetic conjugated polymer nanoparticles as bimodal imaging agents. *J Am Chem Soc*. **2010**;132(28):9833-42.

91. Hashim Z*, et al.* Gd-containing conjugated polymer nanoparticles: bimodal nanoparticles for fluorescence and MRI imaging. *Nanoscale*. **2014**;6(14):8376-86.

92. Kim S*, et al.* Conjugated polymer nanoparticles for biomedical in vivo imaging. *Chem Commun*. **2010**;46(10):1617-9.

93. Abelha T*, et al.* Bright conjugated polymer nanoparticles containing a biodegradable shell produced at high yields and with tuneable optical properties by a scalable microfluidic device. *Nanoscale*. **2017**;9(5):2009-19.

94. Penwell SB*, et al.* Bringing Far-Field Subdiffraction Optical Imaging to Electronically Coupled Optoelectronic Molecular Materials Using Their Endogenous Chromophores. *The journal of physical chemistry letters*. **2015**;6(14):2767-72.

95. Bourke S*, et al.*, editors. Silica passivated conjugated polymer nanoparticles for biological imaging applications. SPIE BiOS; 2017: International Society for Optics and Photonics.

96. Kemal E*, et al.* Bright, near infrared emitting PLGA–PEG dye-doped CN-PPV nanoparticles for imaging applications. *RSC Adv*. **2017**;7(25):15255-64.

97. Chen D*, et al.* Bright Polymer Dots Tracking Stem Cell Engraftment and Migration to Injured Mouse Liver. *Theranostics*. **2017**;7(7):1820.

98. Kuo C-T*, et al.* Optical painting and fluorescence activated sorting of single adherent cells labelled with photoswitchable Pdots. *Nature communications*. **2016**;7.

99. Sun J*, et al.* Two-photon semiconducting polymer dots with dual-emission for Ratiometric fluorescent sensing and bioimaging of Tyrosinase activity. *Analytical chemistry*. **2016**;88(14):7372-7.

100. Ye F*, et al.* A compact and highly fluorescent orange-emitting polymer dot for specific subcellular imaging. *Chem Commun*. **2012**;48(12):1778-80.

101. Meng Z*, et al.* Peptide- Coated Semiconductor Polymer Dots for Stem Cells Labeling and Tracking. *Chem - Eur J*. **2017**;23(28):6836-44.

102. Chen X*, et al.* Small Photoblinking Semiconductor Polymer Dots for Fluorescence Nanoscopy. *Adv Mater*. **2017**;29(5).

103. Zhou L*, et al.* In-situ visual and ultrasensitive detection of phosmet using a fluorescent immunoassay probe. *Sensors and Actuators B: Chemical*. **2017**;241:915-22.

104. Peteanu LA*, et al.* Visualizing Core–Shell Structure in Substituted PPV Oligomer Aggregates Using Fluorescence Lifetime Imaging Microscopy (FLIM). *The Journal of Physical Chemistry C*. **2011**;115(31):15607-16.

105. So WY*, et al.* Effects of Solvent Properties on the Spectroscopy and Dynamics of Alkoxy-Substituted PPV Oligomer Aggregates. *J Phys Chem B*. **2012**;116(35):10504-13.

106. Peteanu LA*, et al.* Exciton–Exciton Annihilation as a Probe of Interchain Interactions in PPV–Oligomer Aggregates. *J Phys Chem B*. **2017**;121(7):1707-14.

107. Makkad SK*, et al.* "π-Conjugated Chromophore Incorporated Polystyrene Nanobeads as Single Optical Agent for Three Channel Fluorescent Probe in Bioimaging Application. *ACS Biomaterials Science & Engineering*. **2017**.

108. Fukui C*, et al.* Fluorescent π-conjugated polymer nanoparticles: A new synthetic approach based on nanoagglomeration via polyion association. *J Mater Res*. **2015**;30(01):10-8.

109. Choi J-s*, et al.* Cross-linked fluorescent supramolecular nanoparticles as finite tattoo pigments with controllable intradermal retention times. *ACS Nano*. **2016**;11(1):153-62.

110. Wang H*, et al.* Preparation of Gemini Surfactant/Conjugated Polymer Aggregates for Enhanced Fluorescence and Bioimaging Application. *ACS Appl Mater Interfaces*. **2017**;9(28):23544-54.

111. Ethirajan A*, et al.* Synthesis of MDMO- PPV Nanoparticles Via In Situ Sulfinyl Precursor Route Polymerization in Miniemulsion. *Macromol Chem Phys*. **2013**;214(16):1859-64.

112. Ye F*, et al.* Semiconducting polymer dots with monofunctional groups. *Chem Commun*. **2014**;50(42):5604-7.

113. Zaquen N*, et al.* Profluorescent PPV-Based Micellar System as a Versatile Probe for Bioimaging and Drug Delivery. *Biomacromolecules*. **2016**;17(12):4086-94.

114. Seo YH*, et al.* Rational design for enhancing inflammation-responsive in vivo chemiluminescence via nanophotonic energy relay to near-infrared AIE-active conjugated polymer. *Biomaterials*. **2016**;84:111-8.

115. Pecher J*, et al.* Nanoparticles from step-growth coordination polymerization. *Macromolecules*. **2007**;40(22):7733-5.

116. Yabu H*, et al.* A simple route for fabricating poly (para-phenylene vinylene)(PPV) particles by using ionic liquids and a solvent evaporation process. *Chem Commun*. **2008**(38):4588-9.

117. Visualizing Chemistry: The Progress and Promise of Advanced Chemical Imaging: *Washington (DC): National Academies Press (US)*; **2006**. 222 p.

118. Dean KM*, et al.* Advances in fluorescence labeling strategies for dynamic cellular imaging. *Nat Chem Biol*. **2014**;10(7):512-23.

119. Advanced Fluorescence Reporters in Chemistry and Biology III: Applications in Sensing and Imaging: *Springer*; **2011**.

120. Pepperkok R*, et al.* High-throughput fluorescence microscopy for systems biology. *Nat Rev Mol Cell Biol*. **2006**;7(9):690-6.

121. Yildiz A*, et al.* Myosin V Walks Hand-Over-Hand: Single Fluorophore Imaging with 1.5-nm Localization. *Science*. **2003**;300(5628):2061-5.

122. Xie XS*, et al.* Living Cells as Test Tubes. *Science*. **2006**;312(5771):228-30.

123. Thompson MA*, et al.* Three-dimensional tracking of single mRNA particles in Saccharomyces cerevisiae using a double-helix point spread function. *Proc Natl Acad Sci*. **2010**;107(42):17864-71.

124. Fernando LP*, et al.* The relative brightness of PEG lipid-conjugated polymer nanoparticles as fluid-phase markers in live cells. *Anal Bioanal Chem*. **2012**;404(10):3003-14.

125. Alford R*, et al.* Toxicity of organic fluorophores used in molecular imaging: literature review. *Molecular imaging*. **2009**;8(6):341.

126. Ahmad Khanbeigi R*, et al.* Surface Chemistry of Photoluminescent F8BT Conjugated Polymer Nanoparticles Determines Protein Corona Formation and Internalization by Phagocytic Cells. *Biomacromolecules*. **2015**;16(3):733-42.

127. Shirakawa H*, et al.* Synthesis of electrically conducting organic polymers: halogen derivatives of polyacetylene, (CH). *J Chem Soc, Chem Commun*. **1977**(16):578-80.

128. Zhang W*, et al.* Bright red-emitting polymer dots for specific cellular imaging. *J Mater Sci*. **2015**;50(16):5571-7.

129. Xu J*, et al.* 'Imperfect' conjugated polymer nanoparticles from MEH-PPV for bioimaging and Fe(III) sensing. *Luminescence*. **2015**;30(4):451-6.

130. Sun K*, et al.* Size-dependent property and cell labeling of semiconducting polymer dots. *ACS Appl Mater Interfaces*. **2014**;6(13):10802-12.

131. Doshi M*, et al.* Conducting polymer nanoparticles for targeted cancer therapy. *RSC Adv*. **2015**;5(47):37943-56.

132. Ritz S*, et al.* Protein Corona of Nanoparticles: Distinct Proteins Regulate the Cellular Uptake. *Biomacromolecules*. **2015**;16(4):1311-21.

133. Tenzer S*, et al.* Rapid formation of plasma protein corona critically affects nanoparticle pathophysiology. *Nat Nano*. **2013**;8(10):772-81.

134. Landfester K. The generation of nanoparticles in miniemulsions. *Adv Mater*. **2001**;13(10):765-8.

135. Ethirajan A*, et al.* Functional hybrid materials with polymer nanoparticles as templates. *Chem - Eur J*. **2010**;16(31):9398-412.

136. Ethirajan A*, et al.* Biodegradable Polymeric Nanoparticles as Templates for Biomimetic Mineralization of Calcium Phosphate. *Macromol Chem Phys*. **2011**;212(9):915-25.

137. Moreno-Vega A-I*, et al.* Polymeric and ceramic nanoparticles in biomedical applications. *J Nanotechnol*. **2012**;2012:10.

138. Ajetunmobi A*, et al.* Nanotechnologies for the study of the central nervous system. *Prog Neurobiol*. **2014**;123:18-36.

139. Qian C-G*, et al.* Conjugated Polymer Nanoparticles for Fluorescence Imaging and Sensing of Neurotransmitter Dopamine in Living Cells and the Brains of Zebrafish Larvae. *ACS Appl Mater Interfaces*. **2015**;7(33):18581-9.

140. Zaquen N*, et al.* Facile Synthesis of Well-Defined MDMO-PPV Containing (Tri) Block—Copolymers via Controlled Radical Polymerization and CuAAC Conjugation. *Polymers*. **2015**;7(3):418-52.

141. Van Severen I*, et al.* Poly(p-phenylene vinylene) derivatives with ester- and carboxy-functionalized substituents: a versatile platform towards polar functionalized conjugated polymers. *Polymer*. **2005**;46(15):5466-75.

142. Deen C*, et al.* A novel carbodiimide coupling method for synthetic peptides. *J Immunol Methods*. **1990**;129(1):119-25.

143. Correa-Llantén DN*, et al.* Gold nanoparticles synthesized by Geobacillus sp. strain ID17 a thermophilic bacterium isolated from Deception Island, Antarctica. *Microb Cell Fact*. **2013**;12:75-.

144. Schwartz BJ. CONJUGATED POLYMERS AS MOLECULAR MATERIALS: How Chain Conformation and Film Morphology Influence Energy Transfer and Interchain Interactions. *Annu Rev Phys Chem*. **2003**;54(1):141-72.

145. Nguyen T-Q*, et al.* Controlling Interchain Interactions in Conjugated Polymers: The Effects of Chain Morphology on Exciton−Exciton Annihilation and Aggregation in MEH−PPV Films. *J Phys Chem B*. **2000**;104(2):237-55.

146. Denk W*, et al.* Two-photon laser scanning fluorescence microscopy. *Science*. **1990**;248(4951):73-6.

147. Pecher J*, et al.* Tailor-Made Conjugated Polymer Nanoparticles for Multicolor and Multiphoton Cell Imaging. *Biomacromolecules*. **2010**;11(10):2776-80.

148. Chambon S*, et al.* Aging of a donor conjugated polymer: Photochemical studies of the degradation of poly[2-methoxy-5-(3′,7′-dimethyloctyloxy)-

1,4-phenylenevinylene]. *J Polym Sci, Part A: Polym Chem*. **2007**;45(2):317-31.

149. Jiang X*, et al.* Specific effects of surface carboxyl groups on anionic polystyrene particles in their interactions with mesenchymal stem cells. *Nanoscale*. **2011**;3(5):2028-35.

150. Raff M*, et al.* Two types of astrocytes in cultures of developing rat white matter: differences in morphology, surface gangliosides, and growth characteristics. *J Neurosci*. **1983**;3(6):1289-300.

151. An Y*, et al.* Interleukin-1 exerts distinct actions on different cell types of the brain in vitro. *J Inflammation Res*. **2011**;2011(4):11-20.

152. Blasi E*, et al.* Immortalization of murine microglial cells by a v-raf/v-myc carrying retrovirus. *J Neuroimmunol*. **1990**;27(2):229-37.

153. Hanisch U-K*, et al.* Microglia: active sensor and versatile effector cells in the normal and pathologic brain. *Nat Neurosci*. **2007**;10(11):1387-94.

154. Block ML*, et al.* Microglia-mediated neurotoxicity: uncovering the molecular mechanisms. *Nat Rev Neurosci*. **2007**;8(1):57-69.

155. Graeber MB. Changing Face of Microglia. *Science*. **2010**;330(6005):783-8.

156. Kettenmann H*, et al.* Physiology of microglia. *Physiol Rev*. **2011**;91(2):461-553.

157. Takeuchi A*, et al.* Macrophage colony-stimulating factor is expressed in neuron and microglia after focal brain injury. *J Neurosci Res*. **2001**;65(1):38-44.

158. Kubitscheck U. Fluorescence microscopy: from principles to biological applications: *John Wiley & Sons*; **2017**.

159. Jaiswal JK*, et al.* Potentials and pitfalls of fluorescent quantum dots for biological imaging. *Trends in cell biology*. **2004**;14(9):497-504.

160. Reisch A*, et al.* Fluorescent Polymer Nanoparticles Based on Dyes: Seeking Brighter Tools for Bioimaging. *Small*. **2016**;12(15):1968-92.

161. Mochalin VN*, et al.* The properties and applications of nanodiamonds. *Nature nanotechnology*. **2012**;7(1):11-23.

162. Heeger AJ. Semiconducting polymers: the Third Generation. *Chem Soc Rev*. **2010**;39(7):2354-71.

163. Yu J*, et al.* Recent Advances in the Development of Highly Luminescent Semiconducting Polymer Dots and Nanoparticles for Biological Imaging and Medicine. *Analytical Chemistry*. **2016**;89(1):42-56.

164. D'Olieslaeger L*, et al.* Tuning the optical properties of poly (p-phenylene ethynylene) nanoparticles as bio-imaging probes by side chain functionalization. *Journal of Colloid and Interface Science*. **2017**.

165. Peters M*, et al.* PPV-Based Conjugated Polymer Nanoparticles as a Versatile Bioimaging Probe: A Closer Look at the Inherent Optical Properties and Nanoparticle–Cell Interactions. *Biomacromolecules*. **2016**;17(8):2562-71.

166. Salatin S*, et al.* Effect of the surface modification, size, and shape on cellular uptake of nanoparticles. *Cell Biology International*. **2015**;39(8):881-90.

167. Shang L*, et al.* Engineered nanoparticles interacting with cells: size matters. *Journal of nanobiotechnology*. **2014**;12(1):5.

168. D'Olieslaeger L*, et al.* Eco-friendly fabrication of PBDTTPD: PC 71 BM solar cells reaching a PCE of 3.8% using water-based nanoparticle dispersions. *Organic Electronics*. **2017**;42:42-6.

169. Staff RH*, et al.* Particle Formation in the Emulsion- Solvent Evaporation Process. *Small*. **2013**;9(20):3514-22.

170. Musyanovych A*, et al.* Preparation of biodegradable polymer nanoparticles by miniemulsion technique and their cell interactions. *Macromolecular bioscience*. **2008**;8(2):127-39.

171. Manceau M*, et al.* Photochemical stability of π-conjugated polymers for polymer solar cells: a rule of thumb. *Journal of Materials Chemistry*. **2011**;21(12):4132-41.

172. Yan M*, et al.* Defect Quenching of Conjugated Polymer Luminescence. *Physical Review Letters*. **1994**;73(5):744-7.

173. Park MVDZ*, et al.* The effect of particle size on the cytotoxicity, inflammation, developmental toxicity and genotoxicity of silver nanoparticles. *Biomaterials*. **2011**;32(36):9810-7.

174. Pan Y*, et al.* Size-Dependent Cytotoxicity of Gold Nanoparticles. *Small*. **2007**;3(11):1941-9.

175. Napierska D*, et al.* Size-Dependent Cytotoxicity of Monodisperse Silica Nanoparticles in Human Endothelial Cells. *Small*. **2009**;5(7):846-53.

176. Zhao X*, et al.* Development of Organic-Dye-Doped Silica Nanoparticles in a Reverse Microemulsion. *Adv Mater*. **2004**;16(2):173-6.

177. Ow H*, et al.* Bright and Stable Core−Shell Fluorescent Silica Nanoparticles. *Nano Lett*. **2005**;5(1):113-7.

178. Zaquen N*, et al.* Controlled/living polymerization towards functional poly (p-phenylene vinylene) materials. *Polym Chem*. **2016**;7(7):1355-67.

179. Klibanov AL*, et al.* Activity of amphipathic poly (ethylene glycol) 5000 to prolong the circulation time of liposomes depends on the liposome size and is unfavorable for immunoliposome binding to target. *Biochimica et Biophysica Acta (BBA)-Biomembranes*. **1991**;1062(2):142-8.

180. Ryan SM*, et al.* Advances in PEGylation of important biotech molecules: delivery aspects. *Expert Opinion on Drug Delivery*. **2008**;5(4):371-83.

181. Fang C*, et al.* In vivo tumor targeting of tumor necrosis factor-α-loaded stealth nanoparticles: Effect of MePEG molecular weight and particle size. *European Journal of Pharmaceutical Sciences*. **2006**;27(1):27-36.

182. Pozzi D*, et al.* Effect of polyethyleneglycol (PEG) chain length on the bio-nano-interactions between PEGylated lipid nanoparticles and biological fluids: from nanostructure to uptake in cancer cells. *Nanoscale*. **2014**;6(5):2782-92.

183. Saraiva C*, et al.* Nanoparticle-mediated brain drug delivery: Overcoming blood–brain barrier to treat neurodegenerative diseases. *J Controlled Release*. **2016**;235:34-47.

184. Jenkins SI*, et al.* 'Stealth'nanoparticles evade neural immune cells but also evade major brain cell populations: Implications for PEG-based neurotherapeutics. *J Controlled Release*. **2016**;224:136-45.

185. Zakaria HM*, et al.* Small Molecule- and Amino Acid-Induced Aggregation of Gold Nanoparticles. *Langmuir*. **2013**;29(25):7661-73.

186. Chakraborty S*, et al.* Assessment of solubilization characteristics of different surfactants for carvedilol phosphate as a function of pH. *Journal of colloid and interface science*. **2009**;335(2):242-9.

187. Schöttler S*, et al.* Protein adsorption is required for stealth effect of poly(ethylene glycol)- and poly(phosphoester)-coated nanocarriers. *Nat Nano*. **2016**;11(4):372-7.

188. Carbonaro M*, et al.* Secondary structure of food proteins by Fourier transform spectroscopy in the mid-infrared region. *Amino Acids*. **2010**;38(3):679-90.

189. Xu Q*, et al.* Scalable method to produce biodegradable nanoparticles that rapidly penetrate human mucus. *J Controlled Release*. **2013**;170(2):279-86.

190. Zeller A*, et al.* Nanostructured coatings by adhesion of phosphonated polystyrene particles onto titanium surface for implant material applications. *ACS Appl Mater Interfaces*. **2010**;2(8):2421-8.

191. Zhang X*, et al.* Importance of Having Low-Density Functional Groups for Generating High-Performance Semiconducting Polymer Dots. *ACS Nano*. **2012**;6(6):5429-39.

192. Soenen SJ*, et al.* The Cellular Interactions of PEGylated Gold Nanoparticles: Effect of PEGylation on Cellular Uptake and Cytotoxicity. *Particle & Particle Systems Characterization*. **2014**;31(7):794-800.

193. Monopoli MP*, et al.* Biomolecular coronas provide the biological identity of nanosized materials. *Nat Nano*. **2012**;7(12):779-86.

194. Fleischer CC*, et al.* Nanoparticle Surface Charge Mediates the Cellular Receptors Used by Protein–Nanoparticle Complexes. *J Phys Chem B*. **2012**;116(30):8901-7.

195. Lundqvist M*, et al.* Nanoparticle size and surface properties determine the protein corona with possible implications for biological impacts. *Proc Natl Acad Sci*. **2008**;105(38):14265-70.

196. Hirsch V*, et al.* Surface charge of polymer coated SPIONs influences the serum protein adsorption, colloidal stability and subsequent cell interaction in vitro. *Nanoscale*. **2013**;5(9):3723-32.

197. Huang K*, et al.* Charged surface groups of nanoparticles and the adsorbed proteins codetermine the fate of nanoparticles upon interacting with cells. *RSC Adv*. **2016**;6(63):58315-24.

198. Gessner A*, et al.* Nanoparticles with decreasing surface hydrophobicities: influence on plasma protein adsorption. *Int J Pharm*. **2000**;196(2):245-9.

199. Rahman M*, et al.* Protein-nanoparticle interactions: *Springer*; **2013**.

200. Sakulkhu U*, et al.* Protein Corona Composition of Superparamagnetic Iron Oxide Nanoparticles with Various Physico-Chemical Properties and Coatings. *Scientific Reports*. **2014**;4:5020.

201. Pisani C*, et al.* The timeline of corona formation around silica nanocarriers highlights the role of the protein interactome. *Nanoscale*. **2016**.

202. Vroman L*, et al.* Identification of rapid changes at plasma–solid interfaces. *Journal of biomedical materials research*. **1969**;3(1):43-67.

203. Aggarwal P*, et al.* Nanoparticle interaction with plasma proteins as it relates to particle biodistribution, biocompatibility and therapeutic efficacy. *Adv Drug Delivery Rev*. **2009**;61(6):428-37.

204. Jeon SI*, et al.* Protein—surface interactions in the presence of polyethylene oxide. *Journal of Colloid and Interface Science*. **1991**;142(1):149-58.

205. Sant S*, et al.* Effect of polymer architecture on surface properties, plasma protein adsorption, and cellular interactions of pegylated nanoparticles. *Journal of Biomedical Materials Research Part A*. **2008**;87(4):885-95.

206. Winzen S*, et al.* Small Surfactant Concentration Differences Influence Adsorption of Human Serum Albumin on Polystyrene Nanoparticles. *Biomacromolecules*. **2016**;17(11):3845-51.

207. Pelaz B*, et al.* Surface Functionalization of Nanoparticles with Polyethylene Glycol: Effects on Protein Adsorption and Cellular Uptake. *ACS Nano*. **2015**;9(7):6996-7008.

208. Ben- Nun A*, et al.* The rapid isolation of clonable antigen- specific T lymphocyte lines capable of mediating autoimmune encephalomyelitis. *European journal of immunology*. **1981**;11(3):195-9.

209. Vandenbark A*, et al.* A myelin basic protein-specific T lymphocyte line that mediates experimental autoimmune encephalomyelitis. *The Journal of Immunology*. **1985**;135(1):223-8.

210. Man S*, et al.* Inflammatory cell migration into the central nervous system: a few new twists on an old tale. *Brain Pathology*. **2007**;17(2):243-50.

211. Kastenbauer S*, et al.* CSF and serum levels of soluble fractalkine (CX 3 CL1) in inflammatory diseases of the nervous system. *J Neuroimmunol*. **2003**;137(1):210-7.

212. Fong AM*, et al.* Fractalkine and CX3CR1 mediate a novel mechanism of leukocyte capture, firm adhesion, and activation under physiologic flow. *Journal of Experimental Medicine*. **1998**;188(8):1413-9.

213. Bazan JF*, et al.* A new class of membrane-bound chemokine with a CX3C motif. *Nature*. **1997**;385(6617):640.

214. Broux B*, et al.* CX 3 CR1 drives cytotoxic CD4+ CD28− T cells into the brain of multiple sclerosis patients. *Journal of autoimmunity*. **2012**;38(1):10-9.

215. Imai T*, et al.* Identification and molecular characterization of fractalkine receptor CX 3 CR1, which mediates both leukocyte migration and adhesion. *Cell*. **1997**;91(4):521-30.

216. Blauth K*, et al.* The role of fractalkine (CX3CL1) in regulation of CD4+ cell migration to the central nervous system in patients with relapsing–remitting multiple sclerosis. *Clinical Immunology*. **2015**;157(2):121-32.

217. Schulz O*, et al.* Intestinal CD103+, but not CX3CR1+, antigen sampling cells migrate in lymph and serve classical dendritic cell functions. *Journal of Experimental Medicine*. **2009**;206(13):3101-14.

218. Meucci O*, et al.* Expression of CX3CR1 chemokine receptors on neurons and their role in neuronal survival. *Proc Natl Acad Sci*. **2000**;97(14):8075-80.

219. Nishiyori A*, et al.* Localization of fractalkine and CX3CR1 mRNAs in rat brain: does fractalkine play a role in signaling from neuron to microglia? *FEBS letters*. **1998**;429(2):167-72.

220. Hatori K*, et al.* Fractalkine and fractalkine receptors in human neurons and glial cells. *J Neurosci Res*. **2002**;69(3):418-26.

221. Cardona AE*, et al.* Control of microglial neurotoxicity by the fractalkine receptor. *Nat Neurosci*. **2006**;9(7):917.

222. Lovett-Racke AE*, et al.* Decreased dependence of myelin basic protein-reactive T cells on CD28-mediated costimulation in multiple sclerosis patients. A marker of activated/memory T cells. *The Journal of Clinical Investigation*. **1998**;101(4):725-30.

223. Scholz C*, et al.* Expansion of autoreactive T cells in multiple sclerosis is independent of exogenous B7 costimulation. *The Journal of Immunology*. **1998**;160(3):1532-8.

224. Markovic-Plese S*, et al.* CD4+ CD28–costimulation-independent T cells in multiple sclerosis. *Journal of Clinical Investigation*. **2001**;108(8):1185.

225. Broux B*, et al.* Pathogenic features of CD4+ CD28–T cells in immune disorders. *Trends in molecular medicine*. **2012**;18(8):446-53.

226. Yan J*, et al.* Dye-doped nanoparticles for bioanalysis. *Nano Today*. **2007**;2(3):44-50.

227. Karlström S*, et al.* Substituted 7-amino-5-thio-thiazolo [4, 5-d] pyrimidines as potent and selective antagonists of the fractalkine receptor (CX3CR1). *Journal of medicinal chemistry*. **2013**;56(8):3177-90.

228. Wollberg AR*, et al.* Pharmacological inhibition of the chemokine receptor CX3CR1 attenuates disease in a chronic-relapsing rat model for multiple sclerosis. *Proc Natl Acad Sci*. **2014**;111(14):5409-14.

229. Cederblad L*, et al.* AZD8797 is an allosteric non-competitive modulator of the human CX3CR1 receptor. *Biochemical Journal*. **2016**;473(5):641-9.

230. Zaquen N*, et al.* Modifiable poly(p-phenylene vinylene) copolymers towards functional conjugated materials. *Polym Chem*. **2016**;7(29):4771-81.

231. Conde J*, et al.* Revisiting 30 years of biofunctionalization and surface chemistry of inorganic nanoparticles for nanomedicine. *Frontiers in chemistry*. **2014**;2.

232. Suart B. Infrared Spectroscopy: Fundamental and Applications. John Wiley & Sons, Ltd; 2004.

233. Beattie DA*, et al.* In situ particle film ATR FTIR spectroscopy of poly (N-isopropyl acrylamide)(PNIPAM) adsorption onto talc. *Physical Chemistry Chemical Physics*. **2014**;16(45):25143-51.

234. Verhoeckx K*, et al.* The impact of food bioactives on health: *Springer*; **2015**.

235. Weissleder R*, et al.* Imaging macrophages with nanoparticles. *Nature materials*. **2014**;13(2):125-38.

236. Dos Santos T*, et al.* Effects of transport inhibitors on the cellular uptake of carboxylated polystyrene nanoparticles in different cell lines. *PloS one*. **2011**;6(9):e24438.

237. Aderem A*, et al.* Mechanisms of phagocytosis in macrophages. *Annual review of immunology*. **1999**;17(1):593-623.

238. Crone C*, et al.* Electrical resistance of a capillary endothelium. *The Journal of general physiology*. **1981**;77(4):349-71.

239. De Laere M*, et al.* Increased Transendothelial Transport of CCL3 Is Insufficient to Drive Immune Cell Transmigration through the Blood–Brain Barrier under Inflammatory Conditions In Vitro. *Mediators of Inflammation*. **2017**;2017.

240. Weksler B*, et al.* The hCMEC/D3 cell line as a model of the human blood brain barrier. *Fluids and Barriers of the CNS*. **2013**;10(1):16.

Curriculum vitae

Martijn Peters was born on October 23rd 1990 in Genk, Belgium. In 2008 he obtained his degree in General Secondary Education (Algemeen Secundair Onderwijs), study option Math-Sciences (Wetenschappen-Wiskunde) at Humaniora Kindsheid Jesu in Hasselt. In the same year, he began his higher education studies at Hasselt University. In 2013, he graduated summa cum laude as Master in Biomedical Sciences with specialization Bioelectronics and Nanotechnology. His thesis entitled 'Multifunctional Polymer Hybrid Nanoparticles for Biomedical Applications' was conducted at the Institute for Materials Research under supervision of Prof. dr. A. Ethirajan. In October 2013, he started his PhD at the Institute for Materials Research of Hasselt University in the Polymer Reaction Design group with a BOF-scholarship from the university. In January 2014 an IWT scholarship was obtained. During this period, he participated in various assignments and courses framed within the Doctoral School for Sciences and Technology. He was active as a member of different teaching teams of various courses in the study programs of Biomedical Sciences. In addition he was an elected member in various policy councils within the university, like board of directors, doctoral school board and faculty council. The results obtained during his PhD work were partially published in international journals and presented on various (inter)national conferences. Also, he presented his scientific work to a lay audience on numerous occasions as a multiple-award winning popular science communicator.

Bibliography

Publications

Publications from this work

- M. Peters, N. Zaquen, L. D'Olieslaeger, H. Bové, D. Vanderzande, N. Hellings, T. Junkers, A. Ethirajan. *PPV-Based Conjugated Polymer Nanoparticles as a Versatile Bioimaging Probe: A Closer Look at the Inherent Optical Properties and Nanoparticle–Cell Interactions.* Biomacromolecules (2016); 17 (8); 2562-2571.

- M. Peters, S. Seneca, N. Hellings, T. Junkers, A. Ethirajan*. Size-Dependent properties of functional PPV-based conjugated polymer nanoparticles for bioimaging*. Manuscript submitted.

- M. Peters, D. Desta, G. Reekmans, P. Adriaensens, J-P. Noben, N. Hellings, T. Junkers, A. Ethirajan. *PEGylation of Functional PPV-Based Conjugated Polymer Nanoparticles: Implications on the Synthetic and Biological Identity.* Manuscript submitted.

Publications from collaborative projects

- S. Kuypers, S. Pramanik, L. D'Olieslaeger, G. Reekmans, M. Peters, J. D'Haen, D. Vanderzande, T. Junkers, P. Adriaensens, A. Ethirajan. *Interfacial thiol-isocyanate reactions for functional nanocarriers: a facile route towards tunable morphologies and hydrophilic payload encapsulation.* Chemical Communications (2015), 51, 15858-15861.
- S. Pramanik, S. Seneca, M. Peters, L. D'Olieslaeger, G. Reekmans, D. Vanderzande, P. Adriaensens, A. Ethirajan. *pH responsive release of hydrophilic payload using biodegradable nanocarriers formed via an interfacial reaction*. Manuscript to be submitted.
- H. Bové, J. Devoght, L. Rasking, M. Peters, A. Jorge-Peñas, H. Van Oosterwyck, M. Roeffaers, M. Ameloot. *Polluting Combustion-Derived Particles Inhibit Human Lung Fibroblast-Mediated Matrix Remodeling via an Oxidant- and Size-Dependent Mechanism at Relevant Doses*. Manuscript submitted.

Conference contributions

Oral presentations:

M. Peters, N. Zaquen, L. D'Olieslaeger, N. Hellings, T. Junkers, A. Ethirajan. *The Dawn of a New Light: PPV-Based Bioimaging Probes*. ChemCYS. Blankenberge, Belgium. March 16th-18th, 2016.

M. Peters, D. Desta, N. Zaquen, L. D'Olieslaeger, G. Reekmans, P. Adriaensens, J-P. Noben, N. Hellings, T. Junkers, A. Ethirajan. *The dawn of a new light: Functionalized PPV-based bioimaging probes*. 7th International Colloids Conference. Sitges, Spain. June 18th-20th, 2017.

Poster presentations:

M. Peters, L. D'Olieslaeger, K. Ranieri, N. Zaquen, C-B. Kowollik, N. Hellings, A. Ethirajan, T. Junkers. Multifunctional Polymer Hybrid Nanoparticles for Biomedical Applications. IAP FS2 7/05 Annual Network Meeting. Ghent, Belgium. September 18th, 2013.

M. Peters, N. Zaquen, L. D'Olieslaeger, N. Hellings, T. Junkers, A. Ethirajan. Poly-(p-phenylene vinylene) based nanoparticles: a versatile bioimaging probe. Annual Meeting of the Belgian Polymer Group. Ghent, Belgium. May 19th-20th, 2014.

M. Peters, N. Zaquen, L. D'Olieslaeger, N. Hellings, T. Junkers, A. Ethirajan. *Poly-(p-phenylene vinylene) based nanoparticles: a versatile bioimaging probe.* Annual Meeting of the Belgian Polymer Group. Ghent, Belgium. May 19th-20th, 2014.

M. Peters, N. Zaquen, L. D'Olieslaeger, N. Hellings, T. Junkers, A. Ethirajan. *Poly-(p-phenylene vinylene) based nanoparticles: a versatile probe for bioimaging.* Advanced Funtional Polymers for Medicine. Liège, Belgium. May 26th-28th 2014.

M. Peters, N. Zaquen, L. D'Olieslaeger, N. Hellings, T. Junkers, A. Ethirajan. *Poly-(p-phenylene vinylene) based nanoparticles: a versatile probe for bioimaging.* µFiBR. Diepenbeek, Belgium. October 3rd, 2014.

M. Peters, N. Zaquen, L. D'Olieslaeger, N. Hellings, T. Junkers, A. Ethirajan. *Shining a Light on Using PPV-based Nanoparticles as a Versatile Bioimaging Probe*. IAP FS2 7/05 Annual Network Meeting. Hasselt, Belgium. September 11th, 2015.

M. Peters, N. Zaquen, L. D'Olieslaeger, N. Hellings, T. Junkers, A. Ethirajan. *Poly-(p-phenylene vinylene) based nanoparticles: a versatile bioimaging probe.* Annual Meeting of the Belgian Polymer Group. Houffalize, Belgium. May 18th-19th, 2015.

M. Peters, N. Zaquen, L. D'Olieslaeger, N. Hellings, T. Junkers, A. Ethirajan. *Poly-(p-phenylene vinylene) based nanoparticles: a versatile probe for bioimaging.* Biomedica. Genk, Belgium. June 2nd-3rd, 2015.

M. Peters, N. Zaquen, L. D'Olieslaeger, G. Reekmans, P. Adriaensens, J-P. Noben, N. Hellings, T. Junkers, A. Ethirajan. *The Dawn of a New Light: Functionalized PPV-based Bioimaging Probes*. IAP FS2 7/05 Annual Network Meeting. Liège, Belgium. September 12th, 2016.

M. Peters, N. Zaquen, L. D'Olieslaeger, N. Hellings, T. Junkers, A. Ethirajan. *The Dawn of a New Light: PPV-based Bioimaging Probes*. Annual Meeting of the Belgian Polymer Group. Hasselt, Belgium. May 23rd-24th, 2016.

Bursaries:

BOF PhD Fellowship entitled "Design and Synthesis of Multifunctional PPV-based Nanoparticles for Multiple Sclerosis Research" for 2 x 2 years starting at October 1st, 2013.

IWT PhD Fellowship entitled "Design and Synthesis of Multifunctional PPV-based Nanoparticles for Multiple Sclerosis Research" for 2 x 2 years starting at January 1st, 2014.

Dankwoord

Dankwoord

Een experiment kan je in je eentje tot een goed einde brengen, een doctoraat echter niet. De afgelopen 4 jaren vormden een onvergetelijke levenservaring, één die ik nooit of te nimmer had kunnen doorstaan zonder de steun en begeleiding van heel wat mensen. Want vele handen maken wetenschappelijk werk. Daarom zou ik deze thesis in schoonheid willen eindigen en de laatste pagina's willen opdragen aan alle personen zonder wie dit alles nooit mogelijk was geweest.

Allereerst wil ik mijn promotor, Prof. Dr Tanja Junkers bedanken. Bedankt voor het vertrouwen in mijn capaciteiten als wetenschapper en mij de mogelijkheid te geven om zelfstandig het pad van een doctoraatsonderzoek te bewandelen. Natuurlijk ook bedankt voor alle wetenschappelijke input en voor de warme ontvangst in de PRD-groep. Het was een fantastische belevenis om deel uit te maken van deze wetenschappelijke bende en dat is mede dankzij jou. Zelden heb ik een groepsleidster mogen meemaken die zo intens bezig is met de ontwikkeling van haar groep alsook van degene die er deel van uitmaken. Van meetings en strategiedagen (inclusief geweldige wijnproefsessies) tot intensieve begeleiding op persoonlijk niveau, een doctoraatstudent mag zich gelukkig prijzen als hij/zij bij jou in de groep terecht komt. Het heeft mij altijd een zelfzeker en gerust gevoel gegeven te weten dat jouw deur altijd voor ons openstaat. Natuurlijk ook heel erg bedankt voor alle steun in mijn "wetenschapscommunicatie shenanigans", wat niet altijd vanzelfsprekend moet geweest zijn. Ik wens jou en de PRD-groep dan ook het beste toe in "the land down under"!

Vervolgens wil ik mijn twee copromotoren bedanken, Prof. Dr Anitha Ethirajan en Prof. Dr Niels Hellings. Anitha, many thanks for introducing me into the wonderful world of nanotechnology. Without you I would have never been able to do this amazing interdisciplinary research. You have always pushed me to work harder and think more critically. I have learned a lot from you during our many interesting discussions. Niels, van harte bedankt voor de wetenschappelijke input en vooral het enthousiasme voor mijn project wat altijd een zeer inspirerend en aanstekelijk effect had. Bedankt voor het vertrouwen en steeds klaar te staan met raad en daad. Ik heb mij altijd zeer welkom gevoeld op BIOMED dankzij jou en je groep.

Ook vond ik het geweldig dat we samen het vak 'popular science communication' hebben kunnen oprichten in de master Biomedische Wetenschappen.

Ik wil ook graag de leden van mijn doctoraatscommissie en -jury van harte bedanken voor de bereidheid tot het evalueren van mijn werk. Een speciale vermelding voor Prof Dr Vanderzande, zonder wie de sulfinyl precursor route er nooit zou zijn geweest. Zonder hem had ik nooit op dit interessante project kunnen werken. Een andere essentieel onderdeel van onderzoek is financiering. Ik wil dan ook het IWT en de UHasselt (BOF) bedanken voor de financiële ondersteuning tijdens mijn doctoraat.

Natuurlijk mag ik niet de vele helpende handen in het lab vergeten. Lien, bedankt voor alle tips & tricks die je mij hebt aangeleerd over de synthese van nanodeeltjes tijdens mijn masterthesis. Ook bedankt voor de vele TEM-beeldjes die je voor mij hebt opgenomen tijdens mijn doctoraat. Deze zware taak belandde vervolgens op de schouders van Senne toen jij vertrok. Senne, bedankt voor de vele uren die ook jij gespendeerd hebt achter de TEM op zoek naar mijn 'kleinere nanodeeltjes'. Uiteindelijk hebben we ze toch maar mooi gevonden. Ook een dikke merci aan Neomy voor het synthetiseren van de materialen voor mijn doctoraatsonderzoek en voor het altijd voor mij klaarstaan als ik vragen had over PPV's. Derese, thank you very much for your help with the AFM measurements and the friendly conversations, which I enjoyed a lot. Bieke, heel erg bedankt voor alle hulp bij de experimenten van het laatste hoofdstuk. Jouw enorme kennis van $CD4^+CD28^-$ T-cellen heeft ervoor gezorgd dat we nog zo veel succesvolle experimenten hebben kunnen verwezenlijken in zo een korte tijd. Natuurlijk ook bedankt aan Gunter en Peter alsook Erik en Jean-Paul voor de hulp bij de NMR- en massaspectrometriemetingen. Er zijn ook vele mensen die onzichtbaar achter de schermen werken om ervoor te zorgen dat we ons onbezorgd op ons onderzoek kunnen storten en die ik daarom zeker niet mag vergeten te bedanken. Daarom nog een dikke merci aan Laurence, Katrien, Huguette, Johnny, Christel[2] (Willems en Bocken) en Iris. Ook mag ik Eugene natuurlijk niet vergeten voor zijn onvermoeide bijstand tijdens het befaamde "exploratiepracticum". We hebben bij momenten serieus wat (groen) gelachen. Bedankt ook aan alle stagestudenten die ik doorheen de jaren heb mogen begeleiden en die mij altijd goed hebben

vooruitgeholpen. Het is geweldig om te zien hoe velen van jullie zijn uitgegroeid tot fantastische wetenschappers.

Door het interdisciplinaire karakter van mijn onderzoek heb ik op verschillende plaatsen en in verschillende groepen mogen vertoeven. Daarom zou ik ook deze graag willen bedanken. Allereerst bedankt aan de volledige PRD-groep (PRD!PRD!PRD!). You guys are awesome. Ik heb in 4 jaar tijd heel wat nieuwe mensen leren kennen, stuk voor stuk unieke personen en wetenschappers. De geweldige sfeer, hilarische autoritten, onze stiekeme interieurarchitectuur ambities die doorschemerde in het continu herschikken van ons kantoor hebben er altijd voor gezorgd dat ik mij enorm geamuseerd heb tijdens mijn doctoraat. Ik wens jullie dan ook allemaal het beste toe! Natuurlijk ook bedankt aan de rest van de OBPC'ers voor de heerlijke frietnamiddagen, groepsactiviteiten, kerstdiners, voetbalweddenschappen, enz. Merci aan de immunologiegroep om mij zo hartelijk te verwelkomen in jullie groep en de fijne sfeer op de bureau en in het labo. Tot slot, ook bedankt aan de gloednieuwe NSI-groep en de biofysicagroep voor alle hulp bij mijn microscopie-experimenten, gezellig lunches en na de uren uitstapjes.

Natuurlijk zijn er nog veel meer mensen aan de UHasselt, instituten, administratieve diensten en doctoral schools die ik nog niet opgesomd heb. Maar als ik dit zou doen dan zou dit dankwoord ongetwijfeld een nieuw thesisboekje worden. Dus bij deze, allemaal enorm bedankt voor alle ondersteuning tijdens de afgelopen 4 jaar.

Dit brengt mij tot het slot van mijn dankwoord waarbij ik mij graag zou richten tot de meest dierbare personen in mijn leven.

Mama en papa, een heel dikke merci voor alle steun tijdens mijn volledige educatieve carrière en ook daarbuiten. Bedankt voor de warme thuisomgeving en om altijd in mij te blijven geloven. Zonder jullie was ik nooit zo ver geraakt. Ook een dikke merci aan de zus, Kai en aan Boni voor de zondagse telefoontjes waarin je ons eraan herinnerde dat we af en toe ook eens moesten ontspannen :-).

Ook mag ik natuurlijk de schoonfamilie niet vergeten. Patric en Brigitte, heel erg bedankt voor de logistieke en emotionele ondersteuning tijdens de afgelopen 4 jaar en voor mij op te nemen in jullie familie. Laurenz, bedankt voor alle hilarische ontspannende momenten en steun. Tanya, though you have only joined the family recently, I am very happy that you did and want to thank you for all the kind and motivating words (#PhDlife).

"Save the best for last" zeggen ze altijd en dat heb dan ook gedaan. De laatste alinea (al verdien je zoveel meer) heb ik speciaal gereserveerd voor mijn geweldige vrouw, Hannelore. Bedankt voor alle onvoorwaardelijke liefde en steun tijdens de afgelopen jaren. Voor het, luisterende oor tijdens onze stoom aflatende wandeltochtjes en alle begrip wat je toonde als het een stressvolle periode was. We zijn er samen toch maar mooi weer eens doorgeraakt! Je bent de beste steun en toeverlaat die iemand zich maar kan wensen. Ook bedankt voor het mooiste moment uit mijn hele PhD-periode, onze trouw. You are simply the best! My first, my last, my everything. Love you.